MODE-LOCKED COLOUR-CENTRE LASERS AND THEIR APPLICATION

Robert S. Grant

A Thesis Submitted for the Degree of PhD
at the
University of St Andrews

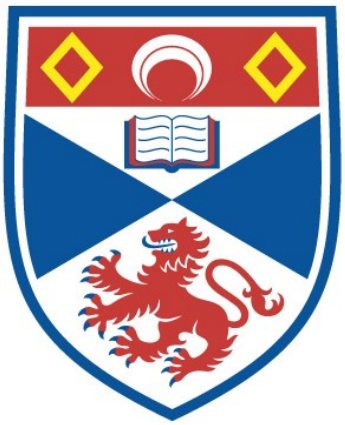

1992

MODE-LOCKED COLOUR-CENTRE LASERS AND THEIR APPLICATION

Thesis submitted for the degree of Doctor of Philosophy

of the University of St. Andrews by

Robert S. Grant, B.Sc.

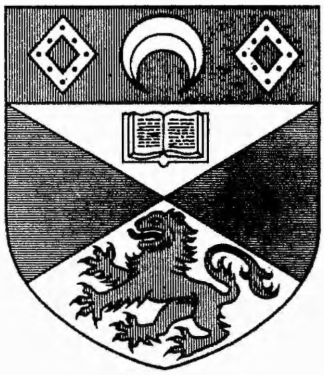

J. F. Allen Physics Research Laboratories
Department of Physics and Astronomy
University of St. Andrews
North Haugh
St. Andrews
Scotland KY16 9SS

September 1991

ProQuest LLC.
789 East Eisenhower Parkway
P.O. Box 1346
Ann Arbor, MI 48106 – 1346

Declaration

I Robert S. Grant hereby certify that this thesis has been composed by myself, that it is a record of my own work, and that it has not been accepted in partial or complete fulfilment of any other degree of professional qualification.

I was admitted to the Faculty of Science of the University of St. Andrews under Ordinance General No 12 on 1 October 1987.

Signed Date 30/9/91

I hereby certify that the candidate has fulfilled the conditions of the Resolution and Regulations appropriate to the Degree of Ph.D.

Signature of Supervisor Date 30/09/91.

Copyright

Abstract

The passive and coupled-cavity mode locking of a LiF:F_2^+ colour-centre laser was studied. Pulses of less than 180 fs were obtained in the 0.85 μm spectral region by passive mode-locking using the saturable absorber dye IR140. Coupled-cavity mode locking, where a length of optical fibre was incorporated in an external control cavity, resulted in the generation of 1.5 ps duration pulses.

Active and coupled-cavity techniques were applied to a KCl:$Tl^0(1)$ colour-centre laser operating in the 1.5 μm spectral region. Coupled-cavity mode locking was obtained using either Fabry-Perot or Michelson interferometer arrangements. Although either arrangement generated similar pulse durations, the Michelson scheme was found to be more stable. Pulse durations of less than 100 fs were routinely obtained from either arrangement by using small-core fibre in which the dispersion minimum coincided with the laser operating wavelength.

The KCl:$Tl^0(1)$ laser was used to study various absorptive and refractive nonlinearities in a 1.5 μm InGaAsP optical amplifier. Pulse distortion caused by gain saturation and loss saturation was studied in the temporal and spectral domains. In addition, cross-phase modulation related to gain saturation was investigated. Self-phase modulation caused by an ultrafast refractive nonlinearity has been observed for the first time, and its nonlinear coefficient n_2 was deduced to be -2×10^{-11} cm^2W^{-1}.

Coupled-cavity mode locking of the KCl:$Tl^0(1)$ laser was also obtained when the InGaAsP amplifier was used, with pulses as short as 280 fs. Self-starting operation was achieved by eliminating parasitic optical feedback from the device facets. Mode locking was observed for amplifier drive currents either above or below transparency, suggesting that saturable gain and saturable loss respectively were the dominant nonlinearities exploited.

The synchronous and coupled-cavity mode locking of a NaCl:OH^- laser operating near 1.57 μm was investigated. Coupled-cavity mode locking using an optical fibre was achieved, but was accompanied by a sawtooth modulation in power output (or pulse duration) related to the short gain storage time of NaCl:OH^-. This was circumvented by substituting the InGaAsP amplifier for the fibre to obtain self-starting mode locking.

Contents

1 Introduction

1.1 Background

Mode-locked lasers have become invaluable tools in many areas of scientific research.[1,2] Optical pulses with durations as short as a few tens of femtoseconds can now be obtained routinely at a number of wavelengths. These ultrashort pulses have a variety of applications, not only in physics but within optoelectronics, chemistry and biology. The field of time-domain spectroscopy has evolved rapidly, with the development of many different techniques to study ultrafast light-matter interactions. Nonlinear propagation of pulses is of interest for optical fibre transmission systems, and attention is being focussed on ultrafast all-optical switching devices using silica, semiconductor or polymer waveguide structures.

The growing list of applications places new demands upon the performance of ultrashort pulse lasers. These include further reductions in pulse duration, increases in pulse energy, and the extension of spectral coverage. Within the visible spectral region, the continuous wave (CW) mode-locked dye laser has been of fundamental importance during the last two decades. Its development, along with amplifiers and pulse compression techniques, has resulted in the generation of optical pulses as short as 6 fs,[3] and femtosecond time-domain techniques have thus become well established.

The development of CW colour-centre lasers has provided picosecond and femtosecond sources for experiments within the near infrared.[4] Like organic dyes, colour-centres in ionic crystals have extensive, homogeneously broadened emission bands, attractive for both tunability and mode locking. Unfortunately, colour-centre crystals generally require to be maintained at 77 K to ensure optimum efficiency, and to minimise bleaching of the centres. The associated cryogenic hardware might be regarded as an unwelcome source of

practical problems, but there are few sources which are competitive within the near-infrared spectral region.

Although titanium-doped sapphire lasers have recently replaced both colour-centre and dye lasers in the 0.7-1.1 μm region, at longer wavelengths around 1.5 μm, the colour-centre laser retains significant advantages over its only realistic rival, the erbium-doped-fibre laser. These parameters include tunability over bandwidths in excess of 100 nm, or pulse durations of less than 100 fs combined with average powers in excess of 50 mW. This spectral region is of particular interest for optical telecommunications research due to the low-loss window in silica-based optical fibres at this wavelength. Colour-centre lasers have been used extensively to study linear and nonlinear pulse propagation in fibres. This has resulted in the demonstration of the potential of optical solitons for trans-oceanic transmission.[5] In addition, colour-centre lasers have also been used to investigate the properties of semiconductor devices, including lasers, amplifiers, modulators, switches[6] and detectors.

In this chapter the optical characteristics of colour-centres are discussed and appropriate laser resonator designs for CW operation, together with techniques for mode locking and pulse measurement are described. Where appropriate, specific technical details of the equipment used in this work have been included. In the final section the propagation of pulses is discussed with particular reference to optical fibres.

1.2 Optical characteristics of colour centres

Colour centres[4,7-9] are point defects (vacancies) in the lattices of ionic crystals formed either during the growth process or by bombardment with high energy particles. Many of these centres have optical absorption bands within the visible part of the spectrum, normally transparent in these crystals, hence the name colour centre. The basic F centre (F for *Farbe*) is an anion vacancy (the site of a halide ion in alkali-halide crystals) containing a single electron, maintaining overall charge neutrality in the vicinity of the vacancy. The electronic states or energy levels of this centre may be likened to those for a particle in a box. This simple model predicts the decrease in energy of the fundamental absorption band with increase in lattice spacing, a trend which is experimentally observed in the alkali-halide crystals from LiF to RbI, and also applies to the more complex aggregate centres formed by

two or more adjacent F centres. This has important implications for lasers based on colour-centres. By exchanging the alkali-halide lattice, different spectral regions can be accessed with the same class of colour-centre.

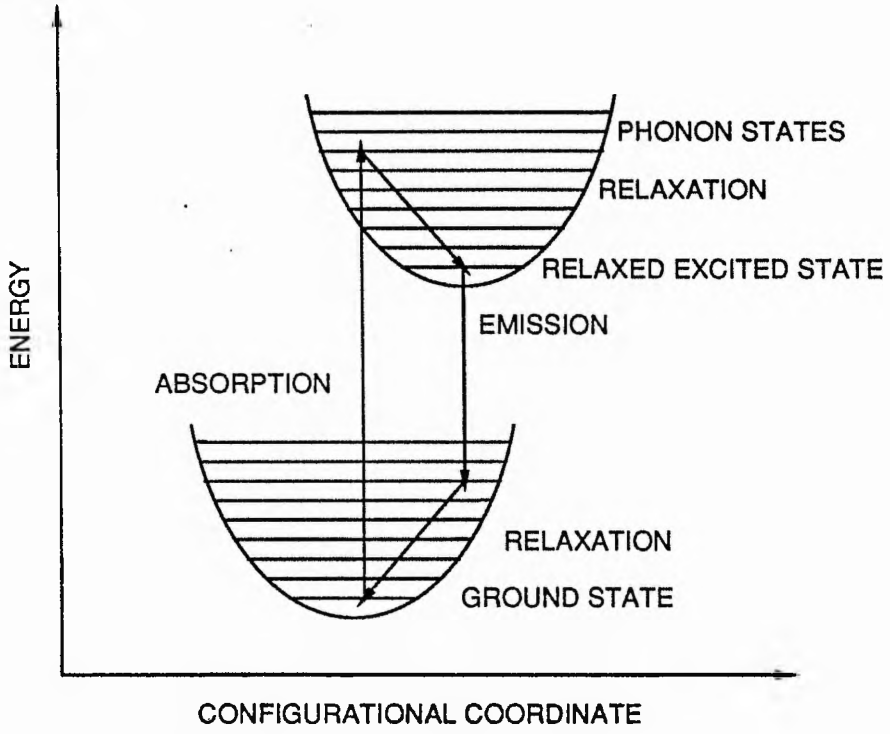

Figure 1.1 Franck-Condon diagram for two vibronically broadened electronic levels, showing the absorption and emission cycle.

Unlike the energy levels of a free atom which are sharply defined, the electronic levels of a colour centre are broadened due to vibrations of the crystal lattice. The vibronic broadening of transitions in colour-centres can be understood by considering the configurational coordinate diagram shown in Figure 1.1, where configurational coordinate refers to the distance from the lattice vacancy to the first shell of neighbouring ions. The electronic states of the centre each have an associated potential well, within which the phonon energy states are represented by horizontal lines. When the harmonic oscillator approximation is applied, the vibronic levels become equally spaced in the parabolic wells. Each phonon level has an associated wave function, and therefore the probability of the upper state absorbing photons is determined by the overlap integral of its wave function with the wave function of the lowest level of the ground state, ie. the Franck-Condon principle. Once the electron is in the excited state, phonons are emitted to bring the electron down to the first

level of the excited state, called the relaxed excited state (RES), before photon emission. The broadening mechanism of the emission line is similar, with the choice of phonon level in the ground state determined by an overlap integral. Without the vibronic coupling to the lattice, not only would the absorption and emission lines be narrow, but there would be no Stokes shift between them. The Stokes shift modifies the simple two level electronic transition into a four level system. The broadening of both the absorption and emission lines is caused by the spread of different phonon numbers involved in the relaxation, each having a statistical probability. Therefore, each colour-centre can absorb or emit at any wavelength within the respective bands, which implies homogeneous broadening.

The vibronic broadening and the Stokes shift of colour-centre transitions is characterised by the Huang-Rhys factor S, which represents the *mean* number of phonons coupled to the electronic states. The basic F centre in alkali-halide crystals is strongly coupled to the lattice and consequently S has a value of 30 to 50 depending on the particular lattice. Large values of S cause a large Stokes shift between the absorption and emission bands, which have approximately Gaussian shapes. On the other hand, the transitions of aggregate centres tend to have much smaller S factors, resulting in a greatly reduced Stokes shift. With S as low as 2 or 3, there will be a probability of some transitions being purely electronic. This particular transition appears as a sharp feature in both the absorption and emission bands, commonly known as the zero-phonon line (ZPL) (see, for example reference 10). In addition, the absorption and the emission bands have a characteristic asymmetric shape, known as Pekarian, and are a mirror image of each other upon reflection around the ZPL. The one and two phonon lines are not as distinct, particularly with increasing temperature, since there are many vibrational modes with different phonon energies and directions in the lattice.

Unfortunately, the basic F centre in alkali-halide crystals is unsuitable as a laser gain medium. For many lattices, luminescence is not observed, since the centre can de-excite nonradiatively. This occurs because the two parabolic wells intersect at an energy lower than the absorption energy. In those lattices where luminescence is observed, the RES is spatially diffuse and its wave function has a small overlap with the terminal state. Furthermore, the RES lies close to the conduction band, and thermal or optical ionisation can readily occur.

The F_A centre, an F centre adjacent to an alkali-metal ion, is suitable for laser use if it relaxes into a double well configuration, known as the $F_A(II)$ centre.[11-14] The impurity ion, usually Li^+, serves to pin down the centre preventing diffusion through the lattice and also causes splitting of the broad absorption band. It retains the large Stokes shift of the F centre with absorption bands in the visible and emission in the 2-4 μm region. The centre can flip its orientation under optical pumping and the pump polarisation must be carefully chosen to give continual reorientation. In addition, its luminescence decay time is temperature dependent down to 4 K indicating the presence of a nonradiative decay path (and hence a quantum efficiency less than unity). The closely related $F_B(II)$ centre consists of an F centre adjacent to two Na^+ ion impurities.

Of the aggregate centres, the singly ionised F_2^+ centre is of greatest interest for CW operation, because it has only a single electron.[13,15-17] Therefore, metastable triplet and quartet type states which cause bottlenecks in the laser cycle are avoided. Its Huang-Rhys factor is around 5 or 6, hence the Stokes shift of the emission band is small, but sufficient to avoid self-absorption. The F_2^+ centre is formed when F centres, formed usually by irradiation at low temperatures, coalesce when the crystal is warmed to room temperature. The crystal is then cooled to 77 K to prevent further aggregation, and results in a quantum efficiency close to unity. To ensure a high ratio of F_2^+ to F_2 centres, the crystal is usually doped with divalent metal ions or OH^- ions, which trap free electrons. Unfortunately, the F_2^+ centre is unstable under intense optical pumping and can reorient and walk through the crystal (this will be discussed with particular reference to the F_2^+ centre in LiF in chapter 2).

Stable F_2^+ -like centres, denoted by $(F_2^+)^*$ and $(F_2^+)^{**}$, have been observed in heavily irradiated NaF, where the respective dopants are divalent metal ions[18] and OH^- ions.[19] More recent spectroscopic studies indicate that these dopant ions perform a different role in NaF, and may be located adjacent to the centres.[20] In additively-coloured crystals, dopant ions can pin down and stabilise F_2^+ -like centres, as with the $F_A(II)$ centres. Impurity alkali-metal ion dopants, eg. Li in KCl, results in $(F_2^+)_A$ centres which emit largely at wavelengths between 2 and 4 μm.[21-23] The addition of OH^- ions (eg. by adding NaOH to NaCl at the melt stage) causes the formation of stable $(F_2^+)_H$ centres associated with O^{2-} ions.[24] This centre will be discussed in chapter 6.

The thallium $Tl^0(1)$ centre in KCl:Tl forms the basis of much of the work in this thesis. It is unusual in that its energy level system is closely related to that of a Tl atom, and hence its absorption and emission bands do not alter significantly when the host lattice is exchanged.[25] In addition, although its absorption and emission bands have a small Stokes shift loosely resembling an F_2^+ centre, it has a relatively long decay time and consequently, a gain cross-section almost an order of magnitude smaller. Its properties will be discussed in detail in chapter 3.

The centres described above generally require to be operated at 77 K for optimum efficiency and longevity. Soviet workers have demonstrated room-temperature, pulsed operation of colour-centre lasers using room-temperature stable, multi-electron centres such as the F_2^- centre in LiF. A review of this work can be found in reference 26.

The characteristics of the many colour-centre transitions are ideal for use as laser gain media. The configurational (vibrational) relaxation process occurs within a timescale of a few picoseconds at 4 K,[27] and is expected to be only tens of femtoseconds at 77 K.[28] Since the photon emission process has a much longer decay, many tens of nanoseconds, many of the centres have an ideal 4 level laser system.

Before discussing the design of the colour-centre laser it is useful to estimate the emission cross-section σ_e. For each of the three different centres used in this thesis, σ_e at the peak of the emission band has been calculated using the standard relation (eg. reference 4)

$$\sigma_e = \frac{\lambda^2 A_{21}}{4\pi n^2 \partial\upsilon} \sqrt{\frac{\ln[2]}{\pi}} \qquad (1.1)$$

where A_{21} represents the Einstein coefficient (given by the quantum efficiency divided by the measured luminescence decay time, ie. η/τ_{rad}), λ is the free space wavelength, and n is the crystal refractive index. The emission band is assumed to be Gaussian shaped with a full width at half maximum (FWHM) of $\partial\upsilon$ (in Hz). Typically, for the F_2^+ and related centres, where η is 1, σ_e is approximately 1×10^{-16} cm^2, similar to that of organic dyes. However, since the radiative decay time of laser active colour centres exceeds the resonator round-trip time, the mode-locking properties are generally not identical to dye lasers.

1.3 Colour-centre lasers

The remarkable similarity of colour-centre transitions with those of organic dyes, implies that similar resonator designs may be appropriate. The first reported colour-centre laser used $F_A(II)$ centres in a flashlamp-pumped rod of KCl:Li,[11] analogous to the dye lasers of that period. A few years later, CW operation of dye lasers was achieved, principally* by using resonators where the dye cell was located at a small waist in the cavity, combined with excitation by an argon ion laser.[29,30] The application of these techniques to colour-centre gain media also resulted in CW operation.[12,13] A collinear (or nearly collinear) alignment of the beam of the pumping laser with the intracavity laser beam allows a highly efficient transfer of power. The small-spot in the gain medium ensures high pump intensities, and hence maximises the small-signal gain.

Typical colour-centre laser crystals are 2 mm thick, with a path length when oriented at Brewster's angle of ~ 2.5 mm. A high optical density at the pump wavelength is desirable because, apart from efficient use of the pump light, it can also reduce the effective pumped volume and hence the threshold pump power, however, too high a density may result in significant concentrations of parasitic centres which absorb in the emission band. Typical optical densities at the pump wavelength range from approximately 0.5 to 2.

Analysis of laser cavities

Although the small spot sizes necessary for the CW operation of dye lasers and colour-centre lasers may be obtained by using a near concentric resonator,[12] this arrangement is sensitive to slight misalignment, and alternative multi-mirror small-spot cavities have been developed. The ubiquitous three mirror cavity, illustrated in Figure 1.2 (a), allows a small beam waist at the gain, yet is relatively easy to align, and furthermore it can be extended to lengths exceeding 1 m to incorporate tuning elements, or to facilitate mode locking.[31] Mathematically, the Gaussian beam within such a cavity can be analysed by reducing the three mirrors to two. This is achieved by imaging the output coupler mirror through the central folding mirror using simple equations.[32] It is found that whilst the stability of the cavity is relatively insensitive to the length of the long arm, the length of the short arm which

* In addition, the dye had to be flowed to allow recovery from a triplet state bottleneck.

includes the gain may be adjusted over a range of only 2 mm or so. The basic principles of these cavities can be illustrated by considering a few simple resonator configurations with dimensions similar to those used in the experiments described in this thesis.

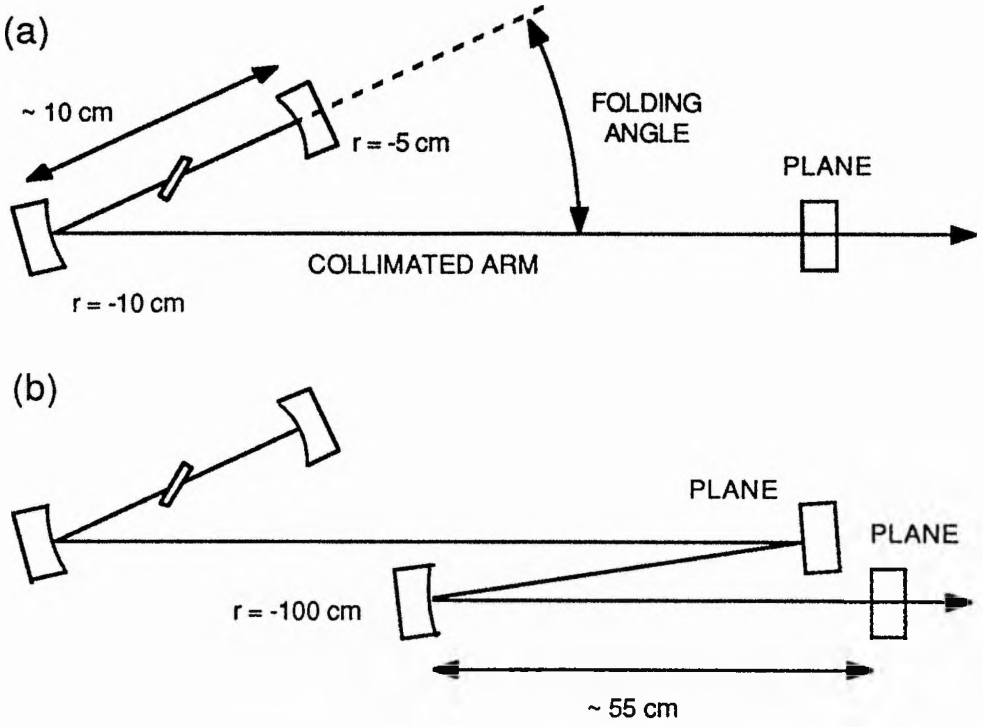

Figure 1.2 (a) The conventional three mirror cavity. (b) When relatively long cavity lengths were required, it was usually extended by incorporating a 1 m radius of curvature mirror in the long arm.

In Figure 1.3 (a) the beam waist size, or spot size, and its distance from the folding mirror is calculated for a three mirror cavity with a total cavity length of 91.5 cm. This distance corresponds to one half of the pump laser length, and is suitable for synchronous mode locking. In all the resonator calculations, the wavelength is assumed to be 1.5 μm. The folding (or collimating) mirror has a focal length of 5 cm and the curved end mirror has a radius of curvature of 5 cm. When these two curved mirrors are exactly 10 cm apart, the beam in the long arm is collimated and resonator is on one edge of its stability zone, and the spot size in the gain tends to zero. As the separation between the two curved mirrors is increased, the spot size rises to a few tens of microns, and then falls to zero as the other edge of the stability zone is reached. In this condition, the waist on the (plane) output coupler tends to zero.

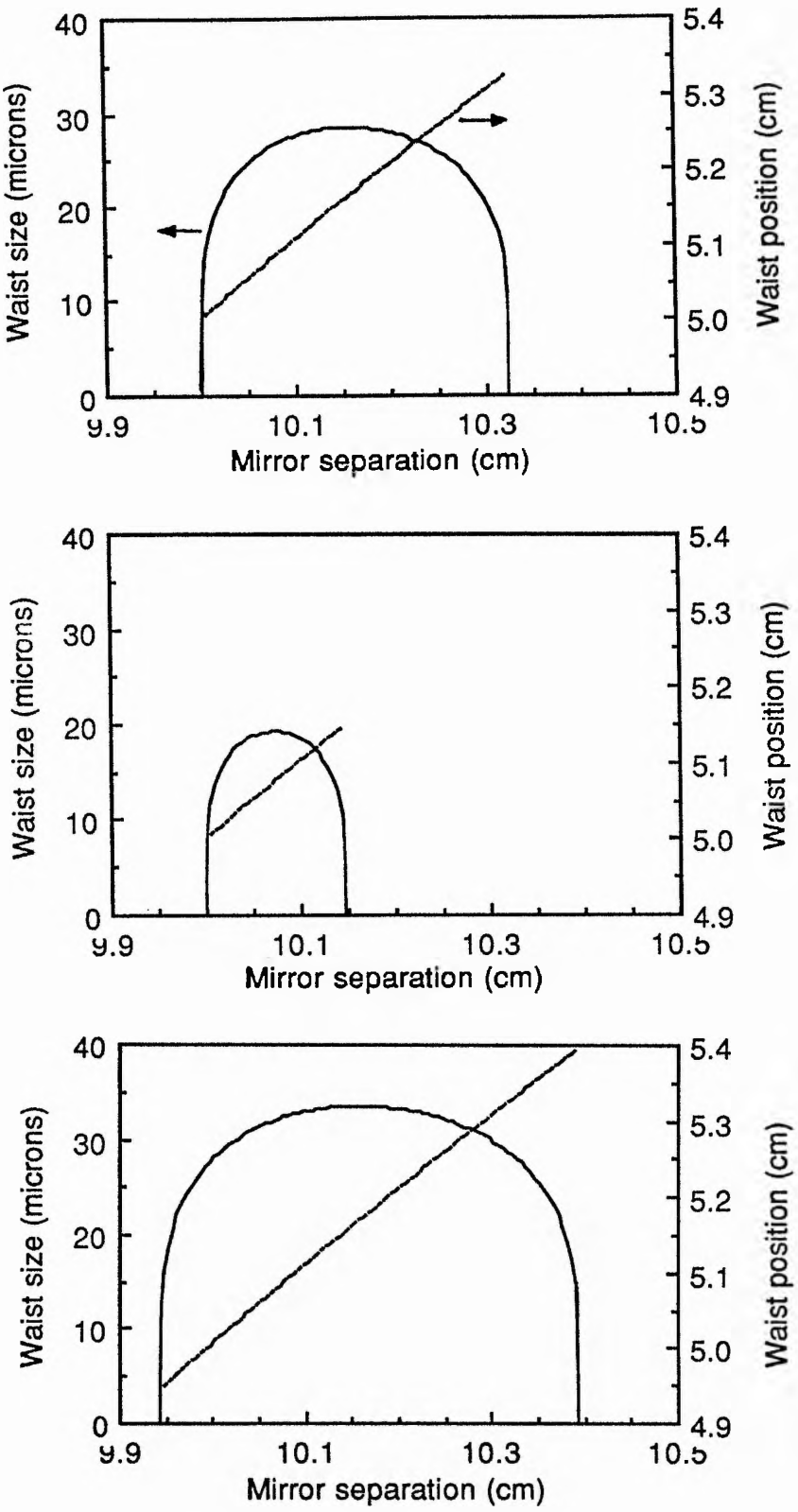

Figure 1.3 Calculated spot sizes for three mirror cavities of 91.5 cm (a) and 183 cm (b) overall length. (c) By incorporating a long radius of curvature mirror into the 183 cm long cavity, the stability characteristics and spot sizes resemble those of the shorter cavity, cf. (a). The waist position is calculated relative to the folding mirror.

The calculation is repeated (see Figure 1.3 (b)) for the case where the length of the long arm has been increased such that the total cavity length is now 183 cm. By comparing the top two graphs, it can be seen that the range of adjustment of the separation of the curved mirrors (and the beam waist) is reduced when the cavity is lengthened. The reduction in waist size can result in poor mode matching of the intracavity beam with the pump beam, and consequently lead to an increased threshold and loss of output power. The smaller stability range makes adjustment more critical, especially if the cavity is not properly compensated for astigmatism which will reduce the stability range even further.

A solution to this problem is to incorporate a concave, long-focal-length mirror in the long arm, as depicted in Figure 1.2 (b). Experimentally, the best results were obtained with a concave mirror of 50 cm focal length located around 55 cm from the plane output coupler. This can be analysed by imaging the output coupler through the 50 cm focal length mirror and then imaging the resultant mirror through the 5 cm focal length folding mirror as described before. This arrangement gives a waist size similar to that of the short cavity and an even larger stability range, see Figure 1.3 (c).

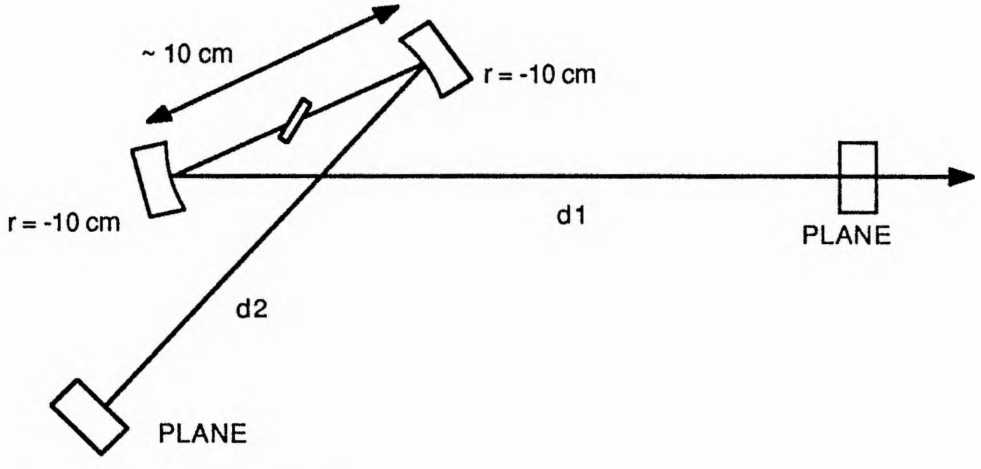

Figure 1.4 Four mirror X type cavity.

An alternative cavity is the four mirror X (or bow tie) type cavity, shown in Figure 1.4. The waist sizes have been calculated for two variants. Figure 1.5 (a) shows the waist size when the long arms are identical in length, and the total resonator length is 183 cm. It can be seen that this configuration gives larger waist sizes than the three mirror cavity of identical length. Strong asymmetry in the arm lengths causes the bisection of the stability

zone (see Figure 1.5 (b)). The zone where the folding mirrors are closer together gives approximately collimated beams in the two arms. In the second zone, with the folding mirrors further apart, the beams tend to be focussed on the two (plane) end mirrors.

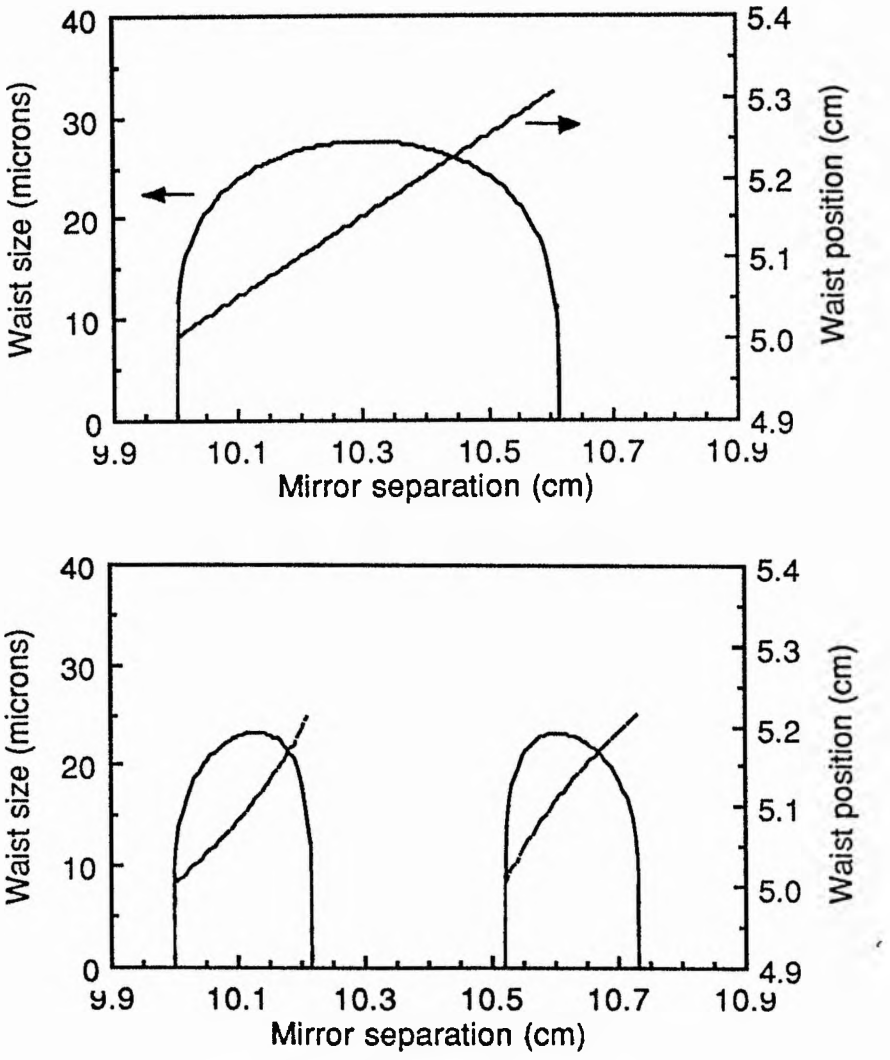

Figure 1.5 Calculated waist sizes and positions for two arrangements of a 4 mirror cavity, both of 183 cm overall length. (a) When the cavity is symmetrical, only one stability zone exists. (b) With strongly asymmetric arm lengths (d1 = 100 cm, d2 = 50 cm), the stability zone bisects. The waist position is given relative to the folding mirror adjacent to the longer of the two arms.

The astigmatism caused by the Brewster-angled colour-centre crystal can be compensated by adjusting the angle of incidence on the folding mirror(s).[32] The angle of incidence ϕ which corrects the astigmatism can be found by solving a pair of equations which describe the contributions of the various astigmatic elements to the path length between the

two curved mirrors in the sagittal and tangential ray planes. The cryostats used in this work were unusual in that the vacuum chamber windows were located in the short arm between the two curved mirrors, and thus contributed considerable astigmatism. It will be shown later that windows (or any other elements) located in the long arm have a much smaller effect on overall cavity astigmatism. For the basic three mirror cavity, incorporating a crystal and the two windows, the two equations are

sagittal rays:

$$d_{air} + \frac{t\sqrt{n_c^2 + 1}}{n_c^2} + \frac{2\,t\sqrt{n_g^2 + 1}}{n_g^2} = R_1 + \frac{f}{\cos\phi} + \delta_x \qquad (1.2)$$

tangential rays:

$$d_{air} + \frac{t\sqrt{n_c^2 + 1}}{n_c^4} + \frac{2\,t\sqrt{n_g^2 + 1}}{n_g^4} = R_1 + f\cos\phi + \delta_y \qquad (1.3)$$

where t is the thickness of the silica windows and the colour-centre crystal, ie. 2 mm, R_1 is the radius of the curved end mirror, 50 mm; f is the focal length of the folding mirror, 50 mm. The terms δ_x and δ_y represent the fine adjustment of the separation of the curved mirrors. The refractive indices of the colour-centre crystal and the windows are n_c and n_g respectively. The equations are solved by subtracting one from the other to eliminate the terms common to both, such as R_1 and d_{air}, and setting $\delta_x = \delta_y$ for compensation. The resulting quadratic in terms of $\cos\phi$ can then be easily solved. Assuming $n_g \approx 1.45$ (fused silica) and $n_c \approx 1.47$ (KCl), the angle of incidence for compensation is approximately 13^0, ie. a folding angle of 26^0.

In the corresponding equations for the 4 mirror cavity, the term R_1 is dropped and the terms in f are multiplied by 2. This gives a folding angle of approximately 19^0 at each of the two folding mirrors. In practice, the laser was built with an angle of approximately 25^0 for both types of cavities. The design of the cryostat prevented any further reduction in the angle, so full astigmatic compensation of the X type cavity was impossible (unless a second folded section was added).

The introduction of astigmatic elements such as Brewster-angled tuning elements in the long arm(s) causes only minor additional astigmatism, providing the resonator is adjusted close to the centre of the stability zone. The difference in effective lengths for the sagittal and tangential ray bundles will usually be small compared to the overall length of the long arm, and as discussed previously, the size and position of the stability zones are only a weak function of this length.

Cavities with two folded sections can also be analysed using similar principles to those described here, although a full discussion is complex and outwith the scope of this thesis. References **33** & **34** discuss the case of a linear cavity with two folded sections.

Calculation of threshold pump power

Using the waist size calculated above, the threshold pump power can be predicted. The gain required at laser threshold, α_T, for the three mirror cavity is given by the relation

$$\alpha_T = \frac{1}{2l} \ln\left(\frac{1}{R_1 R_2 R_2 R_3 T^2}\right) + \kappa \qquad (1.4)$$

where R_1, R_2 and R_3 are the fractional reflectivities of the mirrors, T is the fractional single pass loss (perhaps due to scattering by the windows), whereas κ represents the loss within the gain crystal due to contaminants (units of length^{-1}). The path length in the crystal is given by l ($\approx$ 2.5 mm). Assuming mirror reflectivities of $R_1 = R_2 = 0.995$ and a 20% transmission output coupler, $R_3 = 0.8$, a single pass loss of T = 0.98 and κ approximately 0.2 cm^{-1} (~ 5% in 2.5 mm), the gain required at threshold can be estimated as approximately 0.8 cm^{-1}. The gain at threshold, α_T, is related to the inversion density ΔN_T by the emission cross-section

$$\alpha_T = \sigma_e \Delta N_T \qquad (1.5).$$

As an example, consider the NaCl:OH$^-$ laser described in chapter 6, where the decay time is 150 ns, and σ_e is calculated to be 8 x 10^{-17} cm^2, therefore a ΔN_T of 1 x 10^{16} cm^{-3} will be required to reach threshold. The pump power required to reach this density in an ideal 4 level system, P_T, can be estimated by considering the power which can maintain an inversion

density ΔN_T in a volume V, where the spontaneous decay from the upper laser level has a characteristic time constant τ

$$P_T = \Delta N_T \, h\upsilon_l \, \mu_l \, V / \tau \qquad (1.6)$$

where $h\upsilon_l$ is the energy of the emission photons (~ 0.8 eV) and μ_l is an efficiency factor (~ 0.7) to account for the Stokes shift between the pump laser wavelength and the emission wavelength. The threshold pump power can be estimated once the volume of the excited region is known. The spot size was previously estimated to be ~ 30 μm for 1.5 μm wavelength. It has been shown[32] that the cross-sectional area of the mode in the crystal is given by approximately $A = \pi n w^2 \approx 6 \times 10^{-5}$ cm^2 due to its elliptical shape. Assuming this is approximately constant over the path length in the crystal, the pumped volume is around 1.4×10^{-5} cm^3. Substituting these values into equation (1.6), the pump power at threshold can be estimated to be 90 mW. In practice, the threshold power lies in the range 200-400 mW, since this simple analysis has not taken account of the incomplete mode-matching of the pump and intracavity laser beams.

The output power of the laser is governed by the saturation intensity I_{sat}, defined by

$$I_{sat} = \frac{h\upsilon}{\sigma_e \tau} \qquad (1.7).$$

With mode-locked lasers, it is often more appropriate to use the saturation fluence U_{sat}

$$U_{sat} = \frac{h\upsilon}{\sigma_e} \qquad (1.8).$$

In both cases, $h\upsilon$ denotes the photon energy at the emission wavelength. The saturation energy E_{sat} is given by simply multiplying U_{sat} by the cross-sectional area in the crystal. Typical colour-centre lasers such as NaCl:OH$^-$ have saturation energies of approximately 20 nJ, whereas KCl:Tl^0(1) with its small gain cross-section has an $E_{sat} \approx 140$ nJ.

Design of the laser cryostat

The cryostat used in the lasers described in chapters 2,3 and 5 is shown schematically in Figure 1.6, see also reference 35. (The later design of cryostat used in chapter 6 is outwardly similar, although its internal details differ - see reference 36.) The crystal is clamped to a copper block, or crystal holder. Poor thermal contact between the surfaces due to roughness of the copper is avoided by using a thin sheet of soft indium metal between the crystal and the copper holder. The holder is clamped to a horizontal copper rod by means of a threaded steel rod, which is coaxial with the copper rod. This steel rod screws into a threaded hole in the back of the crystal holder. The other end of the copper rod is connected to the base of the liquid nitrogen tank, which is itself suspended at its (thin) neck from the outer casing to minimise heat conduction. The tank is surrounded by superinsulation and at its base are pockets of *sorb* pellets. The sorb pellets trap atoms and molecules when cooled to cryogenic temperatures, and helped to maintain the vacuum for periods of 3 months or longer. During this period the hold time for the liquid nitrogen in the tank would decrease from ~ 36 to ~ 18 hours. The cryostat was then pumped using a diffusion pump to restore the vacuum.

The optical chamber has two Brewster-angled fused silica (Heraeus Infrasil) windows for access to the crystal. All resonator mirrors are located outside the vacuum chamber. This eliminates stiction that is encountered when the mirrors are located on 'flexible' bellows. In addition, it allows the curved mirrors to be changed (and hence cavity configuration) without disturbing the crystal. This advantage is to some extent offset by the greater distance required between the crystal and the curved mirrors, compared to the compact design of Mollenauer.[4] This results in a larger spot size, and hence higher threshold pump powers.

The lasers were excited in a nearly collinear arrangement as shown in Figure 1.6 (b) which almost entirely eliminates optical feedback to the pump laser and the resultant degradation of its performance. In this scheme, the pump and pumped beams intersect in the crystal and cannot overlap completely over the 2.5 mm path length. Nevertheless, the laser returned a similar performance to the collinearly pumped Burleigh Instruments FCL laser.

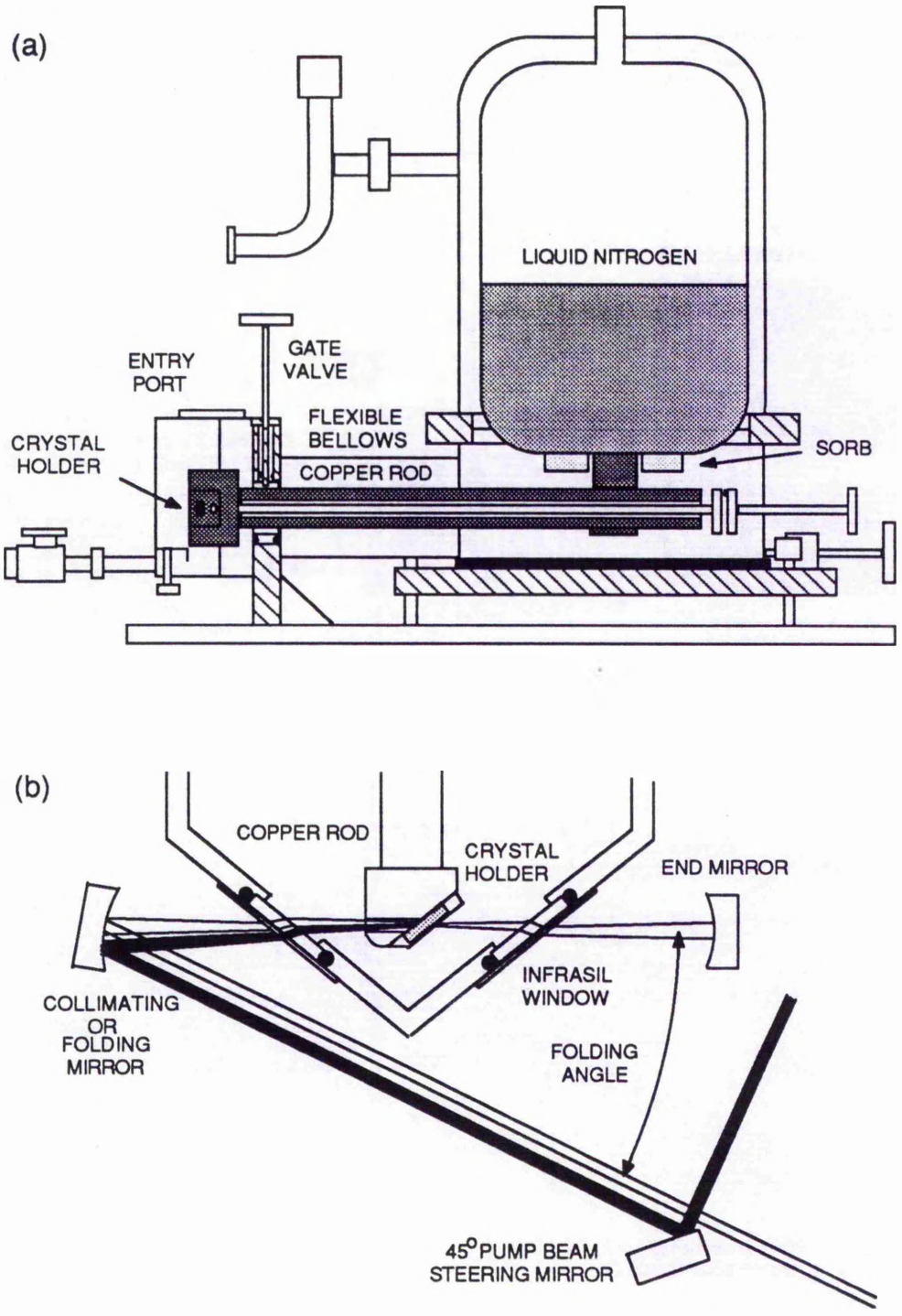

Figure 1.6 (a) Cross-section of the cryostat, showing the optical head to the left of the gate valve assembly. (b) Plan view of the optical head of the cryostat, showing the arrangement of the pump beam and colour-centre beam.

Prior to loading a crystal, the two chambers of the cryostat were evacuated, and separated from each other by closing the gate valve. The tank was then filled with liquid nitrogen, and the front chamber brought upto atmospheric pressure, to permit access. The crystal loading procedure could be completed in less than 10 minutes. The crystals, wrapped in aluminium foil parcels, were kept in a liquid nitrogen storage Dewar. The selected parcel was warmed gradually to room temperature before being unwrapped, to prevent deliquescence of the crystal surfaces. Before clamping the crystal to the holder, the surfaces were inspected and wiped with a tissue. The crystal holder was then lowered through the top access window onto a table within the optical chamber. The access window was then replaced onto its O-ring seat, and the front chamber was pumped down for 1 or 2 minutes. The gate valve could then be opened, uniting the two chambers, and the tank and copper rod assembly could be wound forward to dock with the crystal holder. The steel rod was then wound into the holder to clamp it to the rod. The tank, rod and holder could then be wound back to position the crystal to the best position relative to the windows, in preparation for laser operation.

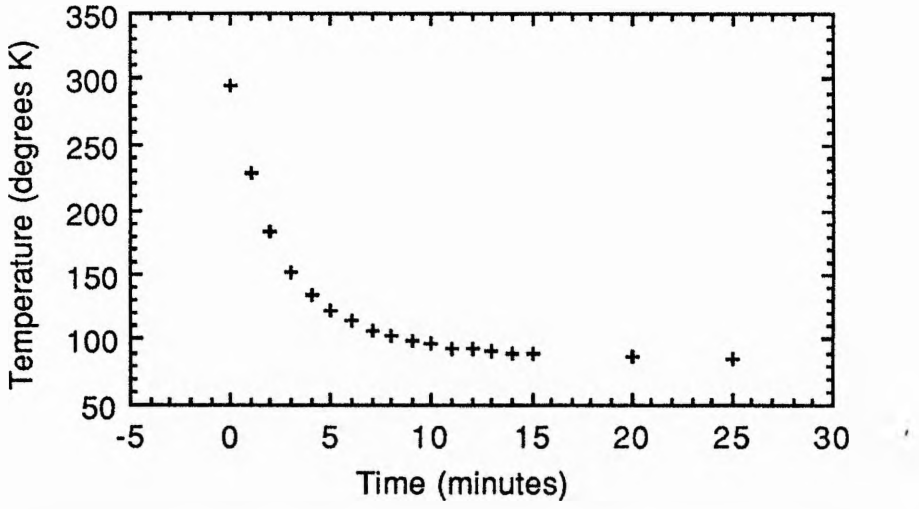

Figure 1.7 Crystal holder temperature after docking with the copper rod (docking at time = 0).

The temperature of the crystal holder was monitored on one occasion using a calibrated platinum resistor, see Figure 1.7. Once clamped to the copper rod, the temperature fell rapidly, eventually stabilising at 83 K after an hour. With 2 W pump power incident on the crystal (KCl:Tl), the temperature of the crystal holder rose to around 90 K, however, the

temperature of the pumped spot on the crystal itself could obviously not be measured. A similar situation has been analysed by Miller at al.,[37] where they estimated the temperature rise ΔT between the edge of the crystal mount at radius w' (≈ 2.5 mm), and some radius w close to the laser spot

$$\Delta T = \left(\frac{P}{2\pi\kappa l}\right) \ln(w'/w) \qquad (1.10).$$

where P is the power load at the laser spot, κ is the thermal conductivity and l is the effective path length over which the power is absorbed, say 1 mm. The thermal conductivity of the alkali-halide crystals at 77 K lies in the range 200-500 mW/(cm.K).[38] For an incident power of 4 W, typically 3 W will be absorbed, of which 30% is lost to the lattice as heat with vibronic relaxation, giving a power load of approximately 900 mW. The temperature rise at the edge of the mode (w ≈ 30 μm) can be estimated as ~ 12-30 K. Although relatively small, this is only at the edge of the spot and not the centre. The effect can be reduced by focussing less strongly, and increasing the length l by using low optical density crystals. Decreasing the radius of the edge of the crystal holder has only a minor effect because of the logarithmic dependence.

1.4 Mode locking (see references 39 & 40)

The shortest pulses that a laser can produce for a given spectral bandwidth will have a time duration of the order of $1/\Delta\omega$ where $\Delta\omega$ is the bandwidth in terms of angular frequency. This is because the time dependence and the frequency dependence of the amplitude and phase of the light form a Fourier transform pair. To produce a pulse of duration less than the round-trip time of the cavity requires an oscillating bandwidth greater than the longitudinal mode spacing. For this pulse to be bandwidth limited, the phases of the longitudinal modes must be accurately controlled or *locked.*

For a given bandwidth, the highest intensity is produced when the various spectral amplitude components, or axial modes in the case of a laser, have an identical phase and interfere constructively, hence the term mode locking. When this is achieved, the laser will emit a single pulse at a repetition frequency dictated by the length of the laser resonator. Between the pulses, the vectorial addition of the axial mode amplitudes results in destructive

interference and negligible intensity. With this perfect mode locking, the frequency of the optical cycles within the temporal envelope of the pulse (ie. the carrier frequency) will be constant.

Mode locking is achieved by incorporating an optical modulator (or switch) within the cavity. There are many techniques to obtain mode locking, but can be classified under either active mode locking, where the modulation is controlled by an external source, or passive mode locking, where the modulation is controlled by the light itself. Some of these techniques rely on assistance from *dynamic* gain saturation, ie. the saturation of the gain by individual pulses rather than by the cumulative effect of many pulses (essentially by average power). Dynamic gain saturation is dominant in gain media where the upper state decay time is of the same order, or shorter, than the cavity round trip time. Laser active colour centres have decay times between 3 and 100 times the round trip time, and although the bulk of the saturation is through average power, there is a dynamic component.

1.4.1 Active mode locking

Loss modulation

Perhaps the most widely applicable technique for mode locking is the actively driven loss modulator.[41,42] When modulated at the cavity round-trip period, it forces a pulse to form in the cavity because light which is correctly timed with the maximum transmission phase of the modulation cycle will be attenuated less than light which passes during the remainder of the cycle. If the modulator is located at one end of the cavity, the residual loss for the pulse itself will be minimal. The loss modulation can be approximated by a sinusoidal window in the time domain which travels at the same speed as the pulse. This means that both the leading and trailing edges of the pulse are attenuated equally. Therefore, the technique does not require additional pulse shaping from dynamic gain saturation, and it is particularly appropriate for mode locking solid state lasers such as Nd:YAG. Because the size of the transmission window is fixed, its effectiveness at shortening the pulse is reduced as the duration becomes shorter, and in general, the technique can only give pulse durations of around 50 ps or longer. This is sufficient for noble gas ion lasers, where the bandwidth of the atomic transition limits the ultimate pulse duration to 50-100 ps.

Typically, modulators installed in commercial ion and Nd:YAG lasers use acoustic standing waves in a transparent medium such as fused quartz. With a drive frequency f, an index grating (transverse to the beam), caused by regions of compression and rarefraction, will form at time intervals of $2f$, which causes light to diffract out of the laser cavity at intervals of $2f$. In the spectral domain, the loss modulation generates sidebands with a spacing almost identical to the longitudinal modes.

Phase modulation

The technique of frequency modulation (FM) mode locking uses a phase modulator instead of a loss modulator. During most of the modulation cycle, rapidly varying refractive index changes progressively shift the light to frequencies outside of the gain bandwidth, where it is attenuated. The pulse is formed at either of the turning points of the refractive index cycle. Pulse shortening occurs when the pulse becomes linearly chirped by the modulator such that its leading and trailing edges are shifted away from the gain peak, and are attenuated. Because there is no direct amplitude modulation, it is a relatively weak process and may not be particularly effective at suppressing a low pedestal or background accompanying the pulse.

Gain modulation by synchronous pumping

Active mode locking may also be achieved by modulating the gain. In lasers which are optically pumped by a second laser, the technique of synchronous pumping is commonly used, whereby the pump, or master laser is mode locked and periodically modulates the gain of the pumped, or slave laser. The slave laser mode locks when its cavity length is adjusted such that its round-trip time matches the time period between the pump pulses (or a multiple or sub-multiple). Unfortunately, the small-signal gain of the slave gain medium decreases slowly with the spontaneous decay of the upper state population, giving a relatively long transmission window. Short pulses can be produced if dynamic saturation is present, hence foreshortening the gain window. Therefore, synchronous mode locking is a particularly suitable for dye lasers.

The cavity length setting is crucial to obtain the shortest pulses. When the length is too short, the pulse arrives in the gain medium ahead of the pump pulse. This causes the

formation of sub-pulses, since the first pulse is now not sufficiently energetic to saturate the gain, and furthermore the upper state is still being populated by the pump pulse after the first pulse has passed. If the cavity is too long, the pulse arrives at the gain behind the pump pulse, resulting in growth and broadening of the pulse leading edge.

Although synchronous pumping of a dye laser using an HeNe laser intracavity was described as early as 1972,[43] the scheme most commonly used was first demonstrated independently by Chan and Sari[44] and by Harris et al.[45] In both experiments, a CW dye laser was synchronously pumped by a mode-locked argon laser located extracavity. Subpicosecond pulses were first obtained by Heritage and Jain[46] who used a synchronously mode-locked dye laser to pump a second dye laser, however their results have been questioned by Van Stryland.[47] He showed that the origin of the exponential wings commonly observed in autocorrelation measurements of synchronously mode-locked dye laser pulses, usually interpreted as a single-sided-exponential pulse shape, could also be caused by considerable variation in pulse duration from one pulse to the next. More recently, pulse durations of 210 fs have been obtained from a dye laser by pumping with a frequency doubled and pulse compressed Nd:YAG laser.[48]

Colour-centre lasers have also been mode locked by synchronous pumping.[4] Although the pulse durations are somewhat longer than with dye lasers, the quality of the pulses are superior, with no evidence of the exponential wings commonly seen on dye laser pulse autocorrelations. Furthermore, the high transmission output couplers commonly used on dye lasers to prevent subpulsing are not required, and indeed for KCl:Tl which has a rather small gain cross-section, a low transmission output coupler is necessary to maximise dynamic gain saturation and obtain stable mode locking. Synchronously mode-locked colour-centre lasers will be discussed in chapters 3 and 6.

1.4.2 Passive mode locking using resistive nonlinearities

Fast saturable absorbers

Mode locking may obtained by simply incorporating into the laser an absorbing medium which bleaches at high intensities. Under suitable pumping conditions, the saturable absorber selects only the most intense noise burst and allows it to grow at the expense of less intense

fluctuations. The burst eventually forms a clean pulse over many cavity round trips, its duration approaching the recovery time of the absorber, typically a few tens of picoseconds. In general, fast saturable absorbers are suited to mode locking (usually flash-lamp pumped) solid state lasers such as Nd:YAG or Nd:glass. To obtain pulse durations shorter than the absorber recovery time, additional pulse shaping from gain saturation is required (see next section).

Slow saturable absorbers

Passive mode-locking of a CW pumped Rhodamine 6G dye laser using the saturable absorber dye DODCI was reported in 1972.[49] Although the absorber dye had a recovery time of several hundred picoseconds, pulses as short as 1.5 ps were obtained. New realised that such short pulses were due to the presence of dynamic gain saturation.[50] Simplistically, when the duration is less than the absorber recovery time, the absorber cleans the leading edge of the pulse, whilst gain saturation cleans the trailing edge. For slow absorber passive mode locking to occur, certain conditions must be fulfilled. Firstly, the absorber must saturate more easily than the gain. New introduced the *s* parameter, which can be defined in terms of the characteristic saturation energies of the absorber, E_{abs} and the gain, E_{gain}. For pulse compression and mode locking to occur, two conditions must be fulfilled.[39] Firstly,

$$s = \frac{E_{gain}}{E_{abs}} > 1 + \frac{\Gamma}{B_0} \qquad (1.11).$$

where Γ and B_0 account for linear losses and small-signal absorption respectively. Secondly, the absorber must recover more quickly than the gain, ie.

$$\tau_{abs} < \tau_{gain} \qquad (1.12)$$

To show how the the pulse shaping arises, the combined action of saturable gain and saturable loss was modelled using parameters typical of a CW dye laser such as the Rhodamine 6G / DODCI system. The initial pulse shape was chosen as squared hyperbolic secant or $sech^2$. After 10 round trips the pulse, shown in Figure 1.8, was compressed asymmetrically resulting in a steeper leading edge. In fact, it was found that the final pulse shape was relatively insensitive to the initial shape, and significant pulse shortening only occurred after the pulse shape adopted the asymmetric profile.

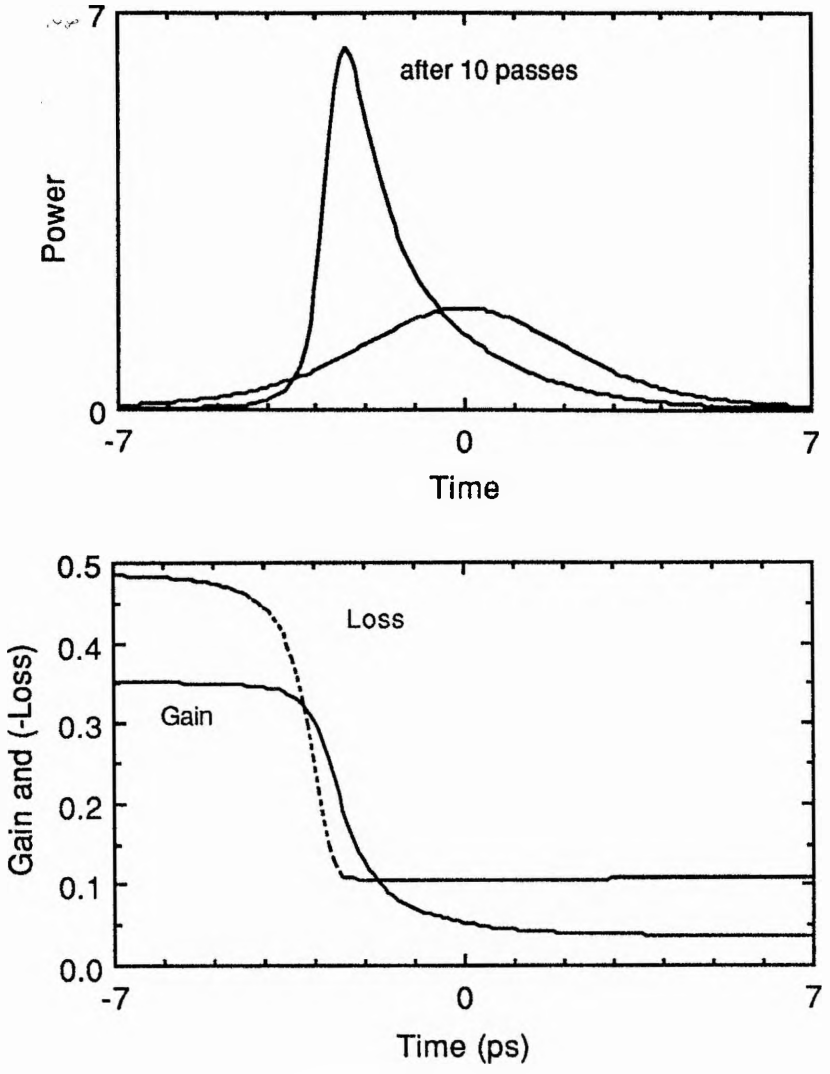

Figure 1.8 Pulse shaping in slow absorber passive mode locking. (a) Compression of the pulse after 10 round trips. The original $sech^2$ pulse is shown for comparison. (b) Corresponding changes in gain (solid line) and loss (dashed line) due to saturation.

Figure 1.8 also shows the changes in saturable gain and absorption (both nonsaturable and saturable components) during the passage of the pulse through the amplifying and absorbing media. These changes are plotted in the local time of the pulse and therefore they appear superimposed here, with absorption plotted in reverse (ie. in terms of gain). The two curves intersect near the peak of the pulse, indicating that the peak is amplified while the leading and trailing edges experience loss. If the recovery times were interchanged, a second window would exist within the recovery phase and noise behind the pulse would grow. If the gain saturates before the absorber, no window would exist and the laser would extinguish or run CW, depending on the small-signal values of gain and loss.

Following New's explanation, a reduction in pulse duration to 0.3 ps was obtained when the saturable absorber was placed in contact with the end mirror.[51] This arrangement results in the formation of a standing wave in the absorber, saturating it more easily. It is possible to obtain this standing wave saturation of the absorber with the collision of two different pulses, whilst spacing the arrival time at the gain medium so as to allow recovery between pulses. This can be achieved most easily by using a ring resonator with the absorber located one quarter of the way round the cavity perimeter from the gain. This technique, called colliding-pulse mode locking (CPM), results in the formation of two pulses, travelling in opposite directions which meet in the absorber. Pulse durations of 90 fs were obtained initially,[52] but this was reduced to 65 fs by careful selection of the mirrors, which were presumed to contribute chromatic dispersion.[53] The full benefit of the enhanced saturation due to the grating formation in the absorber can only be realised when the grating occupies the entire path length within the jet.[54] In other words, the dye jet has to be thinner than the length of the pulse, and so this laser used an 'ultrathin' dye jet, only 10 μm thick.

Further reductions in pulse duration have been achieved by controlling the chromatic dispersion, and compensating for frequency chirp.[55,56] The four-prism sequence used by Valdmanis et al.[56] was capable of providing negative group-velocity dispersion (GVD), and when this feature was combined with the self-phase modulation (SPM) generated in the absorber dye jet, soliton-like pulse shaping resulted in pulses as short as 27 fs. The absorber dye jet was increased in thickness to around 30 μm, indicating that the formation of a strong grating in the absorber was now unnecessary. This was verified when pulses of similar durations were obtained using a linear cavity. Pulses as short as 19 fs have been observed in a similar CPM laser, perhaps due to greater SPM owing to a thicker absorber jet.[57]

In some cases, the conditions for passive mode locking cannot be met, e.g. the gain may have a faster recovery time than the absorber. Furthermore, it may be more convenient to pump the laser with a mode-locked, frequency-doubled Nd:YAG laser. In these cases, hybrid mode locking can be used. In this technique, synchronous mode locking is assisted by a weak saturable absorber, but with the repetition frequency still controlled by the pump pulses.

1.4.3 Passive mode locking using reactive nonlinearities

Methods for obtaining mode locking using artificial saturable absorbers which use reactive (rather than resistive) nonlinearities will be discussed in this section. These techniques rely almost entirely on fast nonlinearities such as the Kerr effect, and therefore they are particularly appropriate for lasers with little or no dynamic gain saturation.

A purely reactive nonlinearity such as self-phase modulation cannot normally be used on its own to mode lock a laser. Amplitude modulation is required to attenuate the leading and trailing edges of the pulse, in order that pulse shortening can be obtained, and to prevent the growth of sub-pulses.

It has been postulated[58] that SPM combined with bandwidth limitation will behave similarly to active FM mode locking, however, in contrast to FM, any low lying pedestal will not be chirped and therefore attenuated by the spectral filter. Pulse shortening using this technique has been reported, but in an actively driven loss-modulated laser.[59]

The combined action of self-phase modulation and anomalous group-velocity dispersion can give rise to soliton-like pulse narrowing, but it cannot induce mode locking per se because it does not cause an increase in the laser emission* with reduction in pulse duration. However, it can be used in conjunction with other effects to reduce the steady state pulse duration and to improve the stability of many lasers, eg. passively mode-locked dye lasers, Ti:sapphire lasers, fibre lasers and coupled-cavity lasers.[60,61]

The following techniques all satisfy the maximum emission principle. The common element in all of them is the conversion of a reactive nonlinearity into amplitude modulation.

Coupled-cavity mode locking

The cornerstone of this thesis is mode locking using coupled-cavity techniques, and hence a comprehensive review of the relevant literature will be given. Its details will be elaborated where appropriate in the following chapters.

Mollenauer and Stolen reported the development of their soliton laser in 1984.[62,63] It consisted of a synchronously mode-locked KCl:Tl^0(1) colour-centre laser with an adjacent control cavity containing a solitonic optical fibre. Pulses from the laser were compressed in

* Passive and self-mode locking of lasers can be explained in terms of the maximum emission principle (MEP), see reference 39.

the fibre due to the combined effects of self-phase modulation and anomalous group-velocity dispersion, and then reinjected back into the main laser cavity. This forced the laser to produce narrower pulses. This feedback process continued until some steady state was reached, where the pulse duration was determined solely by the properties of the fibre. This demonstration was followed by an elaborate theoretical explanation by Haus and Islam,[64] however, at this point, the interference effects at the interface between the two cavities were overlooked by both sets of authors. Theoretical work by If et al. omitted this point too, although curiously, their schematic represented the soliton laser in a Michelson-mirror cavity.[65]

The interference issue was addressed in 1986 by the numerical modelling of Blow and Wood[66] and also by Mitschke and Mollenauer[67] when they provided further experimental results. By this time it was realised that the soliton laser was passively mode-locked and not simply an enhancement of the synchronous mode locking. Theoretical work published subsequent to this also included the interference effect.[68,69] Mitschke and Mollenauer reported[70] the generation of 60 fs pulses by using fibre of lower dispersion than that used previously, and a soliton laser based on a CW pumped, acousto-optically loss modulated laser was demonstrated.[70]

Further modelling by Blow and Wood showed that pulse compression (and hence solitons) was not a prerequisite for mode-locking.[71] They simulated pulse narrowing and pulse broadening by saturable absorption and saturable amplification elements respectively, although they ignored any phase modulation effects. At that point, normally dispersive fibres had been shown to be equally effective in the control cavity, and that similar effects could be obtained with a different gain medium ($LiF:F_2^+$) at normally dispersive wavelengths (see chapter 2).[72,73] Furthermore, acting on the predictions of Blow and Wood, the same authors also used a semiconductor amplifier as the nonlinearity. The soliton laser was therefore a particular type within a new branch of mode locking, referred to here as coupled-cavity mode locking. Blow and Nelson presented their own experimental results using normally dispersive fibre at around the same period.[74,75]

Ouellette and Piché pointed out that the interference effect was the key to understanding the pulse compression mechanism in these lasers.[76] They had previously

reported[77] the passive mode locking of a pulsed TEA CO_2 laser by building the laser in a Michelson-mirror cavity, where one of the two interferometer branches contained a germanium crystal which induced self-phase modulation through the optical Kerr effect. The pulse shaping mechanism was clearly identified as the interferometric addition of one pulse to a phase modulated version of itself. By fine adjustment of the arms of the Michelson interferometer, a saturable-absorber-like effect was obtained.

Mark et al. published their own observations and a theory termed additive pulse mode locking.[78,79] This was essentially the same as the interference effect described by Ouellette and Piché, itself further clarified in a paper where the term interferential mode locking was coined.[80] Short pulses were subsequently obtained with coupled-cavity Nd:YAG[81] and Ti:sapphire lasers.[82,83] In contrast to the colour-centre lasers, it was found that active mode locking was not required to initiate the coupled-cavity mode locking, and like the CO_2 laser[77], they were observed to self-start.[81,83]

More recently, a third cavity arrangement has been demonstrated.[84] The nonlinear Sagnac interferometer has the advantage that the interfering beams travel along identical paths but in opposite directions, and so interferometric length stabilisation is not required. The arrangement has also been implemented using a fibre loop mirror.[85]

Self-focussing combined with aperturing

The observation of self-mode locking in a Ti:sapphire laser by Spence et al.[86] indicated that the nonresonant nonlinearity in the gain crystal was significant. In such a bulk medium, self-phase modulation will be accompanied by a self-focussing action and subsequent work has concentrated on the development of a new mode-locking technique based on this latter effect, termed Kerr-lens mode locking.[87] The self-focussing of the crystal at high intensities causes a change of the beam diameter in the cavity. By positioning an aperture at a position where the beam size decreases with increasing intensity, the self-focussing is converted into amplitude modulation.

Kerr polarisation rotation

A bulk Kerr medium can be used to mode lock a laser by placing quarter wave plates either side and exploiting the Kerr induced polarisation rotation.[88,89] For a polarised laser, and

with the wave plates properly adjusted, the device will pass high intensities, but will be lossy for low intensities.

Second-harmonic generation nonlinear mirror

Stankov and Jethwa[90] obtained passive mode locking by incorporating a second-harmonic generating crystal into the cavity of their pulsed Nd:YAG laser. By replacing the end mirror with a one of relatively low reflectivity at the fundamental wavelength, but highly reflecting at the second harmonic, the combined crystal and dichroic mirror can behave like a fast saturable absorber. To ensure a high conversion efficiency back to the fundamental wavelength on the return pass, a phase matching condition between the second harmonic and the remaining fundamental wave must be satisfied. Due to the dispersion of the air, the optical path lengths of the waves differ and hence phase matching is achieved by adjustment of the distance between the crystal and the dichroic mirror.

1.5 Pulse diagnostic techniques

A fast photodiode coupled to an oscilloscope provides a simple means of monitoring a mode-locked pulse train. The lasers described in this thesis were monitored with either a silicon photodiode (AEG Telefunken BPW 28) or, for wavelengths greater than 1.1 μm, a germanium photodiode (Germanium Power Devices GM4). Although ultrafast photodetectors can resolve pulses of a few picoseconds duration, the sampling oscilloscope required for such a measurement is prohibitively expensive, and so the pulse durations were measured using either a streak camera or an autocorrelator.

1.5.1 The streak camera

Zavoiskii and Fanchenko[91] are credited with the invention of the streak camera, but its full potential was only realised when an electron extraction mesh was incorporated close to the photocathode, giving picosecond resolution.[92] Although streak cameras have a poorer resolution than autocorrelators, they have the significant advantage of response linearity (within their resolution limit) such that the pulse shape can be readily deduced. As will be discussed in the next section, autocorrelation is, by its nature, nonlinear and does not reproduce the pulse directly, and therefore can give somewhat ambiguous data.

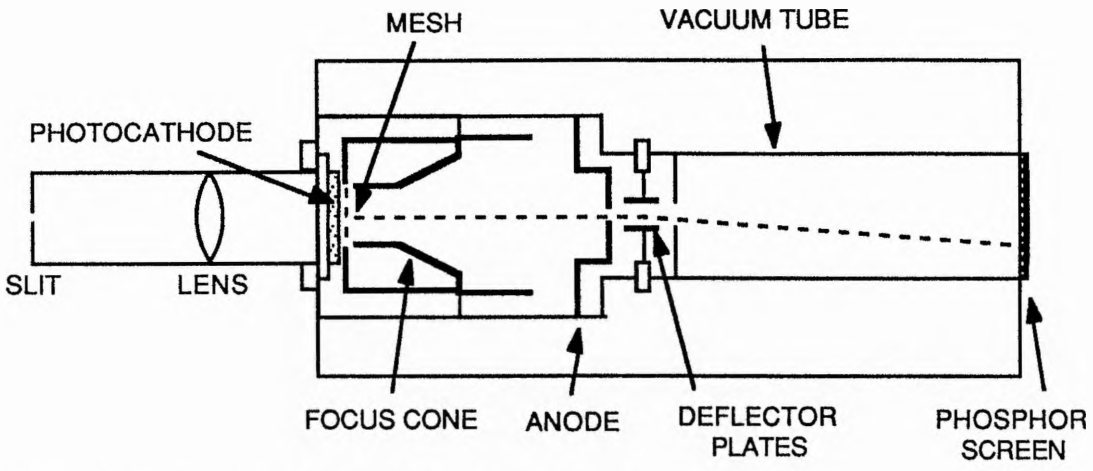

Figure 1.9 Schematic of the Photochron II streak camera

In the work described in this thesis, Photochron II streak cameras were used (shown in Figure 1.9). Light incident on the slit is imaged onto a photocathode at the front end of the camera which is essentially an imaging tube. The incident photons are converted into an electron beam (shown as a dashed line), which is focussed using electrostatic lenses onto a phosphor screen at the far end of the tube, giving an image of the slit. The conversion of photons into charged particles allows one to sweep the image of the slit across the screen by electrostatic deflection. By applying a voltage ramp to a pair of deflectors, the image of the slit is streaked across the screen. When an optical pulse is incident on the slit, it liberates a packet of electrons which, when streaked, results in an image which corresponds to the intensity profile of the pulse, providing that the extent of the image is significantly greater than the static image (ie. no deflection voltage applied).

To ensure good temporal resolution, the photoelectrons liberated at the cathode should have similar velocities (or energies) to reduce their transit-time dispersion. This is achieved by using mesh at a positive relative potential, located only 0.5 mm from the photocathode, to give an extraction field of around 20 kV cm^{-1}. The energy spread of the photoelectrons may be further reduced by operating the photocathode near its long wavelength cutoff. A second effect is related to the spatial resolution of the tube, referred to as the technical time resolution, limited by a combination of the quality of the image reproduction in the tube (spatial resolution) and the streak velocity. Together, these mechanisms limit the resolution of the Photochron II camera to around 700 fs.[93]

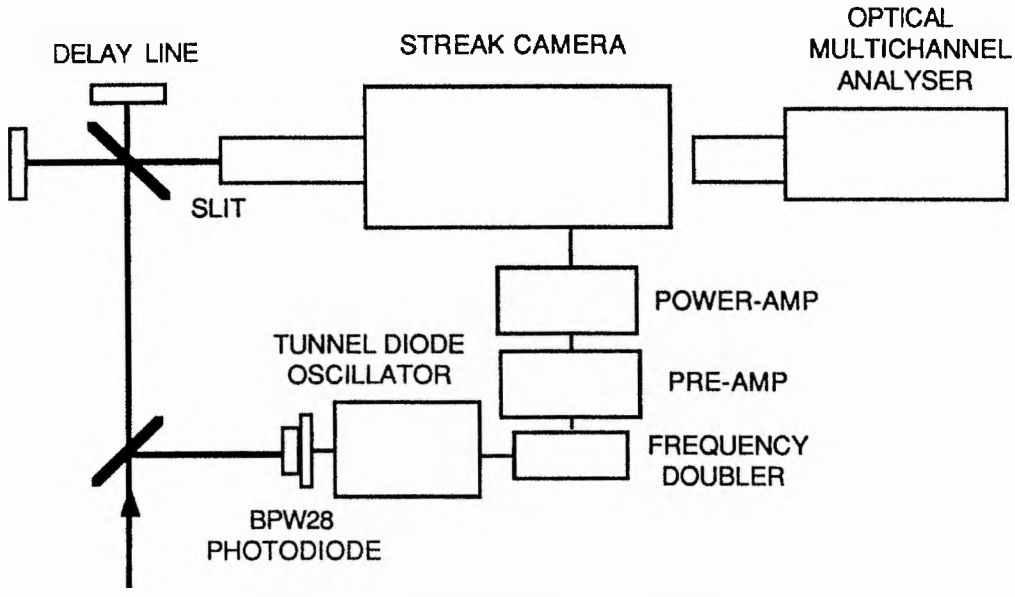

Figure 1.10 Schematic of the synchroscan drive electronics. Optical delay line provides calibration.

In the work described here, where the lasers were operated CW mode locked, the voltage applied to the deflection plates was repetitively ramped in synchronism with the pulse train.[94] This technique, known as synchroscan, enables the pulse duration to be studied in real time by using an optical multichannel analyser (OMA) to monitor the streaked image on the screen. Usually, the deflection plates were driven by a sinusoidal voltage at a frequency of 164 MHz, twice the standard laser pulse repetition frequency. This signal was conveniently derived from the electrical pulse train generated by the monitor photodiode, see Figure 1.10. In the case of the BPW28 silicon photodiode, the pulse train triggered a tunnel diode oscillator, the signal then being frequency doubled and amplified to a power of several watts. For the GM4 germanium photodiode (see chapter 4), the second harmonic of the electrical pulse train was selected by a band pass filter, and then amplified.

With synchroscan, the image on the phosphor is formed by the integration of hundreds of thousands of pulses, which improves the dynamic range of the camera. However, optical pulse timing jitter and electronic jitter in the synchronisation system typically degrades the temporal resolution (from around 1 ps for single shot operation) to around 5 ps, depending on the type of mode locking and the stability of the pulse train. This is particularly apparent with synchronously mode-locked lasers, but can be improved by triggering the oscillator from the slave laser pulses as opposed to the pump laser pulses.

1.5.2 Second-harmonic generation autocorrelation

Pulses of less than around 5 ps duration can, in general, only be measured with optical correlation techniques which indicate the spatial extent (or length) of the pulse. The most common method, proposed independently by Armstrong[95], Weber[96], and Maier et. al.[97] uses second-harmonic generation (SHG) to determine the second-order intensity autocorrelation function $G_2(\tau)$ of a pulse with intensity $I(t)$

$$G_2(\tau) = \int_{-\infty}^{+\infty} I(t)I(t-\tau)dt \qquad (1.13)$$

where τ is the time delay between the two pulses being correlated. The pulse to be measured is split by an interferometer, usually a Michelson equipped with a 50/50 beamsplitter. By changing the length of one of the interferometer arms, the delay τ can be adjusted. After the interferometer, the pulses are focussed into a nonlinear crystal to generate second harmonic. The signal is monitored using a sensitive detector such as a photomultiplier tube (PMT) to ensure a good signal to noise ratio. The response of the detector is much slower than the duration of the pulse and hence the SHG for each delay is averaged, and the autocorrelation integral is performed automatically. Due to the nonlinear dependence of the SHG, there is an enhancement in signal when the two pulses enter the crystal with temporal overlap compared to the case where the pulses enter in succession. By scanning over a range of delay times τ, the autocorrelation function of the pulse can be recorded.

The main advantages of the technique are firstly, that the temporal resolutions better than 10 fs can be achieved by judicious choice of SHG crystal material and thickness. Secondly, unlike a synchroscan streak camera, interpulse timing jitter does not artificially broaden the measured function.

Three geometries of SHG autocorrelators are in general use. The original versions used type II phase matching where the two pulses are polarised orthogonally to each other. In that scheme, SHG is only produced when the pulses have some degree of overlap. The more usual SHG geometry, type I phase matching, can also give 'background free' autocorrelations by using a noncollinear alignment, where the two (similarly polarised) pulses cross-over in the crystal at an angle.[98,99] The SHG caused by the spatial overlap of

the two pulses is generated in a direction bisecting the two SHG beams caused by the pulses individually. Usually, an aperture is positioned on this central beam to prevent the two outer, diverging beams being detected.

The autocorrelators used in this work employed a third technique, where type I phase matching is combined with a collinear geometry, hence simplifying the alignment. This means that the autocorrelation is superimposed on a background, making it difficult to determine whether the pulse is accompanied by a pedestal. Fortunately, this scheme is ideal for making fringe-resolved measurements of the pulses. Normally these fringes, which are caused by the interference of the two pulses in the crystal, are averaged out, giving conventional intensity autocorrelations.

Figure 1.11 shows the shapes expected for the fringe-resolved or interferometric autocorrelation and the averaged version or intensity autocorrelation under various conditions. Interferometric autocorrelations can detect frequency chirp in the pulse because changes in instantaneous phase (and hence carrier frequency) over the duration of the pulse will reduce the visibility of the fringes in the wings of the autocorrelation.[100]

It was mentioned earlier that the autocorrelation gives somewhat ambiguous information about pulse shape. Because the intensity and phase of the optical cycles of a pulse in the time domain are linked with the variations of intensity and phase in the frequency domain by the Fourier transform relations, each pulse has a corresponding spectral shape (and width). Spectral information can therefore assist in the deconvolution of the autocorrelation. The normal procedure is to assume a certain pulse shape, and to divide the autocorrelation FWHM $\Delta\tau$ by a factor specific to that pulse shape, to give the pulse duration. The spectral FWHM $\Delta\tau_p$ should then be measured and the bandwidth-time duration product $\Delta\upsilon\Delta\tau_p$ calculated and compared with the theoretical product expected for the chosen pulse shape.[100-102] Any deviation indicates that the chosen pulse shape is wrong, and/or the pulse is chirped. Table 1.1 lists data for common pulse shapes, all of which are assumed to be unchirped.

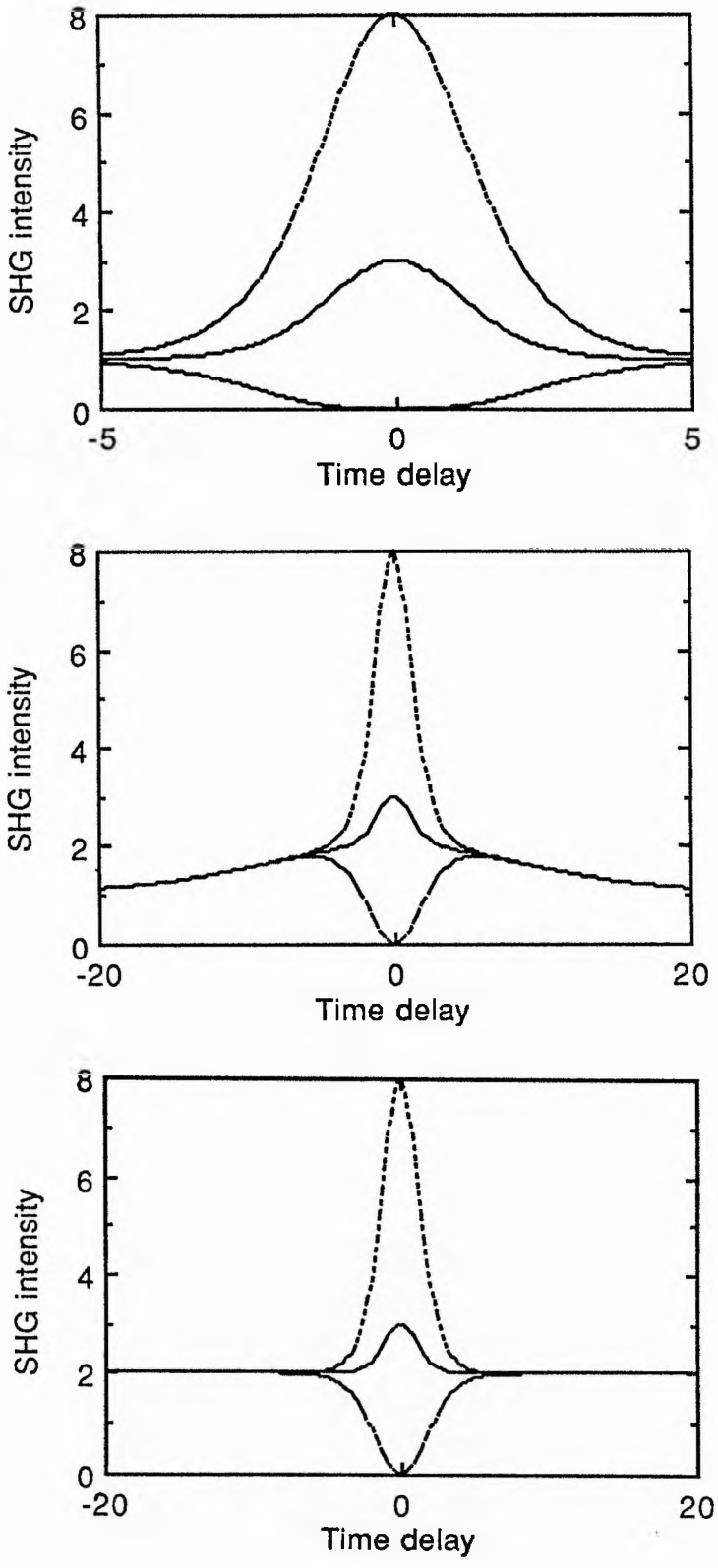

Figure 1.11 Intensity (solid line) and interferometric autocorrelations (envelope shown by dashed line). (a) The 3:1 form expected for a bandwidth limited, chirp-free pulse. (b) The 3:2:1 shape indicates a noise burst, ie. a pulse with considerable, rapidly varying, substructure. (c) A 3:2 ratio expected for a CW laser. The time duration of the spike corresponds to the coherence length.

$I(t)$	$I(\upsilon)$	$G_2(\tau)$	$\Delta\upsilon\Delta\tau_p$	$\Delta\tau/\Delta\tau_p$
e^{-t^2}	$e^{-(2\pi\upsilon)^2}$	$e^{-\tau^2/2}$	0.441	1.414
$sech^2(t)$	$sech^2(\pi^2\upsilon)$	$\frac{3(\tau\cosh\tau - \sinh\tau)}{\sinh^3\tau}$	0.315	1.543*
$\frac{1}{(e^t + e^{-rt})^2}$:				
$r = 3$	-	-	0.278	1.549
$r = 6$	-	-	0.232	1.565
$\frac{1}{1 + t^2}$	-	$\frac{1}{1 + (\tau/2)^2}$	0.221	2.000
$e^{-2\lvert t\rvert}$	-	$(1 + 2\lvert\tau\rvert)e^{-2\lvert\tau\rvert}$	0.142	2.421

Table 1.1 Relationships between temporal, spectral and intensity autocorrelation FWHMs for pulses with intensity profiles described by the following functions: Gaussian, squared hyperbolic secant ($sech^2$), asymmetric $sech^2$ for two values of asymmetry, Lorentzian, and double exponential. The second last column gives the pulse duration-bandwidth products, and the last column lists the factors for correcting the autocorrelation FWHM $\Delta\tau$ to the pulse FWHM $\Delta\tau_p$. Data from references **100-102.**

* 1.897 for interferometric autocorrelations, see reference **102.**

The autocorrelator used in this work is shown schematically in Figure 1.12. The Michelson interferometer was equipped with corner cube reflectors to prevent feedback into the laser, and were of the hollow type with gold coatings to minimise pulse distortion. One corner cube was mounted on a motorised translation stage with a travel of 25 mm, whilst the other was mounted on an 8 inch diameter audio loudspeaker. The speaker allowed real-time monitoring of the pulse, and was essential for interferometric autocorrelations, principally because it enabled the two interfering beams to be correctly aligned, but also because it reduced the influence of mechanical instabilities on the fringe visibility. The speaker was normally driven at a frequency of around 22 Hz, fast enough for real time adjustment of the laser, but sufficiently slow that the maximum range of travel was not compromised (approximately 15 mm). A storage oscilloscope was normally used to record the real-time autocorrelation data, although for broad pulses ($\Delta\tau_p > 30$ ps), the motorised stage was used in conjunction with a chart recorder. In addition, by moving this stage a known distance and introducing a time delay in one arm, it was possible to calibrate the real-time measurements

made with the loudspeaker, since it caused the pulse to move across the oscilloscope screen by an amount equal to this time delay.

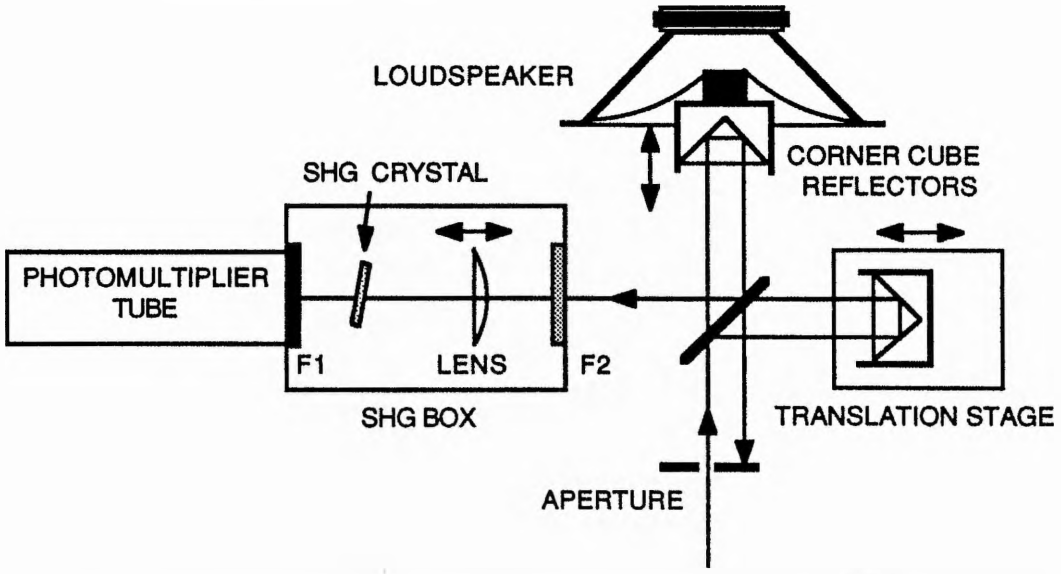

Figure 1.12 Schematic of the SHG autocorrelator. Filter F2 blocks room light but passes the fundamental (eg. a silicon filter was used at 1.5 μm), while filter F1 blocks the fundamental but passes the second harmonic.

When the PMT output was connected to the 50 MΩ input of the oscilloscope the overall frequency response was insufficient for interferometric autocorrelations. The RC time constant was reduced by minimising the length of the coaxial cable from the PMT to the oscilloscope and by incorporating a terminating resistor of 1-5 kΩ. This increased the frequency response to better than 100 kHz, enabling fringe-resolved measurements of subpicosecond pulses. If necessary, the speaker frequency could be reduced by a factor of 5 to give a further improvement. The terminator caused a reduction in electrical signal, however, this was not usually a problem since these short pulses were relatively intense.

The SHG crystals used were all angle tuned for phase matching.[103] The type I phase matching conditions for negative uniaxial crystals ($n_e < n_o$) are summarised by the equations

$$\frac{1}{[n_e(\theta)]^2} = \frac{\cos^2\theta}{n_o^2} + \frac{\sin^2\theta}{n_e^2} \tag{1.14}$$

$$n_e^{2\omega}(\theta) = n_o^{\omega} \tag{1.15}$$

where θ is the angle between the beam and the optic axis for phase matching, n is the refractive index, and ω and 2ω denote the fundamental and second harmonic waves respectively. By rewriting equation (1.14) for the fundamental and for the second harmonic waves and substituting equation (1.15) where appropriate, the phase matching angle can be found in terms of the refractive indicies

$$\sin^2\theta = \frac{[n_o^{\omega}]^{-2} - [n_o^{2\omega}]^{-2}}{[n_e^{2\omega}]^{-2} - [n_o^{2\omega}]^{-2}} \qquad (1.16).$$

Phase-matching angles for SHG for four negative-uniaxial crystals were calculated for the wavelength range 500-1800 nm, see Figure 1.13 (a). The data for the ordinary and extraordinary refractive indicies for the crystals were found from Sellmeier expansions given in the following references: potassium dihydrogen phosphate (KDP): **104**; lithium niobate ($LiNbO_3$): **105**; barium metaborate (BBO): **106**; and lithium iodate ($LiIO_3$): **107**.

Phase matching can be obtained only over a limited bandwidth owing to a difference in phase velocities of the fundamental and second harmonic at the extremities of the pulse spectrum. This effect, called the group-velocity mismatch (GVM) broadens the SHG pulse and can limit the resolution of the autocorrelator. Miller[108] has derived an expression for the phase-matching bandwidth Δλ for an SHG crystal of thickness l

$$\Delta\lambda = \left| 0.442\,\lambda_1 / l \left(\frac{dn_o^{\omega}}{d\lambda_1} - \frac{1}{2}\frac{dn_e^{2\omega}(\theta)}{d\lambda_2} \right) \right| \qquad (1.17)$$

where λ_1 and λ_2 are the fundamental and second harmonic wavelengths respectively. Equation (1.17) applies specifically to negative-uniaxial crystals. One should be careful to calculate the actual gradient of the extraordinary index at the phase-matching angle θ, and not the value for n_e straight from the Sellmeier expansion, which is valid only for an angle of 90°. Phase-matching bandwidths were calculated for an assumed crystal thickness of 1 mm. It can be seen (Figure 1.13 (b)) that the maximum resolution is obtained at the wavelength where the phase-matching angle reaches a minimum.

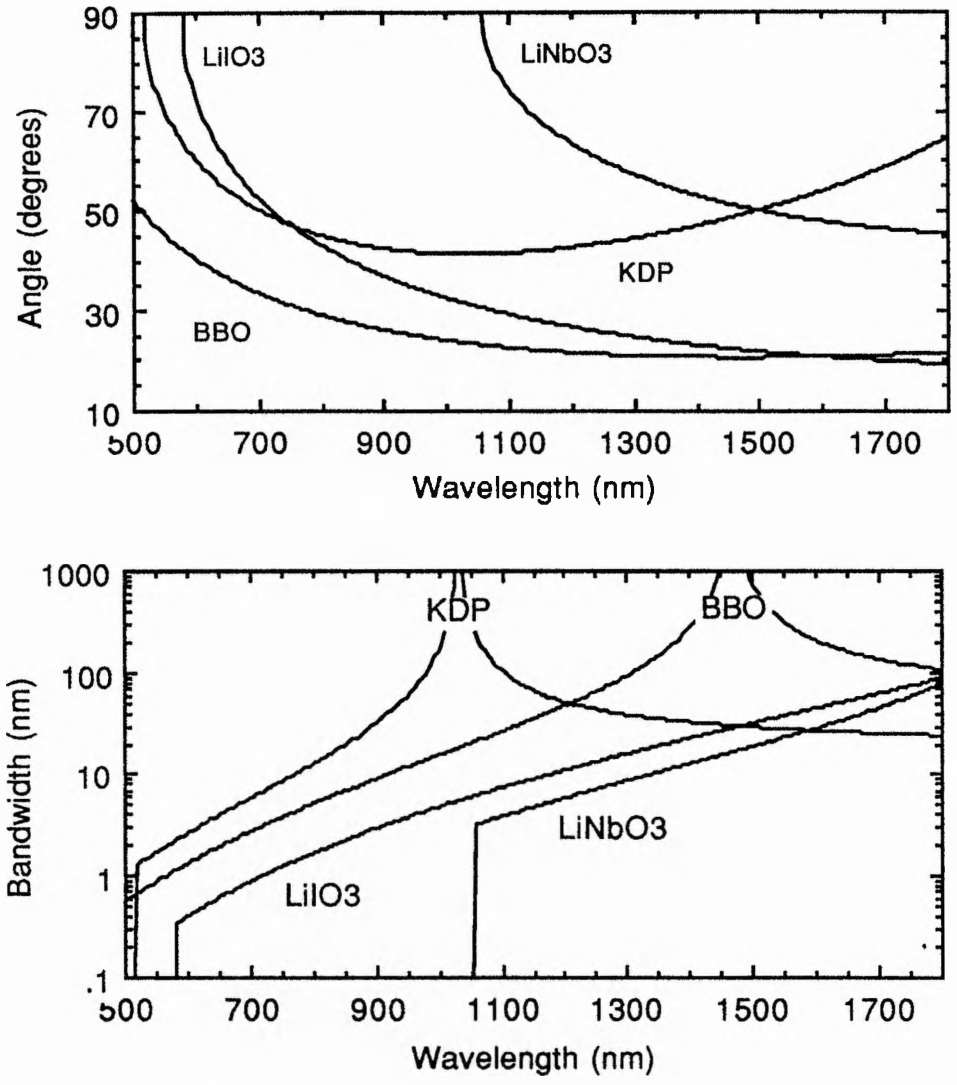

Figure 1.13 (a) Calculated phase matching angles for four SHG crystals in the wavelength range 500-1800 nm. (b) Corresponding phase-matching bandwidths assuming 1 mm thick crystals.

In practice, the choice of crystal will also be influenced by the strength of the nonlinear coefficients at the phase-matching angle. For example, it is recognised that the phase-matching bandwidth of KDP is greater than BBO at 630 nm (each crystal having an identical thickness). However, the much stronger nonlinearity of BBO means that a thin crystal of BBO is superior, both for bandwidth and SHG signal, to a thicker crystal of KDP.[109]

For experiments at 850 nm, 1 mm and 0.36 mm thick pieces of ADP (similar characteristics to KDP) were used, with calculated phase-matching bandwidths of 17 nm and

48 nm respectively. Assuming $sech^2$ pulses, this corresponds to temporal resolutions of 44 fs and 16 fs. At 1.5 μm, $LiNbO_3$ crystals of 2 mm and 0.25 mm thickness were used, giving bandwidths of 9 nm and 74 nm respectively, corresponding to resolutions of 260 fs and 32 fs for $sech^2$ pulses.

In certain cases it should be noted that GVM does not limit resolution. For type I phase matching, Weiner[110] showed that a limited phase-matching bandwidth did not alter the autocorrelations significantly, providing the pulses were bandwidth limited, and that phase matching was obtained at the central frequency. This has been verified experimentally.[109,111] For an unchirped pulse, the carrier frequency is present throughout its entire length, and since the autocorrelator measures the spatial extent of the pulses by coincidence detection at the fundamental frequency, the temporal broadening of the pulses at the second harmonic frequency due to the phase-matching bandwidth is irrelevant. In general, however, the length of the crystal should conform to the conditions described by Miller, because the presence of frequency chirp may not be apparent until after the pulse is measured and the duration bandwidth product calculated!

The principal deficiency of the autocorrelator, the ambiguity of the pulse shape and the lack of chirp information, is being addressed by a number of techniques. The interferometric autocorrelation goes some way in solving the problem, although a full reconstruction of the pulse details is not possible. Naganuma et al.[112] have developed a technique where both an interferometric autocorrelation and an interferogram (Fourier transform of the spectrum) are taken. The pulse is then chirped in a medium whose dispersive properties are known, and the two measurements are repeated. The pulse can then be reconstructed after intensive computation.

1.5.3 Spectral domain measurements

The spectrum of the pulse provides important additional information. As discussed earlier, knowledge of the spectral width and shape can assist in determining the pulse shape. The spectrum of a pulse should be symmetrical, whether the temporal profile is symmetric or not, providing it is unchirped. Under certain circumstances, chirped pulses may have symmetrical

spectra, eg. when the pulse is symmetrical and the chirp is caused by an instantaneous nonlinearity (see reference **102** for examples).

Pulse spectra were measured using diffraction grating monochromators with resolutions of 0.1 nm (1 m Monospek 1000) and 1 nm (25 cm Applied Photophysics). In addition, a scanning plane-parallel Fabry-Perot interferometer proved useful for many experiments, since it allowed real time measurements. Although the maximum finesse was only 60, the resolution could be optimised for the particular measurement being undertaken by adjusting the mirror separation.

The spectra recorded on the interferometer were calibrated by measuring the mirror separation. One of the mirrors, mounted on a precision translation stage, was moved into contact with the other to give the zero-point. For very close separations, this method was found to be inaccurate, presumably because the origin of the mirrors (dielectric stacks) was a few microns beneath the top layers. In these circumstances, the calibration was performed by comparing spectra with those taken with a monochromator, or by examining the mode spacing of a semiconductor laser or amplifier which had been previously measured with a monochromator. By comparing the measurement made by touching the plates together with the calibration using the semiconductor laser modes, a correction distance of approximately 16 μm was deduced. The relations for the free spectral range (*FSR*) were modified to include this factor

$$FSR\ (\lambda) \approx \frac{\lambda^2}{2\ (x + d)} \qquad FSR\ (\upsilon) \approx \frac{c}{2\ (x + d)} \qquad (1.18).$$

The separation measured by touching the mirrors together is denoted by d, and x is the correction factor, 16 μm.

1.6 Pulse propagation

A pulse is sensitive to the media through which it propagates. For example, it may be amplified or absorbed due to the presence of gain or loss. Providing no saturation of the transition occurs, this effect is classified as linear. Other linear effects include spectral filtering, eg. filtering caused by the finite gain bandwidth of an amplifier, and frequency chirping due to group-velocity dispersion. On the other hand, the medium may sense the

pulse if it is particularly energetic (or intense) and react to it. The pulse will, in turn, respond to these changes in the medium. This feedback results in nonlinear behaviour. Apart from the SHG autocorrelator, the nonlinear effects in this work arise from the cubic polarisation, caused by the third-order nonlinear susceptibility, $\chi^{(3)}$. Before discussing the effect of nonlinearities, the linear propagation of pulses in the presence of chromatic dispersion will be discussed, in both bulk media and single-mode fibres.

1.6.1 Chromatic dispersion in bulk media

The large spectral bandwidth associated with an ultrashort pulse means that variations of refractive index with wavelength become important. The rate of change of index with wavelength leads to a spread of phase velocities over the pulse spectrum. This dispersion causes the pulse to travel at the group velocity. The variation of group velocity with wavelength or group-velocity dispersion (GVD) and higher order effects can distort the pulse shape. These variations in index are treated mathematically[113] by using the propagation constant β, which is expanded in terms of a Taylor series :

$$\beta(\omega) = n(\omega)\frac{\omega}{c} = \beta_0 + \beta_1(\omega - \omega_0) + \frac{1}{2}\beta_2(\omega - \omega_0)^2 + \qquad (1.19)$$

where ω_0 is the angular frequency of the wave, and where β_j is defined

$$\beta_j = \left(\frac{d^j\beta}{d\omega^j}\right), \quad \omega = \omega_0 \qquad j = 0,1,2,3.... \qquad (1.20).$$

It can be easily shown that

$$\beta_0 = \frac{n\omega}{c} = \frac{2\pi n}{\lambda} \qquad (1.21)$$

$$\beta_1 = \frac{d\beta}{d\omega} = \frac{1}{c}\left(n + \omega\frac{dn}{d\omega}\right) = \frac{1}{c}\left(n - \lambda\frac{dn}{d\lambda}\right) \qquad (1.22)$$

$$\beta_2 = \frac{d^2\beta}{d\omega^2} = \frac{\lambda^3}{2\pi c^2}\frac{d^2n}{d\lambda^2} \qquad (1.23)$$

$$\beta_3 = \frac{d^3\beta}{d\omega^3} = \frac{-\lambda^4}{4\pi^2c^3}\left(3\frac{d^2n}{d\lambda^2} + \lambda\frac{d^3n}{d\lambda^3}\right) \qquad (1.24).$$

These four terms are related to phase velocity, group velocity, group-velocity dispersion (GVD), and 2nd order GVD. Usually, β_2 is quoted in terms of ps^2/km, but in femtosecond lasers (see chapter 2), the GVD of specific components is normally described by the product of the path length and β_2, in which case the units fs^2 are normally used. For many optical materials, including both insulators and semiconductors, the variation of refractive index with wavelength (and hence the derivatives) can be readily determined by reference to published Sellmeier expansions.

The GVD of transparent optical materials goes through zero and changes sign at some wavelength in the near infrared. At this wavelength, denoted λ_0, the group velocity of a pulse will reach a maximum. On the short wavelength side of λ_0, where *normal* GVD is present (β_2 positive), the red components of a pulse travel faster than the blue components, thus the red components of the pulse spectrum will move to the front and the blue components to the rear of the temporal profile. This leads to both broadening of the temporal profile of the pulse and to a linear upchirp in frequency. Temporal broadening will also occur when β_2 is negative (*anomalous* GVD) but the pulse will be downchirped.

Before quantifying the temporal broadening of pulses due to GVD, some useful expressions will be introduced, following the nomenclature used by Agrawal.[113] He describes the pulse duration by the half-width at the 1/e intensity point, denoted by T_0. For Gaussian pulses, it can be shown that

$$\Delta\tau_p = T_{FWHM} = 1.665\, T_0 \tag{1.25}$$

$$P_0 = \frac{E_{in}}{T_0\sqrt{\pi}} = \frac{E_{in}}{1.134\, \Delta\tau_p} \tag{1.26}$$

where P_0 is the peak power and E_{in} is the pulse energy. Similarly, for $sech^2$ pulses

$$\Delta\tau_p = T_{FWHM} = 1.763\, T_0 \tag{1.27}$$

$$P_0 = \frac{E_{in}}{2T_0} = \frac{E_{in}}{1.065\, \Delta\tau_p} \tag{1.28}.$$

The fractional broadening of an initially unchirped Gaussian pulse of duration T_{in} due purely to GVD is described by the relation

$$\frac{T_{out}}{T_{in}} = \left(1 + \left(\frac{z}{L_D}\right)^2\right)^{1/2} \tag{1.29}$$

where L_D is the dispersion length defined by

$$L_D = \frac{T_0^2}{|\beta_2|} \tag{1.30}.$$

1.6.2 Chromatic dispersion in monomode optical fibres

Optical waveguides have a number of obvious advantages over bulk media. By confining the pulse in the transverse direction, its intensity can be maintained over long distances, limited only by the attenuation of the guide material. In addition, the nonlinear effect of self-focussing can be eliminated by the confinement of the guide. Waveguiding can also be used to obtain low thresholds in lasers, eg. semiconductor lasers and fibre lasers.

The simplest optical guide is formed when the refractive index in the direction transverse to the direction of propagation has a top-hat profile, the raised index forming a *core* which is surrounded by a *cladding*. This type of guide is widely used in optical fibres[114] and in semiconductor lasers. The difference in the refractive indices of the core and cladding can be expressed in two forms

$$\Delta n = n_{core} - n_{clad} = n_1 - n_2 \tag{1.31}$$

or

$$\Delta = \frac{n_1 - n_2}{n_1} \tag{1.32}.$$

In simplistic terms, the light is confined within the core by total internal reflection, however a more accurate picture is given by considering transverse modes. The strength of the guiding, which is determined by the index difference and by the size of the core, is characterised by the normalised frequency V.

For circularly symmetric guides, V is defined by

$$V = \frac{2\pi}{\lambda} a \left(n_1^2 - n_2^2 \right)^{1/2} \tag{1.33}$$

where a denotes the radius of the core. Only the lowest order (fundamental) transverse mode can propagate when $V < 2.405$.[115] Therefore, fundamental transverse mode propagation can be ensured by using a small core radius, or a low index difference. By eliminating the higher order modes, which propagate at different velocities, pulse distortion is greatly reduced. With single-mode fibres, two main sources of group-velocity dispersion can be identified. These are material GVD, as discussed earlier in the context of bulk media, and waveguide GVD.

To fully quantify pulse distortion, the propagation constant β for the mode should be evaluated. This is both complex and tedious, and in many cases the GVD in a single mode fibre is treated by using the approximation that the contributions from the material and the waveguide are unrelated and additive, ie.

$$D = D_m + D_{wg} \tag{1.34}.$$

where D_m and D_{wg} represent the contributions to GVD from the core material and the waveguiding respectively. The material contribution is given by

$$D_m = \frac{d\beta_1}{d\lambda} = \frac{-2\pi c \beta_2}{\lambda^2} = \frac{-\lambda}{c} \frac{d^2 n}{d\lambda^2} \tag{1.35}.$$

The contribution from the waveguide can be calculated from[114,116]

$$D_{wg} = \frac{V n_{clad} \Delta}{\lambda c} \frac{d^2(Vb)}{dV^2} \tag{1.36}$$

where $b = b(V)$ is the normalised eigenvalue or dispersion function, defined by

$$b = \left(\frac{\beta^2}{k_0^2} - n_{clad}^2 \right) \left(n_{core}^2 - n_{clad}^2 \right) \tag{1.37}$$

where k_0 is the wave number $2\pi/\lambda$.

Other useful expressions for optical fibres include the definition for second order GVD:

$$D' = \frac{dD}{d\lambda} = \frac{4\pi c}{\lambda^3}\left(\beta_2 + \frac{\pi c}{\lambda}\beta_3\right) \tag{1.38}$$

and the reciprocal relations for the propagation constants

$$\beta_2 = \frac{-\lambda^2 D}{2\pi c} \tag{1.39}$$

$$\beta_3 = \frac{\lambda^4}{4\pi^2 c^2}(2\lambda^2 D + D') \tag{1.40}.$$

The material GVD of fused silica has a zero at 1.27 μm, however the position of λ_0 can be shifted to longer wavelengths by increasing the waveguide GVD. This is achieved by raising the core/cladding index difference, which in turn requires a smaller core size to maintain the *V* number at a reasonable value, within the range, say ($1.8 < V < 2.4$). Large index differences can be obtained by doping the silica core with germania.[117] Coincidentally, the material dispersion of germania-doped silica has its minima shifted to wavelengths somewhat longer than 1.27 μm. Together, these two effects can shift the λ_0 to 1.55 μm or beyond.

For propagation at λ_0, the central region of the pulse spectrum will travel faster than the components at the edges due to 2nd order GVD (3rd order dispersion).[118] This causes asymmetric temporal broadening since the central spectral region, which leads in time, has more energy than the two outer edges of the spectrum which lag. Thus, the trailing edge develops two distinct carrier frequencies which continuously diverge. The interference of these two frequencies leads to beating and ripples on the pulse trailing edge.

1.6.3 Nonresonant nonlinearities

The third-order nonlinearities may be categorised as resonant or nonresonant.[119] Nonresonant nonlinearities are associated with the optically transparent spectral region of insulators and semiconductors, eg. between 300 nm and approximately 10 μm in silica. The most important effect in the context of this thesis, is the intensity dependent change in

refractive index, which is understood to be caused by the oscillations of bound electrons in response to the AC electric field of the light beam. This effect is relatively weak compared to resonant nonlinearities (discussed later) but it has an essentially instantaneous recovery, since only virtual transitions are involved. For example, in fused silica the associated time constant is estimated to be less than 5 fs.[120] Recent theoretical work has assessed the various contributions to the ultrafast nonlinearity associated with bound electrons in semiconductors and wide bandgap solids.[121] These include the optical Stark effect, two-photon absorption, and the electronic Raman effect.

Nonsaturating, intensity dependent changes in the refractive index, $\Delta n(t)$ can be described by the following rate equation:

$$\frac{\partial(\Delta n)}{\partial t} = \frac{1}{\tau}(n_2 I - \Delta n) \tag{1.41}$$

where τ is the recovery time, $I(t)$ is the optical intensity, and n_2 is the nonlinear index coefficient. This formalism[122] is particularly appropriate for modelling the nonresonant refractive index changes that are observed in the liquid CS_2 (caused by molecular reorientation), which has a recovery time of a few picoseconds.

When the changes in intensity occur on a much faster timescale than the recovery time, then $n_2 I >> \Delta n$ and the resultant changes in the index can be approximated by the integral of the pulse intensity

$$\Delta n(t) = \frac{n_2}{\tau}\int_0^{t_1} I(t)dt = \frac{n_2}{\tau}U(t) \tag{1.42}$$

where $U(t)$ is the fluence of the pulse upto time t_1.

For pulses whose duration greatly exceeds the recovery time (the normal situation in solids), the index change becomes proportional to the optical intensity, ie.

$$\Delta n = n_2 I \tag{1.43}.$$

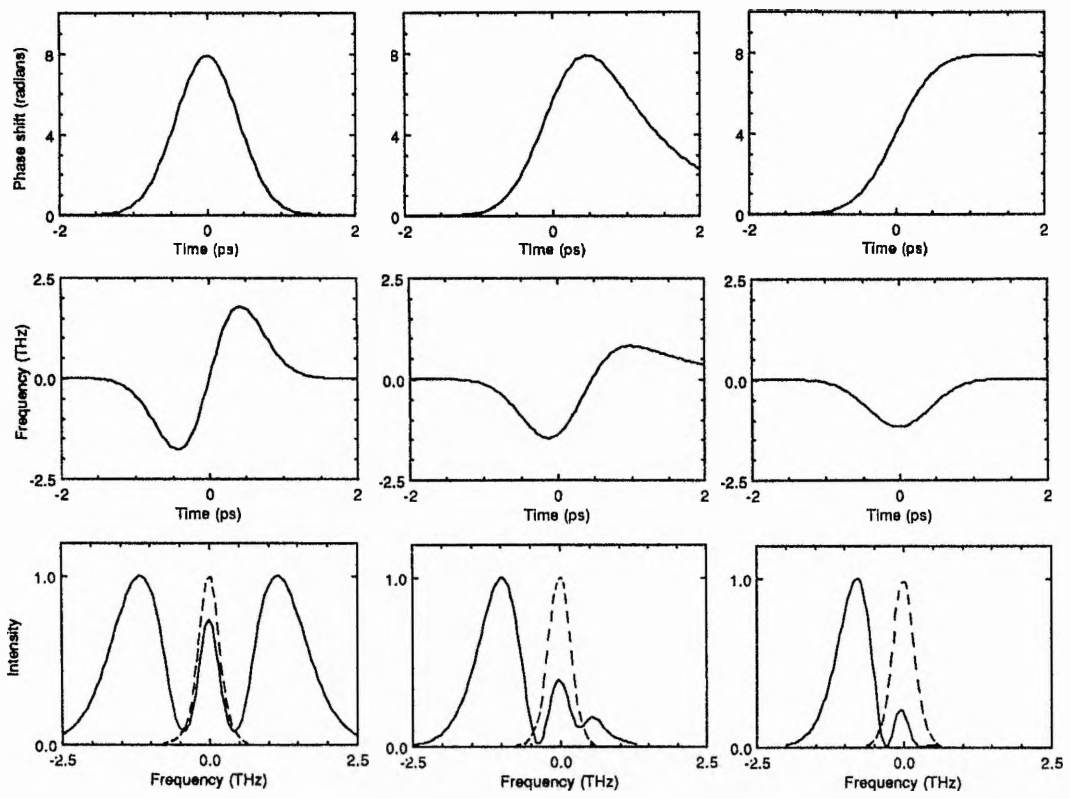

Figure 1.14 The effect of recovery time on the self-phase modulation of a Gaussian pulse of 1 ps FWHM caused by a nonresonant nonlinear refractive index changes. The three rows depict: (from top to bottom) phase shift; frequency chirp; and spectral broadening. The recovery time varies from left to right: instantaneous; 1 ps; and 100 ps. The n_2 (positive) is constant for all three cases, and the pulse energy was adjusted to maintain the maximum phase shift at $5\pi/2$ radians. The pulse energies were in the ratio 1.00 : 1.83 : 95.30 (going from left to right). The pulse shape is directly proportional to the top left graph, and the input spectrum is shown by the dashed lines.

If the change in refractive index $\Delta n(t)$ is maintained for a length L, the optical cycles undergo a shift in phase $\Delta\phi(t)$ given by

$$\Delta\phi = \frac{2\pi L}{\lambda}\Delta n \tag{1.44}$$

where t is the time within the pulse reference frame. This is the self-phase modulation responsible for spectral distortion and changes in carrier frequency, ie. frequency chirp:

$$\Delta\omega = -\frac{\partial\phi}{\partial t} \qquad \Delta\upsilon = \frac{-1}{2\pi}\frac{\partial\phi}{\partial t} \tag{1.45}.$$

The phase shift, frequency chirp and spectral broadening associated with self-phase modulation have distinct forms depending on the ratio of the pulse duration to the recovery time. Three different cases are illustrated in Figure 1.14 (previous page).

1.6.4 Nonlinear pulse propagation in monomode optical fibres

Within bulk media, the intensity dependent changes in refractive index may induce changes in the width of the beam due to the formation of a radial index gradient. If the index increases in response to the beam, the beam will tend to focus. With large index changes, this self-focussing may cause the beam to collapse in on itself and can result in catastrophic damage to a solid medium. By using optical waveguides, such as fibres, these self-focussing effects can be avoided and pure self-phase modulation can be obtained. For nonlinear pulse propagation in optical fibres, the behaviour of a pulse is properly described using the nonlinear Schrödinger equation. This approach is complex and phenomena such as solitons can be discussed without reference to the equation.

Usually, the nonlinear index change is assumed to have an instantaneous recovery. Agrawal[113] has introduced the parameter γ to denote the effective nonlinearity of the fibre

$$\gamma = \frac{n_2\omega}{cA_{\text{eff}}} = \frac{2\pi n_2}{\lambda A_{\text{eff}}} \tag{1.46}$$

where c is the speed of light, and A_{eff} is the area of the mode, typically some 10 to 40% larger than the core area. Using this parameter γ, the nonlinear length L_{NL} can be defined

$$L_{\text{NL}} = \frac{1}{\gamma P_0} \tag{1.47}$$

where P_0 is the peak power of the pulse, which was defined previously in terms of pulse energy. In the absence of GVD, the peak phase shift incurred by the pulse propagating in a fibre of length Z is

$$\phi_{\text{max}} = \frac{Z}{L_{\text{NL}}} \tag{1.48}.$$

With long fibres, Z should be replaced with an effective length Z_{eff} to take account of linear loss α:

$$Z_{eff} = \frac{1 - \exp(-\alpha Z)}{\alpha} \tag{1.49}$$

For normal dispersion, when $L_{NL} >> L_D$, the pulse propagation is dominated by dispersion and an initially unchirped pulse will broaden according to equation (1.29). If $L_D >> L_{NL}$, nonlinearity dominates and the pulse acquires chirp from self-phase modulation and providing the fibre length $Z << L_D$, the pulse does not broaden. In between these two extremes there are no wholly satisfactory analytical methods of accurately quantifying the behaviour of the pulse, and one must resort to numerical simulation. The split-step Fourier method treats the fibre as alternating regions of nonlinearity and GVD. Nonlinearity is treated in the temporal domain and GVD in the spectral domain, necessitating a Fourier transform or inverse transform at the interfaces.

In simple terms, the combination of normal GVD and SPM enhances the temporal broadening of the pulse, which tends to a rectangular profile. The nonlinear chirp adds to the dispersive chirp, with the net effect that the chirp becomes linear over almost the entire length of the pulse. The linear chirp allows efficient pulse compression by using 2nd order dispersive (GVD) elements such as prisms or gratings (see reference **123**).

For anomalous GVD, at some peak power level denoted P_1 when $L_D = L_{NL}$, the chirp from SPM can cancel with the chirp from dispersion and dispersive broadening can be prevented, the pulse maintaining its shape providing there is no significant attenuation.[124] Under these circumstances, a solution to the nonlinear Schrödinger equation is a pulse with a sech^2 intensity profile. This pulse is the fundamental soliton ($N = 1$). At higher power levels, the SPM overwhelms the dispersion and this results in higher order solitons. These pulses narrow and then go through phases of splitting and recombining before reverting to the original sech^2 shape at a distance Z_0, the soliton period. The cycle is repeated every soliton period. The soliton order N is calculated from

$$N = \sqrt{\frac{L_D}{L_{NL}}} \tag{1.50}.$$

The soliton period Z_0 is given by

$$Z_0 = \frac{\pi}{2} L_D \qquad (1.51).$$

When the launched pulse is not precisely sech^2, and/or does not have the correct peak power to conform to a precise soliton order N, it will shed energy in the form of dispersive waves and adjust its width such that it eventually evolves into a soliton.

The nonlinear propagation of pulses in optical fibres will be discussed further in chapter 3, when their use in coupled-cavity mode-locked lasers will be described.

1.6.5 Resonant nonlinearities

Resonant nonlinearities are associated with real transitions, as the name suggests. The complex susceptibility $\chi^{(3)}$ of a transition is composed of an imaginary component, responsible for gain and loss, and a real component which is associated with the refractive index. Given one of these curves for a particular transition, the other may be calculated using the Kramers-Krönig relations.[119] Nonlinearity is obtained when the optical signal is sufficiently intense or energetic to reduce (or saturate) the loss/gain. The change in transmission is accompanied by changes in refractive index. Therefore pulse shaping is accompanied by self-phase modulation. Because real transitions are involved, the recovery times are generally much longer than a mode-locked pulse, and the corresponding self-phase modulation is asymmetric.

These nonlinearities are particularly relevant in passively mode-locked dye lasers. As discussed previously, such lasers rely on pulse shaping from the saturation of both the absorber and the gain to obtain pulse shortening. The associated self-phase modulation is accompanied by a nonresonant contribution from the ethylene glycol in the absorber jet. These effects are essentially negligible in a single pass, but over many round trips will be important and cause additional pulse shaping in the presence of dispersion, and furthermore, might be expected to pull the operating wavelength of the laser. Recently, it has been pointed out that there is considerable SPM associated with gain saturation in semiconductor amplifiers, due to the large small signal gains (~ 1000), and the asymmetry of the gain cross-section with wavelength.[125] This will be discussed in more detail in chapter 4.

1.7 References

1. *Ultrashort Laser Pulses and Applications*, W. Kaiser, ed. (Springer-Verlag, Berlin, 1988).
2. *Ultrafast Phenomena VII*, C. B. Harris, E. P. Ippen, G. A. Mourou, and A. H. Zewail, eds. (Springer-Verlag, Berlin, 1990).
3. R. L. Fork, C. H. Brito Cruz, P. C. Becker, and C. V. Shank, Opt. Lett. **12**, 483 (1987).
4. L. F. Mollenauer, "Color Center Lasers" (chapter 2), in *Laser Handbook, Vol. 4*, M. L. Stitch and M. Bass, eds. (Elsevier Science, Amsterdam, 1985).
5. L. F. Mollenauer and K. Smith, Opt. Lett. **13**, 675 (1988).
6. K. J. Blow, N. J. Doran, and B. K. Nayer, Opt. Lett. **14**, 754 (1989).
7. B. Henderson and G. F. Imbusch, *Optical Spectroscopy of Inorganic Solids* (Oxford University Press, Oxford, 1989).
8. C. R. Pollock, J. Luminescence **35**, 65 (1986).
9. W. Gellermann, J. Phys. Chem. Solids **52**, 249 (1991).
10. W. Gellermann, A. Müller, D. Wandt, S. Wilk, and F. Lüty, J. Appl. Phys. **61**, 1297 (1987).
11. B. Fritz and E. Menke, Sol. State Commun. **3**, 61 (1965).
12. L. F. Mollenauer and D. H. Olson, Appl. Phys. Lett. **24**, 386 (1974).
13. L. F. Mollenauer and D. H. Olson, J. Appl. Phys. **46**, 3109 (1975).
14. K. R. German, J. Opt. Soc. Am. B **3**, 149 (1986).
15. M. A. Aegerter and F. Lüty, Phys. Stat. Sol. (b) **43**, 245 (1971).
16. L. F. Mollenauer, Opt. Lett. **1**, 164 (1977).
17. W. Gellermann, F. Lüty, K. P. Koch, and H. Welling, Opt. Commun. **35**, 430 (1980).
18. L. F. Mollenauer, Opt. Lett. **5**, 188 (1980).
19. L. F. Mollenauer, Opt. Lett. **6**, 342 (1981).
20. D. M. Hofmann, F. Lohse, H. J. Paus, D. Y. Smith, and J.-M. Spaeth, J. Phys. C: Solid State Phys. **18**, 443 (1985).
21. I. Schneider and M. J. Marrone, Opt. Lett. **4**, 390 (1979).
22. I. Schneider and C. R. Pollock, J. Appl. Phys. **54**, 6193 (1983).
23. R. S. Afzal and I. Schneider, J. Appl. Phys. **69**, 4178 (1991).
24. J. F. Pinto, E. Georgiou, and C. R. Pollock, Opt. Lett. **11**, 519 (1986).
25. W. Gellermann, F. Lüty, and C. R. Pollock, Opt. Commun. **39**, 391 (1981).
26. T. T. Basiev, S. B. Mirov, and V. V. Osiko, IEEE J. Quantum Electron. **24**, 1052 (1988).
27. J. M. Wiesenfeld, L. F. Mollenauer, and E. P. Ippen, Phys. Rev. Lett. **47**, 1668 (1981).
28. L. F. Mollenauer, J. Luminescence **31&32**, 9 (1984).
29. O. B. Peterson, S. A. Tuccio, and B. B. Snavely, Appl. Phys. Lett. **17**, 245 (1970).
30. R. L. Kohn, C. V. Shank, E. P. Ippen, and A. Dienes, Opt. Commun. **3**, 177 (1971).
31. H. W. Kogelnik, E. P. Ippen, A. Dienes, and C. V. Shank, IEEE J. Quantum Electron. **QE-8**, 373 (1972).
32. H. Kogelnik, Bell Syst. Tech. J. **44**, 455 (1965).
33. C. E. Wagstaff, M. H. Dunn, A. I. Ferguson, and S. J. Bastow, Opt. Commun. **25**, 379 (1978).
34. K. S. Budil, I. A. McIntyre, and C. K. Rhodes, Opt. Commun. **64**, 279 (1987).

35. N. J. Langford, PhD Thesis (University of London, 1988).
36. C. I. Johnston, PhD Thesis (University of St. Andrews, 1991).
37. D. A. B. Miller, M. H. Mozolowski, A. Miller, and S. D. Smith, Opt. Commun. **27**, 133 (1978).
38. *CRC Handbook of Materials Science, Vol. 1, General Properties*, C. T. Lynch, ed. (CRC Press, Boca Raton, FL, 1974).
39. G. H. C. New, Rep. Prog. Phys. **46**, 877 (1983).
40. A. E. Siegman, *Lasers* (University Science, Mill Valley, CA, 1986).
41. L. E. Hargrove, R. L. Fork, and M. A. Pollack, Appl. Phys. Lett. **5**, 4 (1964).
42. M. DiDomenico, J. E. Greusic, H. M. Marcos, and R. G. Smith, Appl. Phys. Lett. **8**, 180 (1966).
43. P. K. Runge, Opt. Commun. **5**, 311 (1972).
44. C. K. Chan and S. O. Sari, Appl. Phys. Lett. **25**, 403 (1974).
45. J. M. Harris, R. W. Chrisman, and F. E. Lytle, Appl. Phys. Lett. **26**, 16 (1975).
46. J. P. Heritage and R. K. Jain, Appl. Phys. Lett. **32**, 101 (1978).
47. E. W. Van Stryland, Opt. Commun. **31**, 93 (1979).
48. A. M. Johnson and W. M. Simpson, J. Opt. Soc. Am. B **2**, 619 (1985).
49. E. P. Ippen, C. V. Shank, and A. Dienes, Appl. Phys. Lett. **21**, 348 (1972).
50. G. H. C. New, Opt. Commun. **6**, 188 (1972).
51. I. S. Ruddock and D. J. Bradley, Appl. Phys. Lett. **29**, 296 (1976).
52. R. L. Fork, B. I. Greene, and C. V. Shank, Appl. Phys. Lett. **38**, 671 (1981).
53. R. L. Fork, C. V. Shank, R. Yen, and C. A. Hirlimann, IEEE J. Quantum Electron. **QE-19**, 500 (1983).
54. M. S. Stix and E. P. Ippen, IEEE J. Quantum Electron. **QE-19**, 520 (1983).
55. W. Dietel, J. J. Fontaine, and J.-C. Diels, Opt. Lett. **8**, 4 (1983).
56. J. A. Valdmanis, R. L. Fork, and J. P. Gordon, Opt. Lett. **10**, 131 (1985).
57. A. Finch, G. Chen, W. Sleat, and W. Sibbett, J. Mod. Opt. **35**, 345 (1988).
58. J. C. Comly, A. Yariv, and E. M. Garmire, Appl. Phys. Lett. **15**, 148 (1969).
59. A. J. Duerinckx, H. A. Vanherzeele, J.-L. Van Eck, and A. E. Siegman, IEEE J. Quantum Electron. **QE-14**, 983 (1978).
60. H. A. Haus and Y. Silberberg, IEEE J. Quantum Electron. **QE-22**, 325 (1986).
61. H. A. Haus, J. G. Fujimoto, and E. P. Ippen, J. Opt. Soc. Am. B **8**, 2068 (1991).
62. L. F. Mollenauer and R. H. Stolen, Opt. Lett. **9**, 13 (1984).
63. L. F. Mollenauer and R. H. Stolen, in *Ultrafast Phenomena IV* (Springer-Verlag, Berlin, 1984), pp. 2-6.
64. H. A. Haus and M. N. Islam, IEEE J. Quantum Electron. **QE-21**, 1172 (1985).
65. F. If, P. L. Christiansen, J. N. Elgin, J. D. Gibbon, and O. Skovgaard, Opt. Commun. **57**, 350 (1986).
66. K. J. Blow and D. Wood, IEEE J. Quantum Electron. **QE-22**, 1109 (1986).
67. F. Mitschke and L. F. Mollenauer, IEEE J. Quantum Electron. **QE-22**, 2242 (1986).
68. P. Berg, F. If, P. L. Christiansen, and O. Skovgaard, Phys. Rev. A **35**, 4167 (1987).
69. F. Bélanger, J. Opt. Soc. Am. B **5**, 793 (1988).

70. F. M. Mitschke and L. F. Mollenauer, Opt. Lett. **12**, 407 (1987).
71. K. J. Blow and D. Wood, J. Opt. Soc. Am. B **5**, 629 (1988).
72. P. N. Kean, R. S. Grant, D. W. Crust, X. Zhu, D. Burns, and W. Sibbett, in *Technical Digest of Conference on Lasers and Electro-Optics* (Optical Society of America, Washington, D.C., 1988), paper PD7.
73. P. N. Kean, X. Zhu, D. W. Crust, R. S. Grant, N. Langford, and W. Sibbett, Opt. Lett. **14**, 39 (1989).
74. K. J. Blow, D. S. Forrester, and B. P. Nelson, in *Ultrafast Phenomena VI* (Springer-Verlag, Berlin, 1988), pp. 67-69.
75. K. J. Blow and B. P. Nelson, Opt. Lett. **13**, 1026 (1988).
76. F. Ouellette and M Piché, Can. J. Phys. **66**, 903 (1988).
77. F. Ouellette and M. Piché, Opt. Commun. **60**, 99 (1986).
78. J. Mark, L. Y. Liu, K. L. Hall, H. A. Haus, and E. P. Ippen, Opt. Lett. **14**, 48 (1989).
79. E. P. Ippen, H.A. Haus, and L. Y. Liu, J. Opt. Soc. Am. B **6**, 1736 (1989).
80. M. Morin and M. Piché, Opt. Lett. **14**, 1119 (1989).
81. J. R. M. Barr and D. W. Hughes, Appl. Phys. B **49**, 323 (1989).
82. P. M. W. French, J. A. R. Williams, and J. R. Taylor, Opt. Lett. **14**, 686 (1989).
83. J. Goodberlet, J. Wang, J. G. Fujimoto, and P. A. Schulz, Opt. Lett. **14**, 1125 (1989).
84. T. F. Carruthers and I. N. Duling III, Opt. Lett. **15**, 804 (1990).
85. A. G. Bulushev, E. M. Dianov, and O. G. Okhotnikov, IEEE Photon. Technol. Lett. **2**, 699 (1990).
86. D. E. Spence, P. N. Kean, and W. Sibbett, Opt. Lett. **16**, 42 (1991).
87. L. Spinelli, B. Couillaud, N. Goldblatt, and D. K. Negus, in *Technical Digest of Conference on Lasers and Electro-Optics* (Optical Society of America, Washington, D.C., 1991), paper CPDP7.
88. L. Dahlström, Opt. Commun. **5**, 157 (1972).
89. G. Gabetta, D. Huang, J. Jacobson, M. Ramaswamy, H. A. Haus, E. P. Ippen, and J. G. Fujimoto, in *Technical Digest of Conference on Lasers and Electro-Optics* (Optical Society of America, Washington, D.C., 1991), paper CPDP8.
90. K. A. Stankov and J. Jethwa, Opt. Commun. **66**, 41 (1988).
91. E. K. Zavoiskii and S. D. Fanchenko, Sov. Phys. Doklady **1**, 285 (1956).
92. D. J. Bradley, B. Liddy, and W. E. Sleat, Opt. Commun. **2**, 391 (1971).
93. D. J. Bradley and W. Sibbett, Appl. Phys. Lett. **27**, 382 (1975).
94. M. C. Adams, W. Sibbett, and D. J. Bradley, Opt. Commun. **26**, 273 (1978).
95. J. A. Armstrong, Appl. Phys. Lett. **10**, 16 (1967).
96. H. P. Weber, J. Appl. Phys. **38**, 2231 (1967).
97. M. Maier, W. Kaiser, and J. A. Giordmaine, Phys. Rev. Lett. **17**, 1275 (1966).
98. E. P. Ippen and R. L. Fork, Appl. Phys. Lett. **27**, 488 (1975).
99. R. L. Fork and F. A. Beisser, Appl. Opt. **17**, 3534 (1978).
100. J.-C. M. Diels, J. J. Fontaine, I. C. McMichael, and F. Simoni, Appl. Opt. **24**, 1270 (1985).
101. K. L. Sala, G. A. Kenney-Wallace, and G. E. Hall, IEEE J. Quantum Electron. **QE-16**, 990 (1980).
102. A. Finch, PhD Thesis (University of St. Andrews, 1989).

103. A. Yariv, *Quantum Electronics* (3rd edition, John Wiley, New York, 1988).
104. K. W. Kirby and L. G. DeShazer, J. Opt. Soc. Am. B **4**, 1072 (1987).
105. M. V. Hobden and J. Warner, Phys. Lett. **22**, 243 (1966).
106. D. Eimerl, L. Davis, S. Velsko, E. K. Graham, and A. Zalkin, J. Appl. Phys. **62**, 1968 (1987).
107. M. M. Choy and R. L. Byer, Phys. Rev. B **14**, 1693 (1976).
108. R. C. Miller, Phys. Lett. **26A**, 177 (1968).
109. K. L. Cheng, W. Bosenberg, F. W. Wise, I. A. Walmsley, and C. L. Tang, Appl. Phys. Lett. **52**, 519 (1988).
110. A.M. Weiner, IEEE J. Quantum Electron. **QE-19**, 1276 (1983).
111. A. M. Weiner, J. G. Fujimoto, and E. P. Ippen, Opt. Lett. **10**, 71 (1985).
112. K. Naganuma, K. Mogi, and H. Yamada, Appl. Phys. Lett. **54**, 1201 (1989).
113. G. P. Agrawal, *Nonlinear Fiber Optics* (Academic Press, San Diego, 1989).
114. D. Davidson, "Single-Mode Wave Propagation in Cylindrical Optical Waveguides" (chapter 3), in *Optical Fiber Transmission*, E. E. Basch, ed. (Howard Sams, Indianapolis, 1987).
115. D. Gloge, Appl. Opt. **10**, 2252 (1971).
116. B. J. Ainslie and C. R. Day, J. Lightwave Technol. **LT-4**, 967 (1986).
117. L. G. Cohen, C. Lin, and W. G. French, Electron. Lett. **15**, 334 (1979).
118. D. Marcuse, Appl. Opt. **19**, 1653 (1979).
119. P. N. Butcher and D. Cotter, *The Elements of Nonlinear Optics* (Cambridge University Press, Cambridge, 1990).
120. A. B. Grudinin, E. M. Dianov, D. V. Korobkin, A. M. Prokhorov, V. N. Serkin, and D. V. Khaidarov, JETP Lett. **46**, 221 (1987).
121. M. Sheik-Bahae, D. C. Hutchings, D. J. Hagan, and E. W. Van Stryland, IEEE J. Quantum Electron. **27**, 1296 (1991).
122. Y. R. Shen and M. M. T. Loy, Phys. Rev. A **3**, 2099 (1971).
123. W. J. Tomlinson, R. H. Stolen, and C. V. Shank, J. Opt. Soc. Am. B **1**, 139 (1984).
124. L. F. Mollenauer, R. H. Stolen, and J. P. Gordon, Phys. Rev. Lett. **45**, 1095 (1980).
125. G. P. Agrawal and N. A. Olsson, IEEE J. Quantum Electron. **25**, 2297 (1989).

2 The LiF:F_2^+ laser

2.1 Introduction

Mollenauer demonstrated the suitability of the F_2^+ colour-centre as a laser gain medium in 1977 with NaF crystals,[1] and later with several other alkali-halide lattices including LiF.[2-4] In the LiF lattice, the F_2^+ centre emits in the deep red / near infrared spectral region around 900 nm, where dye laser performance and operational lifetimes deteriorate. Coincidentally, in terms of laser properties, it is one of the most dye-like of the colour-centres, and the mode-locking behaviour of the LiF:F_2^+ colour centre laser is broadly similar to a dye laser. The relatively large gain cross-section allows the generation of picosecond pulses by synchronous mode locking and subpicosecond pulses by slow absorber passive mode locking.

Langford et al. have previously reported both the synchronous mode-locking characteristics[5] and the passive mode locking[6] of a LiF:F_2^+ laser where the saturable-absorber dye IR140 was used. In this chapter, the group-velocity-dispersion compensation of the passively mode-locked laser will be described. In addition, the coupled-cavity mode locking of the laser using an optical fibre as the control-cavity nonlinearity will be discussed.

2.2 The F_2^+ centre in LiF

In chapter 1 the F_2^+ colour-centre was briefly mentioned. The F_2^+ (or M^+) centre in LiF was identified and studied in the 1960s, long before their potential as laser gain media was recognised.[7,8] The centre consists of two F centres in nearest neighbour sites, i.e. in the direction <110>, and therefore there are 6 possible orientations of the centre. The axis of symmetry gives rise to polarisation sensitive transition moments, and for randomly oriented centres, at least one orientation is not efficiently excited by polarised light. The centre has a single electron, and hence the allowed electronic transitions are somewhat similar to an H_2^+

ion. These levels are shown in a simplified diagram in Figure 2.1, where the H_2^+ nomenclature has been used to label the states. In LiF, the F_2^+ centre is obtained after the thermal aggregation of F centres which are created by bombardment with high energy electrons (or X-rays) at low temperatures. The relatively small lattice dimensions of LiF shifts the energy levels of the centre such that the $2p\sigma_u$ -> $1s\sigma_g$ emission band of the laser transition appears at wavelengths bordering on the visible part of the spectrum.

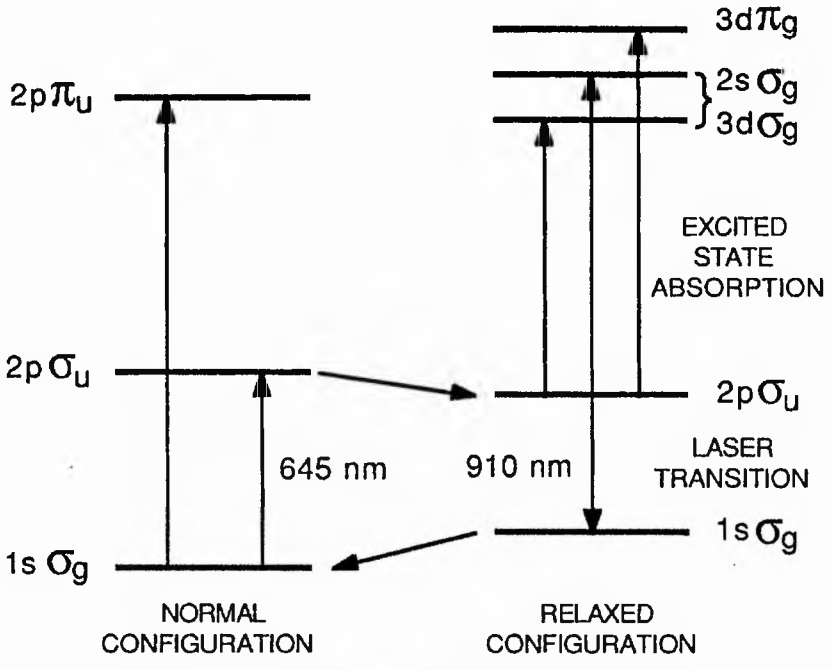

Figure 2.1 Energy-level structure of the F_2^+ centre in LiF (adapted from reference 4).

Unfortunately, the centre is not particularly stable under intense optical excitation, and if the electron reaches any of the states lying above the $2p\sigma_u$ level (usually by multiphoton excitation), the centre will pivot around one of the vacancies and change orientation.[4] Successive reorientation causes a random walk of the centre through the crystal until it meets other defects and loses its identity, or when its orientation is such that it no longer absorbs the polarised pump beam. The pertinent optical properties of the centre are summarised in Table 2.1.

The preparation of LiF laser crystals has previously been described by Smith[11] and hence the procedure will be discussed here only briefly. Nominally pure LiF boules, obtained from Harshaw or BDH (Merck), were annealed to distribute impurities and remove stresses prior to processing. The impurities include divalent metal ions such as Mn^{2+} which perform

the important rôle of trapping the free electrons created during the aggregation process. The boules were cut along (100) planes to give crystals of dimensions (10 x 10 x 3) mm^3, which after subsequent polishing were reduced to a thickness of approximately 2 mm.

Parameter	Value	Reference
Refractive index of LiF	1.39	9
Absorption peak	645 nm	7
Emission peak	910 nm	7
Emission FWHM	52 THz	8
τ_{rad}	29 ns	10
η (quantum efficiency)	1	1,10
σ_{em}	1.1×10^{-16} cm^2	

Table 2.1 Optical characteristics of the F_2^+ centre in LiF at 77 K.

The crystals were enclosed in aluminium foil packets and submersed in liquid nitrogen prior to irradiation. A Van de Graff generator was used to generate 1.5 MeV electrons, with a dosage of approximately 3 minutes at a current density of 0.5 mA cm^{-2}. The crystals were stored in a liquid nitrogen Dewar and only retrieved immediately before installation. The crystal loading procedure was described in chapter 1.

2.3 The krypton pump laser

The availability of argon and krypton ion lasers with multiwatt powers in TEM_{00} beam profiles has been instrumental in the development of efficient CW dye, colour-centre and Ti:sapphire lasers. The LiF:F_2^+ laser was pumped by a Spectra-Physics 171-01 krypton ion laser. For CW and passively mode locked operation of the colour-centre laser, the krypton laser was operated simultaneously on the 647 nm and 676 nm lines to maximise the available pump power. In this configuration, output powers of 5-6 W were observed (specification 4.6 W), but this gradually declined to around 3 W over the life of the plasma tube, normally around 1500-2000 hrs.

The krypton laser was also acousto-optically mode locked on the more powerful of the two lines (647 nm) for synchronous and coupled-cavity mode locking of the LiF laser. This section concentrates on the acousto-optic mode locking characteristics of the krypton laser.[12] Pulses substantially less than 100 ps duration on all the main transitions have been reported for a similar laser to the one described here.[13]

The laser was mode locked using a Spectra-Physics model 342 acousto-optic mode locker, which replaced the usual high reflector mirror holder. The model 342 mode-locker assembly consists of a Brewster-angled prism, to which the radio frequency (r.f.) transducer is bonded, and a high reflectivity mirror. The assembly enclosure incorporates an oven and thermistor so that a preset temperature can be maintained.

The prism has ultrasonic resonances spaced at intervals of approximately 400 kHz, but the transducer itself is optimised for frequencies in the vicinity of 41 MHz, consistent with the 82 MHz fundamental pulse repetition frequency of the 1.83 m long resonator. The 41 MHz signal was generated by a Racal 9081 synthesiser and amplified with a broadband r.f. power amplifier. A voltage standing-wave-ratio (VSWR or SWR) meter, inserted in the line between the amplifier and the mode locker, was used to optimise the drive frequency with respect to the resonances. Because the resonant frequencies of the prism increase with increasing temperature, the chosen resonance is approached from low frequencies. As the resonance is approached, the SWR meter falls, indicating a more efficient transfer of power to the mode locker. The resonant frequency then increases as the prism rises in temperature, and this should be slowly followed by the drive frequency until the SWR reading approaches a minimum. If the optimum frequency is inadvertently exceeded, the input power will drop, and the resonant frequency will fall. This in turn further reduces the power coupled into the prism, and a situation known as "thermal runaway" can develop. The mode locker used here had relatively poor resonances, with a lowest SWR reading of 4.

The mode locker was initially driven with relatively low r.f. powers to allow laser oscillation while the cavity length was adjusted to roughly match the chosen resonance. The r.f. power could then be raised, and the frequency increased to reduce the SWR reading together with a corresponding decrease in cavity length to maintain mode locking. This process was repeated until the r.f power reached the 400-800 mW range, with the SWR

reading indicating around 5. A synchronously scanning streak camera, driven from the BPW28 Si photodiode / tunnel diode arrangement as described in chapter 1, was used to monitor the pulses and optimise the drive frequency. Pulses of less than 100 ps were routinely obtained, with 81 ps being the shortest duration observed (tube current 45 amps), see the streak camera intensity profiles depicted in Figure 2.2.

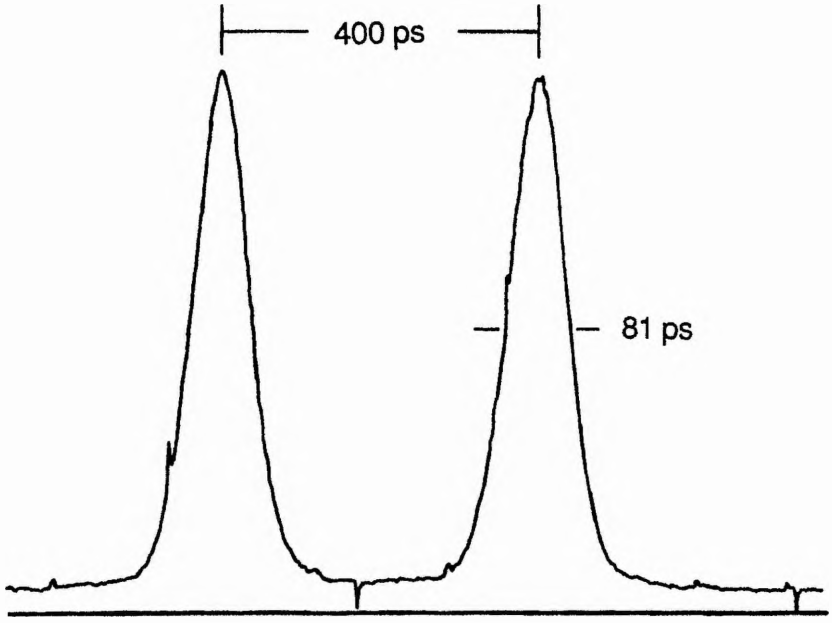

Figure 2.2 Streak camera intensity profile of the shortest pulses observed for the krypton laser (calibration pulse produced by the optical delay line).

Operation	647.1 nm	676.4 nm
CW	2.40 W	1.15 W
Mode locked	0.93 W	0.40 W

Table 2.2 Comparison of typical CW and mode-locked average output powers on the red lines at a tube current of 45 amps.

When mode locked, the average output power decreased by a factor of approximately 2.2, see Table 2.2. This is due to the short decay times[14,15] of the Ar^+ and Kr^+ laser transitions[16], typically 7-9 ns. The 12 ns cavity round-trip time means that many of the

excited ions decay spontaneously before the pulse passes and induces stimulated emission, and in addition, the pulse energy rather than the average power will saturate the gain.

The variations in both pulse duration and in output power with frequency detuning were studied. The shortest pulses were always obtained by frequency detuning some 2-4 kHz below the frequency for maximum average power, as shown in Figure 2.3. Further negative detuning resulted in a decrease in average power to around 600 mW, followed by an increase back to around 1 W (not shown). This dip in power has been attributed to spectral-hole burning,[17] however a simpler explanation is that it corresponds to a change from single pulsing into a regime of double pulsing as observed by Willson.[18] If the pulse arrives early in the open cycle of the modulator, the trailing edge will tend to lengthen, however perhaps due to dynamic gain saturation, this manifests itself as a distinct secondary pulse. For positive detuning, the pulses broadened asymmetrically, and the pulse train exhibited noise. Further positive detuning caused the laser to fall below threshold (not shown). After studying these characteristics the laser could be mode locked without using the streak camera. Once the drive frequency for maximum output power was located, the frequency was simply reduced by some 2-3 kHz, such that the output power dropped by about 10%.

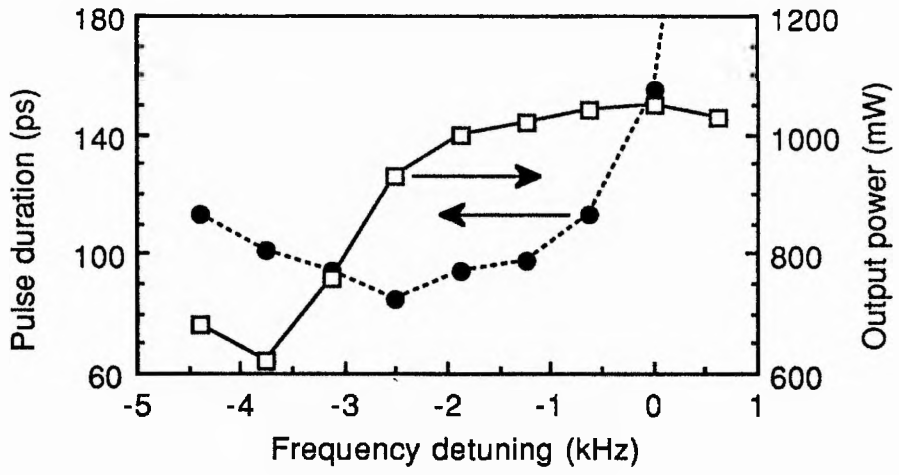

Figure 2.3 Variation of pulse duration and average power with frequency detuning (zero detuning is chosen as the frequency for maximum power).

2.4 Passive mode locking

The observation of passive mode locking of a LiF:F_2^+ colour-centre laser at 870 nm using the slow saturable absorber dye IR140* verified the dye-like nature of this colour centre.[6] Pulses as short as 390 fs were achieved using a travelling-wave ring resonator, and 1.3 ps with a linear resonator. One of the most important advances in passively mode-locked dye lasers in the 1980s was the control of cavity group-velocity dispersion (GVD) by using prisms. This led to pulse durations substantially less than 100 fs as previously discussed in chapter 1. This section describes the performance of the passively mode-locked LiF laser when a four-prism set was included in the cavity to control the dispersion.

The four-prism arrangement, devised and demonstrated by Fork et al.[19] and shown in Figure 2.4, has a low insertion loss since the prisms can be made from high quality optical glass, and all the prism-air interfaces are presented to the beam at Brewster's angle. It operates independently from the other cavity elements and can be incorporated in a linear or ring resonator as an element in its own right. In a linear cavity, only two prisms are required, since the cavity end mirror can be placed at the plane marked MM, and the beam retroreflected.

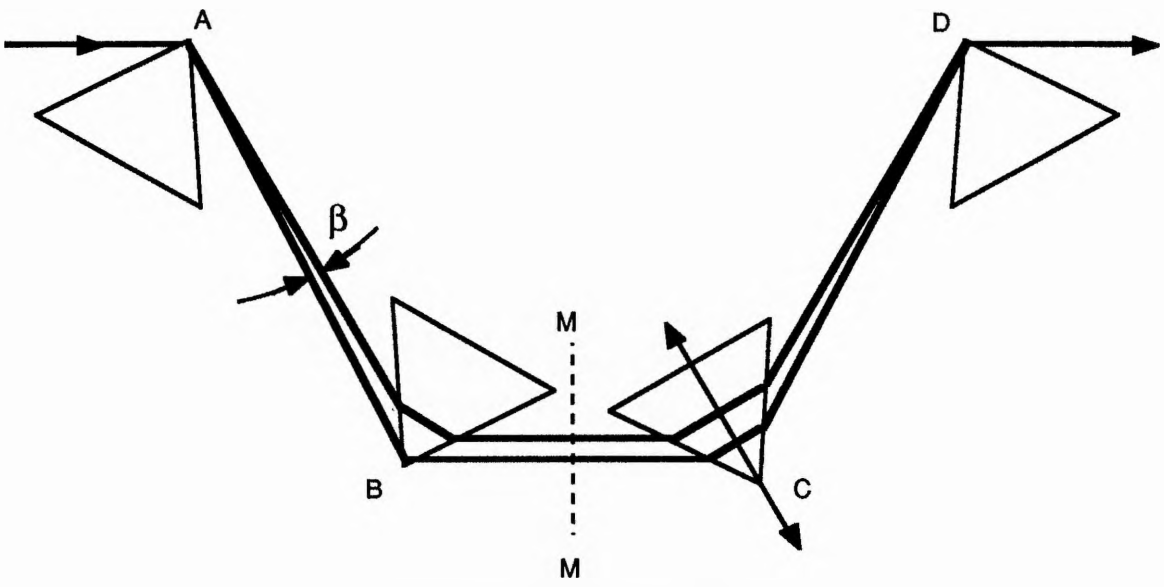

Figure 2.4 Prism arrangement for adjustable GVD (adapted from reference **19**).

* 5,5'-Dichloro-11-diphenylamino-3,3'-diethyl-10,12,-ethylene-thiatricarbo-cyanine perchlorate (molecular weight 779). Obtained from Lambda Physik GmbH.

Two distinct contributions to GVD can be identified. In addition to the prism material, the geometry of the arrangement provides GVD, since the optical path length P is wavelength dependent. It was shown that this contribution, represented by the second derivative of optical path length P with wavelength λ, can be approximated by the expression

$$\frac{d^2P}{d\lambda^2} = 4l\left(\left(\frac{d^2n}{d\lambda^2} + \left(2n - \frac{1}{n^3}\right)\left(\frac{dn}{d\lambda}\right)^2\right)\sin\beta - 2\left(\frac{dn}{d\lambda}\right)^2\cos\beta\right) \qquad (2.1)$$

where n is the refractive index of the prism material, l is the prism separation AB (AB = CD), and β is the angle between the two spectral components considered. The angle β is small, so $\cos\beta \sim 1$. The term $l \sin\beta$ may be approximated by twice the spot size, say 3 mm for operation at 860 nm. The expression can be further simplified by insertion of the refractive index and the related dispersion terms for the prism material - fused silica. The Sellmeier expansion published by Malitson[20] gives (at 860 nm): $n = 1.452$, $dn/d\lambda = -0.01527\ \mu m^{-1}$ and $d^2n/d\lambda^2 = +0.02793\ \mu m^{-2}$. Equation (2.1) can now be rewritten as

$$\frac{d^2P}{d\lambda^2}(\text{mm}\,\mu m^{-2}) = 0.342 - (1.87 \times 10^{-3})\, l\ (\text{mm}) \qquad (2.2).$$

The GVD in femtosecond lasers is usually represented in terms of the second derivative of phase ϕ with angular frequency ω. It can be shown that

$$\frac{d^2\phi}{d\omega^2} = \frac{\lambda^3}{2\pi c^2}\frac{d^2P}{d\lambda^2} \qquad (2.3).$$

Substituting (2.2) into (2.3)

$$\frac{d^2\phi}{d\omega^2}(fs^2) = 385 - 2.10\, l\ (\text{mm}) \qquad (2.4).$$

The contribution from the material dispersion is given by

$$\frac{d^2\phi}{d\omega^2} = L\beta_2 = \frac{L\lambda^3}{2\pi c^2}\frac{d^2n}{d\lambda^2} \qquad \text{where } L \text{ denotes the path length} \qquad (2.5)$$

$$= 31\ fs^2 \text{ per 1 mm of silica} \qquad (2.6).$$

Combining equations (2.4) and (2.6) gives the total GVD of the arrangement

$$\frac{d^2\phi}{d\omega^2}\ (\mathrm{fs}^2) = 31\ L\ (\mathrm{mm}) + 385\ - 2.1\ l\ (\mathrm{mm}) \qquad (2.7)$$

where L is the total path length of the beam in the four prisms and l is the prism separation. It can be seen that the total GVD of the arrangement can be chosen to be either positive or negative. The GVD may be adjusted by simply translating one of the prisms across the beam in the direction as indicated on prism C in Figure 2.4, hence changing the path length within the glass. The symmetry of the beam geometry through the prism means that the cavity alignment remains unchanged, although the cavity length is altered slightly. Furthermore, the arrangement can compensate for the other dispersive elements within the cavity, namely the infrasil cryostat windows, the ethylene glycol in the dye jet, and the LiF crystal.

Component	$d^2\lambda/dn^2$ (μm^{-2})	Path (mm)	$L\ \beta_2$ (fs^2)
LiF crystal	+ 0.01563 (ref. 9)	2.5	+ 44
Ethylene glycol	?	0.1	?
2 silica windows	+ 0.02793	4.8	+ 151
4 silica prisms	+ 0.02793	12.0	+ 377
Geometrical			+ 385 - 2.1 l
Mirror coatings			?
Total			+ 957 - 2.1 l

Table 2.3 GVD budget for a ring cavity at 860 nm (positive β_2 = normal GVD).

Before construction of the laser cavity, it was necessary to consider the various sources of GVD in the cavity, and formulate a budget, shown in Table 2.3. This allowed an estimate to be made of the minimum prism separation required to ensure that the total cavity GVD could be adjusted through zero. The total GVD in the cavity, excluding the effects of mirrors and the ethylene glycol, indicates that a prism separation of greater than 460 mm is sufficient for net anomalous dispersion. The contribution from the dye jet is probably insignificant (at 610 nm, it has been estimated to be less than + 8 fs^2 [21]). The contribution

from the mirror coatings was also unknown but was assumed at this stage to be small, since the operating wavelength was well within their high reflectivity band. To compensate for these unknown factors, the prism arrangement was usually assembled with a separation of approximately 600 mm.

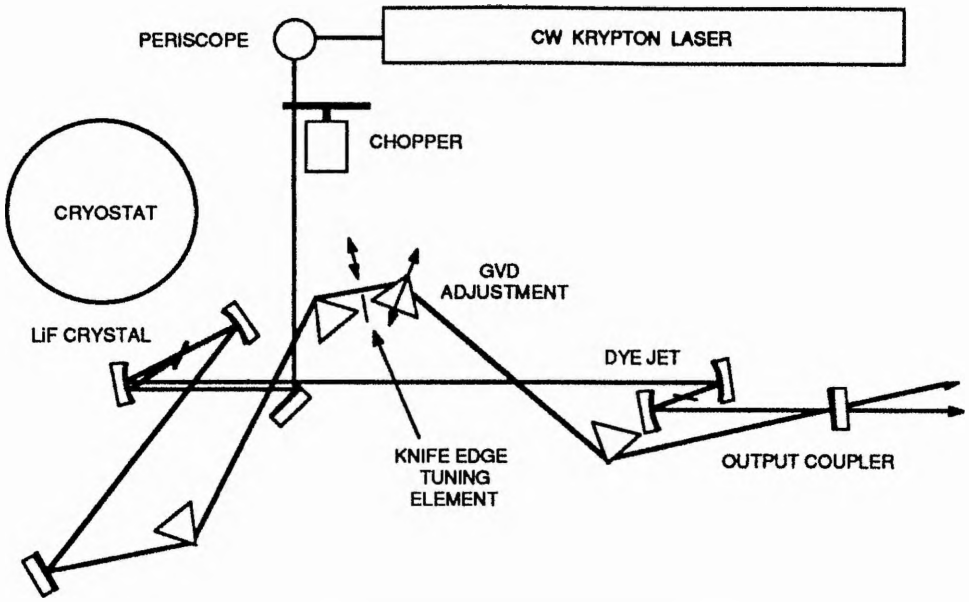

Figure 2.5 Colliding-pulse mode-locked LiF laser with GVD compensation.

Earlier work[6] indicated that the colliding-pulse mode-locked (CPM) travelling-wave resonator generated shorter pulses than a linear arrangement. The laser, shown schematically in Figure 2.5, was excited in the nearly collinear alignment as described in chapter 1 by the krypton laser operating CW on the 647 nm and 676 nm lines, chopped with a duty cycle of 10%. The cavity was formed by two 10 cm radius of curvature (RoC) highly reflecting (HR) mirrors surrounding the gain, two 5 cm RoC HR mirrors surrounding the absorber, one plane HR mirror and one plane output coupler. The resonator was constructed by extending a simple 4 mirror X-type cavity, adding a second folded section for the dye jet, and reflecting the long arms into a ring. Using an infrared viewer (FJW Industries Find-R-Scope), the luminescence was imaged at distances of at least twice the lengths of the cavity arms to ensure that the laser ran in a collimated mode, with no small waists other than at the gain and absorber.

In preliminary experiments, multiple pulsing was frequently noted at particular wavelengths, and this was traced to the construction of some of the mirrors. These mirrors had a computer designed 73 layer structure with the layer thicknesses increasing with depth into the stack, similar to a geometric or arithmetic progression type coating.[22] This type of construction results in an extended bandwidth, in this case 750-1050 nm, but is accompanied by rapid phase shifts at a several distinct points (resonances) within the band. These resonances give rise to significant first and higher order GVD, and hence severe pulse distortion.[23,24] They were replaced by curved HR mirrors of custom-built, double quarter-wave stack construction[25] to provide high reflectivity in bands centred on the LiF emission and on the red pump laser lines. The 800-1000 nm stack was deposited after the 600-800 nm stack to minimise GVD at the LiF wavelengths.[23] Both the plane mirror and the output coupler were conventional quarter-wave stacks. The output coupler had a reflectivity of approximately 97% at 900 nm and 95% at 850 nm.

The four-prism set occupied the long leg between the plane HR mirror and the output coupler. The relatively long round-trip time of approximately 26 ns was dictated largely by the 60 cm prism separation, although it also partly compensated for the relatively long upper state lifetime of the gain. The theoretical work has shown that CPM lasers with gain media whose recovery time is longer than the round-trip time require to be excited well above threshold for optimum operation.[26]

The saturable-absorber dye IR140 is a rigidised cyanine lasing dye, normally dissolved in dimethyl sulfoxide (DMSO) when used as a gain medium.[27] However, it has been established[11] that as a saturable absorber, the dye may be dissolved in the much safer solution of 10% propylene carbonate to 90% ethylene glycol. The dye solution was forced through a standard dye laser jet nozzle by a nylon meshing-gear pump, magnetically coupled to an electric motor to minimise vibration transfer. The thickness of the dye jet was estimated to be approximately 80 μm by examination of the fringes formed by the interference of the reflections from the jet surfaces (see appendix 1).

With the original mirror coatings, the laser could not reach threshold at a number of wavelengths in the vicinity of 870 nm where passive mode locking had been previously observed.[6] The new coatings permitted smooth tuning over a much wider range, and

therefore could support much greater bandwidths. Mode locking was established with around one twentieth of the usual dye concentration by tuning the laser much closer than before towards the 810 nm peak of the IR140 absorption[11].* A razor edge, positioned between the second and third prisms, was used to tune the wavelength, since at this location the chromatic components of the beam were spatially dispersed. As the dye concentration was increased, the laser would extinguish unless the razor position was relaxed slightly, allowing the laser run at longer wavelengths. However, if the tuning razor was moved too far, the laser would oscillate CW. Typical dye concentrations used at the two extremes of the tuning range of the passively mode locked laser were 2×10^{-5} mol l^{-1} at 845 nm and 4×10^{-4} mol l^{-1} at 875 nm, with pump powers in the range 3-5 W. Over this range of wavelengths, pulses of less than 400 fs duration were obtained routinely. With the optimum setting of the GVD, pulses less than 200 fs were achieved ($sech^2$ pulse shape assumed). A typical intensity autocorrelation and corresponding spectrum is shown in Figure 2.6.

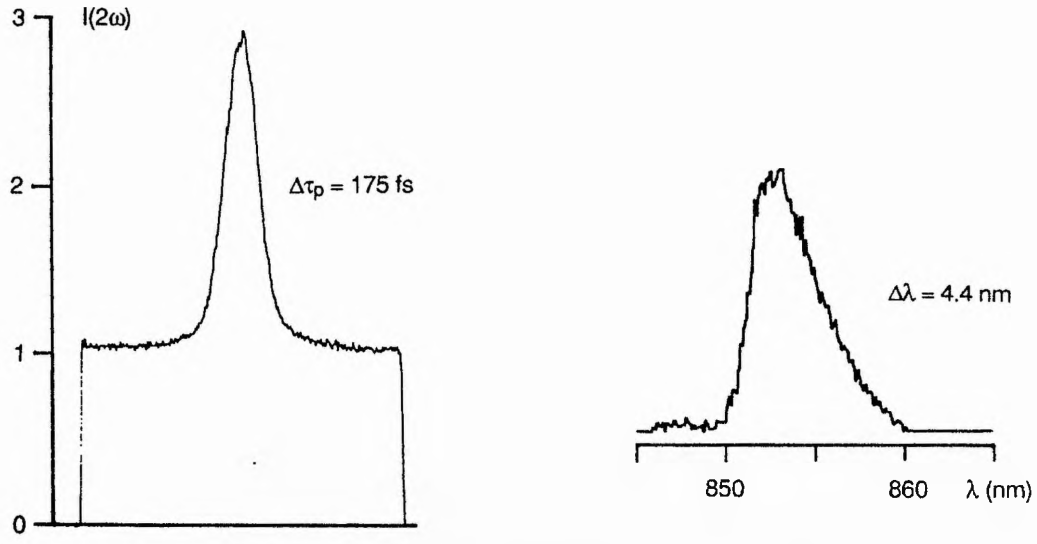

Figure 2.6 Intensity autocorrelation and spectrum for the GVD compensated LiF ring laser.

It was found that the pulse duration was only weakly dependent on the amount of glass in the cavity. This can be explained by considering the low GVD of the silica prisms at this wavelength. The three interferometric autocorrelations depicted in Figure 2.7 were taken for differing amounts of intracavity glass. The pulse duration was 200 fs at the optimum

* Langford[28] has implied the existence of a photoisomer peaking at longer wavelengths, however IR140 generally does not exhibit a photoisomer due to its rigidised structure[29].

setting (c), rising to 220 fs (b) and 250 fs (a) for increases in glass above the optimum setting of 5 mm and 7 mm respectively. The flat, fringe-free wings of autocorrelation (c) is commensurate with low frequency chirp. Decreasing the glass from the optimum caused the laser to go unstable.

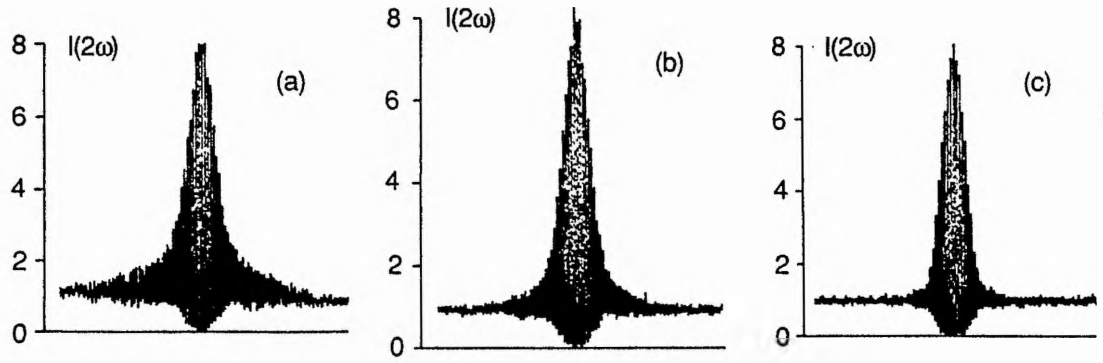

Figure 2.7 Interferometric autocorrelations for different prism settings.

The output power was observed to fade once short pulses were established and hence during the recording of results. The laser required frequent adjustment to maintain the level of second harmonic, and the crystal position had to be moved every 60 minutes or so. This rapid deterioration was initially attributed to the relatively large pump powers used, but a more likely explanation is that multiphoton excitation of the centre occurred, due mainly to the intracavity photons of the intense short pulses, possibly assisted by the pump photons. The average power of the two output beams was approximately 15 mW each, giving output pulse energies of ~ 0.4 nJ and peak output powers of approximately 2 kW. The corresponding intracavity values were estimated to be 8 nJ and 40 kW, i.e. a peak intensity in the LiF crystal of some 3 GW cm^{-2}, compared with the (CW) pump laser intensity of ~ 0.3 MW cm^{-2}.

The optical length of the 180 fs pulses in the dye jet can be estimated as approximately 40 μm, whereas the path length in the jet is ~ 100 μm. This indicates that, at this pulse duration, the grating formed by the colliding pulses occupies only the central region of the absorber, hence the advantage of CPM is reduced, and similar durations should be observable using a linear cavity. Pulses of around 250 fs were easily obtained for a GVD compensated linear cavity, and occasionally, it produced pulses as short as those obtained using the ring cavity.

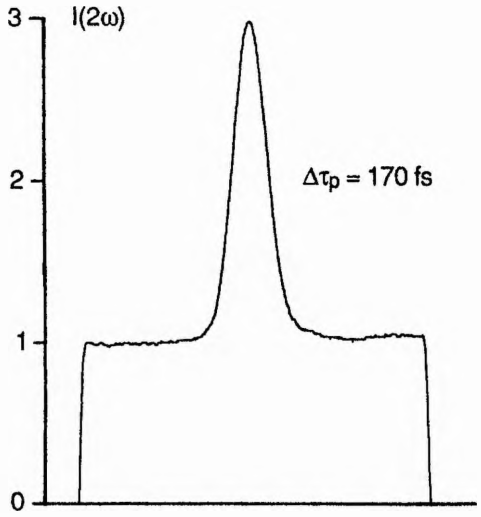

Figure 2.8 Intensity autocorrelation for the basic CPM laser with prisms removed.

The prism sequence was removed from the ring laser to briefly investigate the performance of the basic CPM laser, now equipped with the new mirror coatings enabling operation at shorter wavelengths than previously. To obtain mode locking, a wedged-dielectric-coating tuning element (Spectra-Physics) was used to tune the wavelength towards the IR140 absorption. Pulses of around 250 fs were obtained routinely, with shorter pulses appearing intermittently for periods of a several milliseconds at a time. These pulses had durations as short as 160 fs, and were for that limited timescale, perfectly stable as evidenced by the autocorrelation shown in Figure 2.8. It was not possible to maintain operation on this shorter duration, indicating that, although the prisms were not required to generate short pulses, they did stabilise the laser.

The shortest pulses obtained from the laser were considerably longer than those observed with most GVD-compensated passively mode-locked dye lasers, in particular the Rhodamine 6G / DODCI lasers discussed in chapter 1. The fact that the laser could generate equally short pulses without the prism sequence implies that self-phase modulation due to Kerr effect in the dye jet and the LiF crystal was not important, since stable operation would then be associated with net negative GVD. Using the data provided for the Rh6G / DODCI laser of Valdmanis et al.,[30] eg. peak power (190 kW), mirror RoC, and jet thicknesses, the peak phase shift due to Kerr-like SPM can be estimated to be 3-4 times greater than that

obtained in the LiF / IR140 laser. Thus, the soliton-like pulse shaping mechanisms are not as significant in the laser described here, at least for the 180 fs pulses obtained.

The fact that the laser operated stably for glass paths longer than that for the shortest pulse may indicate that down chirp was dominant. The most likely origin of the chirp is the off-resonance absorption saturation, as observed by Dietel et al.[31-33], and Kühlke[34]. The chirp from resonant (slow) nonlinearities cannot, in general, be used to compress the pulse. Usually, either the leading edge or the trailing edge can be compressed at the expense of expanding the other edge. However, for passively mode-locked lasers, the pulse energy is often much larger than the saturation energy of the absorber, hence the absorber will only chirp the front portion of the pulse. This leads to an up chirp on the leading edge and down chirp over the central, most intense region of the pulse. The normal GVD introduced by the prisms would be expected to compensate for the down chirp over the main part of the pulse, but stretch the low, leading edge.

The LiF / IR140 laser is unusual in that mode locking occurs on the short wavelength side of the gain peak (910 nm) and on long wavelength side of the absorber peak (810 nm). This means that the ratio of the absorber cross-section to the gain cross-section changes rapidly across the spectrum of the pulse, whereas with the Rhodamine 6G / DODCI laser this variation is relatively small since the pulse lies on the long wavelength side of both the gain and the absorber. In effect this ratio is essentially the s parameter defined by New (see for example reference 35).

The effect of this variation in s over the pulse spectrum can be discussed qualitatively. At the short wavelength range of the pulse spectrum, the absorption will always outweigh the gain, even when both saturate, giving attenuation. At the centre of the spectrum, both the absorber and the gain saturate such that there is net gain for the central part of the pulse and loss for the leading and trailing edges, as described in chapter 1. Finally, at the long wavelength end, the small-signal absorption is weak while the small-signal gain is large, permitting CW oscillation. In the LiF / IR140 laser, the oscillation of these CW components is prevented by the razor edge tuning element. This large variation in s across the region of mode locking may be the fundamental limit to the pulse duration.

The LiF laser has also been passively mode locked[36] using the saturable absorber dye DaQTEC (peak absorption at 933 nm[37]), where pulses as short as 130 fs were obtained without using prisms. The LiF / DaQTEC laser operated at a wavelength of 934 nm, on the peak of the absorption and close to the peak of the gain, minimising the spectral variation of *s* and possibly verifying the above hypothesis. Prisms were probably not required because the pulses were exactly on resonance with the absorber, hence minimising chirp.

2.5 Coupled-cavity mode locking

In chapter 1, coupled-cavity mode locking was introduced, and the experiments of Kean et al.[38] were briefly discussed. After the demonstration of mode locking using normally dispersive fibre in the control cavity of the KCl:Tl laser, the technique was applied to the LiF laser at 900 nm, where solitonic fibre was obviously not available. This was the first demonstration of coupled-cavity mode locking at wavelengths shorter than λ_o, and showed conclusively that anomalous GVD was not required for successful operation.

The LiF colour-centre laser was configured in the normal three-mirror, astigmatically-compensated cavity, lengthened to 183 cm for synchronous mode-locking. An output coupler with a reflectivity of approximately 88% was used, giving a threshold pump power of some 500 mW. This mirror, manufactured by Spectra-Physics for use in synchronously mode-locked dye lasers, had a concave reflecting surface (RoC = -157 cm), to allow an extension in cavity length without compromising the stability range.

Typically, pump powers of ~ 900 mW were available from the mode-locked krypton laser, and this resulted in mode-locked output powers from the colour-centre laser of around 40-60 mW. This power was subsequently increased to around 100 mW by in situ optical treatment of the crystals using an argon laser (see appendix 2). These improved power outputs were only implemented in the later stages of the work described in this section.

The control cavity was appended directly onto the output coupler (see Figure 2.9), and a beamsplitter reflected approximately 70% of the laser output towards the control-cavity fibre. The fibre, manufactured by Andrew Corporation,[39,40] was monomode at the operating wavelength and also polarisation-maintaining due to its elliptical cross-section (1.25 x 2.5 μm). The small dimensions dictate a large core / cladding index difference of

0.034 to ensure good guiding properties, and this has been obtained by doping the core with GeO_2 (germania). The output beam was coupled into and out of the fibre using 20x microscope objectives that were previously incorporated in the 1.5 μm system of Kean.[41] The axis of the fibre was carefully aligned with the polarisation of the input beam. The objectives were broadband (1100-1550 nm) antireflection coated on all surfaces apart from the flat surface nearest to the focus. (Equivalent objectives coated for the 800-1050 nm band were not available.) Index matching oil[42] filled the space between this uncoated surface and the fibre, thereby reducing parasitic optical feedback due to reflections from the fibre ends. Such precautions are required in any mode-locked laser, since optical feedback in general tends to disrupt mode locking.[43]

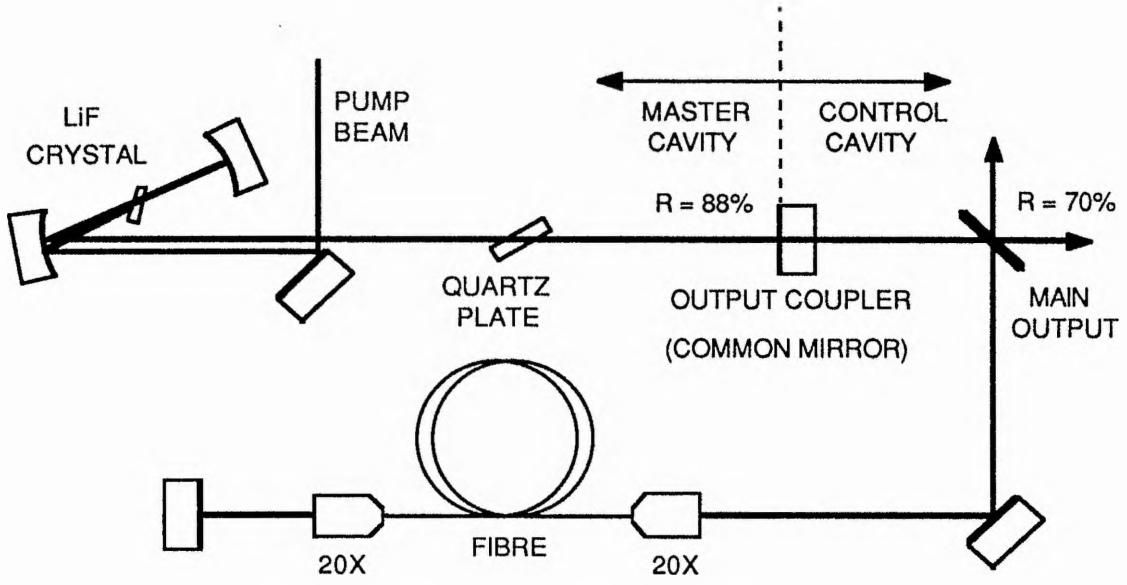

Figure 2.9 Schematic of the coupled cavity LiF laser. 20x: microscope objective.

With a beam block inserted in front of the optical fibre, the synchronous mode locking was optimised. With the oscillating bandwidth restricted by a single quartz birefringent plate[44] of 1.6 mm thickness, pulses of 3-5 ps duration were obtained (Gaussian pulse shape assumed). The beam block was then removed, and the coupling into the fibre optimised. With no light coupled in the return direction, it was noticed that the pulse broadened slightly and an increase in noise was apparent on the second-harmonic signal. This indicated that there was some feedback from the fibre ends in spite of the precautions described earlier. The coupling of the return beam was established by adjusting the end

mirror of the control cavity to obtain parasitic feedback, since at this stage, the length of the control cavity was not matched precisely to the master cavity. By minimising the autocorrelator second-harmonic signal, the return coupling could be easily optimised.

The control cavity length was adjusted by moving either the end mirror, or the combined input objective and input fibre end which were mounted on a translation stage. The fibre lengths used in the experiment, 217 and 467 cm, required the control cavity to be a multiple of the master cavity length to ensure that the feedback pulses were correctly timed with the master cavity pulses. For the final length adjustment, the synchronously mode-locked pulses were monitored using a fast photodiode in conjunction with a sampling oscilloscope, or alternatively, a streak camera was used. By blocking and unblocking the control cavity, it was possible to see a second, much smaller pulse lying either in front of, or behind the main pulse. The control cavity length was then adjusted in the appropriate direction to make the two pulses approximately coincident. The final length adjustment was achieved by monitoring the autocorrelator. At the matching point, regular interferometric fluctuations were observed as the length was scanned. To obtain short pulse operation, it was necessary to make alternate changes in the master cavity length and the control cavity length (of a few microns) in an iterative process.

The autocorrelation for the shortest pulses from the coupled cavity laser is shown in Figure 2.10, together with an autocorrelation for the synchronously mode-locked laser pulses for comparison. For a fibre length of 217 cm, pulse durations of between 1.3 and 1.5 ps were recorded.* This was achieved with estimated average powers of 15-20 mW in the fibre. Somewhat longer pulses of 1.5 to 1.9 ps were obtained for a fibre length of 467 cm, which had slightly lower power requirements as might be expected. The pulses were only half the length of those obtained by synchronous mode locking, but the clean shape indicated that the quality of the mode locking was superior, with no evidence of cusp-like wings. The variation in the background level is probably caused by small ($<< \lambda$) changes in the length of the control cavity relative to the master cavity.

* The mode locking was not sufficiently stable to allow spectral measurements and hence the calculation of a bandwidth-duration product. A sech^2 pulse shape was assumed because this was found to fit the results of Kean.[41]

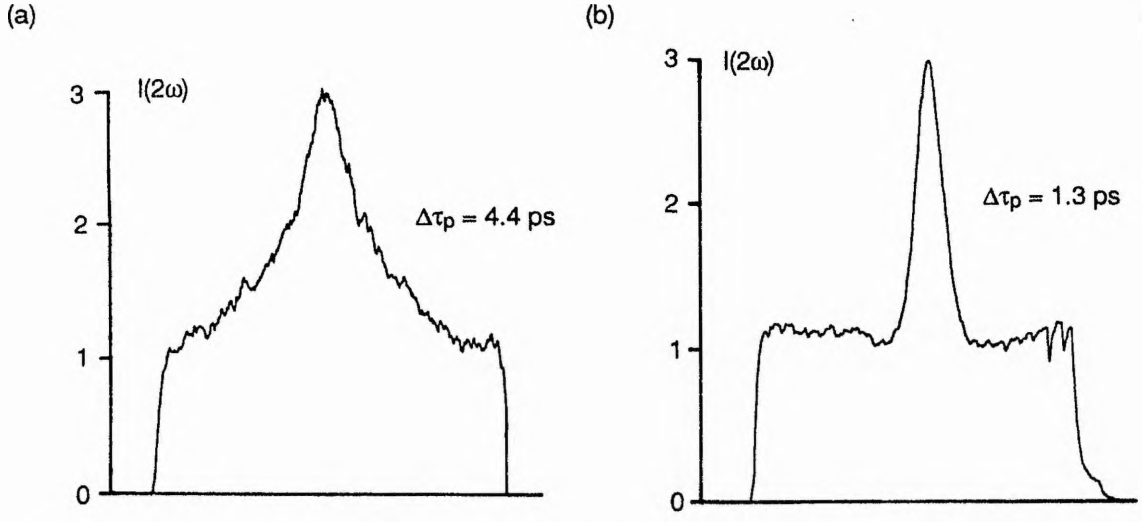

Figure 2.10 Autocorrelations for (a) synchronous mode locking and (b) coupled-cavity mode locking.

The short pulse tended to flash up on the oscilloscope for only one or two scans of the autocorrelator. This behaviour should be compared to the coupled-cavity KCl:Tl laser, where the second-harmonic signal tended to float up and down on a timescale of a few seconds. This instability was related to small changes in the phase mismatch angle between the optical cycles of the interfering pulses, and was consistent with excessive vibration on the optical table. This was attributed to the cooling water in the krypton laser. Even in the brief glimpses of short pulse operation, a second instability, caused by a small mismatch in the lengths of the cavities from optimum could be observed. The effect of a small deviation in length can be seen in the intensity autocorrelation shown in Figure 2.11, where regular dropouts (at ~ kHz frequency) are clearly visible. This instability is related to the relatively short upper state lifetime of LiF:F_2^+ (29 ns) compared to KCl:Tl. Because coupled-cavity mode locking is a form of passive mode locking,[45] the pulse repetition frequency is determined by the cavity lengths, and not by the pump pulses. Therefore, any mismatch in the repetition frequencies of the coupled-cavity and pump lasers results in beating between the two lasers. The gain available to the LiF pulse is a strong function of the time delay between it and the krypton laser pump pulse at the gain crystal due to the inability of the LiF:F_2^+ centre to store gain over the pump pulse period. The 29 ns lifetime of LiF means that the small-signal gain seen by the coupled-cavity pulse falls by 34% over a 12 ns pump-pulse period (cf. KCl:Tl : 0.7%, NaCl:OH^- : 8%).

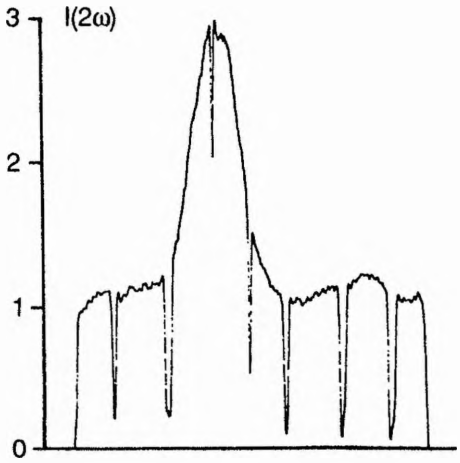

Figure 2.11 Intensity autocorrelation exhibiting beating effects due to a length mismatch with the pump laser.

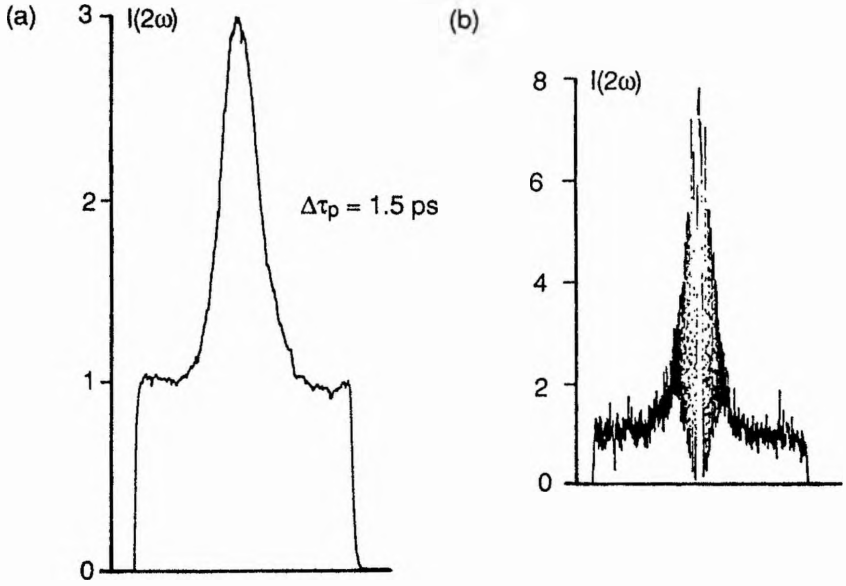

Figure 2.12 Intensity and interferometric autocorrelations for the coupled-cavity laser.

Interferometric autocorrelations for the pulses from the coupled-cavity KCl:Tl laser had been observed to be relatively free of chirp.[41] Similar measurements on the LiF laser, see Figure 2.12, indicated that the pulses were not chirp free. The most likely cause is the large amount of GVD present at these wavelengths, particularly in the fibre itself. The GVD of the fibre at 900 nm is estimated to be of the order of $D \approx -150$ ps/(nm.km), boosted by the germania doping and waveguide dispersion. GVD compensation in the control cavity by using a diffraction grating would probably have eliminated this chirp if it was caused by the fibre, however recent experiments with couped-cavity Ti:sapphire and Nd:glass lasers has

shown that GVD compensation in the main cavity is sufficient and easier to implement since less dispersion is required, see chapter 7 for discussion and references.

2.6 Summary

The addition of a four-prism set to a colliding-pulse mode-locked LiF laser has resulted in the generation of stable pulses of less than 180 fs duration at wavelengths around 850 nm. It was contended that the dominant source of nonlinear chirp in the laser is the down chirp associated with the off-resonance saturation of the IR140 absorber dye. In addition, the spectral filtering effect of the combination of the gain and absorber has been discussed.

Coupled-cavity mode locking has been observed, but the short upper state lifetime of LiF makes it unlikely that stable operation will be possible with mode-locked excitation. CW pumping circumvents this problem,[36] but then initiation may be difficult and additional modulation would probably be required. In any event, LiF lasers (and its dye laser competitors) are of less practical relevance due to the recent development of reliable mode-locked Ti:sapphire lasers.

2.7 References

1. L. F. Mollenauer, Opt. Lett. **1**, 164 (1977).
2. L. F. Mollenauer, D. M. Bloom, and A. M. DelGaudio, Opt. Lett. **3**, 48 (1978).
3. L. F. Mollenauer, "Color Center Lasers" (chapter 6), in *Quantum Electronics, part B*, C. L. Tang, ed. (Academic Press, New York, 1979).
4. L. F. Mollenauer, "Color Center Lasers" (chapter 2), in *Laser Handbook, Vol. 4*, M. L. Stitch and M. Bass, eds. (Elsevier Science, Amsterdam, 1985).
5. N. Langford, K. Smith, and W. Sibbett, Opt. Commun. **64**, 274 (1986).
6. N. Langford, K. Smith, and W. Sibbett, Opt. Lett. **12**, 903 (1987).
7. J. Nahum and D. A. Wiegand, Phys. Rev. **154**, 817 (1967).
8. J. Nahum, Phys. Rev. **158**, 814 (1967).
9. H. H. Li, J. Phys. Chem. Ref. Data **9**, 561 (1980).
10. L. Bosi, C. Bussolati, and G. Spinolo, Phys. Lett. **32A**, 159 (1970).
11. K. Smith, PhD Thesis (University of London, 1985).
12. S. J. Heising, S. M. Jarrett, and D. J. Kuizenga, IEEE J. Quantum Electron. **QE-7**, 205 (1971).
13. L. L. Steinmetz, W. A. Bookless, and J. H. Richardson, Appl. Opt. **19**, 2663 (1980).
14. W. R. Bennett, Jr., P. J. Kindlmann, G. N. Mercer, and J. Sunderland, Appl. Phys. Lett. **5**, 158 (1965).
15. S. H. Koozekanani and G. L. Trusty, J. Opt. Soc. Am. **59**, 1281 (1969).
16. W. B. Bridges and A. N. Chester, IEEE J. Quantum Electron. **QE-1**, 66 (1965).
17. I. S. Ruddock and R. Illingworth, J. Phys. E **18**, 121 (1985).
18. J. P. Willson, PhD Thesis (University of London, 1982).
19. R. L. Fork, O. E. Martinez, and J. P. Gordon, Opt. Lett. **9**, 150 (1984).
20. I. H. Malitson, J. Opt. Soc. Am. **55**, 1965 (1965).
21. S. De Silvestri, P. Laporta, and O. Svelto, IEEE J. Quantum Electron. **QE-20**, 533 (1984).
22. Coating sequence information provided by B. Michael Lunt, Technical Optics Ltd., Onchan, Isle of Man.
23. P. Laporta and V. Magni, Appl. Opt. **24**, 2014 (1985).
24. D. N. Christodoulides, E. Bourkoff, R. I. Joseph, and T. Simos, IEEE J. Quantum Electron. **QE-22**, 186 (1985).
25. A. F. Turner and P. W. Baumeister, Appl. Opt. **5**, 69 (1966).
26. M. S. Stix and E. P. Ippen, IEEE J. Quantum Electron. **QE-19**, 520 (1983).
27. M. Maeda, *Laser Dyes* (Academic Press, Tokyo, 1984).
28. N. J. Langford, PhD Thesis (University of London, 1988).
29. J.-P. Fouassier, D.-J. Lougnot, and J. Faure, Opt. Commun. **23**, 393 (1977).
30. J. Valdmanis and R. L. Fork, IEEE J. Quantum Electron. **QE-22**, 112 (1986).
31. W. Dietel, E. Döpel, D. Kühlke, and B. Wilhelmi, Opt. Commun. **43**, 433 (1982).
32. W. Dietel, J. J. Fontaine, and J.-C. Diels, Opt. Lett. **8**, 4 (1983).
33. J. J. Fontaine, W. Dietel, and J.-C. Diels, IEEE J. Quantum Electron. **QE-19**, 1467 (1983).
34. D. Kühlke,W. Rudolph, and B. Wilhelmi, IEEE J. Quantum Electron. **QE-19**, 526 (1983).

35. G. H. C. New, IEEE J. Quantum Electron. **QE-10**, 115 (1974).
36. C. I. Johnston, D. E. Spence, R. S. Grant, and W. Sibbett, Opt. Commun. **73**, 370 (1989).
37. M. D. Dawson, T. F. Boggess, and A. L. Smirl, Opt. Lett. **12**, 590 (1987).
38. P. N. Kean, X. Zhu, D. W. Crust, R. S. Grant, N. Langford, and W. Sibbett, Opt. Lett. **14**, 39 (1989).
39. R. B. Dyott, J. R. Cozens, and D. G. Morris, Electron. Lett. **15**, 380 (1979).
40. Sample of Andrew Corporation fibre and characteristics provided by I. H. White, then at the Department of Engineering, University of Cambridge.
41. P. N. Kean, PhD Thesis (University of St. Andrews, 1989).
42. Halocarbon Oil 700 (refractive index $n = 1.41$), Halocarbon Products Corporation. UK supplier: KMZ Chemicals Ltd., Leatherhead, Surrey.
43. M. Hassinger and F. E. Lytle, Opt. Commun. **48**, 125 (1983).
44. A. L. Bloom, J. Opt. Soc. Am. **64**, 447 (1974).
45. F. M. Mitschke and L. F. Mollenauer, IEEE J. Quantum Electron **QE-22**, 2242 (1986).

3 The KCl:Tl laser : part I

3.1 Introduction

The NaCl:F_2^+ colour-centre laser[1] was the first relatively high power, tunable, CW mode-locked picosecond source to operate in the vicinity of the 1.55 μm telecommunications low-loss window, but in common with other F_2^+ centre lasers, it suffered from fading effects associated with reorientation of the centres. Fortunately, a more stable laser was developed using colour centres formed in KCl doped with thallium,[2] which could cover essentially the same spectral region, but with crystal lifetimes of 6-12 months. These KCl:Tl crystals have, until recently, been used in commercial colour-centre lasers manufactured by Burleigh Instruments. Perhaps most significantly from the point of view of this thesis, the KCl:Tl colour-centre laser formed the basis for the soliton laser[3], which represented an archetype and benchmark for coupled-cavity mode-locked lasers.

In this chapter the KCl:Tl laser is described and mode locking using active and coupled-cavity techniques is discussed. Coupled-cavity mode locking by using optical fibres in the control cavity is included within this chapter, while the exploitation of a semiconductor diode amplifier will be considered in chapter 5.

3.2 The $Tl^0(1)$ centre in KCl:Tl

Lasers using KCl and KBr doped with Tl were initially demonstrated by Gellermann et al. in 1981, when they identified the centre as an F_A centre perturbed by a Tl^+ ion.[4] Spectroscopic measurements identified it to be a neutral Tl atom perturbed by the field of an adjacent anion vacancy, resulting in the more commonly used $Tl^0(1)$ centre designation.[5] In publications by Mollenauer et al., related laser properties were considered more comprehensively (see Figure 3.1 and Table 3.1).[2,6] The energy level system is closely related to atomic thallium, with the

upper and lower laser levels labelled ψ and ϕ respectively. The Stokes shift of the emission band (from 1040 nm to 1520 nm) is small, almost F_2^+ like, but the band itself is narrower than an equivalent F_2^+ transition. Because of its close relation to atomic thallium, the peak wavelength of the absorption and emission bands of the centre are not significantly dependent upon the lattice dimensions.[4]

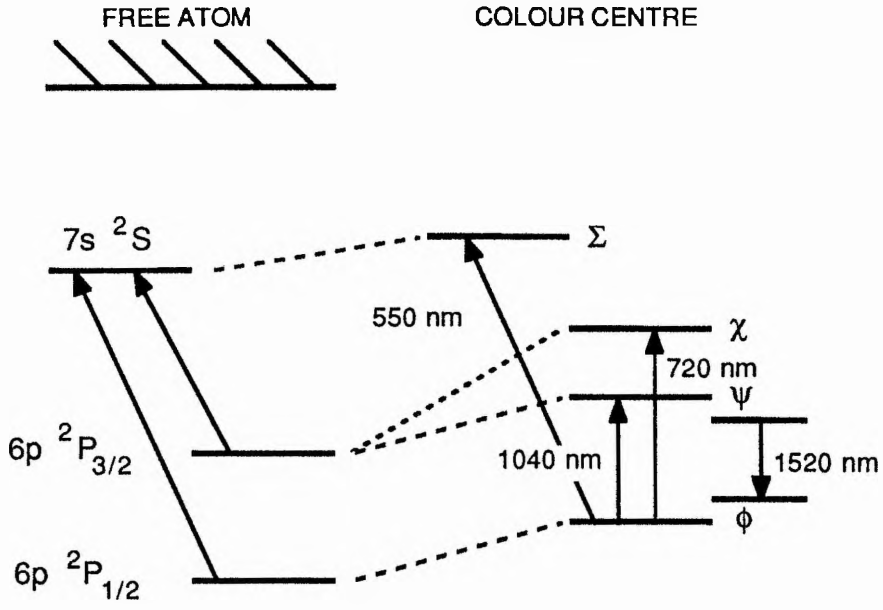

Figure 3.1 Energy level diagrams for the thallium atom and the $Tl^0(1)$ colour-centre.

Parameter	Value	Reference
Refractive index of KCl	1.47	6
Absorption peak	1040 nm	6
Emission peak	1520 nm	6
Emission FWHM	19.5 THz	6
τ_{rad}	1.6 μs	6
η (quantum efficiency)	1	6
σ_{em}	1.3×10^{-17} cm^2	

Table 3.1 Optical characteristics of the $Tl^0(1)$ centre in KCl:Tl at 77 K.

A most significant feature is the relatively long (1.6 μs) radiative decay time and small emission cross-section. It should be noted that although the decay time is similar to that of titanium doped sapphire, the gain cross-section of the $Tl^0(1)$ centre is much larger.*

The centres are formed in KCl crystals doped with ~ 0.2 mol % Tl^+ ions. Firstly, F centres are created by irradiating the crystal with an electron beam whilst at a temperature of approximately -130 ^{0}C.[2] The crystals are then exposed to light for around 30 minutes in order to ionise the F centres. The Tl^+ ions capture the free electrons and become $Tl^0(0)$ centres. If the process occurs at a temperature of ~ -30 ^{0}C then the anion vacancies can migrate through the lattice and bind themselves to the $Tl^0(0)$ centres (which appear negative within the lattice) forming the $Tl^0(1)$ centres. An imaginary line joining the Tl nucleus and the vacancy lies in the <100> direction, with the polarisation (E vector) of the laser transition parallel to this axis. A large fraction of the centres formed are stable at temperatures approaching 290 K, providing they are kept in darkness, although all the crystals used here were stored at 77 K to prolong their shelf-lives.

The growth of good quality KCl:Tl crystals is difficult and all the crystals used in the laser described here were grown and irradiated by the University of Utah and supplied by Burleigh Instruments. The crystals, approximate dimensions (9 x 5 x 2) mm^3 were mounted in a modified crystal holder which held them at an angle of 45^0, as in the Burleigh FCL laser. The most probable reason for this unusual orientation is that the Burleigh laser was originally developed for crystals using the F_A(II) type centres, which require continual reorientation by pumping on all possible axes of symmetry.

The first crystal used in this work had seen over 12 months service in the group's Burleigh FCL laser prior to installation, but surprisingly, it was superior to all the subsequent crystals. The quality of crystals supplied by Burleigh continued to deteriorate, with many of the later ones having relatively low optical densities, ≈ 0.5. These crystals were low in output power, around 120 mW for 1.8 W pump power (as opposed to 200 mW with the first crystal), and faded to 60 mW output within 6 months.

* This is because the emission of the KCl:Tl centre has a quantum efficiency of unity (compared to ~ 70% for Ti:sapphire), and is at a much longer wavelength, together with a narrower bandwidth.

3.3 The Nd:YAG pump laser

Both the KCl:Tl laser and the NaCl laser (see chapter 6) were excited using a Spectra-Physics model 3800 Nd:YAG laser operating at 1064 nm. Although similar in configuration to the earlier series 3000 laser, it is more powerful, with an output power specification of 10 W (against 7.5 W) in linearly-polarised, fundamental-transverse-mode, CW mode-locked operation. The laser was equipped with a Spectra-Physics 3246 acousto-optic modulator and Spectra-Physics 452A/453 mode-locker drive electronics, and an electronic feedback system to stabilise the average output power. The characteristics and operation of the laser will be described in this section.

Vital to the design of powerful, fundamental-transverse-mode solid-state lasers are resonator designs which compensate for the lensing action of the laser rod under intense optical pumping.[7] Arising from a radial temperature gradient, this thermal lensing effect is considerable in lamp-pumped solid-state lasers due to the inefficient conversion of optical power emitted by the exciting lamp into laser output power.[8] It has been clearly shown that resonator stability can only be obtained for a limited range of rod focal lengths (and thus lamp input powers).[9,10]

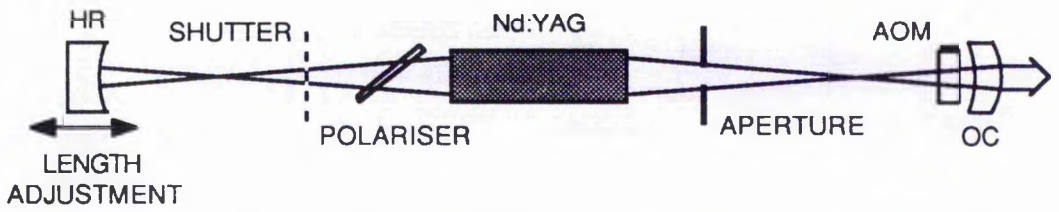

Figure 3.2 Configuration of the Spectra-Physics model 3800 Nd:YAG laser. AOM: acousto-optic modulator; HR: high reflector; OC: output coupler.

The Spectra-Physics lasers employ a symmetrical resonator configuration, where the rod is located approximately midway between two end mirrors of identical radii of curvature, see Figure 3.2. The positive lens in the rod formed under intense optical pumping is compensated by the concave curvature of the end mirrors. Apart from the focal length of the rod, the other main constraint in the design of the resonator geometry is the requirement for a cavity length of approximately 182 cm, to allow compatibility of the mode-locking electronics with the Spectra-Physics ion lasers.

The model 3800 laser has a gold-coated, elliptical cross-section, flooded pump cavity where the Nd:YAG rod and the arc lamp axes are located in parallel at the two focal axes of the ellipse. The Nd:YAG rod is of standard dimensions, i.e. 79 mm in length and 4 mm in diameter, with a doping level of ~ 0.6%.[11] Both ends are anti-reflection coated, with a small wedge to prevent etalon effects. The lateral surfaces have a roughened finish in an effort to obtain uniform distribution of the lamp power within the rod volume.[12] The high pressure CW krypton-arc lamp is typically operated at a current of 28-29 amps at ~ 145 volts (a power input of 4.1 kW), compared to ~ 17.5 amps at ~ 155 volts (2.7 kW) for the earlier series 3000. The higher operating current has necessitated the use of an increased diameter lamp bore, up from 4 mm to 5 mm, which causes a reduction in overall efficiency.[12]

The pump chamber is flooded with deionised water, continuously circulated in a closed loop from a tank in the power supply, where the heat is transferred to an external water supply. Both the rod and the lamp are enclosed in individual, concentric, glass flow tubes to maximise the water velocity over the surfaces of the rod and lamp in order to extract heat. It has been shown that laser stability can be improved by using flow rates at which the Reynolds number corresponds to turbulent rather than laminar flow.[13]

The resonator is equipped with a Brewster-angled quartz plate to polarise the emission, causing a reduction in output power owing to the birefringence of the Nd:YAG crystal.[14] The acousto-optic modulator is located adjacent to the output coupler. Because the ratio of the rod radius to the beam diameter in the rod exceeds 2, there is negligible aperturing by the gain medium, and therefore the resonator requires an aperture to induce fundamental-transverse-mode operation.[10]

The radii of curvature of the two mirrors have been reduced from 60 cm to 50 cm for the model 3800.[15] The effect of this change can be understood by studying the stability characteristics and the spot sizes in the cavity for varying rod focal lengths.[9] For Nd:YAG lasers, the focal length is approximately inversely proportional to the electrical input power to the lamp.[10] Figure 3.3 shows the calculated spot sizes of the mode in the rod for both the type 3800 and 3000 lasers, clearly showing two distinct stability zones, caused by a slight asymmetry in the rod position.

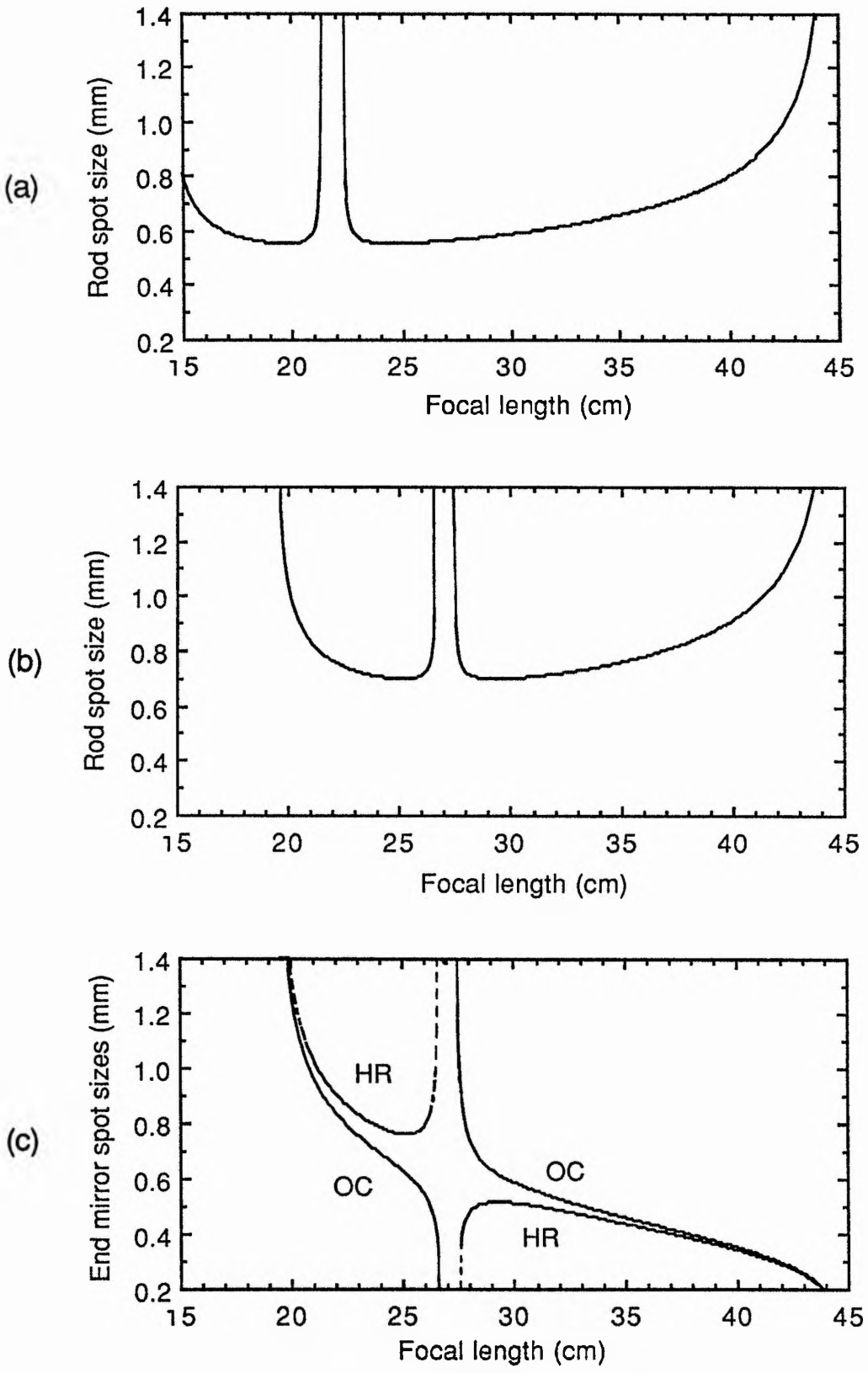

Figure 3.3 Calculated spot sizes (radii) in the rod for (a) the series 3000 and (b) model 3800 lasers. Figure (c) shows the calculated spot sizes on the mirrors for the model 3800 laser.

The 3800 system has an increased spot size, about 0.75 mm, at the expense of a decrease in the range of stable lamp powers. This is in agreement with the work of De Silvestri et al. who showed that these two factors are inversely related[9]. Both lasers are understood to operate with rod focal lengths corresponding to the right-hand zone.[11] For optimal operation, the rod focal lengths should lie in the ranges 27-35 cm for the series 3000 and 32-38 cm for the model 3800, implying that the thermal lensing is more severe in the earlier model. This is partially explained by the higher efficiency of the smaller bore lamp in the 3000. The spot sizes on the end mirrors for the 3800 are also shown in Figure 3.3.

In general, the model 3800 was less stable than the previous model. With careful alignment and adjustment of the current, the amplitude specification of 4% peak-peak could be met, but with thermal cycling over a period of several days the resonator required readjustment to reach power and stability specifications. The most significant amplitude fluctuations were located at frequencies below 100 Hz. In addition, when expanded on a nearby wall, the beam profile was observed to jitter around on a similar timescale, a problem not apparent with the series 3000. It is not clear whether this was a fluctuation of the transverse mode or beam pointing.

Four possible causes of the instabilities were considered. Firstly, the increased diameter of the optical mode when using the model 3800 optics brings the edge of the beam closer to the turbulent water flow. When the mirrors were exchanged for the series 3000 set, the amplitude stability was greatly improved to approximately 2%, with a much less critical alignment, however this was achieved at the expense of a 20-30% reduction in output power with only a minor improvement in the beam movement. Secondly, the increased bore of the lamp might cause a more unstable arc. Thirdly, there is significantly more vibration of the lasing unit compared to the previous model, perhaps due to the design of the cooling water circuit around the chamber. Finally, the laser is designed for the 60 Hz US grid, and so under operation with a 50 Hz supply, the pump will revolve some 17% slower thereby reducing the water flow, perhaps into the regime of mixed laminar and turbulent flow.[13]

For much of the work described in this thesis, the laser was operated with the series 3000 optics to maximise stability. The CW power and stability characteristics of the laser with those optics are shown in Figure 3.4, where the aperture was 1.0 mm in diameter.

Typically, powers in excess of 14 W could be achieved with the 3800 optics (1.1 mm aperture). With those optics, it was possible to reach the edge of the first stability zone, as evidenced by a decrease in output power and stability as the current approached 30 amps, indicating a rod focal length of ~ 28 cm. As would be expected by consulting the stability diagrams in Figure 3.3, no such problem was encountered when the 3000 optics were used. The amplitude stability of the laser is critically dependent on the alignment of the optical mode within the rod. Fortunately, it was found that this alignment also corresponded closely (although not precisely) to that which gave maximum output power. When the most stable operating current was determined, the electronic feedback circuit, which used a photocell to monitor the laser output power, was switched on to control the lamp current automatically. This light control system improved the amplitude stability to ~ 1%, but did not reduce the beam movement.

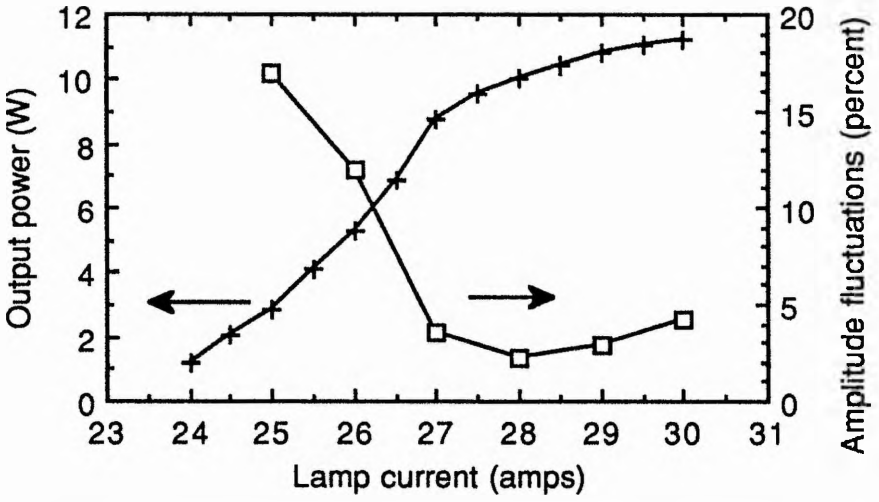

Figure 3.4 CW output power and amplitude stability with the series 3000 optics installed.

The acousto-optic mode locking of the laser was investigated. The anti-reflection coated modulator had crystal resonances separated by approximately 250 kHz. Its position and angle was initially adjusted by maximising the diffraction of a HeNe beam, aligned collinear with the Nd:YAG beam by using the output coupler, aperture and rod (the shutter was closed to prevent oscillation). The Spectra-Physics mode-locking drive electronics were equipped with an oven driver and an electronic feedback system as described by Klann et al. in order that high powers could be coupled into the device whilst reducing the possibility of

thermal runaway.[16] The usual procedure of approaching the resonance from low frequencies was followed, as described in chapter 2. The pulses were monitored on a streak camera driven in synchronism with the pulses by using the usual BPW 28 photodiode and tunnel diode oscillator scheme described in chapter 1.

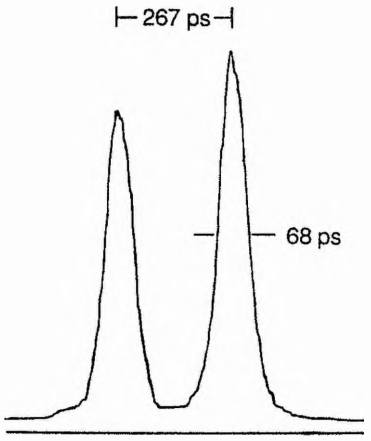

Figure 3.5 Streak camera images of the shortest Nd:YAG laser pulses.

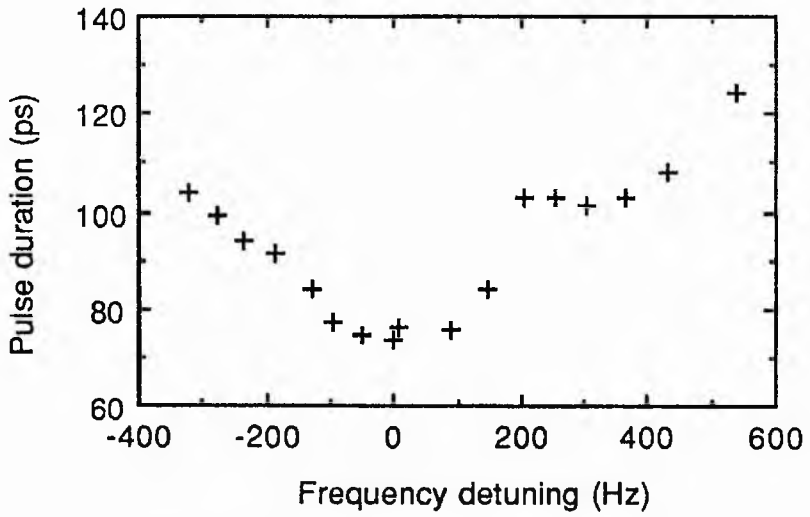

Figure 3.6 Variation in pulse duration with frequency detuning.

By using r.f. powers of around 1.2 W, approaching the maximum recommended, and by fine adjustment of the alignment of the resonator and mode locker, pulse durations as short as 68 ps were obtained (streak profiles shown in Figure 3.5). The dependence on pulse duration with frequency detuning is depicted in Figure 3.6. At each extreme, the pulse train exhibited spiking which at greater detunings developed into self-Q switching as described by

Kean et.al. with reference to the series 3000 laser.[17] For the optimum alignment of the mode locker, a band of spiking was observed in the vicinity of the frequency corresponding to the shortest pulses. This regime was avoided by detuning the drive frequency by ~ 100 Hz, at the expense of slightly longer pulses.

The ratio of the intracavity pulse energy ≈ 700 nJ, to the characteristic saturation energy ≈ 7 mJ (for a spot size of 0.75 mm), is of the order of 10^{-4}, indicating little dynamic gain saturation (emission cross-section ≈ 6.5×10^{-19} cm^2, see reference **12**). Therefore, the mode locker plays the dominant role in the pulse shaping and sideband generation process. This was consistent with the observation that the average output power was only reduced by a few percent when the laser was mode locked, unlike the krypton laser described in the previous chapter.

3.4 Characterisation of the CW KCl:Tl laser

The KCl:Tl laser was initially constructed in the usual three mirror configuration. Since the infrared viewer could not detect 1.5 μm light, the initial alignment of the luminescence was achieved using apertures and a large area germanium photodiode (Germanium Power Devices GM8). It was essential to place a silicon, long-wave pass filter in front of the diode to block the 1064 nm pump light not absorbed in the KCl:Tl crystal. The pump beam was chopped with a 25% duty cycle for average pump powers greater than 2 W to prolong the life of the crystal.

For this characterisation, the Nd:YAG laser was operated CW and the length of the colour-centre laser cavity adjusted to 80-100 cm to maximise the output power. A fused silica Brewster-angled prism was inserted into the collimated arm for wavelength tuning. The power transfer characteristics for chopped and unchopped pump light are shown in Figure 3.7. Input power refers to the power incident on the folding mirror, and is some 10% less than the power before the 45^0 pump steering mirror. The best slope efficiency of approximately 15% was obtained with a 20% transmission output coupler. With many crystals, the optimum output coupler was nearer 12% transmission due to lower optical densities.

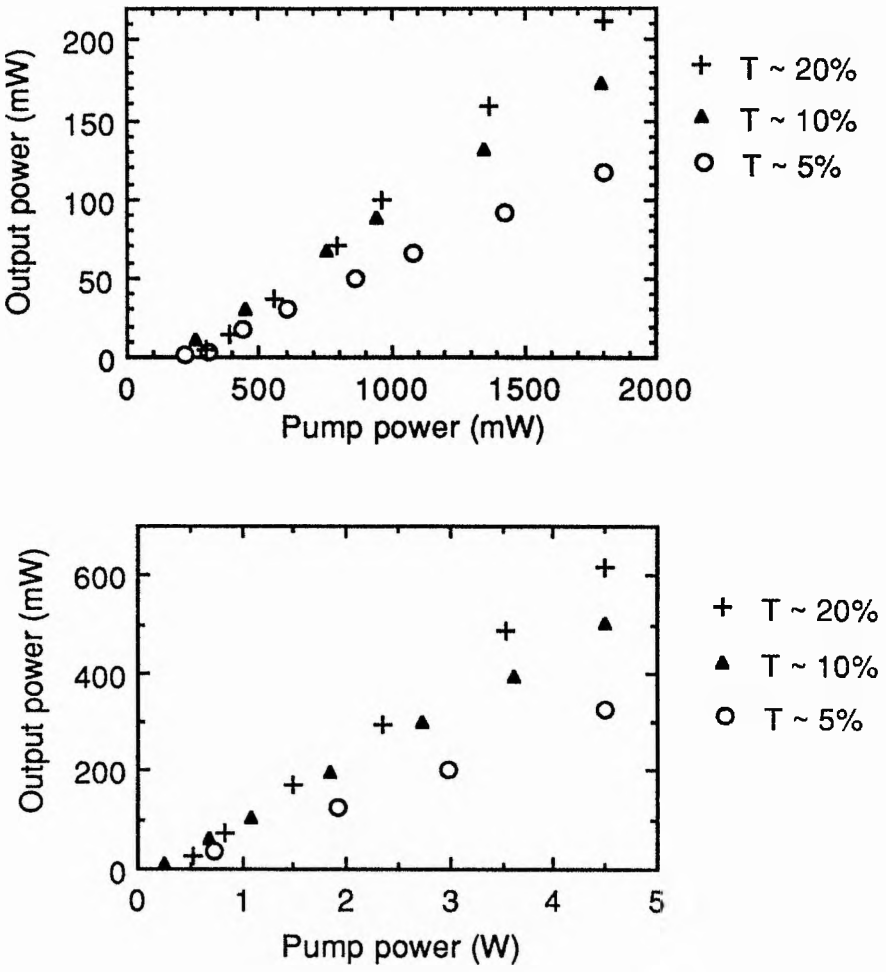

Figure 3.7 Power transfer characteristics with (a) CW and (b) CW chopped excitation. In the case of chopped operation, the recorded average powers have been multiplied by a factor of four to allow comparison with unchopped operation.

The wavelength tunability was investigated for pump powers of 1.8 W and 4.5 W (chopped), see Figure 3.8. These curves are exceptional, and in general, most crystals only produced useful powers at wavelengths between 1460 and 1560 nm.

Threshold pump powers as low as 170 mW could be obtained. The variation of threshold pump power with wavelength is depicted in Figure 3.9.

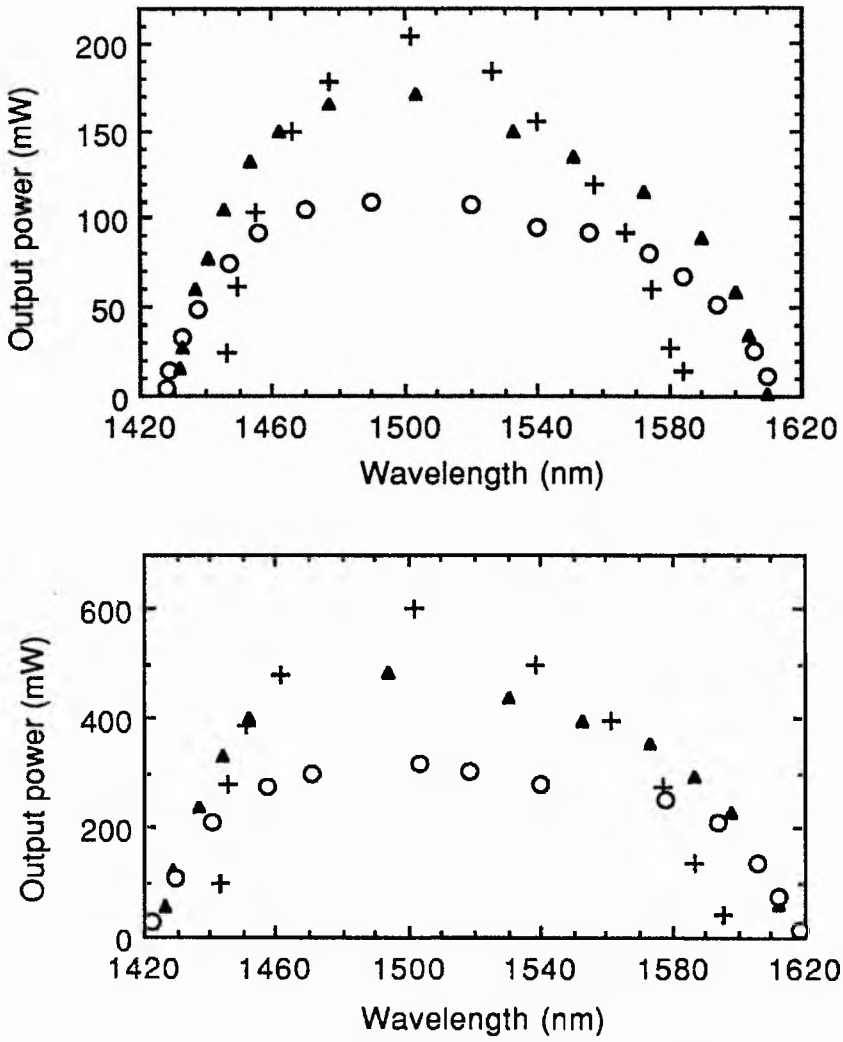

Figure 3.8 Tuning curves for pump powers of (a) 1.8 W and (b) 4.5 W. The symbols refer to the same output couplers as in the previous two figures.

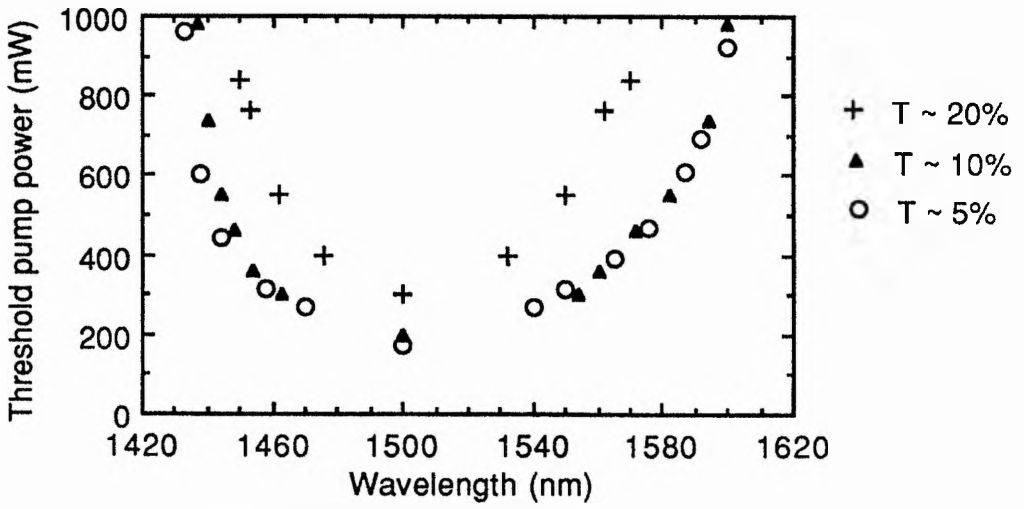

Figure 3.9 Variation of threshold pump power with wavelength.

3.5 Synchronous mode locking

The long decay time and small gain cross-section of the $Tl^0(1)$ centre means that active mode locking by synchronous pumping is not particularly effective. The long decay time of 1.6 μs compared to the 12 ns spacing of the pump pulses reduces the gain modulation to a small ripple on a large DC background. The gain will tend to saturate through average power rather than dynamically, although the dynamic component can be increased by ensuring high intracavity powers, and this has resulted in pulses as short as 8 ps.[8] This unusual regime for synchronous mode locking was modelled by Yasa[18] and by Kelly et al.[19]. The output power of the KCl:Tl laser is similar for either CW or mode-locked operation, and the oscillation threshold with synchronous pumping is largely insensitive to cavity length detuning. The behaviour is unlike synchronously mode-locked dye lasers where oscillation occurs only within a small range of cavity length detunings. Whereas synchronously mode-locked dye lasers require an output coupler with a high transmission (say 30 or 40%) for stable operation and to prevent subpulse formation, no such problem was encountered with the KCl:Tl laser, provided a bandwidth limiting element was incorporated.

At the time of this investigation, there were no wedged output couplers available, and so the cavities investigated used only mirrors having high reflectivity (HR) coatings, with laser output being derived either by the insertion of a pellicle into the cavity, or by using the leakage through a HR mirror. Both linear and ring type cavities were studied.

The three-mirror, standing-wave cavity was extended to 182 cm, and a 2 mm-thick quartz birefringent plate replaced the prism for bandwidth limitation and frequency tuning. The leakage power from the HR end mirror was 2.2 mW for 2 W pump power, sufficient to allow autocorrelation measurements. The high intracavity powers were expected to produce relatively short pulses. Indeed, pulses in the ranges 10-12 ps, 8-11 ps and 7-10 ps duration were recorded for pump powers of 2 W, 4 W and 6 W respectively. This downward trend with increasing pump power was in agreement with previous observations.[2] With a pellicle inserted to extract a more useful output power of 2 x 52 mW, 11 ps pulses could still be obtained for a pump power of 2 W.

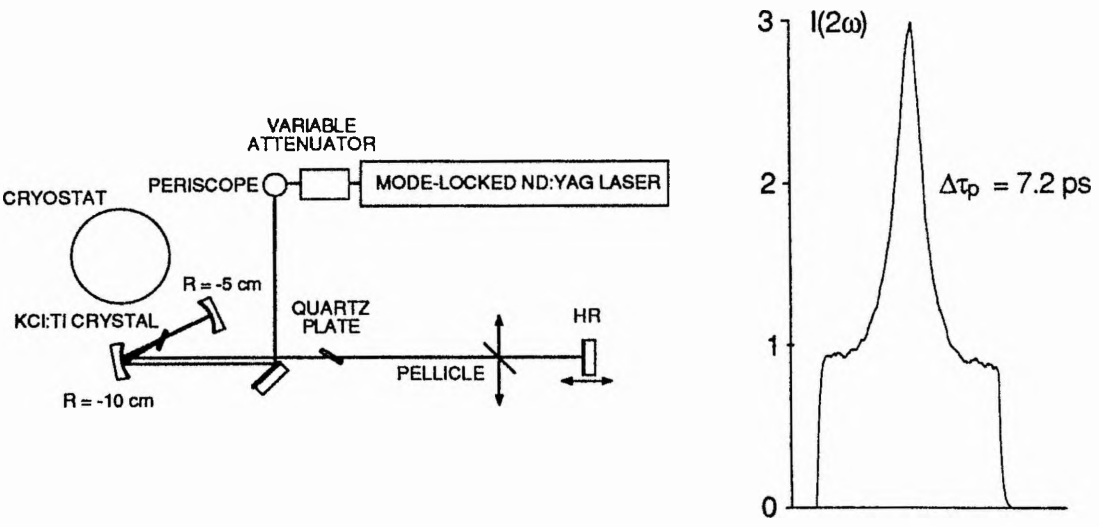

Figure 3.10 Schematic of the linear cavity and an autocorrelation of the shortest pulses obtained.

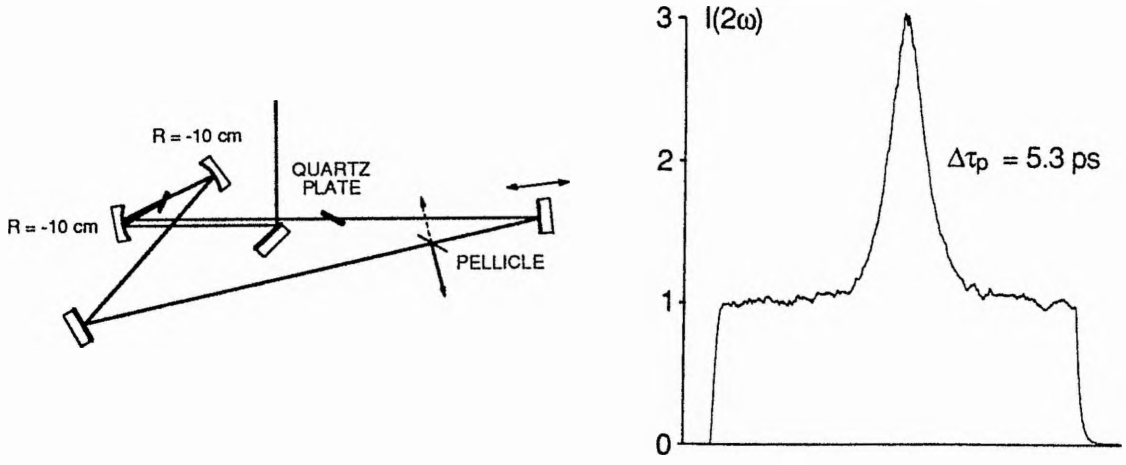

Figure 3.11 Schematic of the ring cavity and corresponding autocorrelation.

In the ring cavity, the laser was expected to operate in the bidirectional, colliding-pulse operation as observed with dye lasers[20,21] and a LiF:F_2^+ laser.[22] As the correct cavity length for mode locking (perimeter ≈ 12 ns) was approached, the two outputs became noisy. The outputs, measured on two identical photodiodes, were added together using an oscilloscope. This revealed that the total output was steady, and that the noise on one output was the mirror image of the noise on the other output. At the correct cavity length, the laser tended to operate largely unidirectionally, although it could be made to switch direction readily by slight adjustment of the resonator or pump beam steering optics. In this unidirectional mode of operation pulses of approximately 6 ps duration were observed, see Figure 3.11. Pulses can also be forced to collide in the gain medium by using a standing-

wave cavity in which the gain is located equidistant from each end mirror. This was attempted, but the output was too unstable to make any measurements.

The behaviour of the laser in the two latter configurations can be explained by considering the effects of spatial hole burning. Pulses colliding in the gain medium form a standing wave and the resultant spatial hole burning will induce a gain (and index) grating in the crystal. Although one direction of oscillation will be preferred due to the asymmetry of the pump beam direction in the crystal, the grating couples the pulses together by scattering energy from one pulse into the other as they pass through each other (essentially a four-wave mixing process). The reason for the stable bidirectional operation of dye lasers and the LiF:F_2^+ laser is probably due to the much shorter decay times of these media. This means that there is significant decay of the population (and hence the grating) between collisions. With media with decay times much longer than the round-trip time, a strong grating can only form after many round trips. The formation of this grating will be weakened by two effects. Firstly, the pump pulses will tend to replenish any burnt regions of the gain every 12 ns. Secondly, for a grating to be reinforced over many round-trips, the optical path length of the cavity must be fixed for timescales of microseconds or longer. In practice, vibrations and acoustic effects alter the length and the cross coupling between the pulses is weak. These factors explain the tendency of the ring cavity to oscillate unidirectionally, and also its sensitivity to perturbations.

3.6 Acousto-optic mode locking

Since pulse shaping from dynamic gain saturation is relatively weak with KCl:Tl, active mode locking by loss modulation is appropriate. This was confirmed by Pinto et al. who used an acousto-optic loss modulator to obtain pulses as short as 6 ps.[23] This technique was briefly evaluated, as a loss modulator was readily available.

A Spectra-Physics 342 prism-type modulator, similar to the one described in chapter 2, was used and driven by the same Racal synthesiser and amplifier arrangement. This particular mode locker, which had an SWR of around 2 at best, was driven with r.f. powers in the range 1-2 W. The colour-centre laser was configured in the X-type cavity, depicted in

Figure 3.12, with the mode locker situated next to one end mirror with the (wedged) output coupler at the opposite end. A 4-mm-thick quartz plate was used for bandwidth limitation.

The shortest pulse durations, approximately 27 ps (assuming a Gaussian profile), were obtained with the modulator assembly spaced around 3 mm from the HR end mirror, see Figure 3.12. Reducing this separation increased the average power output by upto 40%, but resulted in broader pulses and lower stability. Obviously, when the mirror and the modulator are separated by 3 mm, the pulse cannot make a double pass through the device at the peak of the transmission window, resulting in a power reduction. However, the extra loss experienced by the leading and trailing edges of the pulse is greatly increased, and this is responsible for the better pulse shaping.

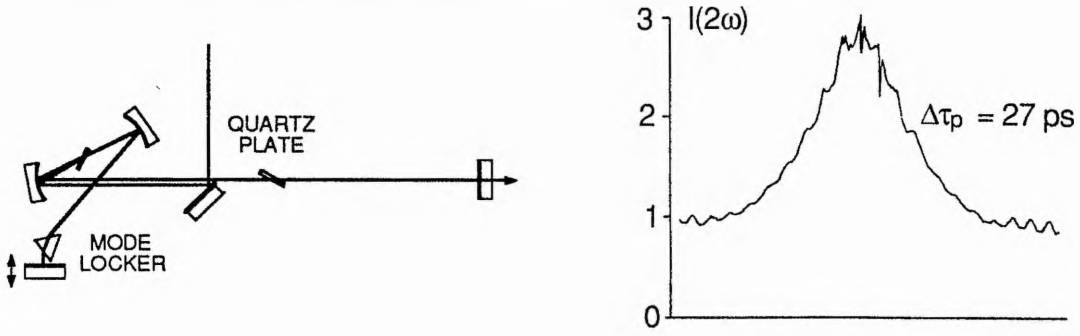

Figure 3.12 Schematic of the acousto-optic mode-locked laser and corresponding autocorrelation.

The pulse durations were not strongly dependent on pump power, suggesting that dynamic gain saturation played a minor rôle, although more stable pulses were produced by increasing the reflectivity of the output coupler. This can be explained by considering that lengthening the cavity decay time increases the effective number of round-trips the pulse makes through the modulator. With a CW pump power of 1.8 W, the laser had average output powers of 100 mW, 110 mW, and 80 mW with output couplers of 7%, 12% and 22% transmission respectively.

The modulation depth of the device was measured by studying the diffraction of a CW 1.5 μm beam from the colour-centre laser (with the modulator located outside the cavity). Only one pair of sidebands could be observed. Each sideband had ~ 5% of the power of the undeflected beam. Therefore, a total of approximately 9% of the incident average power was deflected, indicating a peak modulation depth of some 18%. This modest

modulation depth is not surprising when it is realised that diffraction efficiency scales approximately with (wavelength)$^{-2}$.[24] It is expected that a more efficient modulator would produce shorter pulses.

3.7 Coupled-cavity mode locking using optical fibres

Although the use of optical fibres as control-cavity elements is now well established, this section will cover new work in which it is shown that both the steady state operation and the conditions for starting can be influeneced by the choice of resonator configuration.

3.7.1 Comparison of Michelson and Fabry-Perot arrangements

In the first chapter, the work of Ouellette and Piché was described.[25] Morin and Piché later pointed out[26] that the nonlinear Michelson interferometer arrangement was basically the same as the double cavity arrangement of the soliton laser[27] and its derivatives.[28,29] The experiment described in this section relates to the mode locking of the coupled cavity KCl:Tl laser when either the conventional Fabry-Perot or the less-common Michelson arrangements were employed. (N.B. The coupled-cavity LiF laser described in chapter 2 used the Fabry-Perot arrangement.)

Description of the Fabry-Perot and Michelson configurations

The Fabry-Perot cavity arrangement, shown in Figure 3.13 (a), consists of two standing-wave cavities placed end to end connected by a partially transmitting mirror common to both cavities, one containing the gain medium and the other the nonlinearity. These are generally referred to as the master and control cavities respectively. Normally, the ratio of the intracavity powers in the two cavities is of the order of 10:1, and therefore the system can be thought of as a laser cavity with an optical feedback loop. Useful output power is usually derived by inserting a beamsplitter in the control cavity, as shown. In order that the feedback pulse is correctly timed with the master cavity pulse, the length of the control cavity must be equal to the master cavity, or some multiple if a particularly long fibre is used.

The Michelson cavity, depicted in Figure 3.13 (b), consists of single cavity in which the output coupler has been replaced with a Michelson interferometer arrangement, thus creating a laser with three end mirrors. The two interferometer branches, one of which

contains the nonlinearity, are required to be matched in length to ensure the interference of the pulses. The arrangement can also be thought of as a two cavity arrangement, where the arm containing the gain medium is common to both cavities. With this concept, one can visualise more easily the conditions for stretching the nonlinear branch when using long fibres. To ensure pulse interference, the length of the nonlinear branch should be extended in multiples of the combined length of the gain arm (trunk) and the linear branch (since this length will determine the pulse repetition frequency).

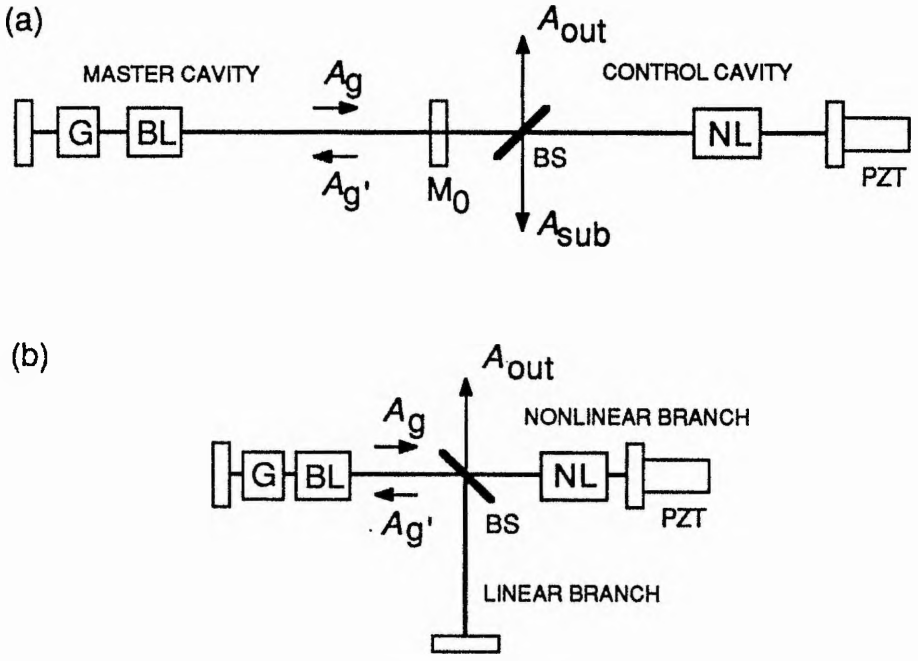

Figure 3.13 Simplified schematic of (a) the Fabry-Perot and (b) Michelson cavity configurations. G:gain; BL:bandwidth limitation; NL:nonlinear element, BS:beamsplitter.

With both arrangements, the amplitude of the output beam, denoted as A_{out} (see Figure 3.13) and the beam returning to the gain medium, $A_{g'}$ are each comprised of two or more beams. The interference effects in each configuration are subtly different. For the Fabry-Perot arrangement, these beams are related to the wave A_g by the following expressions:

$$A_{g'} = A_g [r + (1 - r^2)(1 - b^2)\theta\{\exp(i\phi) - (1 - b^2)\theta r \exp(i2\phi) + ...\}] \quad (3.1)$$

$$A_{out} = A_g b (1 - r^2)^{1/2} [1 - (1 - b^2)\theta r \exp(i\phi) + (1 - b^2)^2\theta^2 r^2 \exp(i2\phi) - ...] \quad (3.2)$$

where r is the (amplitude) reflectivity of the common mirror, *b* is the reflectivity of the beamsplitter, θ is the double-pass transmission of the nonlinear medium, and ϕ denotes the phase-mismatch angle of the feedback signal. In both equations, terms of the order of exp(i2ϕ) and higher account for optical ringing within the control cavity. The equivalent expressions for the Michelson cavity are

$$A_g' = A_g [r^2 + \theta(1 - r^2)\exp(i\phi)] \tag{3.3}$$

$$A_{out} = A_g r (1 - r^2)^{1/2} [1 - \theta\exp(i\phi)] \tag{3.4}$$

where A_g is the wave travelling from the gain towards the Michelson interferometer, A_g' is the return wave, and r is the interferometer beamsplitter reflectivity. In this case, the expressions are much simpler because there are no ringing effects, since the Michelson is a two beam interferometer, whereas the Fabry-Perot arrangement gives rise to multiple beam interference. This is the fundamental difference between the two arrangements. When using waveguides, this is not as important as it might seem, because θ is much less than 1 due to coupling losses. When using optical fibres, θ was estimated to be approximately 0.7, ie. a combined in and out overall intensity throughput of ~ 50% (input coupling efficiencies were approximately 60-70%). Ringing then becomes insignificant after 3 or 4 round trips of the control cavity. On the other hand, if a bulk nonlinear medium were to be used in the control cavity, θ would be close to 1 and ringing effects would be significant, and the Michelson scheme would definitely be advantageous.

To compare the two arrangements objectively, the beamsplitter and mirror reflectivities were chosen such that the power levels in the fibre and the feedback levels were similar. The two configurations were implemented as shown in Figure 3.14. Due to the availability of beamsplitters and mirrors, there is a difference for the Fabry-Perot configuration compared to the simplified diagram in Figure 3.13. The role of the beamsplitter in the Fabry-Perot arrangement was taken by a mirror of 63% reflectivity, equivalent to 37% in Figure 3.14. The common mirror M_0 had a transmission of either 12% or 22%. In the Michelson configuration, a partially transmitting mirror of 93% or 88% reflectivity was used as a beamsplitter.

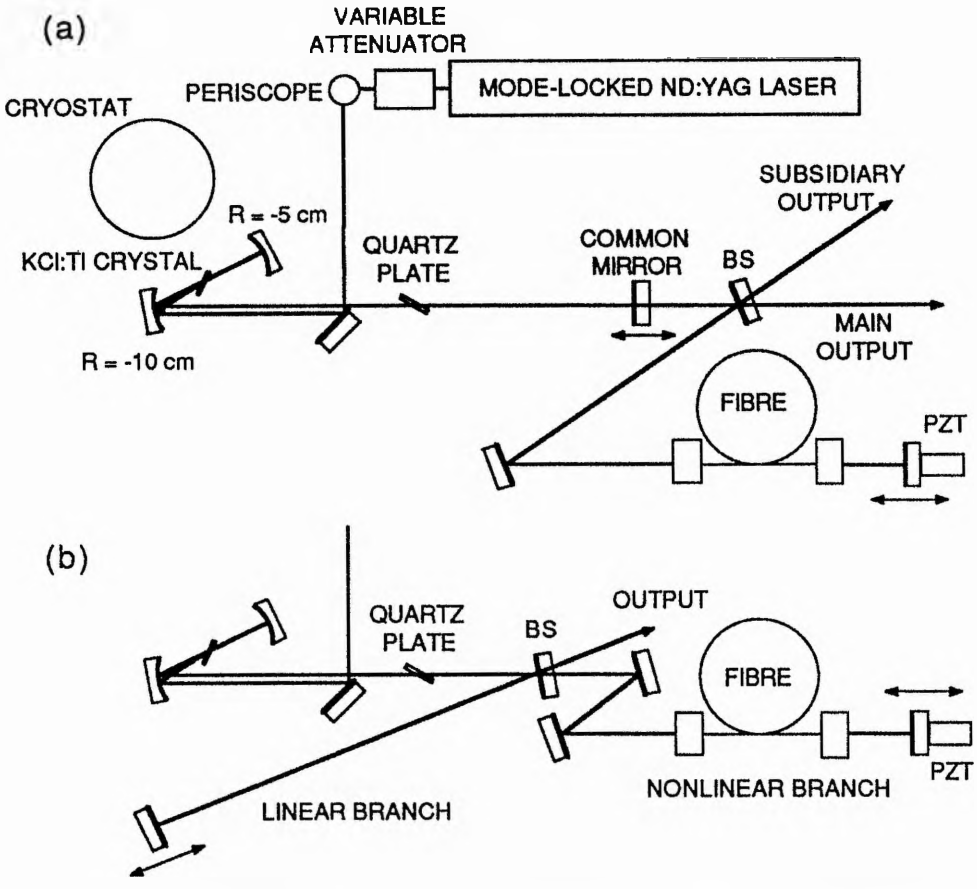

Figure 3.14 Experimental implementation of the (a) Fabry-Perot and (b) Michelson configurations.

The first two terms in the equations (3.1)-(3.4) listed above were evaluated to determine the ratio of the feedback amplitude to the intracavity amplitude (feedback level) and the ratio of the amplitudes of the interfering output beams.

Cavity		Feedback level	Ratio of output amplitudes
Fabry-Perot #1	M_0, $r^2 \sim 88\%$	1 : 17.7	1 : 0.41
Fabry-Perot #2	M_0, $r^2 \sim 78\%$	1 : 9.1	1 : 0.39
Michelson #1	BS, $r^2 \sim 93\%$	1 : 19.0	1 : 0.7
Michelson #2	BS, $r^2 \sim 88\%$	1 : 10.5	1 : 0.7

Table 3.2 Ratios of wave amplitudes at points of interference.

In terms of feedback level, Fabry-Perot #1 is approximately equivalent to Michelson #1, etc. However, the ratio of the two output wave amplitudes are dissimilar with both of these

pairings. The significance of this factor will be discussed later. The useable output power from each arrangement was similar, approximately 30 mW.

Light was coupled into and out of the fibre using the arrangement illustrated in Figure 3.15. The coupling lenses (Melles-Griot 06 GLC 002) had a numerical aperture of 0.50, and were antireflection coated for 1550 nm. The final surface (closest to the focus) was left uncoated, and index-matching oil (Halocarbon Oil 700, chapter 2: reference 42) filled the space between this surface and the fibre end to reduce parasitic optical feedback. This fluid was held in perspex cylinders which fitted onto the lenses using O-rings for sealing. Movement of the fibre end relative to the lens was accommodated by using flexible tubes (the central section of a modelling balloon), spanning between the perspex cylinder and a brass ring which could slide along the fibre chuck (Newport FPH-S). Fluid loss was minimised by carefully reaming the bore of the ring to ensure a snug fit.

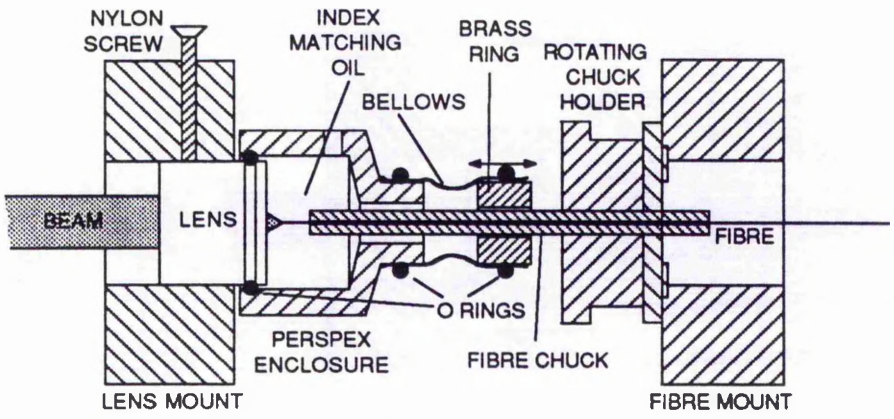

Figure 3.15 Cross-section of index matching oil cell.

Electronic stabilisation system

As is normal for this coupled-cavity technique, stabilisation of the cavity (branch) lengths was necessary.[30] This was achieved by using an electronic stabilisation system which controlled the length of the control cavity by movement of a small dielectric mirror mounted on a piezo-electric translator (PZT) (Photon Control MGS 7.5 or MGS 15). The feedback system was an upgraded version of one used by Kean,[31] itself loosely based on the circuitry described by Mitschke and Mollenauer.[30] The system relies on the interferometric modulation in output power as one cavity length is scanned relative to the other. As discussed

in previous chapters, short pulses are only observed at interferometric intervals, implying that operation is associated with a particular phase difference between the interfering optical cycles. Because this particular phase bias is associated with a power level, the length of the control cavity can be maintained to a high degree of accuracy (estimated to be around 10 nm) by using the feedback system.

The system, shown in Figure 3.16, compares a sample of the laser output power level with that of a reference level, using a differential amplifier. Whilst each phase bias is associated with a unique power level, each power level can have two possible phase biasses, therefore a polarity control is required to select the correct phase. The error signal is then integrated and amplified to drive the PZT. The integration process damps the overall frequency response of the system and reduces the loop gain in the vicinity of the PZT resonance, hence preventing positive feedback and oscillation.

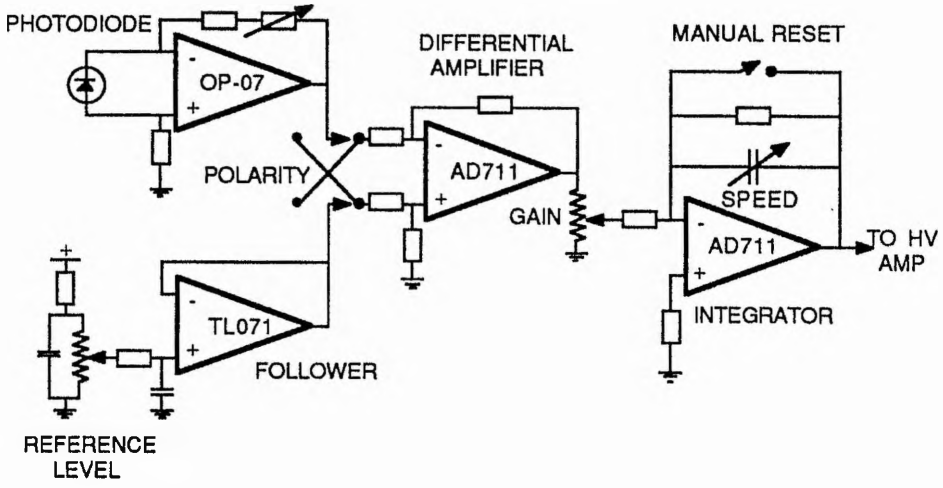

Figure 3.16 Schematic of the electronic feedback system.

Special attention was paid to the reduction of power supply ripple and the elimination of earth loops. Many of the op-amps were upgraded from 741 and CA3140 types to AD711 for increased speed with reduced noise, and an OP-07 type was used for low noise amplification of the photodiode signal. The final amplification stage (not shown) used an op-amp amplifier with a gain of 4, followed by a simple high voltage amplifier based on two HEXFETs. The effective frequency response of this final stage, output $V \approx 0$-140 V, was improved by increasing the maximum current output to approximately 50 mA, since the

impedance of a PZT is almost entirely capacitive. Additional circuitry (not shown) automatically resets the PZT at the central position ($V \approx 70$ V) when it reaches either end of its range of travel.

Experimental results : anomalous GVD fibre

Initial studies were made using anomalous group-velocity dispersion (GVD) fibre as the control-cavity nonlinear medium. This fibre[33] was similar to that used in the original soliton laser, ie. polarisation preserving, with a GVD constant $D \approx +15$ ps/(nm.km) at the 1.5 μm operating wavelength, and a modal area quoted as 65 μm^2 [27] or 86 μm^2 [31]. The fibre length L was chosen after comparing the power available in the control cavity with the power requirements for $N = 2$ soliton propagation.

The conditions reported by Mollenauer and Stolen[27] can be summarised

$$L = Z_0/2 \tag{3.5}$$

$$N = \sqrt{\frac{L_D}{L_{NL}}} = 2 \tag{3.6}$$

where Z_0 is the soliton period, and L_D and L_{NL} are the dispersion and nonlinear lengths respectively, as introduced in chapter 1. Using these two relations, the steady-state pulse duration T_{FWHM} can be calculated from fibre parameters such as the GVD and the length:

$$T_{FWHM} = \sqrt{\frac{6.22\,\lambda^2\,|D|\,L}{\pi^2\,c}} \tag{3.7}$$

where c is the speed of light, and λ is the free space wavelength. The corresponding pulse energy in the fibre E_p depends on the the modal area A_{eff} and nonlinear index coefficient n_2

$$E_p = 1.328\,\frac{\lambda^2 A_{eff}}{\pi\, n_2}\sqrt{\frac{|D|}{c\,L}} \tag{3.8}.$$

Assuming a modal area of 75 μm^2 and $n_2 = 3.2 \times 10^{-16}$ cm^2W^{-1} (fused silica) for a fibre length of 157 cm these relations imply a pulse energy of approximately 400 pJ (average power 33 mW at the 82 MHz pulse repetition frequency), and a $T_{FWHM} \approx 330$ fs. The two equations show that by reducing GVD, the pulse duration and the required pulse energy

decreases. It can be shown that for a fixed average intensity in the fibre (ie. L is varied), the steady-state pulse duration is proportional to the GVD of the fibre.

In preliminary experiments, the pulses were somewhat longer than predicted by the above relations, and the power requirements were higher. The spectra of the pulses were highly structured with deep, narrow channels at irregular intervals. This problem was traced to the double-stack folding mirror, which was causing significant higher order GVD (see chapter 2). When this was replaced by a gold-coated mirror, the pulses and power requirements were in accord with the above calculations. Subsequently, in order to improve the efficiency of the laser, the gold mirror was replaced by a custom designed double-stack dielectric coating with the stacks deposited in the correct order.

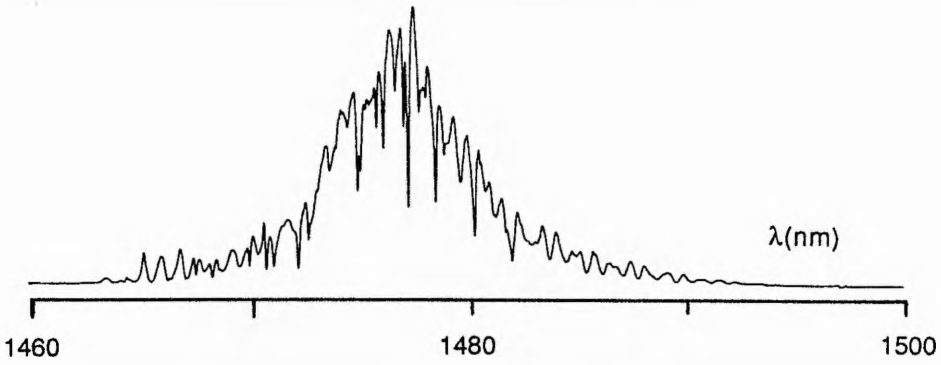

Figure 3.17 Spectrum of a 400 fs pulse obtained during initial experiments. The irregular, deep modulation was caused by a mirror coating, see text.

The cavity lengths were matched using the techniques described in chapter 2. The electronic stabilisation system was then used to interferometrically lock the two cavities together. With both arrangements, stable mode locking was obtained by limiting the oscillating bandwidth with a single quartz birefringent plate of 0.8 mm thickness. For the Fabry-Perot cavity, with a mirror M_0 transmission of 12%, pulse durations as short as 330 fs were obtained, decreasing to 280 fs when the transmission of this mirror was increased to 22%, see Figure 3.18 (a). These durations were obtained for estimated average power levels in the fibre of approximately 25-30 mW, cf. above calculations. The pulses from the control cavity (the subsidiary output) were significantly shorter, at around 180 fs in both cases (Figure 3.18 (b)). The pulse duration from the main and subsidiary outputs is plotted against the estimated average power in the fibre in Figure 3.19.

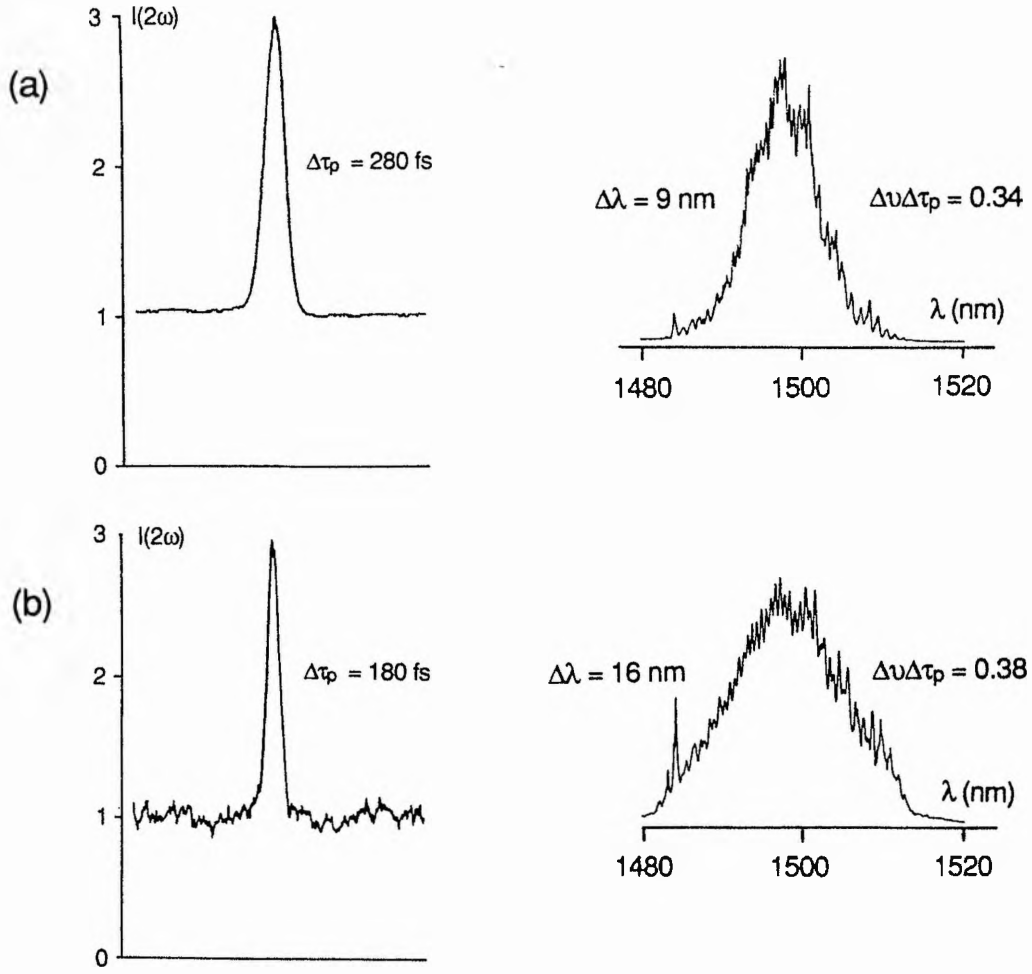

Figure 3.18 (a) Autocorrelation and spectrum for pulses obtained using the Fabry-Perot arrangement: main output. (b) Corresponding data for the subsidiary output.

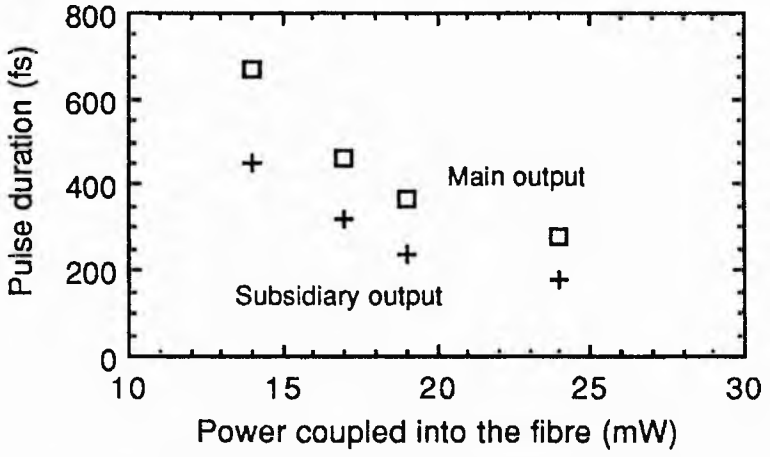

Figure 3.19 Pulse duration as a function of the estimated average power in the fibre.

Using the Michelson cavity the laser produced a similar performance, where pulse durations as short as 310 fs were generated using a 93% reflectivity beamsplitter, and 290 fs when this beamsplitter had a lower reflectivity of 88%, see Figure 3.20. While both configurations gave similar average output powers, around 30-50 mW, the output of the Michelson scheme was significantly more stable, and in particular, the PZT stabilisation system was able to maintain mode locking when the average power fluctuations in the master cavity reached around 20% peak-to-peak. This level of instability was induced by switching the Nd:YAG light control stabilisation system off, and slight misalignment combined with the beam movement. In comparison, with the Fabry-Perot configuration, the PZT stabilisation electronics could not tolerate fluctuations of 10%, and as a result, sporadic drop-outs of the mode locking occurred.

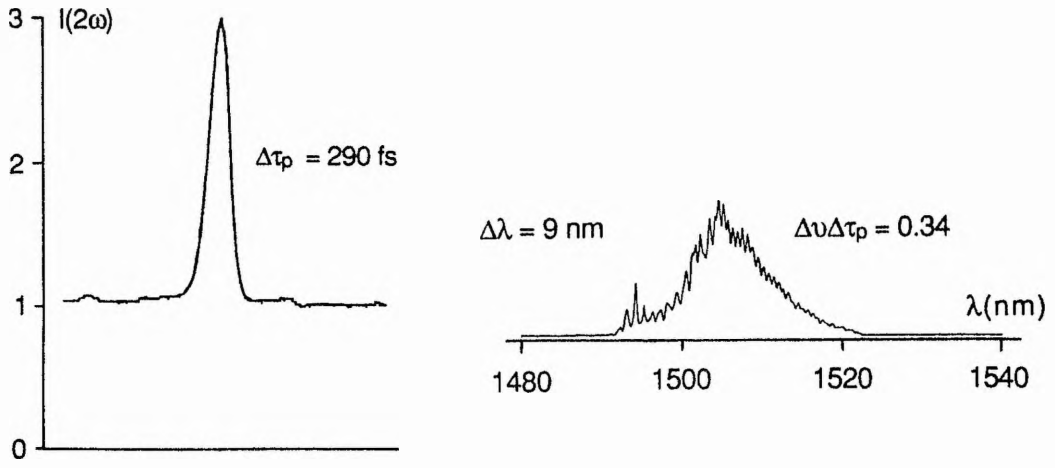

Figure 3.20 Autocorrelation and spectrum for pulses obtained from the Michelson arrangement.

The compactness of the Michelson cavity, compared to the Fabry-Perot arrangement, makes it less vulnerable to vibrations and this is partly responsible for its better stability. The tolerance of pump power fluctuations can be understood by considering the reactions of the stabilisation system. If the pump power fluctuates, the power levels within the coupled-cavity laser also fluctuate, inducing the stabilisation electronics to make an unnecessary adjustment in the length (phase) mismatch to bring the power at the photodiode back to the preset reference level. Excessive power fluctuations can cause the mismatch to exceed the range of phase biasses associated with stable mode locking, resulting in an abrupt cessation of the

short pulse operation. If the depth of the interferometric modulation of the output beam power can be increased, then the stabilisation electronics will become less sensitive to these perturbations. By referring to the last column of Table 3.2, it can be seen that that the Michelson arrangement has an inherently larger interferometric modulation in its output beam that the output from the Fabry-Perot arrangement.* This was also observed experimentally, and explains the greater tolerance of the Michelson arrangement to fluctuations in pump power.

Under stable operating conditions, the optimum pulse durations and corresponding average power requirements agree remarkably well with those calculated assuming $N = 2$ soliton operation, but several points require to be addressed. Firstly, the pulse duration returning from the control cavity was always shorter than the pulse exiting the main cavity (see also reference **31**). Secondly, stable operation can be achieved for a wide range of average powers in the fibre. The experimental results indicate that even in an optimum operation the pulse in the fibre never reaches the $N = 2$ soliton condition. This is because in that situation the feedback pulse would not be frequency chirped, and furthermore, its temporal and spectral shape would be similar to the master cavity pulse. The laser cannot operate successfully under those conditions for the following reasons. It can be easily deduced that the interference of two identical pulses produces a third pulse, which is a replica of the two pulses forming it, providing the time delay between the two interfering pulses is limited to within a few optical cycles. In general, the pulse returning along the main cavity towards the bandwidth limiting element and the gain medium must be shorter than the one travelling in the opposite direction, because spectral filtering, chromatic dispersion and dynamic gain saturation will broaden the pulse temporally.

For both configurations, increasing the average power in the fibre beyond ~ 35 mW resulted in unstable operation.[34] This is characterised by the appearance of one or more sharp spikes superimposed within, or on the edges of the broad spectrum of the short pulse, as depicted in Figure 3.21. These spikes were less than 0.2 nm wide, but could jitter over 1 or 2 nm. By Fourier transform considerations, their width implies that they are associated

* When the ringing terms for the Fabry-Perot configuration are included in the evaluation in Table 3.2, the shape of the modulation is modified slightly, but the overall depth of modulation is not significantly altered.

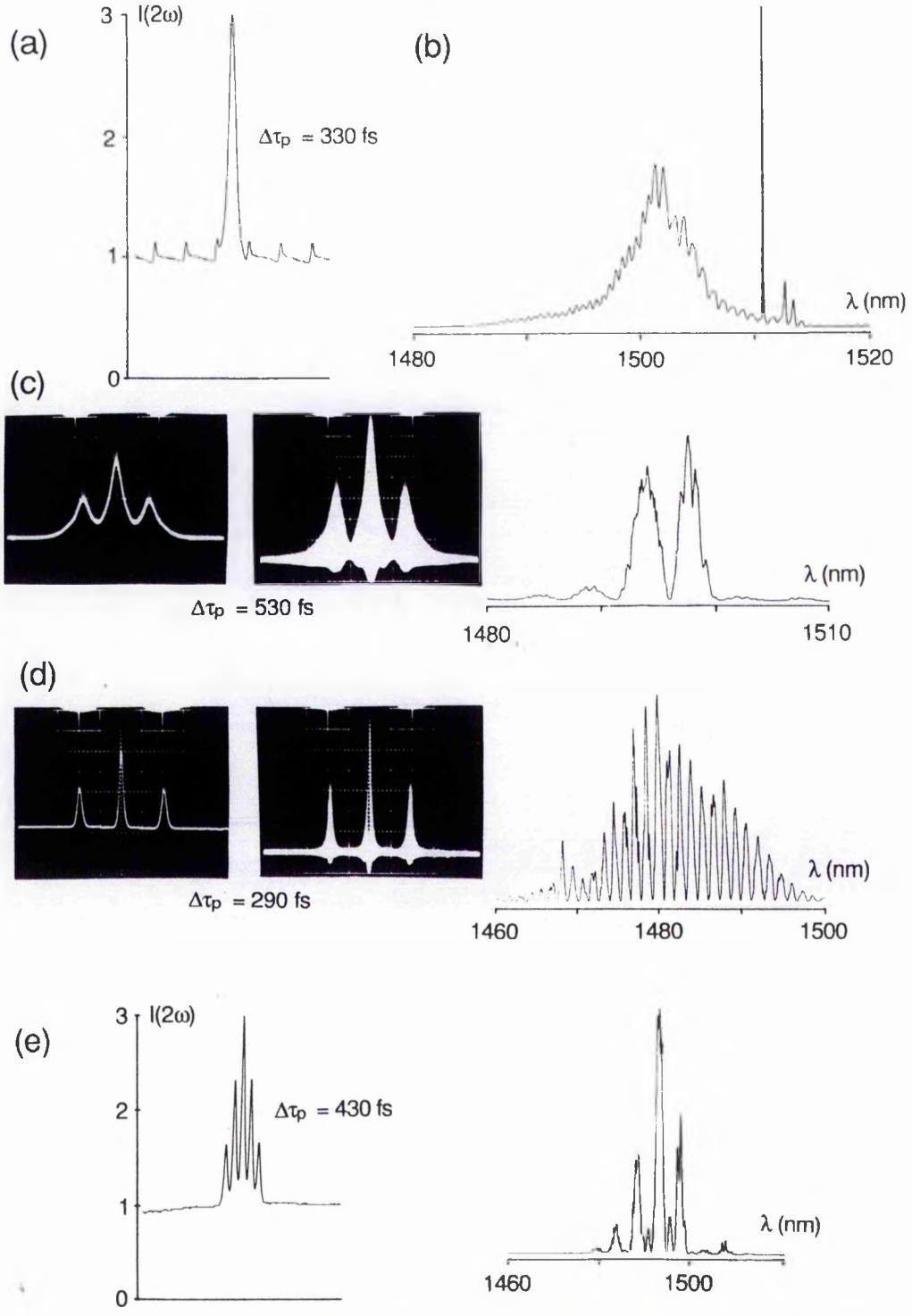

Figure 3.21 Examples of unstable operation. (a) Amplitude modulation on the pulse train, seen here as ripples passing through the autocorrelation. Frequency of this modulation was related to the beating between the pump laser and coupled-cavity laser. (b) Spectrum showing pedestal component. This effect was usually seen in combination with (a). (c) - (e) Intensity and interferometric autocorrelations together with corresponding spectra for multiple pulsing. The fringes in the cross-correlated pulses extends down into the wings, indicating that the pulses interfering with each other occupy the same frequency space.

with a pedestal or background. The proportion of power in the spike was usually less than 10%, and not surprisingly, the autocorrelator could not detect any corresponding rise in background level. At higher power levels and particularly with strong coupling between the cavities, double pulsing was observed (see Figure 3.21), as previously reported by Mollenauer and Stolen.[35] The associated spectra indicated that the two pulses had the same carrier frequency because the overall width was consistent with the duration of a single pulse, while the modulation was consistent with the pulse separation. The 100% modulation in Figures (c) and (d) indicates that the two pulses had approximately equal power. At even higher power levels, this was followed by triple and higher-order pulsing. These effects are universal since they have also been observed with normal GVD fibre, and are not associated with higher-order solitons.

Experimental results : erbium-doped fibre

The comparison of the two cavity arrangements was extended to shorter pulses by using an alternative, nonsolitonic fibre. Pulse durations of less than 100 fs have been obtained[36] at modest powers by using erbium-doped fibre[37] in the control cavity. A 19 cm length of this particular[36] fibre, which has a germania-doped-silica core of around 4.6 μm diameter, a Δn of 0.020, was incorporated into the control cavity. The Δn is consistent with a GeO_2 doping level of 13-14% by molecular percentage. The erbium ion doping level was 6×10^{18} cm^{-3}, approximately 0.06 % by weight (or ~ 0.01% by molecular percentage). This doping level causes a maximum small signal loss of ~ 7 dB/m in the vicinity of 1.54 μm. The powers used here (>15 mW average) were sufficient to bleach the absorption in the 19 cm length. This was verified by the measuring the saturation of the absorption at 1500 nm using a 290 cm length of the fibre (see Figure 3.22), where almost complete bleaching was observed for coupled powers of only 10 mW. The long time constants associated with the transition, of the order of 10 ms, means that the saturation of the absorption occurs through the cumulative effect of many tens of thousands of pulses, and dynamic saturation (and therefore pulse shaping) is nonexistent.

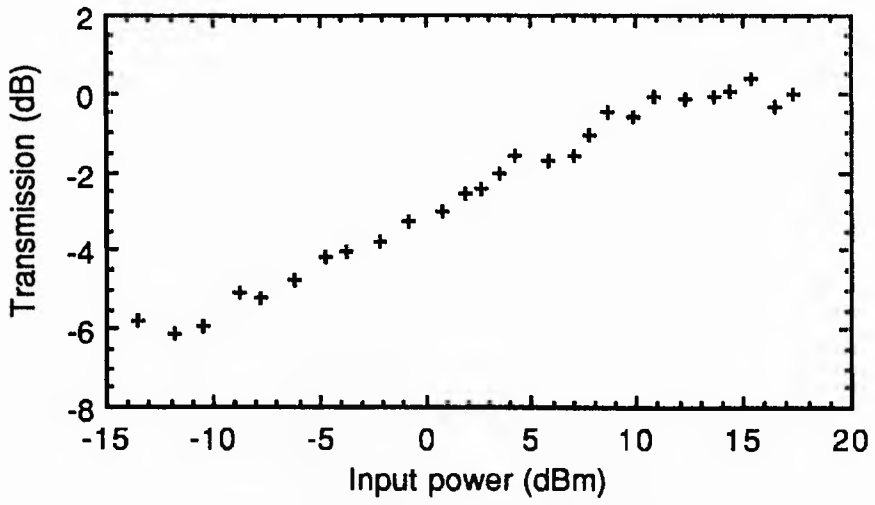

Figure 3.22 Absorption saturation at 1500 nm for a 290 cm length of fibre (corrected for coupling losses).

Mode locking was obtained in both arrangements for average power levels in excess of 15 mW in the fibre, with the shortest pulses recorded for an estimated intrafibre power range of 20-30 mW, with unstable operation at higher powers. Neither arrangement required a birefringent filter for stable operation. In the Fabry-Perot arrangement, pulse durations as short as 75 fs were recorded (see Figure 3.23 (i)) with a mirror M_0 of 88% reflectivity, with similar durations obtained for the 78% reflectivity mirror. The pulses returning from the control cavity (Figure 3.23 (ii)) were strongly frequency chirped and considerably longer, the autocorrelation having a full width half maximum of 370 fs, indicating that the fibre had normal GVD (this will be discussed later). The double-lobed spectral broadening indicates a peak phase shift of around $3\pi/2$ radians.

Pulse durations as short as 90 fs were obtained using the Michelson configuration with a beamsplitter reflectivity of 93% (Figure 3.24). Although these pulses were slightly longer than those obtained when using the Fabry-Perot cavity, the laser performance was noticeably more stable. In decreasing the beamsplitter reflectivity to 88%, the pulse durations increased to ~ 110 fs, and the associated relatively large bandwidth-duration products of 0.65, together with the interferometric autocorrelation data confirmed the existence of substantial frequency chirp. Unstable operation of the laser occurred for powers in excess of 25-30 mW in the fibre, with sharp spikes appearing in the spectrum. Multiple pulsing was not observed with this short length due to the power requirements, but was evident for much longer fibre lengths. Both configurations gave similar useful power outputs of ~ 40 mW.

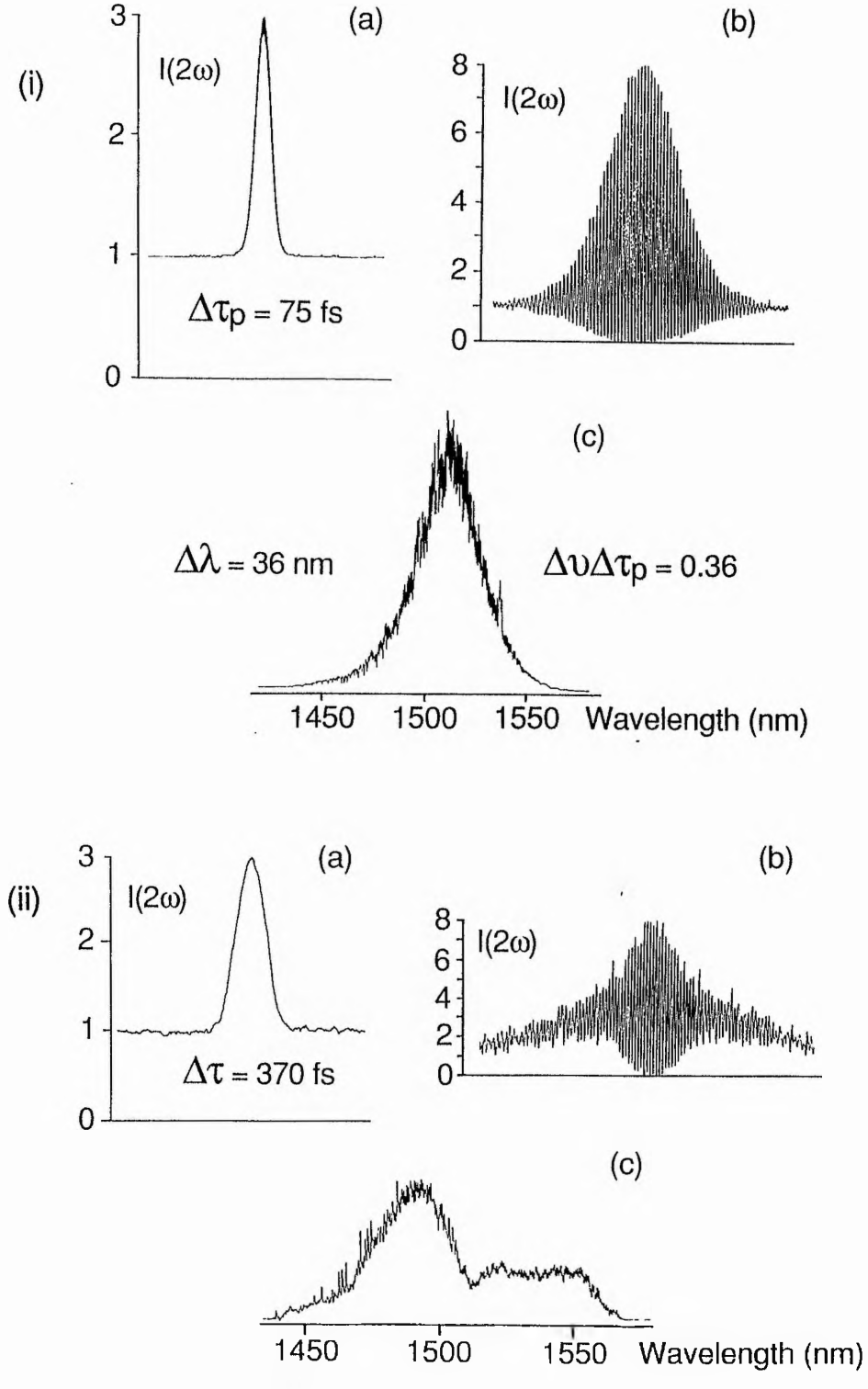

Figure 3.23 (i) Intensity and interferometric autocorrelations and spectrum for the shortest pulses obtained from the main output of the Fabry-Perot arrangement. (ii) Corresponding data for the subsidiary output.

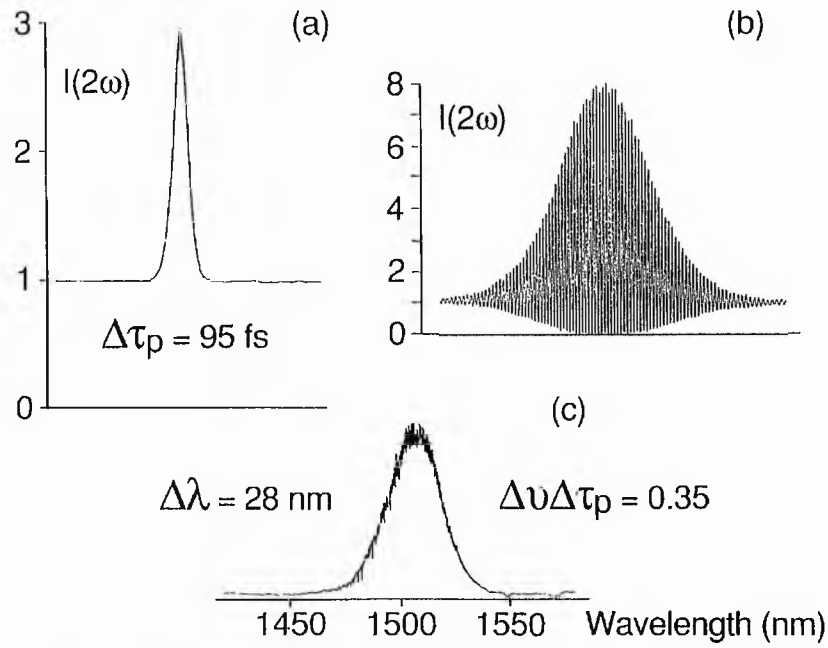

Figure 3.24 Intensity and interferometric autocorrelations and spectrum for typical pulses obtained with the Michelson arrangement.

The pulse spectra were narrower than the 74 nm phase-matching bandwidth of the 0.25 mm-thick $LiNbO_3$ crystal in the autocorrelator, but it was realised some time after the measurements that the silicon filter used to prevent room light entering the SHG box may have caused significant pulse broadening due to GVD. The second derivative of refractive index with wavelength was determined to be +0.197 μm^{-2} at 1500 nm by reference to a Sellmeier expansion.[38] This corresponds to a β_2 of 1.18 $fs^2\mu m^{-1}$. The effect of this dispersion can be gauged by using equation (1.29) in chapter 1 (although this applies solely to pulses with a Gaussian profile). Consider the broadening of a Gaussian pulse of 75 fs FWHM, ie. a 1/e half-width of T_0 = 0.045 ps. These values of β_2 and T_0 give a dispersion length L_D of 1716 μm. The filter was 500 μm thick, giving a broadening of approximately 4%. For two filters, the predicted broadening is close to 16%.

Experimental measurements of the temporal broadening due the Si filter were made later when the coupled-cavity laser was rebuilt for another experiment. Using the Michelson configuration, and with the Si filter removed from the autocorrelator, the pulses had a chirp free interferometric autocorrelation of 160 fs at the FWHM, giving a pulse duration of 85 fs assuming a $sech^2$ profile (Figure 3.25). The intensity autocorrelation had a FWHM of 155 fs, translating into a pulse of 100 fs for the assumed $sech^2$ profile. The discrepancy after

deconvolution indicates that the pulse shape is not precisely $sech^2$. To maximise the broadening, two similar Si filters were placed in the beam. The intensity autocorrelation was broadened by a factor of approximately 40%, and frequency chirp was visible in the wings of the interferometric autocorrelation. This amount of broadening is considerably more than expected. It might be attributed to the dielectric coatings on the filter (long pass edge filter on one side and antireflection on the other), inaccuracies in the Sellmeier expansion, or to the shape of the pulse. Certainly, it does indicate that the Si filter should be removed from the SHG box when the pulses are shorter than around 80 fs.

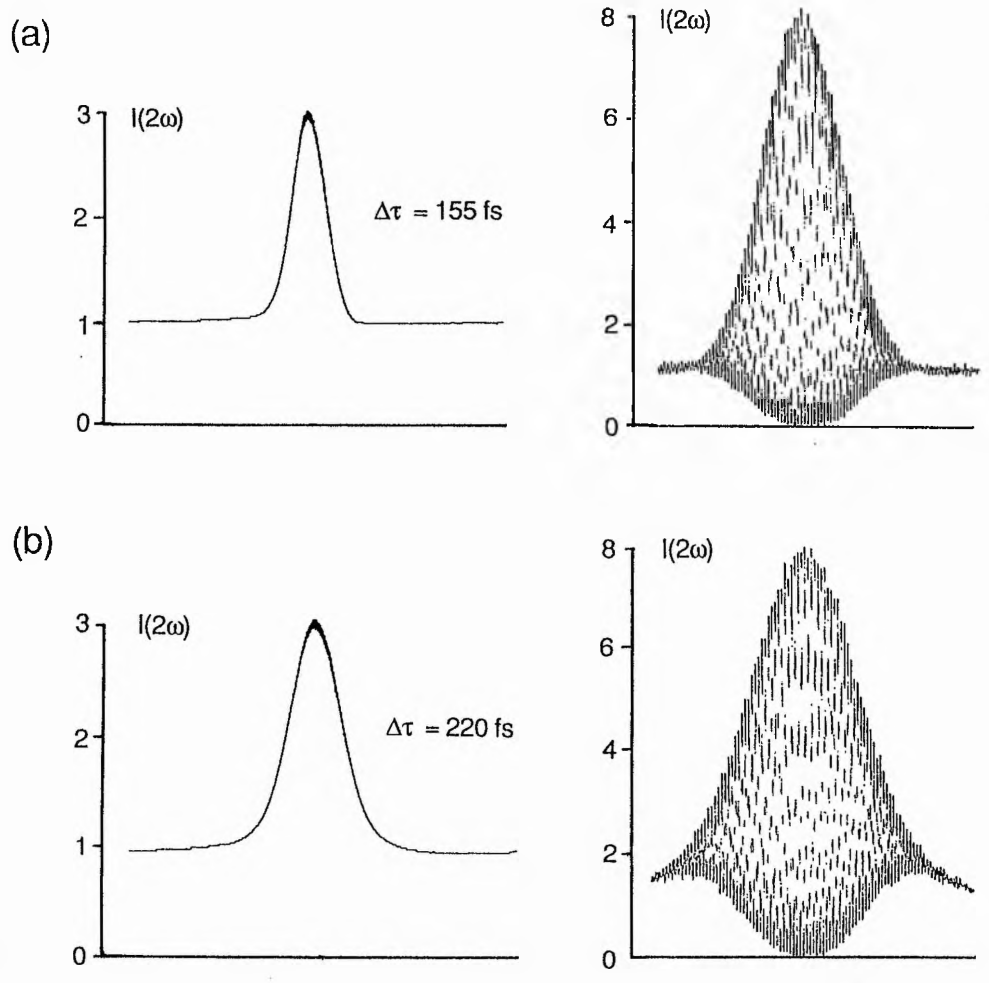

Figure 3.25 Temporal broadening of pulses by 1 mm of silicon. (a) Intensity and interferometric autocorrelations for pulses directly from the laser. (b) Measurements repeated with two silicon filters placed in the beam path.

3.7.2 Self-starting coupled-cavity mode locking

In general, coupled-cavity mode-locked colour-centre lasers use some additional mode-locking technique such as synchronous pumping to initiate the process. Once coupled-cavity mode locking is established, the synchronous pumping plays no significant role in the mode-locking since the laser runs passively, whereby the repetition frequency is determined by the cavity lengths and not by the pump pulse periodicity.[32] This was verified by monitoring the pulse repetition frequency using a fast photodiode and a frequency counter. The frequency was found to be almost directly related to the length of the master cavity, but could be pulled by a few tens of Hz by detuning the control-cavity length.

The observations of mode locking in continuously pumped coupled-cavity CO_2,[25] Nd:YAG,[39,40] and Ti:sapphire[41] lasers has provided impetus to demonstrate the so-called self-starting of mode locking in coupled-cavity colour-centre lasers. In simple terms, the mode-locking will start to evolve when the amount of amplitude modulation in the master cavity (caused by the nonlinearity in the control cavity) exceeds some critical value, at which it can dominate opposing mechanisms such as gain saturation, spontaneous noise and mode competition. Obviously, the probability for self-starting can be increased by using a long fibre with a small core to increase the effective nonlinearity, and also by raising the coupling between the two cavities.

Self-starting was not obtained in either the Fabry-Perot or Michelson configurations, and even increased coupling and the use of fibres as long as 10 m was insufficient to induce mode locking. An alternative approach is to increase the peak intensities that occur naturally in the CW pumped laser. By locating the gain medium in the centre of the cavity, strong mode beating should occur because two adjacent longitudinal modes will oscillate due to the effects of spatial hole burning. (When the laser is configured with the gain close to an end mirror, the laser will tend to operate predominantly in a single mode, since the side modes which can benefit from the unburnt gain will be located many longitudinal mode spacings from the lasing mode, see reference 42.)

The Fabry-Perot arrangement used is depicted in Figure 3.26. The master cavity length remained at ~ 182 cm and the common mirror transmission was 22%. With CW excitation there was a significant enhancement in the SHG autocorrelation signal when the

gain medium was within a few millimetres of the cavity centre. There was also an enhancement when the cavity length was precisely matched to the Nd:YAG laser (which was presumably oscillating on two or more axial modes) but this did not appear to help the self-starting. Examination of the output on a fast photodiode showed the dominant modulation was at twice the fundamental cavity frequency. This implies that two pulses or noise bursts were present in the cavity, colliding with each other in the gain. This was unexpected, and suggests that the laser prefers to operate with a gain grating.

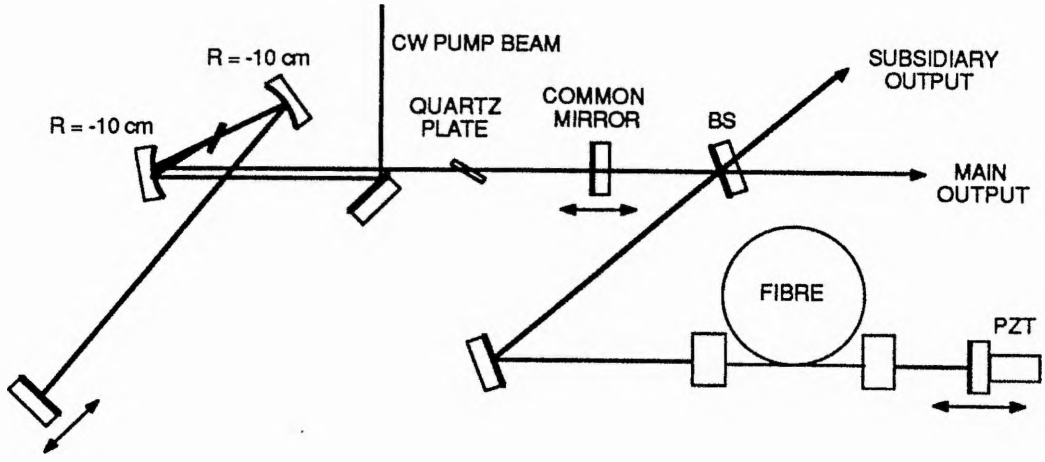

Figure 3.26 Cavity arrangement used for self-starting.

Once feedback from the control cavity was established, the mode-beating frequency changed to the fundamental cavity frequency (82 MHz). Mode locking was obtained with a 265 cm length of Corning dispersion-shifted fibre (Corguide 1524)[43] and a single 4-mm-thick quartz plate for bandwidth limitation. This fibre was used in preference to the erbium-doped fibre because long lengths could be used without incurring significant loss. The reliability of the self-starting was improved by increasing the beamsplitter (BS) reflectivity from 63% to 78%. Pulses of ~ 0.7 ps duration were recorded (see Figure 3.27) with 50-60 mW power in the fibre, but the associated spectra had two narrow features implying the presence of a pedestal or a CW background. These two features were reminiscent of those observed by Zhu et al.[34] which were attributed to modulational instability, however, the fibre used here had normal GVD at the operating wavelength of 1.5 μm. With the scanning Fabry-Perot interferometer, it was apparent that only one of these features was present at any

one time, and that the rate of switching between these features could be controlled by adjustment of the PZT stabilisation electronics. This switching also caused amplitude noise clearly evident on the autocorrelation trace. The spectra of the pulses returning from the fibre had the double-lobed shape, characteristic of a $3\pi/2$ radians peak phase shift.

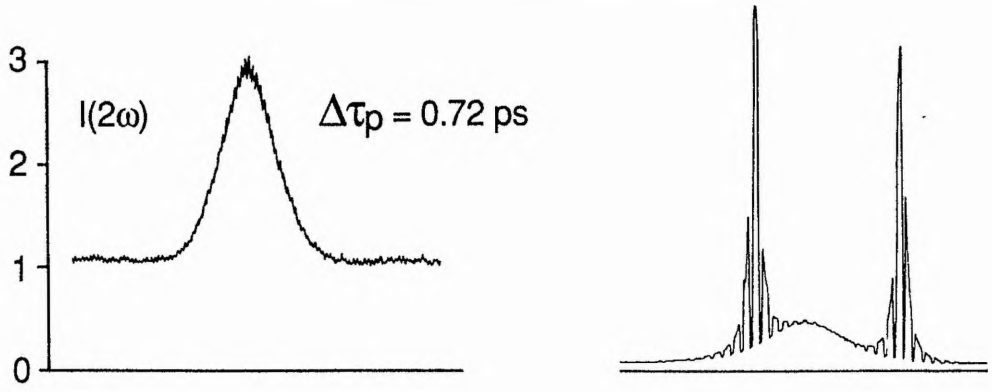

Figure 3.27 Autocorrelation and spectrum for self-starting operation.

The general behaviour indicated that the peak power in the fibre was too large for the fibre length (this will be discussed later). Normally, either the power level or the fibre length would be reduced to achieve stable operation, but this would have prevented self-starting of the mode locking. This instability would probably be alleviated by restricting the steady-state pulse duration by adding further bandwidth limitation, but unfortunately no suitable cavity elements were readily available for this purpose.

Since stable operation at pulse durations of 100 fs requires the use of much shorter fibres, further reductions in the threshold power will be required. Stable self-starting operation when using an optical fibre has been observed by Sucha with a stabilised $NaCl:OH^-$ laser, where similar Corning fibre was used.[44] The product of Sucha's fibre length and average power is considerably less than that used by the KCl:Tl laser described above. Apart from the gain media characteristics, the only significant difference between the two lasers is the treatment of the fibre ends by Sucha. By polishing the ends to an angle off true, he may have eliminated parasitic feedback. A theory[45] on self-starting has indicated that $NaCl:OH^-$ is less likely to self-start than KCl:Tl due to the larger emission cross-section, and therefore it appears that the treatment of the fibre ends and the reduction of other sources of parasitic feedback may be the key to further reduction in the threshold power for self-starting.

3.7.3 Fibre group-velocity dispersion measurements

The length of fibre in the control cavity means that this leg has considerable GVD compared to the master cavity. This is apparent when one attempts to tune the laser to a different wavelength. Readjustment of the control-cavity length is required in order to re-establish mode locking. This change in cavity length with wavelength is directly due to the difference in group delay between the radiation in the two cavities. This length tuning effect was utilised to estimate the GVD of the three fibres used in this work. The technique measures the group delay directly since it essentially detects the length of maximum fringe visibility.

At each measurement wavelength, the length of the main cavity was readjusted for optimum synchronous mode locking. These length changes amounted to much less than 5 μm over a 100 nm tuning range. The length of the control cavity was then readjusted to give the shortest coupled-cavity mode-locked pulse. At the extremities of the tuning range, coupled-cavity mode locking was sometimes not observed due to the diminished power of the laser, and the length corresponding to maximum fringe visibility was noted instead.

The length measurements are shown in Figure 3.28. It is immediately apparent that two of the curves have turning points within the tuning range of the laser, corresponding to the zero-GVD wavelengths. The result for the erbium-doped fibre is broadly in agreement with the observations of Zhu and Sibbett, who used identical fibre.[46] They compared the pulses from the main output of their coupled-cavity laser with those of the subsidiary output as the laser was tuned in the vicinity of 1.5 μm. They observed that the pulse broadened in the fibre at 1508 nm and was compressed at 1540 nm wavelength, with negligible distortion at 1534 nm. The mechanism for this pulse shaping was cited as GVD due to the erbium transition. Its contribution to GVD can be estimated by reference to susceptibility data published by Desurvire.[47] The contribution to GVD by the transition can be calculated after analysing the plotted data for the real susceptibility $\chi(\lambda)$ (see Figure 3(a) in reference 47). The refractive index $\Delta n(\lambda)$ is given by[47]

$$\Delta n(\lambda) \approx \frac{1}{2n} \mathrm{Re}[\chi(\lambda)] \qquad (3.9).$$

The greatest curvature of the susceptibility data is in the vicinity of 1520 nm, where the maximum rate of change of the gradient is ~ -1.4 x 10^{-8} nm^{-2}, ie. a GVD constant D of approximately +70 ps/(nm.km). Even allowing for the higher doping level of the fibre modelled, it appears to be a significant effect.

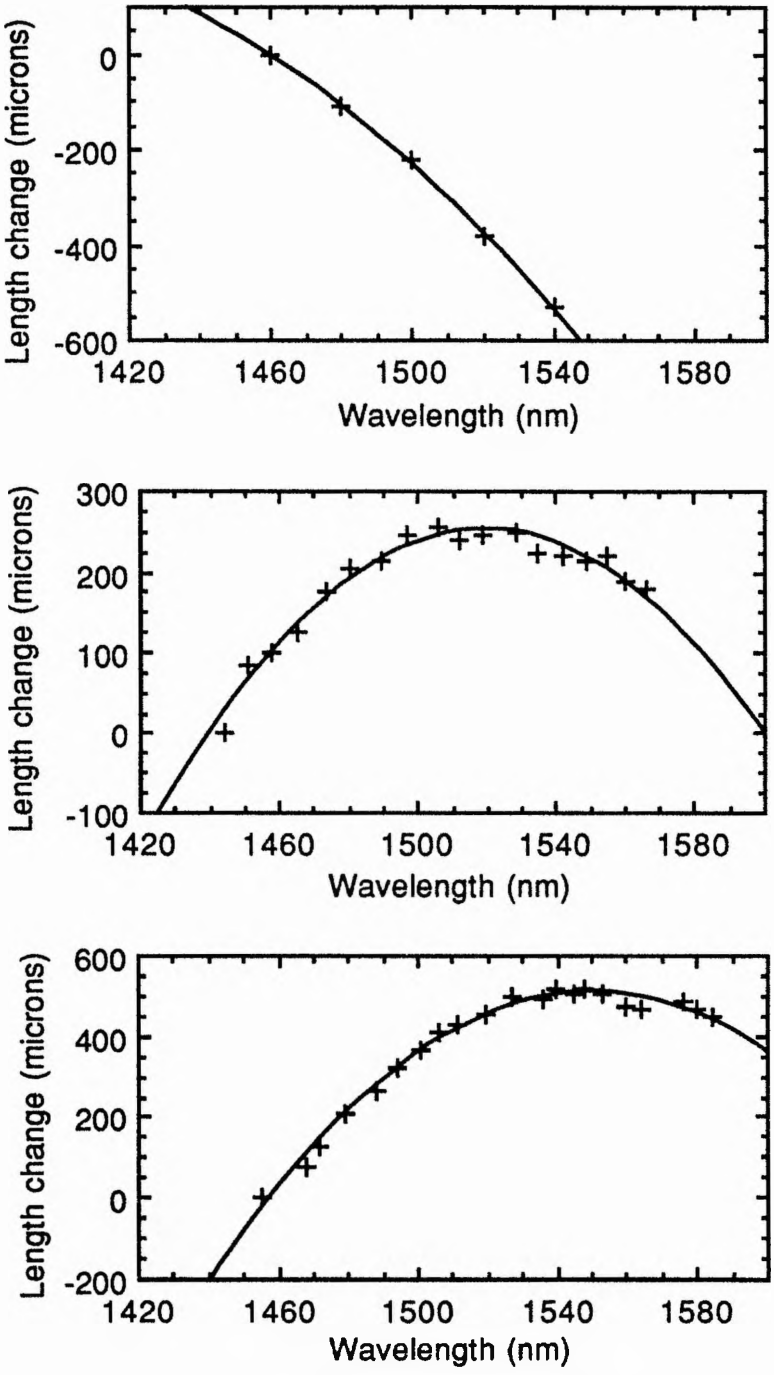

Figure 3.28 Group-delay curves for (a) 157 cm of AT & T soliton laser fibre, (b) 413 cm of STC Technology Er-doped fibre, and (c) 507 cm of Corning dispersion-shifted fibre.

The experiment has not detected the dispersion associated with the transitions, perhaps because the spectra of the pulses were broader (in excess of 5 nm) than the features themselves. Furthermore, the transition is almost bleached when the measurement is undertaken, thereby reducing the GVD. These effects would also influence the previous measurements of Zhu and Sibbett,[46] and both experiments were probably detecting the background GVD of the fibre.

The actual GVD of each fibre was estimated by fitting the results to a quadratic (ie. second-order GVD is assumed to be constant), correcting the terms for the fibre lengths and converting from length delay into time delay, and then taking the derivative of the quadratic. The resultant expressions for D are listed in Table 3.3, together with the λ_0 and D at 1500 nm predicted by the expressions.

Property	AT & T pol. pres.	STC erbium-doped	Corning
D (ps/(nm.km))	-133.85 +0.0986λ(nm)	-96.39 +0.0634λ(nm)	-120.34 +0.0776λ(nm)
λ_0 (nm)	1357	1520	1550
D at 1500 nm	+14.1	-1.3	-3.9

Table 3.3 GVD data for the three fibres.

Although an approximate technique, the values of dispersion for the AT & T solitonic fibre agrees with published data, and the λ_0 of the Corning fibre is consistent with its specification. STC Technology had no dispersion measurements for the erbium-doped fibre, presumably because the high loss due to the transition prevents the use of conventional measurement techniques. A computer program was written to model the dispersion characteristics of the basic germanosilicate fibre, ignoring the influence of the erbium transition. The material and waveguide contributions were calculated using the expressions given in chapter 1.

When calculating the waveguide contribution, the second derivative of $b(Vb)$ with respect to V is required, see equation (1.39). Normally, $b(V)$ should be determined by numerically solving an eigenvalue equation consisting of Bessel functions. The Pascal

package was not equipped with Bessel functions, so to simplify the analysis, the values for the second derivative of $b(Vb)$ with respect to V were copied from a graph published by Chang.[48] Twenty points over the range ($0.75 < V < 3.00$) were noted, and fitted with two fifth order polynomials covering the ranges ($0.75 < V < 1.15$) and ($1.15 < V < 3.00$). These polynomials deviated from the published graph by less than 0.03.

The material dispersion of the germania-doped core was derived from Sellmeier expansions originally published by Adams[49] (corrected in reference **50**). The values for 13.5 molar % germania-doped silica was used for the core and those for pure silica were used for the cladding. Expansions for both quenched glass ($\Delta n \approx 0.022$, material $\lambda_0 \approx 1373$ nm) and annealed glass ($\Delta n \approx 0.020$, material $\lambda_0 \approx 1435$ nm) were tried. This level of doping gives a Δn close to the value quoted by STC Technology (0.020).

For quenched glasses and a core radius of 2.3 μm, the predicted λ_0 of the fibre is ~ 1453 nm, whereas by reducing the core radius to 2.215 μm, the λ_0 can be shifted to 1520 nm. On the other hand, if the values for annealed glasses are used, the fibre λ_0 for a core radius of 2.3 μm is 1725 nm. This can be reduced to 1520 nm by increasing the core radius to 2.48 μm. Figure 3.29 compares that theoretical prediction with a quadratic fit to the measured delay curve.

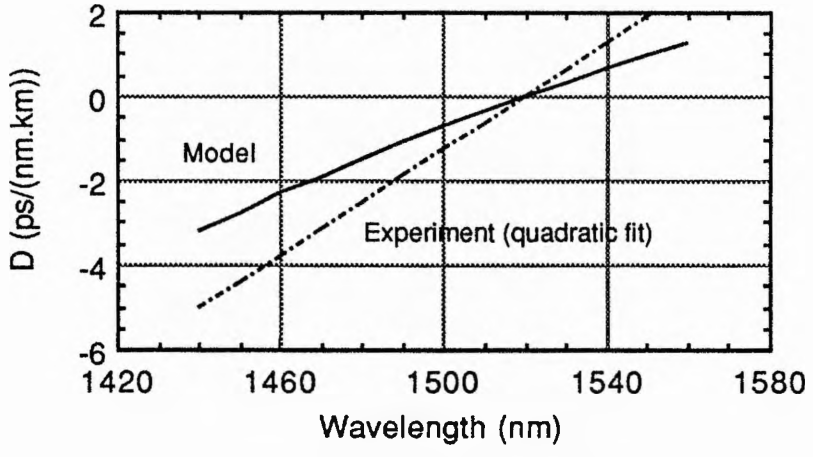

Figure 3.29 Measured and modelled GVD of the germanosilicate fibre, using values for annealed glasses and assuming a core radius of 2.48 μm. The dashed line shows the values predicted by the quadratic fit to the measured group-delay curve. The discrepancy in the gradients indicates a difference in the second order GVD.

The λ_0 of the fibre is therefore very sensitive to the thermal history of the glass, and to the core radius. Different Sellmeier expansions published[51-53] for ostensibly similar glasses gave different values of λ_0 from those above, and it must be concluded that only direct experimental measurements can be trusted.

This technique for measuring GVD could be improved. Dispersive elements in the cavities other than the fibre were neglected, since their combined dispersion was expected to be much less than that of the long fibre. Higher accuracy could have been achieved by using the Michelson arrangement, with the cryostat and the quartz tuning plate common to both cavities, and where an identical pair of coupling lenses could have been inserted into the linear arm.

3.7.4 Discussion

It is now recognised that self-phase modulation in the optical fibre is the principal mechanism involved in the mode locking. Many of the effects observed in these lasers can be explained by reference to the time-domain models,[54-56] and in particular, the amplitude phasor diagram discussed by Mark et al[57], illustrated in Figure 3.30. The horizontal arm represents the phasor of the wave recirculating within the master cavity (or in returning from the linear branch), while the circle represents the locus of the phasor of the wave returning from the control-cavity (or nonlinear branch). By adding the two phasors, the amplitude and phase of the wave returning towards the gain medium may be calculated. It can be clearly shown that the control cavity modifies the reflectivity of the end mirror of the master cavity.

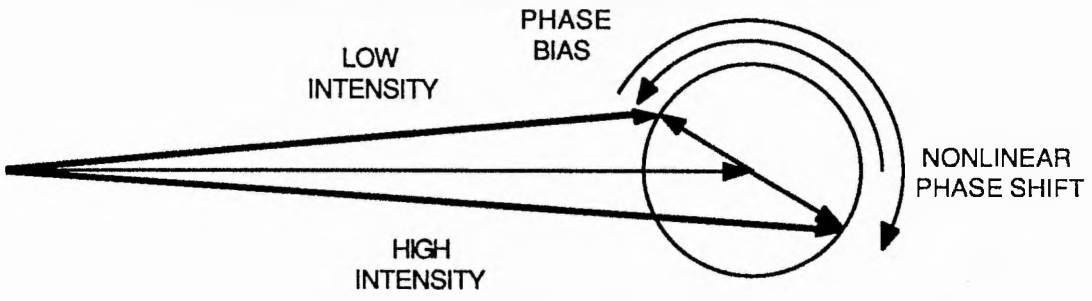

Figure 3.30 Phasor diagram representing the addition of the wave from the nonlinear branch to the wave from the linear branch.

Using this picture, the combined effect of the initial phase bias ϕ_i plus an additional intensity dependent phase shift caused by the fibre ϕ_{nl} can be visualised. Pulse shortening

can be obtained when the resultant phasor for the low intensities is shorter that the phasor for high intensities (see diagram). If the nonlinear phase shift exceeds π radians, the resultant goes "round the top" and starts to shorten, reducing the pulse shortening effect. In practice, nonlinear phase shifts upto $3\pi/2$ radians were often attained before instabilities such as pedestals were observed. It is clear that if the intensity dependent phase shift exceeds 2π radians there will be two maxima in the effective reflectivity before and after the peak of the pulse. This may explain observations of multiple pulsing. These pulses may evolve from a single pulse which splits ad infinitum until a steady state is reached, where the average power in the fibre determines the number of pulses supported.

For phase shifts exceeding around $\pi/2$ radians, some phase modulation will be transferred into the main cavity pulse as well as the amplitude modulation. By studying Figure 3.30, this phase modulation will have a form similar to the SPM in the fibre, but will be have peak value much less than a radian, although it may accumulate over many round trips. In practice, bandwidth limitation or anomalous GVD in the master cavity will curtail this effect.

The rôle of fibre GVD in coupled-cavity lasers requires to be clarified. Although coupled-cavity mode locking works for either sign of GVD, the magnitude of the GVD will influence the steady-state pulse duration, particularly with near-infrared colour-centre lasers which have broad gain bandwidths and where the master cavity GVD is small. In the initial stages of mode locking, when the pulse is perhaps many hundreds of picoseconds in duration, there will be insignificant temporal distortion of the pulse in the fibre due to dispersion. However, as the pulse becomes shorter, GVD will have an increasingly important effect. For anomalous GVD fibre, the temporally compressed pulses cannot interfere effectively with (and therefore exert any influence over) the leading and trailing edges of the master cavity pulse. As discussed earlier, the chirp of the feedback pulse will, in any case, be reduced as the $N = 2$ soliton condition is approached. With normally dispersive fibre, the pulse will broaden temporally and tend to flatten. The rate of change of the nonlinear phase over the central portion of the pulse, the part which interferes with the master cavity pulse, will tend to decrease and slow the rate of pulse shortening. Therefore to produce the shortest pulses, low GVD is required as in any other mode-locked laser.

For anomalous GVD, the pulse duration will be proportional to the square root of GVD (L fixed), if we accept the predictions based on the $N = 2$ soliton condition. Thus, the pulse is predicted to vanish in the limit as D approaches zero. Obviously, higher order effects such as third-order dispersion in the fibre and GVD and finite gain bandwidth in the main cavity prevent this. Logically, we might expect the pulse to reach a minimum duration at the zero GVD wavelength and then rise as the normal GVD regime is entered.

Yakymyshyn at al.[58] obtained the shortest pulses from their coupled-cavity NaCl:OH^- laser at the fibre λ_0 but they interpreted this as a filtering effect of the quartz birefringent tuning plate. This is seems unlikely because Zhu and Sibbett have shown that under conditions where the pulse duration is artificially limited by the birefringent plate, the minimum pulse duration decreases slightly with increasing wavelength.[59] In addition, Zhu has shown that the bandwidth $\Delta\lambda$ of a birefringent plate is proportional to the square of the wavelength.[60] In terms of frequency, the bandwidth can be shown to be constant. Therefore, no strong dependence of pulse duration with wavelength due to the birefringent plate should be expected, unless different orders are used.

The low GVD of the erbium-doped fibre is therefore consistent with its excellent sub-100 fs performance. It has another important advantage over modern dispersion-shifted fibres such as the Corning fibre. The design is similar to that of early dispersion-shifted fibres where waveguide dispersion is increased by using a small core combined with a large index difference. This results in a relatively high effective nonlinearity for the erbium-doped fibre. Assuming a mode field radius 1.1 times the geometrical radius, and a nonlinear index n_2 similar to fused silica (3.2×10^{-16} cm^2W^{-1}), gives a nonlinearity of $\gamma \approx 6.7$ $km^{-1}W^{-1}$. (The usual 5/6 factor has not been included since the polarisation will be maintained over the short lengths used here.) The effective nonlinearity for the Corning fibre, is considerably less because its waveguide dispersion is induced by a segmented core design which maintains the mode field radius at values similar to conventional fibres.[61] From experimental data (see chapter 4), $\gamma \approx$ 2-3 $km^{-1}W^{-1}$, which is consistent with the published mode-field radius.[61]

It should also be noted that the high germania content of the erbium-doped fibre might boost the n_2. The presence of germania in optical fibres is known to assist the optical Kerr rotation effect[62] and also improve the cross-section for Raman scattering.[63] Heavy metal

ions such as lead have been found to directly increase the n_2. For example, in silica glasses where the molecular percentage of PbO exceeds 50%, enhancements in n_2 of over 10 times have been observed.[64,65] However, it is unlikely that the erbium ions will increase the nonresonant n_2 by any significant amount since their molecular percentage amounts to only around 0.01%.

The resonant n_2 associated with the erbium transitions is over 10^5 times stronger that the nonresonant index of fused silica,[66] but its effect is negligible in the CW mode locked experiments here because it has a slow recovery time, around 10 ms, and it saturates at values of $\Delta n_{sat} \approx 10^{-6}$.[47] In the steady state, the maximum index change seen by the pulse will be equal to the index change Δn during the recovery phase. Assuming an 82 MHz pulse repetition frequency

$$\Delta n \approx \Delta n_{sat} (1 - \exp[-(12 \times 10^{-9}) / (10 \times 10^{-3})]) \approx 1.2 \times 10^{-12}. \quad (3.10)$$

The resultant phase shift for a path length of 40 cm is insignificant :

$$\Delta\phi = \frac{2\pi L}{\lambda} \Delta n \approx 2 \times 10^{-6} \text{ radians} \quad \text{QED.} \quad (3.11)$$

The high effective nonlinearity of the erbium-doped fibre assists because a relatively short fibre can be used, thereby minimising the pulse distortion due to GVD. For lasers operating at the zero-GVD wavelength, the effects of second-order GVD would also be minimised by using a shorter length of the small core fibre. A full understanding of the possible influence of secondary effects in the propagation of the sub-100 fs pulses in the erbium-doped fibre, such as second-order GVD, self-Raman effect and self-steepening, is not possible without modelling the propagation of the pulse using the split-step Fourier method. The pulse returning from the fibre is certainly severely distorted (Figure 3.23(b)). Given that the pulses propagate close to the zero-GVD wavelength, it is conceivable that the second-order GVD plays some rôle, and if the GVD due to the erbium transition is as large as implied by Desurvire's data[47] then it too will be important.

3.8 Summary

Pulses as short as 6 ps were obtained using synchronous mode locking and durations of approximately 20 ps with acousto-optic loss mode locking. Coupled-cavity mode locking using a Michelson arrangement has been shown to be preferable to the conventional Fabry-Perot arrangement, with pulse durations of less than 100 fs obtained by using erbium-doped fibre in the control cavity/branch. Self-starting has been observed when using a symmetrical master cavity, but not with completely stable steady-state operation. The average power required for self-starting exceeded that for stable operation once mode locking was established. The coupled-cavity laser has been used to measure the GVD of relatively short lengths of optical fibres. In this application, the Michelson scheme would be preferable, since it would allow the gain medium and tuning element to be common to both interfering cavities, thus improving accuracy.

3.9 References

1. L. F. Mollenauer, R. H. Stolen, and J. P. Gordon, Phys. Rev. Lett. **45**, 1095 (1980).
2. L. F. Mollenauer, N. D. Vieira, and L. Szeto, Opt. Lett. **7**, 414 (1982).
3. L. F. Mollenauer and R. H. Stolen, Opt. Lett. **9**, 13 (1984).
4. W. Gellermann, F. Lüty, and C. R. Pollock, Opt. Commun. **39**, 391 (1981).
5. E. Goovaerts, J. Andriessen, S. V. Nistor, and D. Schoemaker, Phys. Rev. B **24**, 29 (1981).
6. L. F. Mollenauer, N. D. Vieira, and L. Szeto, Phys. Rev. B **27**, 5332 (1983).
7. L. M. Osterink and J. D. Foster, Appl. Phys. Lett. **12**, 128 (1968).
8. W. Koechner, Appl. Opt. **9**, 2548 (1970).
9. V. Magni, Appl. Opt. **25**, 107 (1986).
10. S. De Silvestri, P. Laporta, and V. Magni, IEEE J. Quantum Electron. **QE-23**, 1999 (1987).
11. Nd:YAG rod specification provided by Robert Schricker, Lee Laser Inc., 3718 Vineland Road, Orlando, FL 32811, USA.
12. W. Koechner, *Solid-State Laser Engineering* (2nd edition) (Springer-Verlag, Berlin, 1988).
13. J. F. Nester, IEEE J. Quantum Electron. **QE-6**, 97 (1970).
14. W. Koechner and D. K. Rice, IEEE J. Quantum Electron. **QE-6**, 557 (1970).
15. Mirror specifications provided by Joe Mastromarino, Spectra-Physics GmbH, Siemensstrasse 20, Darmstadt-Kranichstein, W-6100, Germany.
16. H. Klann, J. Kuhl, and D. von der Linde, Opt. Commun. **38**, 390 (1981).
17. P. Kean, K. Smith, and W. Sibbett, Opt. Commun. **61**, 129 (1987).
18. Z. A. Yasa, Opt. Lett. **8**, 277 (1983).
19. S. Kelly, G. H. C. New, and D. Wood, Appl. Phys. B **47**, 349 (1988).
20. J. P. Heritage and E. D. Isaacs, in *Digest of Conference on Lasers and Electro-Optics* (Optical Society of America, Washington, D.C., 1981), paper WL3.
21. P. G. May, W. Sibbett, and J. R. Taylor, Appl. Phys. B **26**, 179 (1981).
22. N. Langford, K. Smith, and W. Sibbett, Opt. Lett. **12**, 817 (1987).
23. J. F. Pinto, C. P. Yakymyshyn, and C. R. Pollock, Opt. Lett. **13**, 383 (1988).
24. A. Yariv, *Quantum Electronics* (3rd edition) (John Wiley, New York, 1989).
25. F. Ouellette and M. Piché, Opt. Commun. **60**, 99 (1986).
26. M. Morin and M. Piché, Opt. Lett. **14**, 1119 (1989).
27. L. F. Mollenauer and R. H. Stolen, Opt. Lett. **9**, 13 (1984).
28. K. J. Blow and B. P. Nelson, Opt. Lett. **13**, 1026 (1988).
29. P. N. Kean, X. Zhu, D. W. Crust, R. S. Grant, N. Langford, and W. Sibbett, Opt. Lett. **14**, 39 (1989).
30. F. M. Mitschke and L. F. Mollenauer, Opt. Lett. **12**, 407 (1987).
31. P. N. Kean, PhD Thesis (University of St. Andrews, 1989).
32. F. M. Mitschke and L. F. Mollenauer, IEEE J. Quantum Electron. **QE-22**, 2242 (1986).
33. R. H. Stolen, W. Pleibel, and J. R. Simpson, IEEE J. Lightwave Technol. **LT-2**, 639 (1984). Sample of fibre provided by L. F. Mollenauer, AT&T Bell Labs., Holmdel, NJ 07733, USA.
34. X. Zhu, P. N. Kean, and W. Sibbett, IEEE J. Quantum Electron. **25**, 2445 (1989).

35. L. F. Mollenauer and R. H. Stolen, in *Ultrafast Phenomena IV* (Springer-Verlag, Berlin, 1984), pp. 2-6.
36. X. Zhu, P. N. Kean, and W. Sibbett, Opt. Lett. **14**, 1192 (1989).
Samples of fibre provided by K. C. Byron of STC Technology, Harlow, Essex.
37. R. J. Mears, L. Reekie, I. M. Jauncey, and D. N. Payne, Electron. Lett. **23**, 1026 (1987).
38. B. Tatian, Appl. Opt. **23**, 4477 (1984).
39. J. R. M. Barr and D. W. Hughes, Appl. Phys. B **49**, 323 (1989).
40. J. Goodberlet, J. Jacobson, J. G. Fujimoto, P. A. Schulz, and T. Y. Fan, Opt. Lett. **15**, 504 (1990).
41. J. Goodberlet, J. Wang, J. G. Fujimoto, and P. A. Schulz, Opt. Lett. **14**, 1125 (1989).
42. N. D. Vieira and L. F. Mollenauer, IEEE J. Quantum Electron. **QE-21**, 195 (1985).
43. Fibre provided by R. A. Baker of STC Technology, Harlow, Essex.
44. G. Sucha, Opt. Lett. **16**, 922 (1991).
45. E. P. Ippen, L. Y. Liu, and H. A. Haus, Opt. Lett. **15**, 183 (1990).
46. X. Zhu and W. Sibbett, Opt. Commun. **76**, 340 (1990).
47. E. Desurvire, J. Lightwave Technol. **8**, 1517 (1990).
48. C. T. Chang, Appl. Opt. **18**, 2516 (1979).
49. M. J. Adams, *An Introduction to Optical Waveguides* (John Wiley, Chichester, 1981).
50. D. Davidson, "Single-Mode Wave Propagation in Cylindrical Optical Waveguides" (chapter 3), in *Optical Fiber Transmission*, E. E. Basch, ed. (Howard Sams, Indianapolis, 1987).
51. J. W. Fleming, Electron. Lett. **14**, 326 (1978).
52. J. W. Fleming, Appl. Opt. **23**, 4486 (1984).
53. H. R. D. Sunak and S. P. Bastien, IEEE Photon. Technol. Lett. **1**, 142 (1989).
54. J. Mark, L. Y. Liu, K. L. Hall, H. A. Haus, and E. P. Ippen, Opt. Lett. **14**, 48 (1989).
55. E. P. Ippen, H. A. Haus, and L. Y. Liu, J. Opt. Soc. Am. B **6**, 1736 (1989).
56. M. Morin and M. Piché, Opt. Lett. **14**, 1119 (1989).
57. J. Mark, L. Y. Liu, K. L. Hall, H. A. Haus, and E. P. Ippen, in *Digest of Colloquium on Applications of Ultrashort Pulses for Optoelectronics* (IEE, London, 1989), paper 10.
58. C. P. Yakymyshyn, J. F. Pinto, and C. R. Pollock, Opt. Lett. **14**, 621 (1989).
59. X. Zhu and W. Sibbett, J. Opt. Soc. Am. B **7**, 2187 (1990).
60. X. Zhu, *Report on the Study of Birefringent Plates* (1st year report) (University of St. Andrews, 1988).
61. V. A. Bhagavatula, M. S. Spotz, and W. F. Love, Opt. Lett. **9**, 186 (1984).
62. K. C. Byron, Electron Lett. **23**, 1324 (1987).
63. A. S. Davison and I. H. White, Electron. Lett. **23**, 1343 (1987).
64. I. Thomazeau, J. Etchepare, G. Grillon, and A. Migus, Opt. Lett. **10**, 223 (1985).
65. D. W. Hall, M. A. Newhouse, N. F. Borrelli, W. H. Dumbaugh, and D. L. Weidman, Appl. Phys. Lett. **54**, 1293 (1989).
66. R. A. Betts, T. Tjugiarto, Y. L. Xue, and P. L. Chu, IEEE J. Quantum Electron. **27**, 908 (1991).

4 Nonlinear pulse propagation in an InGaAsP optical amplifier

4.1 Introduction

The development of semiconductor diode lasers for optical telecommunications has included laser chips optimised specifically for signal amplification. These semiconductor optical amplifiers[1-3] have been fabricated for either the 800-900 nm spectral region using GaAs / AlGaAs, or the 1200-1600 nm band using InGaAsP / InP.

Semiconductor lasers usually rely on the Fresnel reflectivity (≈ 30%) of the cleaved facets to achieve oscillation. This implies a single pass gain at threshold of around 3.3, or approximately +5 dB. When biassed below threshold, this basic laser may be used as a Fabry-Perot (FP) amplifier, with gains as large as 25 dB or more due to multiple passes of the chip. This large gain can only be obtained within narrow pass bands at the axial mode resonances, the spectral positions of which are highly sensitive to temperature and current fluctuations. These effects can be circumvented by depositing antireflection coatings on the facets such that the signal makes only a single pass thereby eliminating the resonances. These travelling-wave (TW) amplifiers require higher currents (and therefore higher carrier densities) than their FP counterparts to achieve a similar gain, but have 3 dB gain bandwidths of around 50 nm. In practice, perfect antireflection coatings with broad bandwidths are difficult to achieve and a modulation of a few dB is usually observed across the gain spectrum (known as gain ripple), and the performance is then classified as near-travelling wave (NTW).

In parallel with the development of semiconductor lasers and amplifiers, there have been numerous studies of their absorptive and refractive $\chi^{(3)}$-related nonlinearities. These nonlinearities involving real states can be subdivided into slow (~ 1 ns) effects related to

interband transitions, and fast (~ 1 ps) effects related to intraband relaxation. Many experiments and theoretical studies have been undertaken, and these have permitted a deeper understanding of the underlying physical mechanisms involved.

The KCl:Tl laser described in chapter 3 was utilised in an investigation of both the absorptive and refractive nonlinearities of a 1.5 μm InGaAsP optical amplifier. In the following section some relevant theory is introduced, and in particular, a model for describing the amplification of optical pulses in travelling-wave semiconductor amplifiers is discussed.[4,5] The characterisation of the linear and nonlinear properties of the amplifier provides a background for the following chapter, in which its use as the control-cavity nonlinearity in the coupled-cavity KCl:Tl laser is described.

4.2 Theory

In semiconductors which have a direct bandgap, such as GaAs, electron-hole pairs have a high probability of recombining radiatively. Populations of electron-hole pairs may be created optically by the absorption of photons whose energy exceeds the bandgap energy. More conveniently, large nonthermal populations can be created in the depletion region of a forward biassed p-n junction. This simple scheme forms the basis for light emitting diodes and diode lasers[6-9].

Early GaAs lasers used this basic p-n junction, or homostructure, which provided neither carrier confinement nor optical waveguiding, resulting in high threshold current densities. The room temperature threshold current density was reduced by a factor of approximately 50 (to around 1 kA cm^{-2}) with the development of the double heterostructure. This consists of a thin, lightly doped (p-doping) GaAs active region sandwiched between n-doped and p-doped AlGaAs, shown schematically in Figure 4.1. The AlGaAs has a larger bandgap and a lower refractive index than the GaAs active region. The bandgap structure results in potential well which localises the carrier population, and the refractive index differences constitute a slab waveguide with the active region as the core.

With electrical pumping, electrons occupy the conduction band and the hole population in the valence band has a corresponding increase. The electron and hole populations can be characterised by quasi-Fermi energy levels lying in the conduction and

valence bands respectively. As the pumping is increased, these quasi-Fermi levels move away from the bandgap region. A population inversion can be achieved at relatively modest carrier density levels, approximately 1.5×10^{18} cm^{-3} electrons (or holes) in InGaAsP lasers. The gain peak shifts progressively to shorter wavelength as the band occupancies increase, until oscillation is obtained, clamping the carrier density.

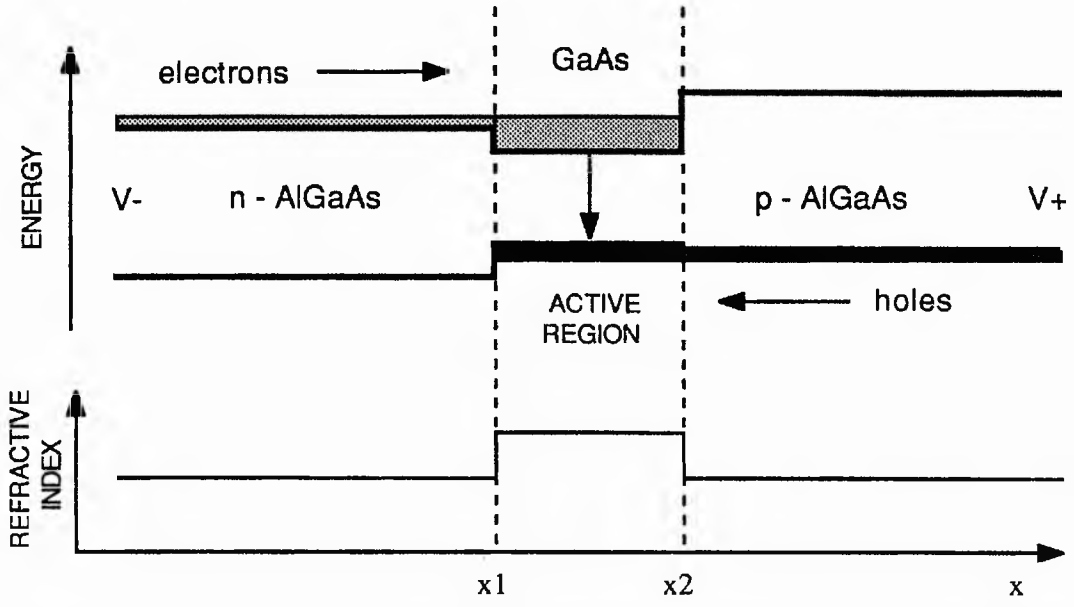

Figure 4.1 Schematic representation of the energy band structure (upper sketch) and the refractive index (lower sketch) across the junction of a strongly forward-biassed double-heterostructure GaAs/AlGaAs laser (adapted from references **6**, **7**).

To prevent the device oscillating in several filaments in the plane of the junction, the carriers can be confined laterally to a narrow region by using a stripe contact. Generally, to achieve fundamental transverse mode operation, optical waveguiding in the lateral plane of the junction is required. This may be achieved by using a weak guiding technique such as the ridge guide, or by strong index guiding where the active region is surrounded on all four sides by composition with a lower index, resulting in a so-called buried heterostructure.

Before deriving the theory to model the spectral and temporal distortion of pulses caused by gain saturation, some important concepts will be introduced. For many calculations it is useful to know the proportion of optical power in the fundamental transverse mode which overlaps with the active region. Fortunately, this can be easily estimated for strongly guiding structures. The width of the active region is usually greater than one or two

wavelengths, hence the optical confinement (or filling factor) in this dimension approaches 100%. The thickness of the active region is typically 100-200 nm, and so confinement in this direction may be only 50% or so, with a good fraction of the mode propagating in the surrounding cladding. The confinement factor Γ is defined by

$$\Gamma = \frac{\int_{x1}^{x2} I \, dx}{\int_{-\infty}^{+\infty} I \, dx} \tag{4.1}$$

where I is the intensity, and x1 and x2 define the active region as shown in Figure 4.1. In other words, Γ represents the fraction of optical power propagating within the active region. For strongly guiding structures fabricated in the InGaAsP / InP system, the confinement factor for the fundamental transverse (TE) mode is approximated by[10]

$$\Gamma = 22\, d^2 / (1 + 22\, d^2) \tag{4.2}$$

where d is the thickness of the active region, (x2 - x1), in microns.

The spontaneous recombination of carriers within the active region occurs through various mechanisms, each with its own dependence on the carrier density. These mechanisms are represented in the following expression for the recombination rate

$$R = AN + BN^2 + CN^3 \tag{4.3}$$

where the constants A, B and C account for nonradiative recombination, radiative recombination and Auger (nonradiative) recombination respectively and N represents the charge carrier density (ie. the electron density). It follows that the carrier lifetime τ_c is given by

$$\tau_c = N/R \tag{4.4}.$$

Typical values for A, B and C are listed in Table 4.1. Nonradiative recombination occurs at impurities or defects, and on interfaces or surfaces, and is the dominant effect at low carrier

densities ($\approx 10^{17}$ cm^{-3}), whilst Auger recombination, which is particularly significant in long wavelength InGaAsP, dominates at high carrier densities ($> 3 \times 10^{18}$ cm^{-3}).

Process	Symbol	Value	Reference
Monomolecular	A	1×10^{8} s^{-1}	9
Bimolecular	B	1×10^{-10} cm^{3}s^{-1}	9
Auger	C	4×10^{-29} cm^{6}s^{-1}	1

Table 4.1 Recombination constants for 1.5 μm InGaAsP.

The expressions required for the modelling of the amplifier will now be derived. On timescales longer than the intraband relaxation (ie. > 1 ps), the gain is homogeneously broadened and the carrier dynamics in the active region (neglecting diffusion effects) can be described using the differential equation[4]

$$\frac{\partial N}{\partial t} = \frac{I}{qV} - R(N) - \frac{a(N - N_t)\, c\, \varepsilon_o\, E_{rms}}{h\upsilon} \tag{4.5}$$

where I is the current through the active region, volume V, and $q = 1.602 \times 10^{-19}$ C. The final term accounts for stimulated emission, and $h\upsilon$ is the photon energy. The intensity is represented by $c\varepsilon_o E_{rms}$, where E_{rms} is the rms electric field. The term $a(N - N_t)$ gives the gain in the active region, where a is the differential gain constant (two times the usual emission cross-section σ_{em}), typically $2\text{-}3 \times 10^{-16}$ cm^2, and N_t denotes the carrier density for transparency, where stimulated emission is balanced by stimulated absorption. The carrier density is averaged over the active region, and diffusion across or along the guide is neglected.

At the steady state with no input signal, the carriers introduced into the active region by the current I are balanced by recombination R

$$R = I/qV \tag{4.6}.$$

If current leakage is assumed to be zero (a good approximation at low and moderate current levels), then I represents the amplifier drive current. Equations (4.3) and (4.6) enable the drive current I to be calculated for given values of carrier density N.

The characteristic 1/e recovery time of the gain is not the carrier (or spontaneous) lifetime τ_c as in most other laser media, since the recombination rate is a function of the carrier density, as shown in equation (4.3). Eisenstein et al.[11] have derived a simple expression for the recovery time τ_{rec} by replacing the right hand side of equation (4.3) with a Taylor expansion around a steady state carrier density N_g. If the level of saturation is modest, only the first two terms of the expansion are required, thus

$$R = R(N_g) + (N-N_g)\frac{dR(N_g)}{dN} \tag{4.7}.$$

The recovery of the carrier density after a short pulse has induced stimulated emission can be described by substituting equation (4.7) into (4.5) and neglecting the stimulated emission term:

$$\frac{dN}{dt} = \frac{I}{qV} - R(N_g) + N_g\frac{dR(N_g)}{dN} - N\frac{dR(N_g)}{dN} \tag{4.8}.$$

This can now be solved for $N(t)$

$$N(t) = C_1 \exp\left(- \frac{dR(N_g)}{dN} t \right) + C_2 \tag{4.9}$$

where C_1 and C_2 are constants. Thus, for fluctuations in carrier density around the steady-state carrier density N_g, the characteristic recovery time is given by

$$\tau_{rec} = \left(\frac{dR(N_g)}{dN}\right)^{-1} \tag{4.10}.$$

In amplifiers where the antireflection coatings are of a quality sufficient to prevent oscillation at single pass gains of approaching 30 dB, the carrier density can reach 5×10^{18} cm^{-3}, giving recovery times of less than 300 ps. It has also been pointed out that some structures may have even faster recoveries due to diffusion from carrier storage reservoirs.[11]

To simplify the modelling of the amplifier, the recombination term $R(N)$ will be replaced by N/τ_{rec} This approximation is not significant for this work, where the pulse durations are much shorter than the recovery time. The intensity I within the active region is given by

$$I \approx \Gamma P/A \tag{4.11}$$

where P is the power in the mode and A is the cross-sectional area of the active region. Equation (4.5) can now be replaced by

$$\frac{\partial N}{\partial t} = \frac{I}{qV} - \frac{N}{\tau_{rec}} - \frac{\Gamma a(N - N_t)P}{h\upsilon A} \tag{4.12}.$$

Since $I/qV = N_0/\tau_{rec}$ where N_0 is the steady-state carrier density associated with the drive current I, (4.12) can be rewritten as

$$\frac{\partial N}{\partial t} = \frac{N_0 - N}{\tau_{rec}} - \frac{\Gamma a(N - N_t)P}{h\upsilon A} \tag{4.13}.$$

The gain $g(N)$ in the optical mode is given by

$$g(N) = \Gamma a\,(N - N_t) \tag{4.14}.$$

N.B. g amplifies the optical power P such that

$$\frac{\partial P}{\partial z} = gP \tag{4.15}.$$

It follows that

$$\frac{\partial g}{\partial t} = \Gamma a \frac{dN}{dt}$$

$$= \frac{\Gamma a(N_0 - N)}{\tau_{rec}} - \frac{\Gamma agP}{h\upsilon A} \tag{4.16}.$$

The saturation energy E_{sat} is defined

$$E_{sat} = \frac{h\upsilon A}{\Gamma a} \tag{4.17},$$

and the small signal gain g_0 at the drive current is

$$g_0 = \Gamma a(N_0 - N_t) \tag{4.18},$$

hence, equation (4.16) can be rewritten as

$$\frac{\partial g}{\partial t} = \frac{g_0 - g}{\tau_{rec}} - \frac{gP}{E_{sat}} \tag{4.19}.$$

This equation still holds in the reference time frame of the pulse. The product gdz represents the gain for a short length dz of the amplifier guide. The exponential gain factor $h(t)$ for an amplifier of length L is defined

$$h(t) = \int_0^L g(z,t)\, dz \tag{4.20},$$

where

$$\exp[h(t)] = \frac{P_{out}(t)}{P_{in}(t)} \tag{4.21}.$$

Hence by integrating (4.19) over the length of the amplifier, and using equation (4.15), it can be shown that

$$\begin{aligned} \frac{dh(t)}{dt} &= \frac{g_0 L - h(t)}{\tau_{rec}} - \frac{P_{out}(t) - P_{in}(t)}{E_{sat}} \\ &= \frac{g_0 L - h(t)}{\tau_{rec}} - \frac{P_{in}(t)}{E_{sat}}(\exp[h(t)] - 1) \end{aligned} \tag{4.22}.$$

By integrating this equation over the time frame of the pulse, $h(t)$ can be determined, and hence $P_{out}(t)$.

The energy band structure in semiconductor lasers causes a shift of the peak gain to shorter wavelengths as the carrier density increases, and hence the differential gain peaks at a

shorter wavelength than the peak of the gain itself.[12] The asymmetry of the differential gain in the semiconductor laser means that the corresponding refractive index changes (calculated using the Kramers-Krönig relations) are much larger than for a simple atomic transition of a similar gain. The effect is treated by the introduction of the linewidth-enhancement factor α,[13] defined as[14]

$$\alpha = - \frac{d\,[Re\{\chi(N)\}]\,/dN}{d\,[Im\{\chi(N)\}]\,/dN} \qquad (4.23).$$

This concept can be understood more easily by using an equivalent expression[15] directly relating the change in refractive index dn with change in carrier density dN:

$$\frac{dn}{dN} = - \frac{\alpha\lambda a}{4\pi} \qquad (4.24).$$

Typically, α has a value of the around 4 or 5, although it can vary considerably over the gain bandwidth, increasing towards the long wavelength end of the profile.[15,16] This effect is responsible for the abnormally large linewidths of single mode semiconductor lasers, and the chirping in current modulated and gain switched lasers. It is also causes a strong index grating to be formed when light at two wavelengths are present, giving highly efficient nearly degenerate four-wave mixing.[17-19]

The changes in refractive index $\Delta n(t)$ which accompany the changes in carrier density will cause phase shifts $\Delta\phi(t)$ of the optical signal (see chapter 1).

$$\Delta\phi(t) = \frac{2\pi L}{\lambda} \Delta n(t) \qquad (4.25).$$

Using equation (4.24) the index change for one small section of the guide can be expressed as

$$\Delta n(t) = - \frac{\alpha\lambda a}{4\pi} \Gamma(N_0 - N(t)) \qquad (4.26)$$

where the confinement factor Γ has been included, since we now wish to determine the effective index change for the mode and not the active region alone. The total phase shift experienced by one position (time t) on the pulse is the integral of the index change along the length of the guide:

$$\Delta\phi(t) = \frac{2\pi}{\lambda}\int_0^L \Delta n(t)\, dz$$

$$= \frac{\alpha}{2}\int_0^L g(t)\, dz$$

$$= \frac{\alpha}{2} h(t) \qquad (4.27).$$

Therefore, the pulse becomes phase modulated as it saturates the gain of the amplifier. In the measurements of pulse distortion, the pulse duration was much shorter than the recovery time, and hence the resulting spectral broadening associated with this self-phase modulation (SPM) was asymmetric, as discussed in chapter 1.

A computer program was written in Pascal (listed in Appendix 3) to model the pulse shaping and the SPM associated with gain (and loss) saturation. The first section calculates the carrier densities at the small-signal gain level and at transparency using the Newton-Raphson method, and then estimates the differential gain coefficient. The characteristic recovery time is calculated using equation (4.10). The main section integrates equation (4.22) over 1000 points using the Runge-Kutta method, and determines the power and phase of the output pulse at 100 points over the pulse profile. Finally, the spectrum $S(\omega)$ of the output pulse at 100 points is calculated by the Fourier transform

$$S(\omega) = \left| \int_{-t}^{+t} [\, P_{out}(t)\,]^{1/2} \exp[\, i\phi_{out}(t) + i(\omega - \omega_0)t\,]\, dt \right|^2 \qquad (4.28)$$

where the integration has been performed using Simpson's rule.

Before leaving this discussion, it will be useful to introduce the effect known as 'nonlinear gain suppression' or simply 'nonlinear gain'. This phenomenon is responsible for

the anomalous damping of relaxation oscillations in response to electrical transients,[20,21] and restricts the modulation bandwidth of high-speed diode lasers.[22,23] It has been attributed to various mechanisms, but to spectral hole burning in particular.[20] Recent experiments with InGaAsP current modulated lasers indicate that the mechanism has a very fast recovery (70-100 fs), consistent with spectral hole burning.[24,25] However, direct time-domain measurements of transmission using pump-probe techniques show a different mechanism, with a recovery time of approximately 1 ps.[26] This latter effect has been attributed to heating of the carrier population, since it always decreases the transmission, even at sub-transparency drive current levels. These effects will be discussed in later subsections when pump-probe measurements of the amplifier will be described.

4.3 Amplifier characteristics

The amplifier used throughout this work was a 350 μm long, InGaAsP double-channel planar-buried heterostructure (DCPBH) with antireflection coatings on both facets, fabricated by STC Technology Ltd, Harlow, Essex. The active region has a cross-section of 1.5 x 0.17 μm^2, with a confinement factor of approximately 0.39, calculated using equation (4.2). The chip is understood to be similar to those developed by STC as high power lasers[27] and probably has a thin (≈ 0.1 μm) InGaAsP anti-meltback (AMB) layer on the p-side of the active region to prevent meltback of the active layer during the liquid phase epitaxial (LPE) growth of the cladding (see Figure 4.2). An AMB layer of this thickness has been shown to have only a minor effect on the confinement factor.[8]

The amplifier was mounted p-side down on a standard dual-facet (DF) mount to aid the conduction of heat away from the active region. In all the experiments, the amplifier was supplied by DC current from a constant current source (Coutant LM100/15), via a milliammeter monitor. The light output from the guide was collected using a diode collimating lens having a numerical aperture of 0.5 (Melles-Griot 06 GLC 002). To estimate the collection efficiency of the lens, the entire output was measured with a 5-mm-diameter photodiode positioned within 1 mm of the facet. By comparing this to the signal obtained with the lens collimating the beam onto the diode, the efficiency was found to be approximately 0.6 (-2 dB). For this measurement, the amplifier was operated well above

laser threshold to ensure that the directional stimulated emission from the guide would dominate any spontaneous emission. The DF mount did not permit the use of a second collimating lens for input coupling, and an antireflection coated 20x microscope objective with a longer working distance was used instead.

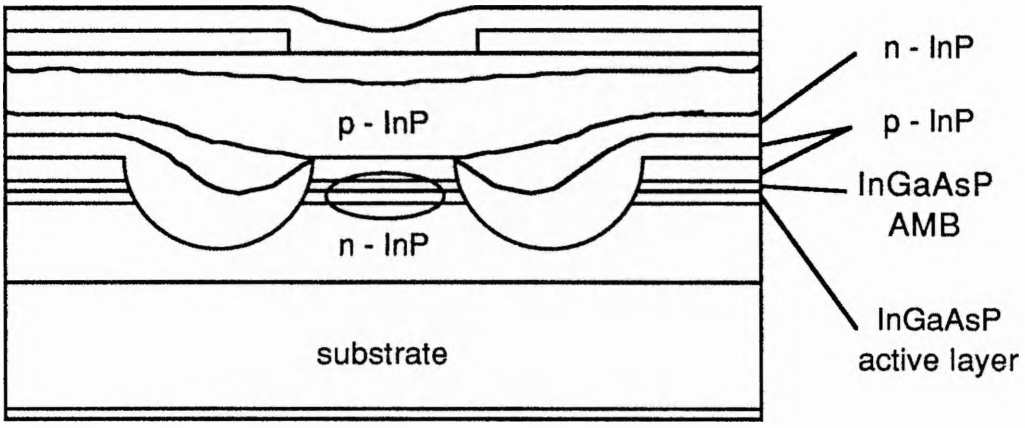

Figure 4.2 Cross-section of the STC high-power DCPBH laser. The optical mode is represented by the ellipse. (after reference **27**)

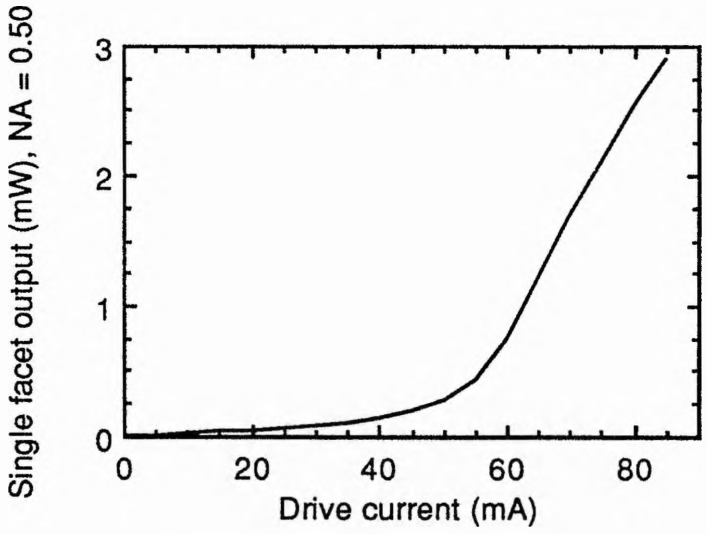

Figure 4.3 Light / current characteristic of the amplifier used here.

The light / current characteristic depicted in Figure 4.3, shows the oscillation threshold at approximately 55 mA. This laser emission was polarised in the plane of the junction (TE). The spectral characteristics of the emission in the current range 20-60 mA were studied using the 1 m scanning monochromator (see Figure 4.4). The output beam from the amplifier was chopped and the signal at monochromator exit slit was monitored by a

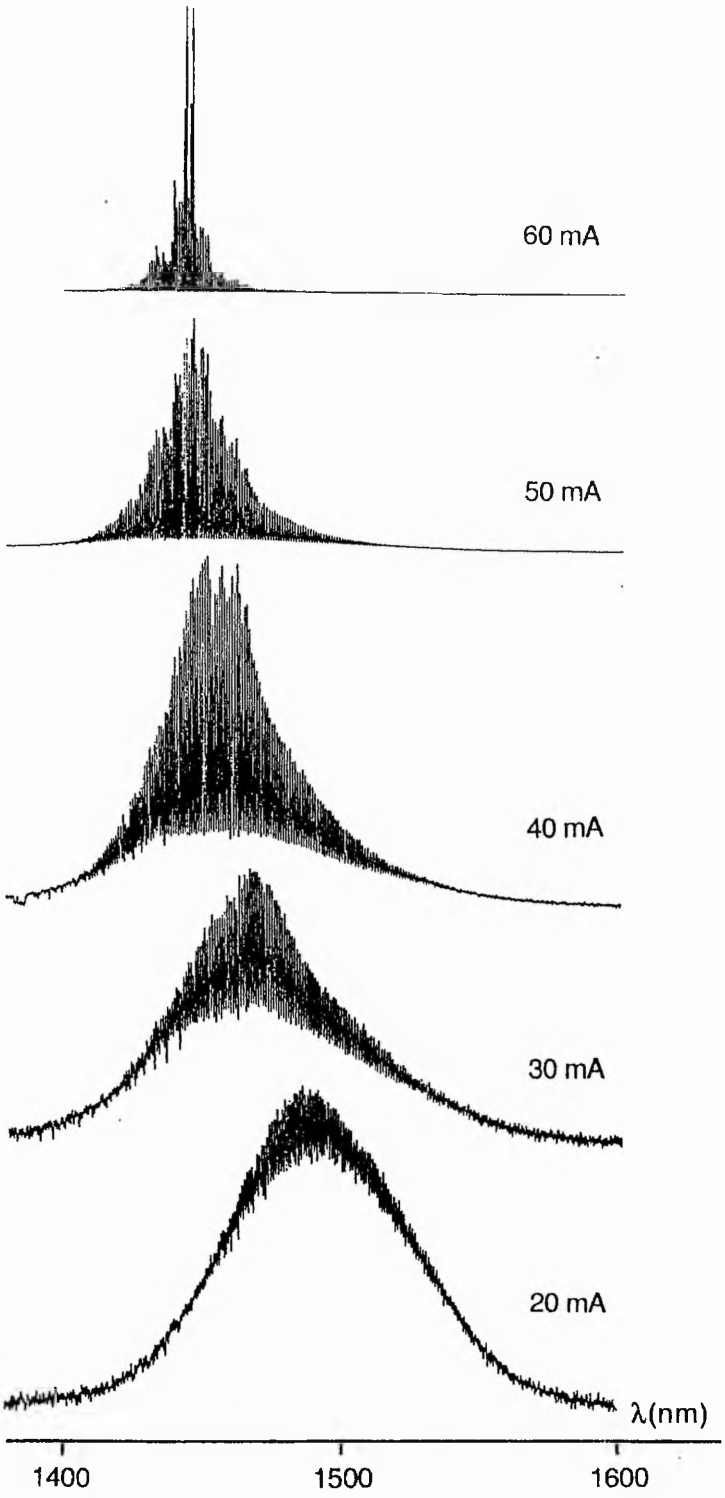

Figure 4.4 Spectral characteristics of the spontaneous emission from the amplifier guide at various current levels (with the detector gain adjusted to normalise the peak intensities).

germanium photodiode where lock-in detection was used to increase the signal-to-noise level. These spectra clearly show the axial mode structure, even at currents well below threshold. This deep modulation is caused by the multiple pass amplification of spontaneous emission, termed "regenerative amplification". No particular polarisation was selected in these measurements. A trace taken later for the TE component only at 40 mA was not significantly different from the equivalent scan presented here, although the peak appeared to be shifted by about 10 nm to longer wavelengths. As the drive current was increased towards threshold, the emission band became narrower and shifted to shorter wavelengths due to bandfilling. At 60 mA the device had reached threshold, and the peak emission wavelength became fixed at around 1460 nm, and for currents in excess of 80 mA (not shown), the emission was predominantly in a single longitudinal mode.

When light is coupled into the amplifier, it can create carriers through the absorption of photons, or can induce recombination of carriers through stimulated emission. At currents below transparency the creation of carriers will dominate, whilst at currents larger than transparency, the carrier density will suffer a net depletion. These changes in carrier density cause changes in the voltage across the junction. At a some current level, denoted the transparency current,[28] the carrier density is such that these two processes are in equilibrium and no change in voltage occurs when light is coupled into the device.

The transparency current of the amplifier was measured using this phenomenon. The input signal was chopped and a monitor signal from the milliammeter was fed to a chart recorder. This allowed the background current to be subtracted using the offset function. (N.B. a lock-in amplifier could also have been used.) The optoelectronic signal obtained for an input signal at 1500 nm is shown in Figure 4.5. This graph indicates a transparency current of approximately 6 mA. Using this technique, the transparency current was determined for a range of wavelengths, shown in Figure 4.6. As might be expected by considering the band structure model, the current level (or carrier density) must be increased to achieve transparency at the shorter wavelengths.

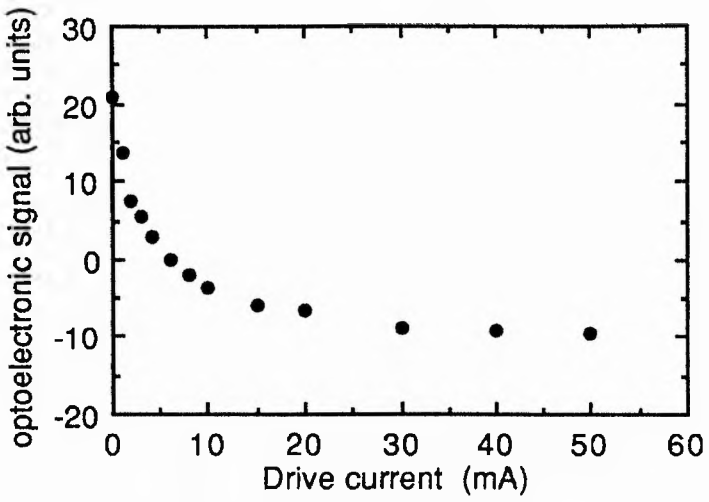

Figure 4.5 Variation of optoelectronic signal with amplifier drive current at 1500 nm wavelength.

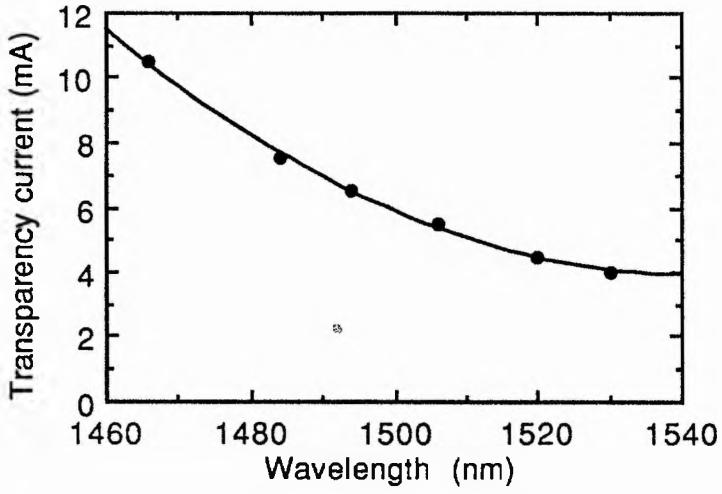

Figure 4.6 Variation of the transparency current with wavelength.

Unfortunately this method does not give the absolute value of transparency, since losses due to scattering do not influence the carrier density (or more precisely, changes in the junction voltage due to shifts of the Fermi-levels). The scattering loss could be as much as 10 cm^{-1}, equivalent to around -1.5 dB.[1] These losses can usually be neglected when modelling amplifiers at high gains. Knowledge of both the output collection efficiency and the transparency current allows one to estimate the input coupling efficiency, and hence the chip (or internal) gain. Typical coupling efficiencies of 0.12 (-9.2 dB) were measured by this method, increasing to around 0.15 (-8.2 dB) after a 3x beam expander was inserted before the input objective. Since the scattering losses cannot be easily measured, the values of gain

and loss described in the following sections do not incorporate a correction for scattering. Where appropriate, estimates will be made for the effect of scattering on the measurements.

The small-signal transmission for TE polarised CW light was measured for a range of drive currents at a fixed wavelength of 1500 nm, see Figure 4.7. All the power measurements were made with large area germanium photodiodes (Germanium Power Devices GM8). The signal was usually amplified using a simple op-amp circuit, but it was necessary to apply a voltage bias across the photodiode (using a 9 V battery) to obtain a linear response. When measuring the power transmitted by the device, care was taken to filter out the light which had not been coupled into the mode. This was achieved by using a simple spatial filter arrangement, where light exiting the guide was passed through an aperture placed around 2 m from the chip. The focussing and alignment of the amplifier exit lens was set after turning the current upto 80 mA and using the stimulated emission to simulate the transmitted signal.

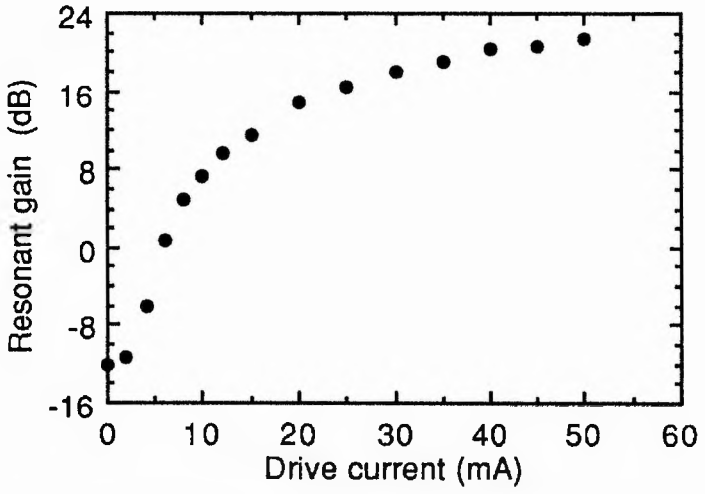

Figure 4.7 Small-signal gain at 1500 nm. Slight adjustment of the wavelength was made to obtain resonant enhancement at the high currents.

The saturation-like roll-off in the gain is caused partly by Auger recombination limiting the carrier density, and also by a shift in the peak gain to shorter wavelengths due to band filling. The effect of Auger recombination on the carrier density can be shown by using equation (4.6) to determine the carrier density as a function of drive current (see Figure 4.8). Clearly, the Auger recombination reduces the carrier density (and hence gain) for a given

drive current. The variation of both the carrier lifetime and the characteristic recovery time with drive current are shown in Figure 4.9 (calculated using equations (4.4) and (4.10)).

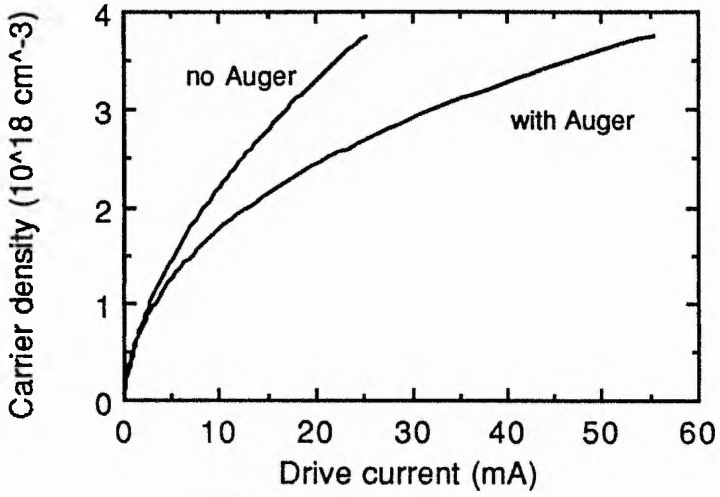

Figure 4.8 Effect of Auger recombination on carrier density.

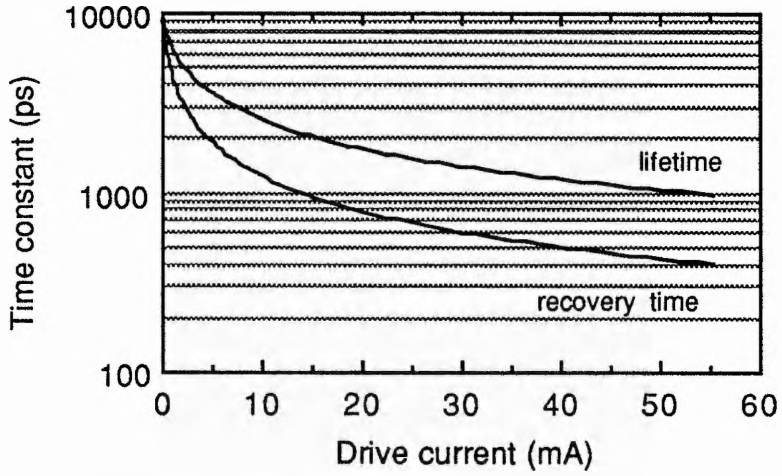

Figure 4.9 Calculated carrier lifetime and recovery time.

At currents of 20 mA and above, the resonant gain G_{max} was measured, together with the modulation or ripple in gain (G_{max} - G_{min}). These data, shown in Table 4.2, enable the internal gain G_{int} to be calculated with the equation [29]

$$G_{int} = \frac{G_{max} + G_{min}}{2} \frac{(1 - F^2)^2}{1 + F^2} \tag{4.29}$$

where

$$F = \frac{X^{1/2} - 1}{X^{1/2} + 1} , \qquad X = \frac{G_{max}}{G_{min}} \tag{4.30}.$$

The mean modal facet reflectivity is given by

$$(R_1 R_2)^{1/2} = F / G_{\text{int}} \qquad (4.31).$$

I (mA)	G_{max} (dB)	Ripple (dB)	G_{int} (dB)	Reflectivity
20	15.3	1.0	14.8	1.9×10^{-3}
30	18.5	1.8	17.6	1.8×10^{-3}
40	20.8	3.0	19.3	2.0×10^{-3}
50	21.8	3.9	19.8	2.1×10^{-3}

Table 4.2 TE gain ripple measurements at 1500 nm.

The data imply a mean reflectivity of approximately 0.2 %, and the device may be classified as near-travelling wave. At 40 mA, the TM gain was estimated to be only ~ 13 dB, although at lower currents the difference between TE and TM was not as marked. This polarisation sensitivity of the gain is related to the oblong cross-section of the active-region, resulting in different confinement factors for the fundamental TE and TM modes.

The small-signal resonant TE gain at a drive current of 40 mA was measured over range of wavelengths (see Figure 4.10). The peak gain is in the vicinity of 1480 nm, in close agreement with the peak of the spontaneous emission at this current level.

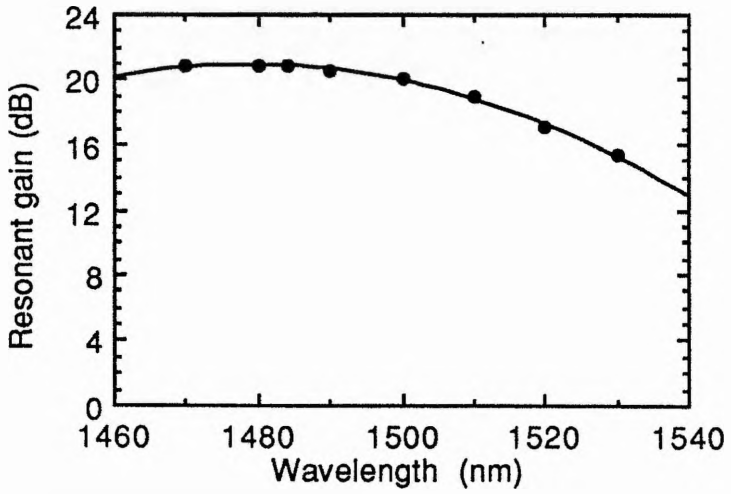

Figure 4.10 Small-signal gain at 40 mA drive current.

4.4 Nonlinear Transmission

As the optical power coupled into the guide is increased, the gain (or loss) will tend to decrease or saturate, resulting in nonlinear behaviour. Saturation occurs because of the finite number of carriers within the active region ($NV \approx 3 \times 10^8$ at 40 mA), and the non-zero recovery time.

4.4.1 Conventional transmission measurements

The transmission characteristics of the amplifier in the saturation regime were investigated using both CW light and mode-locked pulses of various durations. Pulses of around 30 ps duration were generated by synchronously mode locking the KCl:Tl laser, while 1 ps and 200 fs pulses were obtained using coupled-cavity mode locking. The interpulse spacing of 12 ns was sufficiently long to allow a complete recovery of carrier density before the following pulse. Figure 4.11 shows the transmission measurements for drive currents of 40 mA and 2 mA at around 1500 nm, where the small-signal internal gains are approximately +19 dB and -10 dB respectively. Input average power levels in the range -10 dBm* to +5 dBm were coupled into the guide, much greater than the levels encountered in an optical communications network, but were similar to those encountered when the device was used as the control-cavity nonlinearity (see chapters 5 and 6). Note that the 82 MHz pulse repetition frequency of the mode-locked laser corresponds to a pulse energy of approximately 12.2 pJ per 1 mW average power, ie. -10 dBm ≈ 1.2 pJ and +5 dBm ≈ 38 pJ.

At these power levels, saturation behaviour is clearly evident, i.e. a decrease in transmission for the gain regime and an increase in transmission in the absorption regime. The onset of saturable gain and saturable loss occurs at approximately similar power levels, consistent with broadly similar values of differential gain (gain cross-section) at these widely differing carrier densities. In terms of average power, the amplifier saturates more easily with pulses than for CW light, since the recovery time of the amplifier is much less than the pulse repetition period of the colour-centre laser. The amplifier would have performed more efficiently if the pulse repetition frequency had been around 1 GHz. At higher frequencies,

* Power expressed in decibels relative to 1 mW, where 1 mW has the value 0 dBm, ie. P(dBm) = 10 x $\log_{10}$[P(mW)/1 mW], eg. 0.1 mW = -10 dBm.

the saturation characteristic for 30 ps pulses and CW light would become similar (in terms of average power), since the saturation would be governed by the average power of the pulse train rather than pulse energy (see for example reference 30).

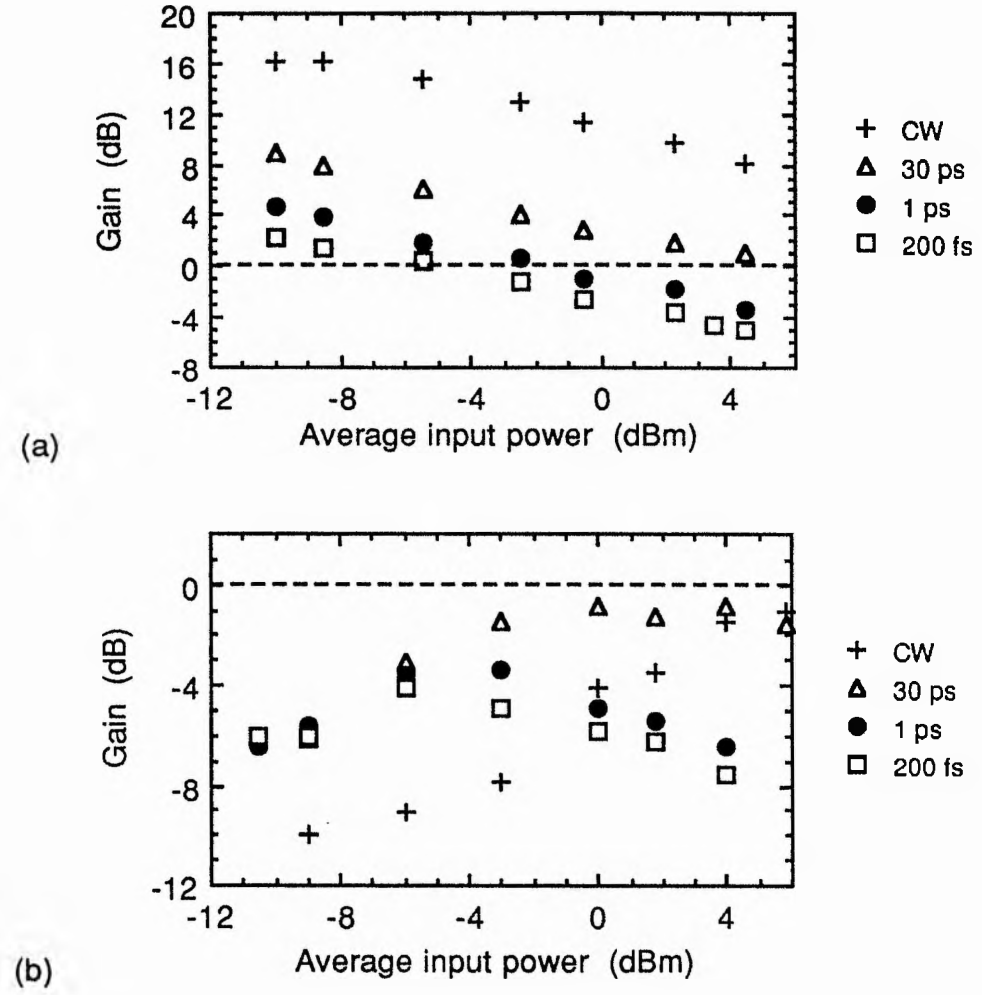

Figure 4.11 Transmission measurements at drive currents of (a) 40 mA and (b) 2 mA.

The behaviour of the transmission for the 1ps and 200 fs pulse durations is more complex. For example, in the gain regime the transmission for these shorter pulses is significantly less than for the 30 ps pulses. Note that the saturation gradients for all three pulse durations are similar. In the absorption regime, the transmission for the shorter pulses initially follows the 30 ps characteristics with saturation evident, but as the average power is increased above -3 dBm, the transmission decreases once more. All three pulse durations are much shorter than the characteristic recovery times, therefore we would expect that the saturation would be determined by the pulse energy alone.

These anomalous decreases in transmission for the very short pulse durations might be considered to be a manifestation of nonlinear gain suppression, but spectral hole burning cannot account for the effects observed here. Firstly, at 40 mA drive current, the gain turns into loss at high pulse energies, but spectral hole burning by definition, would not be expected to reduce the transmission below the transparency level. Secondly, in the loss regime, spectral hole burning would enhance the saturation effect and drive the transmission towards transparency at large pulse energies, contrary to the experimental results.

To clarify these results, further transmission measurements were made at the transparency current (≈ 6 mA). In this case, there is an equal probability of stimulated emission and stimulated absorption, and no change in transmission is expected. The measurements, shown in Figure 4.12, show an intensity dependent loss, consistent with the preceding observations in the gain and loss regimes.

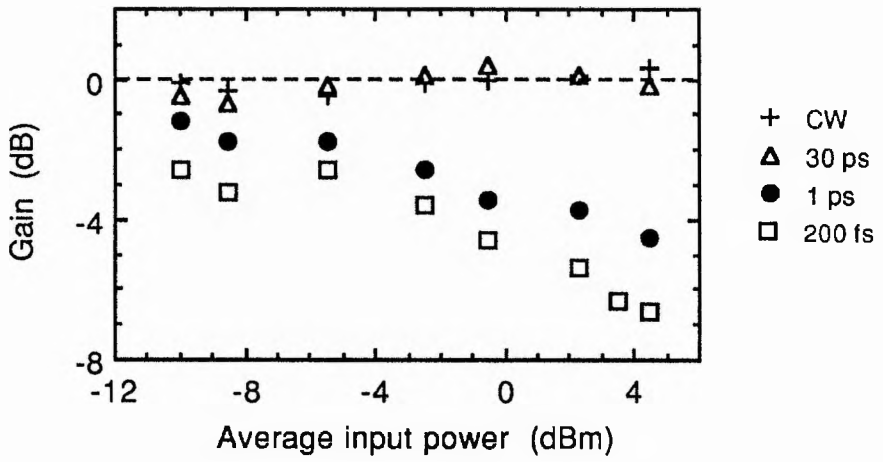

Figure 4.12 Transmission measurements at the transparency current.

After the completion of this work, it was found that gain measurements for an amplifier using a variety of pulse durations had been previously been reported (see references 31 and 32). In contrast to the observations presented here, no pulse duration dependence was apparent in the gain roll-off characteristics. This is probably due to the use of a fibre / grating compression system and solitonic compression to obtain picosecond and femtosecond pulses respectively. These techniques can only compress a fraction of the input pulse, giving rise to long pedestal features. More recently, Hall et al.[33] have reported a pulse duration dependence, and have treated it by saying that the saturation energy is reduced for the shorter

pulses. Although this is phenomenologically incorrect (because the very similar observations presented above at the high drive current show that the gain goes negative at high input powers), it is useful when describing modest degrees of saturation.

4.4.2 Time-resolved transmission measurements

Further information on the saturation characteristics and mechanisms may be elucidated by performing time-resolved transmission measurements. The recovery transient in gain following the saturation of an amplifier by a short pulse can be measured directly using a pump-probe type measurement, where a pulse which is sufficiently energetic to partially saturate the gain is followed into the device by a much weaker probe pulse. This probe pulse is polarised orthogonally to the pump pulse, so as to allow discrete detection after passage through the guide. By varying the time interval between the pump and probe pulses with an optical delay line, it is possible to perform time-resolved transmission measurements with a resolution determined by the pulse duration. The photodiode which detects the probe-pulse train only monitors the average power and does not resolve the individual pulses (in a manner similar to that of the photo-multiplier tube in the SHG autocorrelator described in chapter 1).

As mentioned earlier, pump-probe measurements of transmission on lasers and amplifiers have previously been reported. These have centred almost entirely on devices fabricated in the GaAs[34-36] material system, although some details of measurements on an InGaAsP amplifier were presented at a conference prior to the work undertaken here.[26] In those experiments the long transient associated with the recovery of the carrier density - interband relaxation - was ignored and only delays of less than 10 ps were considered. Ultrafast transients have been resolved and associated with the recovery of carriers within their respective bands, that is, intraband relaxation. Principally, they show a sharp decrease in transmission immediately following the pump pulse, followed by a recovery on a timescale of approximately 1 ps. This downward transient was observed for bias currents associated with gain, absorption, and even transparency, indicating that it is not related to spectral hole burning (SHB), which in any case, is expected to recover on an even faster timescale. Futhermore, the results were not consistent with an intensity-dependent absorption such as two-photon absorption (2PA), which would exhibit an instantaneous recovery. Instead the

observations have been attributed to an elevation of carrier temperature relative to the lattice temperature, called carrier heating.[37,38] In the situation here, the pulse duration is less than the characteristic carrier cooling time, and the term dynamic carrier heating (DCH) has been used to describe the effect.

The experimental arrangement is shown schematically in Figure 4.13. Pulses having durations around 90 fs were produced using the coupled-cavity KCl:Tl laser, configured in the nonlinear Michelson interferometer scheme described in the chapter 3. This configuration allowed drop-out free, stable operation for extended periods with amplitude stability better than 1%. A Faraday optical isolator (Optics For Research, Bismuth-Iron-Garnet film) was used to eliminate feedback into the laser. Measurements were made of the pulses transmitted by the isolator to confirm that it did not distort the 90 fs pulses (see chapter 5).

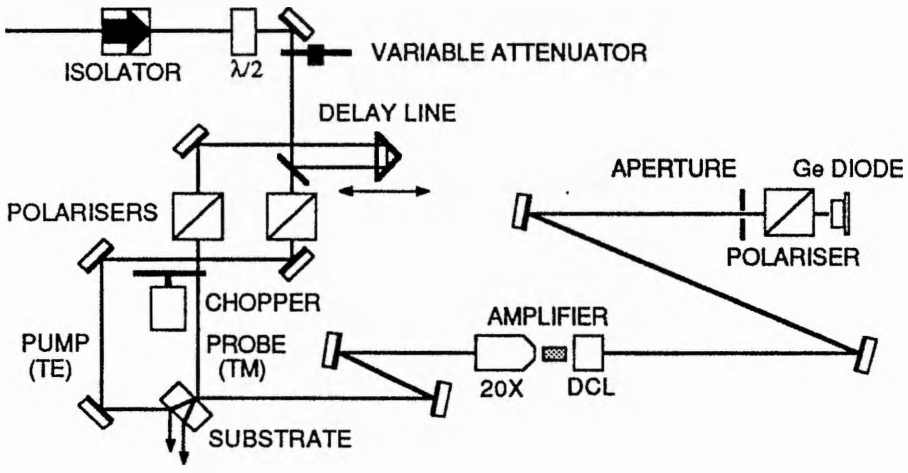

Figure 4.13 Schematic of the pump-probe experiment. DCL: diode collimating lens; λ/2: half-wave plate.

The pump and probe pulses were derived at a beamsplitter and then polarised in TE and TM orientations respectively by Glan-Taylor polarisers. (TM polarisation corresponds to the electric field vector perpendicular to the surface of the page.) The half-wave plate was used to adjust the power ratio between the pump and probe beams. Typically, this ratio was set to approximately 300:1, which ensured that the probe pulse did not saturate the device. The probe pulses were routed via a variable optical delay line which consisted of a hollow corner-cube reflector mounted on a motorised translation stage.

An analyser polariser was placed after the usual aperture to block the pump pulses. The probe pulse train, which was chopped, was detected by the large area germanium photodiode and then amplified with the usual op-amp circuit. The signal was then further amplified by a lock-in amplifier to reduce noise and eliminate any background. In the initial experiments, the pump-pulse energy coupled into the guide was restricted to low and moderate energies but sufficient to cause saturation effects.

Figure 4.14 depicts pump-probe scans made with modest pump pulse energies. The transparency regime will be described first. The downward carrier heating transient, with a recovery time of approximately 1 ps is clearly observed. At a drive current of 40 mA, corresponding to gain, a rapid downward transient is followed by a two-stage recovery to settle at a level lower than when the probe was ahead of the pump pulse. This is consistent with a net decrease in carriers, since after the intraband processes are complete, the transmission is determined by the carrier density. In other words, the pump pulse has removed some of the carriers by stimulated emission, thereby reducing the gain for the following probe pulse.

With the drive current reduced to 2 mA, the downward transient is again observed and since a net increase in carriers occurs due to saturable absorption, the transmission settles at a higher level. However, the most significant feature is the fast upward transient which precedes the dip caused by carrier heating. This feature has a symmetrical shape with a FWHM of around 180 fs, and might be associated with spectral hole burning. Indeed, SHB may be the cause of the initially rapid recovery in the downward transient observed at 40 mA, since in the gain regime, SHB causes a decrease in transmission and will add to the effects of carrier heating.

Measurements were also made for higher pump-pulse energies, around 6 pJ (see Figure 4.15). The fast transients were observed again but the carrier heating dip appeared to dominate the fast upward spike at 2 mA drive current. More significantly, for all drive currents the transmission increased following the completion of intraband relaxation. This shows that a net increase in carriers in the active region has taken place, presumably due to intensity-dependent absorption in the active region.

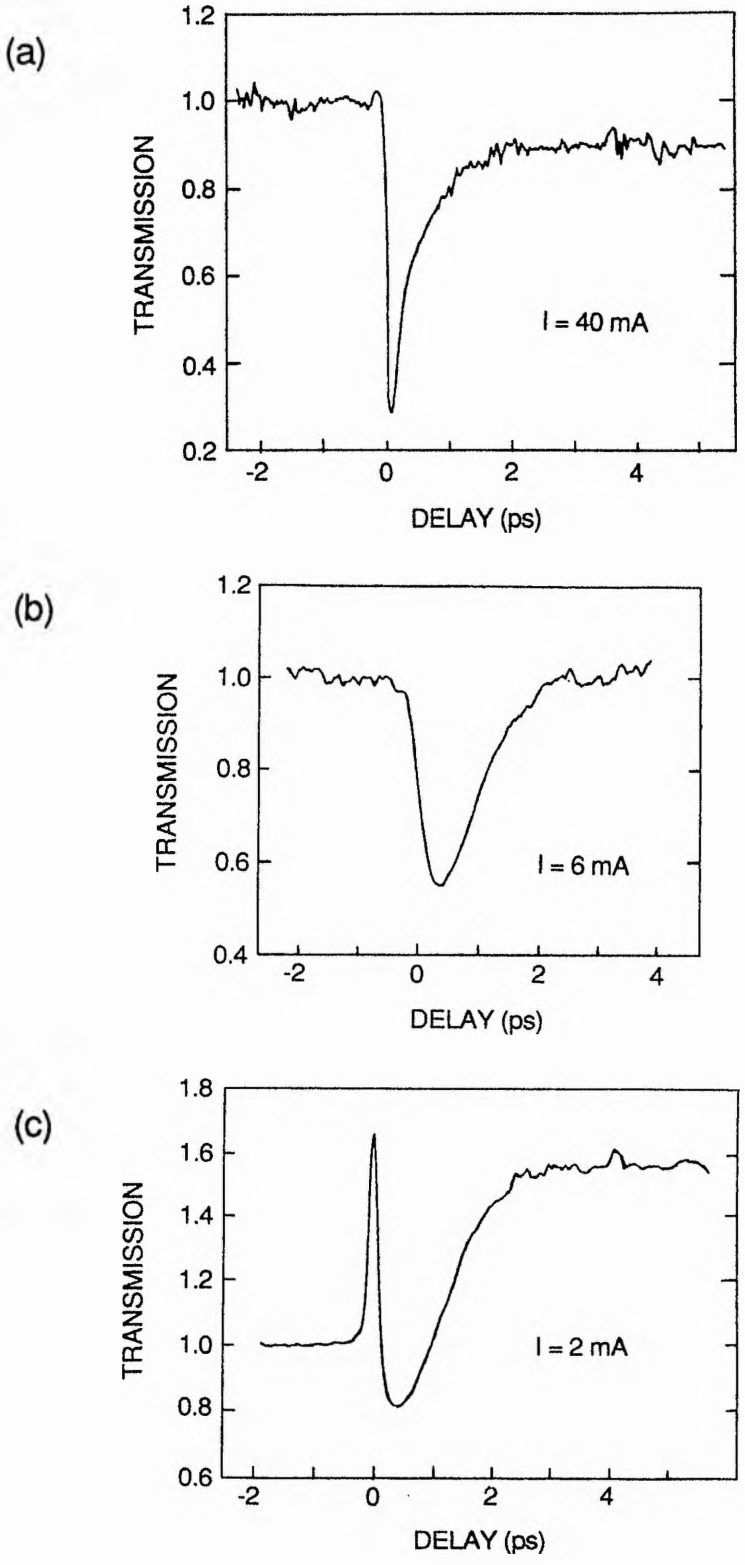

Figure 4.14 Time-resolved, (relative) transmission at modest pump pulse energies. (a) Gain, pump energy ≈ 40 fJ. (b) Transparency, pump energy ≈ 0.5 pJ. (c) Loss, pump energy ≈ 1 pJ.

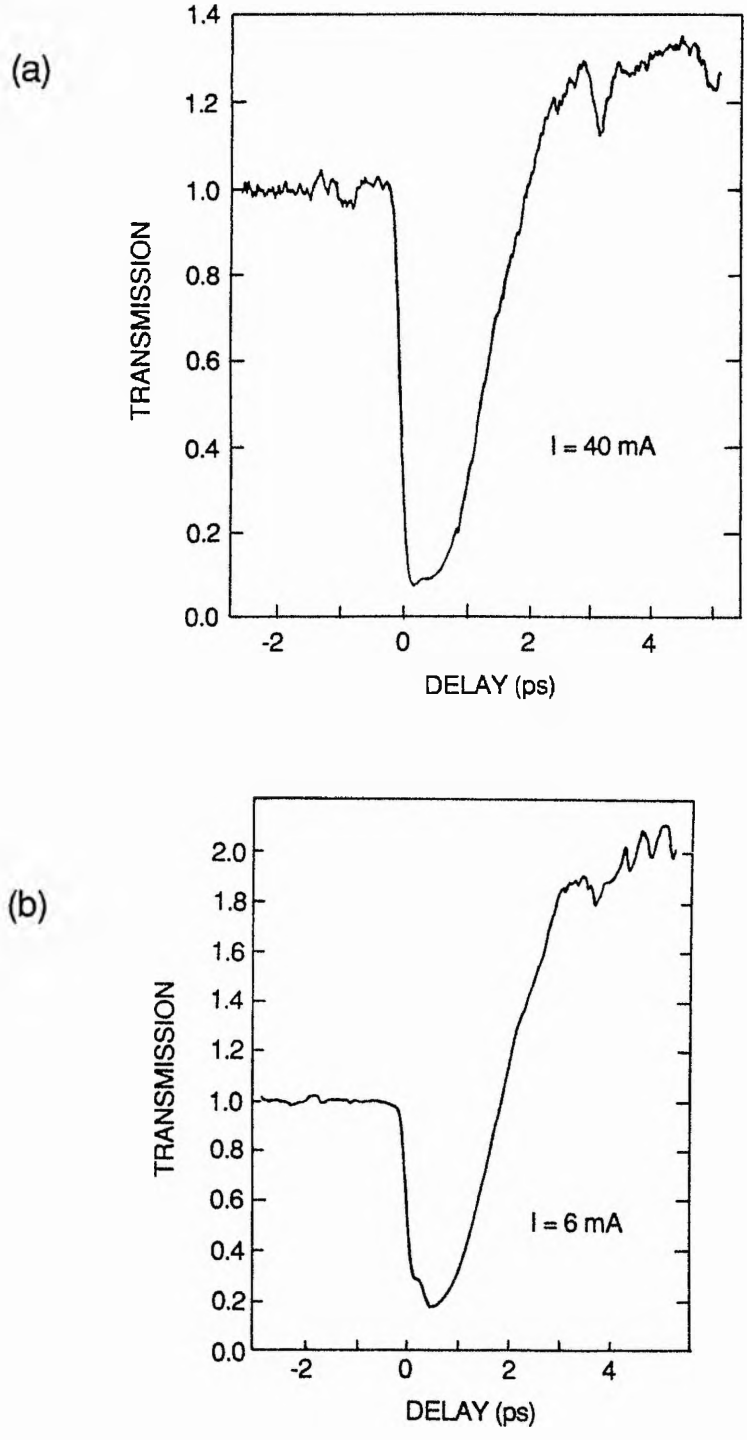

Figure 4.15 Time-resolved, (relative) transmission at a pump-pulse energies ≈ 6 pJ. The regimes of (a) gain and (b) transparency are shown.

After the completion of this work, further details of the experiment by Hall et al. on a 1.5 μm amplifier were published.[39] These results are in general agreement with the observations presented here, indicating that the dynamics are related to the physics of the material and not to a particular device structure. They also reported an ultrafast transient, but in the regime of gain, it opposed carrier heating, and hence was inconsistent with spectral hole burning. Their data does not include measurements at the higher pulse energies used in the work described in this thesis, where the transmission settles to a higher level than before the pump pulse irrespective of drive current level. The data of Hall et al. did show a fast upward spike for subtransparency drive currents, which could be associated with spectral hole burning, but this feature was not as significant as in the data shown above. The greater prominence of the femtosecond transients in this data may be due to the much shorter pulses used and hence higher resolution (Hall et al. used pulses of 180 fs duration), although it should be stated that group-velocity dispersion is likely to cause significant pulse distortion in both experiments. Pulse distortion will be discussed within chapter 5.

4.4.3 Discussion

Both sets of transmission measurements show that nonlinear absorption affects the propagation of ultrashort pulses within active semiconductor waveguides. The evidence from the pump-probe experiment points to carrier heating as the principal mechanism. The complete intraband relaxation process consists of the following sequence of events. An ultrashort pulse extracts gain through the stimulated recombination of electrons and holes which are resonant with the photon energy. The pulse therefore burns a hole in the gain profile. This depletion of carriers of a particular energy recovers by the process of carrier thermalisation, which is understood to have a time constant of 50-100 fs. Thermalisation is a redistribution of energy amongst the carriers by inelastic carrier-carrier collisions. There are indications that thermalisation through the scattering between similar carriers (i.e. e-e, h-h) is considerably more efficient than e-h scattering, which is largely elastic due to the difference in masses.[40] After thermalisation, all the carriers have become aware of the presence of the short pulse, and the saturation of the gain becomes homogeneous. The carrier temperature then comes into equilibrium with the lattice temperature by scattering of the carriers with the

lattice. In fact, the processes of carrier-carrier scattering and carrier-lattice scattering run concurrently, although carrier-carrier scattering is more efficient.

Stimulated emission is expected to heat the carrier temperature (relative to the lattice), since electrons are removed from close to the bottom of the conduction band, while stimulated absorption will cool the carriers, giving decreased gain and decreased loss respectively. As discussed earlier, only decreases in transmission have been observed, independent of the drive current, hence only the term carrier heating has been used to describe the observed effects.[34-36] This anomaly was explained by considering the effect of free-carrier absorption (see Figure 4.16), in particular the phonon-assisted absorption of photons by electrons in the conduction band.[35] Electrons are elevated high up in the band and cause considerable heating of the distribution, dominating carrier cooling due to stimulated absorption. This also explains why carrier heating has been observed at transparency. The decrease in transmission caused by carrier heating is equivalent to a nonlinear absorption, and this effect alone may be responsible for the net increase in carriers that was observed in the pump-probe measurements depicted in Figure 4.15.

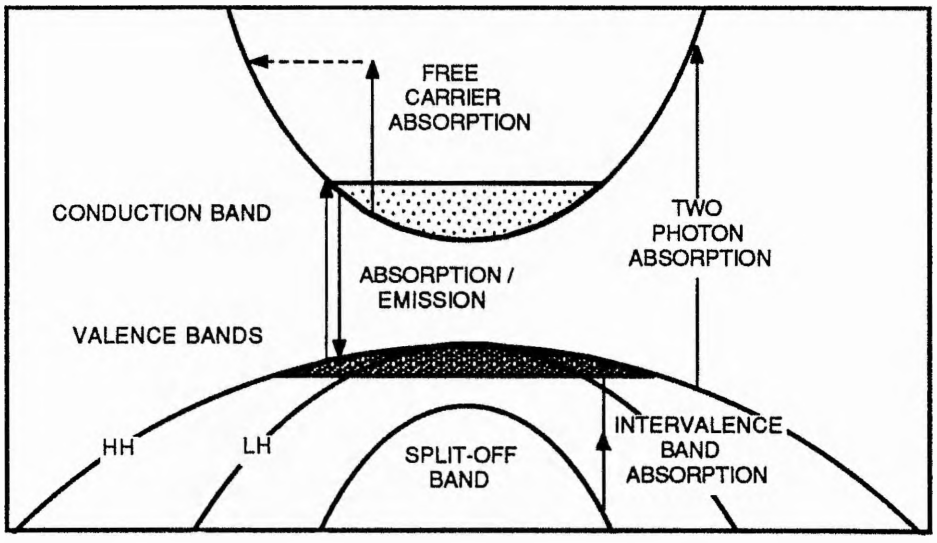

Figure 4.16 Schematic of the band structure of the active region showing free-carrier absorption and two-photon absorption.

One nonlinear absorption mechanism in semiconductor lasers and amplifiers which has received scant attention is two-photon absorption (2PA), see references 22, 23 & 41. Recently, there has been considerable interest in 2PA in passive semiconductor waveguides

due to the potential application of nonresonant refractive index changes for all-optical switching devices.[42,43] Theoretical work has indicated that the variation of the 2PA coefficient β with wavelength is broadly similar for many different semiconductors, and furthermore, it may be scaled from one semiconductor to another.[44-46] Recent experiments with quarternary waveguides indicate that these rules may be successfully applied to this material system.[47,48]

The scaling formula published by Van Stryland et al.[45,46] relates β to the refractive index n and the bandgap energy E_g(eV)

$$\beta = 3100\,(E_p)^{1/2}\,F\,/\,n^2\,E_g^3 \tag{4.32}$$

where n is the refractive index, and E_p(eV) is an energy parameter which is only weakly material dependent, normally taken as approximately 20 eV. The parameter F is given by

$$F = \frac{(2h\upsilon/E_g - 1)^{3/2}}{(2h\upsilon/E_g)^5} \tag{4.33}$$

where $h\upsilon$ is the photon energy. Using these relations, β can be estimated for the various material compositions present in the amplifier.

Layer	E_g (eV)	n	β (cm/GW)
Active region	0.80	3.6	[61]
AMB layer	1.04	3.35	49
InP cladding	1.35	3.17	21

Table 4.3 Calculated two-photon absorption coefficients. Bandgap energy of the AMB layer taken from reference **27**, and refractive indices taken from reference **8**. The bandgap energy of the active region of this particular device is assumed to be 0.80 eV (≈ 1550 nm) to be consistent with gain profile measurements. Probing wavelength is 1500 nm (0.826 eV).

Here, it has been assumed that the two-photon transition is allowed in the active region. Although 2PA is not expressly forbidden when the photon energy is greater than the bandgap energy, it would not be expected to take place if a significant population of holes (or

electrons) were present within the valance (or conduction band) band, such that they extended to include energies corresponding to the base (or top) of the 2PA transition.[49] Certainly, 2PA is allowed in the AMB and InP cladding layers, and pump-probe measurements[41] in multiple-quantum well (MQW) amplifiers, where a large proportion of the mode field travels in the "cladding" and barrier layers, have shown evidence for an instantaneous nonlinear absorption.

It can be shown that the effective β coefficient for 2PA in the active region (if it is allowed) will be reduced by a factor of approximately two, due to the creation of one carrier pair for every two photons absorbed, and the subsequent contribution of that carrier pair to stimulated emission. This reduction factor will not apply if the pulse is shorter than the intraband relaxation process, and so if 2PA dominates carrier heating, an increase in β would be expected for pulses shorter than around 1 ps. If the experimental measurements at transparency shown in Figure 4.12 (corrected for the pulse shape - see reference 50) are plotted in terms of the reciprocal transmission against peak input power (see Figure 4.17), an effective β for the device can be determined.

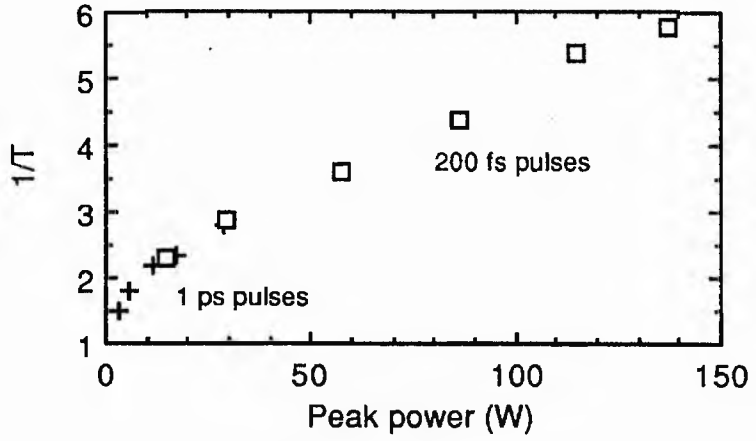

Figure 4.17 Plot of the inverse transmission at transparency. The decrease in the gradient for the shorter, more intense pulses indicates a reduction in β.

The data indicates an effective value of β of the order of 30 cm/GW at low intensities, decreasing to around 15 cm/GW at the higher intensities. This is more consistent with carrier heating than 2PA, since for pulses shorter that the carrier heating recovery time (~ 0.7 ps), the absorption caused by hot carriers will be proportional to the pulse energy rather than the

peak power, hence resulting in a reduction in β for the shorter pulses. Further work is required to clarify the rôle of 2PA.

Recent theoretical work[51,52] and experiments[53] have examined the contribution of carrier heating to nonlinear gain suppression, and have shown that under typical conditions, its effect is of a similar magnitude to spectral hole burning.

4.5 Temporal and spectral distortion of pulses

The temporal and spectral distortion of pulses will occur mainly due to the saturation of the interband transition. For pulse durations comparable with the intraband relaxation time, additional effects are likely to become significant, eg. pulse broadening due to nonlinear absorption. Although the model devised by Agrawal and Olsson[4,5] ignores these weaker effects, it will assist in their identification when the experimental results are described.

4.5.1 Modelling

The parameters used in the model will approximate to those in the actual device. Current leakage is assumed to be negligible, and the recombination coefficients are as described in Table 4.1. The linewidth enhancement factor α was taken to be 5. In the two sets of results presented here, the amplifier was modelled for drive currents of 40 mA and 2 mA, i.e. regimes of gain and loss respectively. Table 4.4 summarises the data output by the program for an assumed gain of +19 dB at 40 mA drive current and a transparency current of 6 mA.

Parameter	Symbol	Value
Carrier density at I_t	N_t	1.36×10^{18} cm^{-3}
Carrier density at 40 mA	N_{40}	3.27×10^{18} cm^{-3}
Differential gain	a	1.67×10^{-16} cm^2
Saturation energy	E_{sat}	5.2 pJ
Recovery time	τ_{rec}	490 ps

Table 4.4 Predictions by the model for a drive current of 40 mA (gain).

The input pulses were assumed to be Gaussian shaped (bandwidth limited) with a FWHM of 30 ps. Figure 4.18 shows the gain as a function of input pulse energy, as computed by the program, while Figure 4.19 depicts the temporal profile, phase shift, frequency chirp and spectral profile of the output pulse for a number of different input pulse energies. The pulse is distorted asymmetrically due to the slow recovery time of the gain, with greater amplification of the leading edge (left side) leading to a steepening of the front of the pulse. Eventually, the amplified portion becomes a step-like feature superimposed on the input pulse (shown dashed). The phase of the front of the pulse is shifted forward, while at the rear this phase shift is less marked. This leads to a stretching of the optical cycles and chirping to longer wavelengths. As the pulse energy increases, the chirp becomes larger and it moves forward to the front of the pulse, leaving the trailing edge largely unchirped. This means that only the leading edge becomes spectrally broadened, and the bulk of the pulse remains more or less at the original wavelength.

It can be shown that the maximum possible phase shift ϕ_{max} (in radians) is proportional to the small signal gain G_0 (in decibels) and the linewidth enhancement factor α

$$\phi_{max} = \frac{G_0}{10} \ln[10] \frac{\alpha}{2} \qquad (4.34).$$

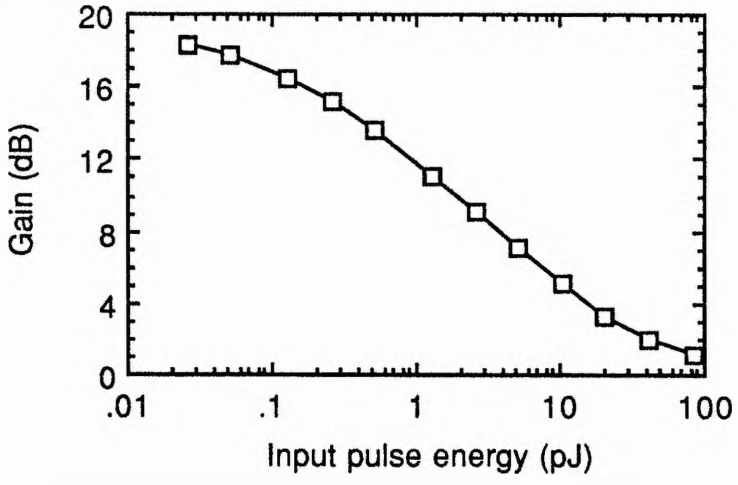

Figure 4.18 Computed gain as a function of pulse energy. G_0 = +19 dB, E_{sat} = 5.2 pJ

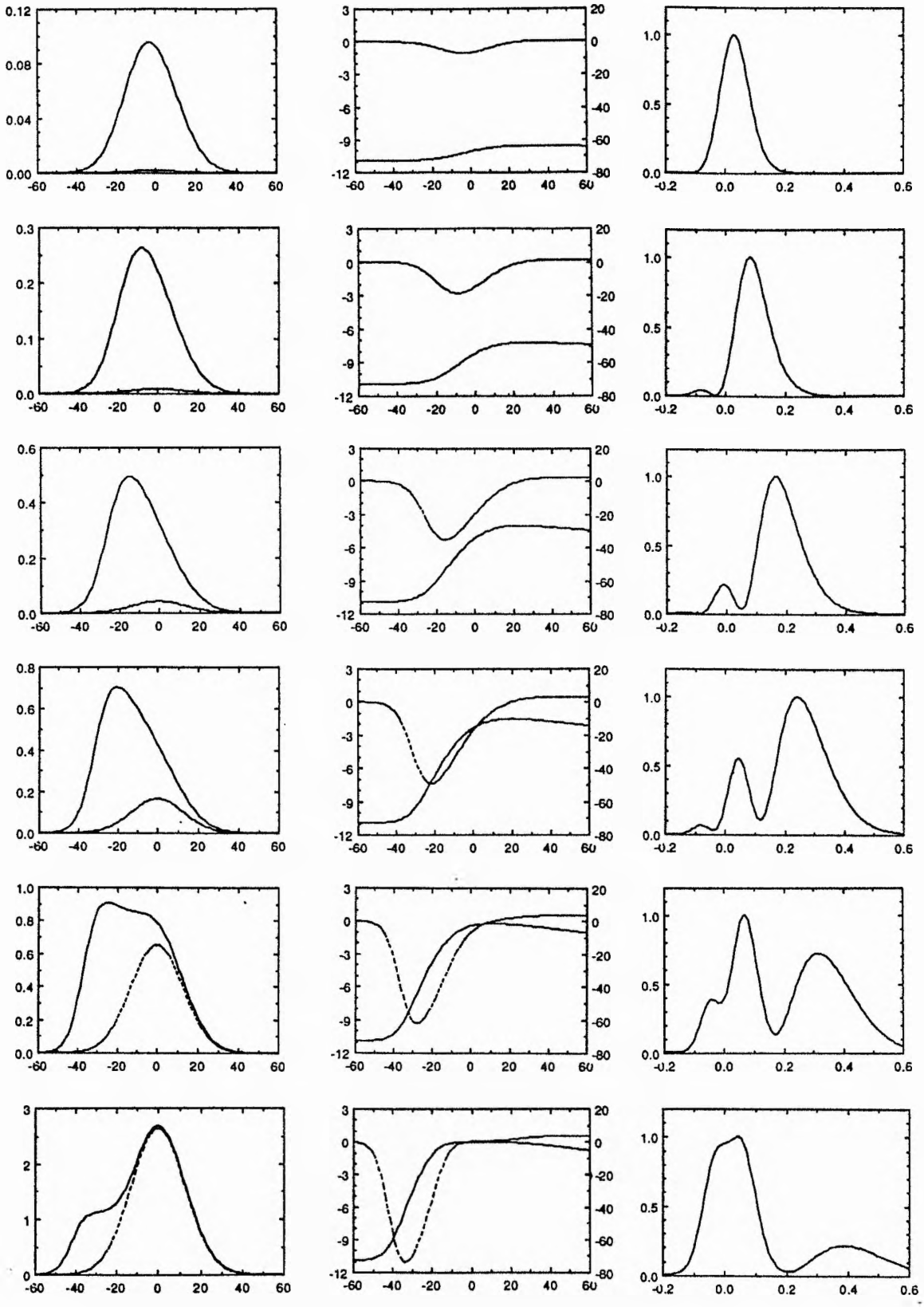

Figure 4.19 Pulse distortion related to gain saturation for input pulse energies of (top to bottom) $E_{sat}/100$, $E_{sat}/20$, $E_{sat}/4$, E_{sat}, 4 x E_{sat}, and 16 x E_{sat}. The left hand column shows the output pulse (Y axis in W, X axis in ps) , while the right hand column shows the spectrum (X axis in nm). The centre column shows $\Delta\phi$ (left hand Y axis in radians) and $\Delta\upsilon$ (right hand Y axis in GHz), with the X axis in ps.

The model was also used to study the effects of absorption saturation. Absorption was simulated by setting the drive current below transparency and entering the gain as negative. The parameters determined by the model for a small signal transmission of -10 dB at a drive current of 2 mA are listed Table 4.5. Although the model predicts a lower saturation energy at this low current, the input pulse energies in the model are labelled relative to the saturation energy determined for gain (5.2 pJ) in order that a comparison can be made. Figure 4.20 shows the computed transmission of the 30 ps pulses as a function of pulse energy, clearly showing an increased transmission at the higher pulse energies.

Parameter	Symbol	Value
Carrier density at I_t	N_t	1.36×10^{18} cm^{-3}
Carrier density at 2 mA	N_2	0.72×10^{18} cm^{-3}
Differential gain	a	2.67×10^{-16} cm^2
Saturation energy	E_{sat}	3.2 pJ
Recovery time	τ_{rec}	3300 ps

Table 4.5 Parameters used for a drive current of 2 mA (loss).

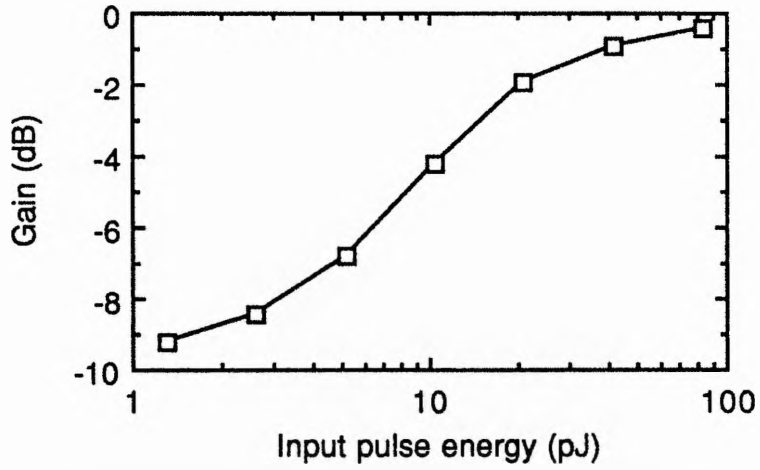

Figure 4.20 Computed gain as a function of pulse energy. G_0 = -10 dB, E_{sat} = 3.2 pJ

The associated pulse distortion is shown in Figure 4.21. As might be expected, pulse shortening is obtained by the erosion of the leading edge. Again, the distortion is asymmetric because of the long recovery time relative to the pulse duration. The increase in carrier

density caused by the bleaching of the transition gives rise to a decrease in refractive index. Therefore, the spectral broadening is to shorter wavelengths. This form of self-phase modulation has also been predicted in the theoretical work of Finlayson et al.[54] As the pulse energy is increased, only the leading edge is chirped since the pulse it is sufficiently energetic to saturate the transition alone. Therefore, the remainder of the pulse passes through unchirped.

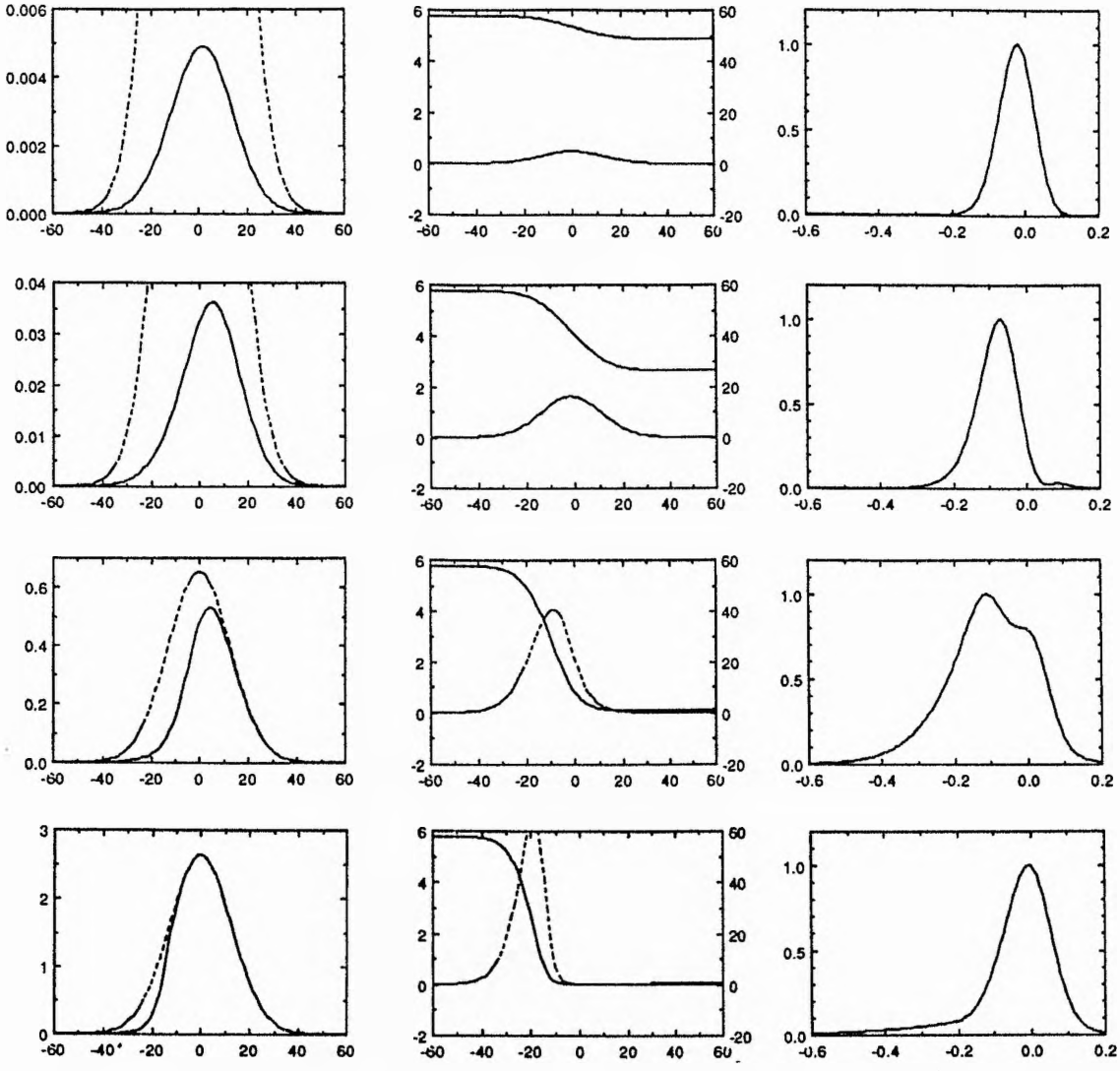

Figure 4.21 Pulse distortion related to absorption saturation for input pulse energies of (top to bottom) $E_{sat}/4$, E_{sat}, 4 x E_{sat}, and 16 x E_{sat}. The left hand column shows the output pulse (Y axis in W, X axis in ps) , while the right hand column shows the spectrum (X axis in nm). The centre column shows $\Delta\phi$ (left hand Y axis in radians) and $\Delta\upsilon$ (right hand Y axis in GHz), with the X axis in ps.

4.5.2 Experiment

The synchronously mode-locked KCl:Tl laser was again used as the pulse source for this experiment. The pulse profiles were measured directly using a Photochron II streak camera equipped with an extended S1 photocathode. The deflection plates were driven using a sine wave derived by filtering the second harmonic of the electrical pulse train generated by a fast germanium photodiode (Germanium Power Devices GM4). Although the resolution of the camera in this set up was probably no better than 5 ps, it was sufficient to resolve the 25 ps pulses. The spectra were measured using the scanning Fabry-Perot interferometer described in chapter 1. A schematic of the experiment is illustrated in Figure 4.22, while Figure 4.23 shows the temporal and spectral profiles of the input pulses.

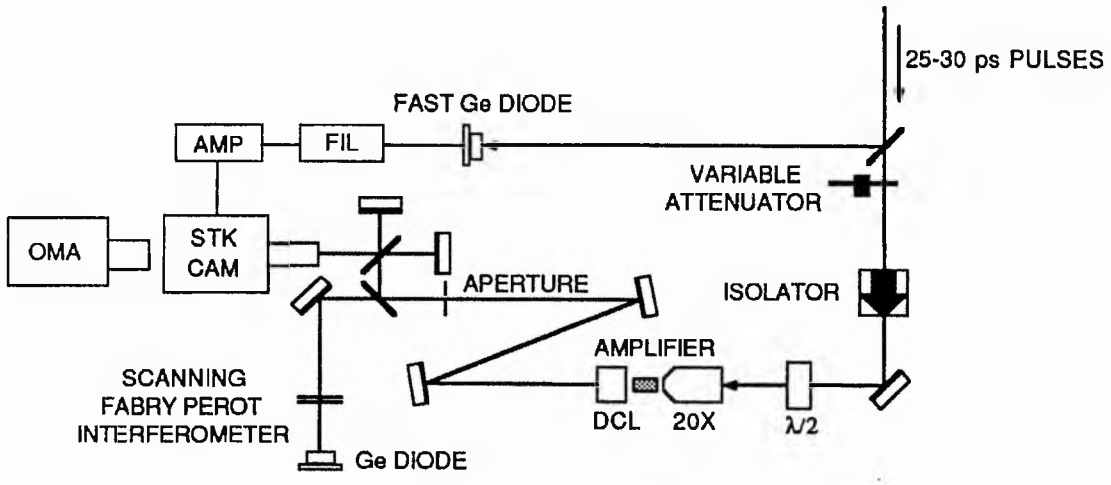

Figure 4.22 Experimental arrangement used to measure distortion of the pulses.

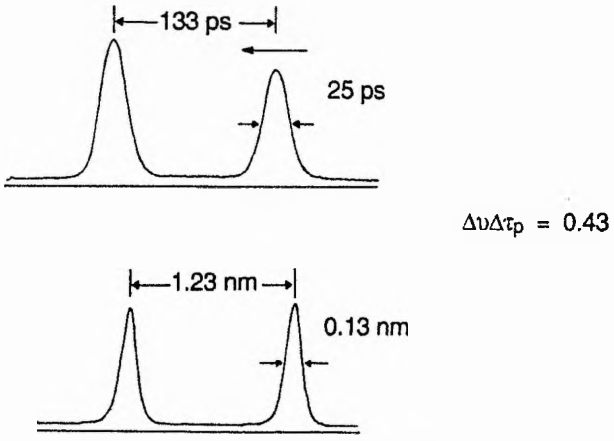

Figure 4.23 Temporal and spectral data for the input pulses.

In the gain regime (Figure 4.24), the amplified portion on the leading edge of the output pulses can be easily identified, with the predicted double lobed profile reproduced. The spectra broadened to longer wavelengths, with the expected double-lobed shape. At higher energies, the outer lobe diminished, but at still higher energies, the spectra are broadened to both sides of the central wavelength. This effect can be seen more clearly in Figure 4.25, which depicts spectra taken when the laser was more stable.

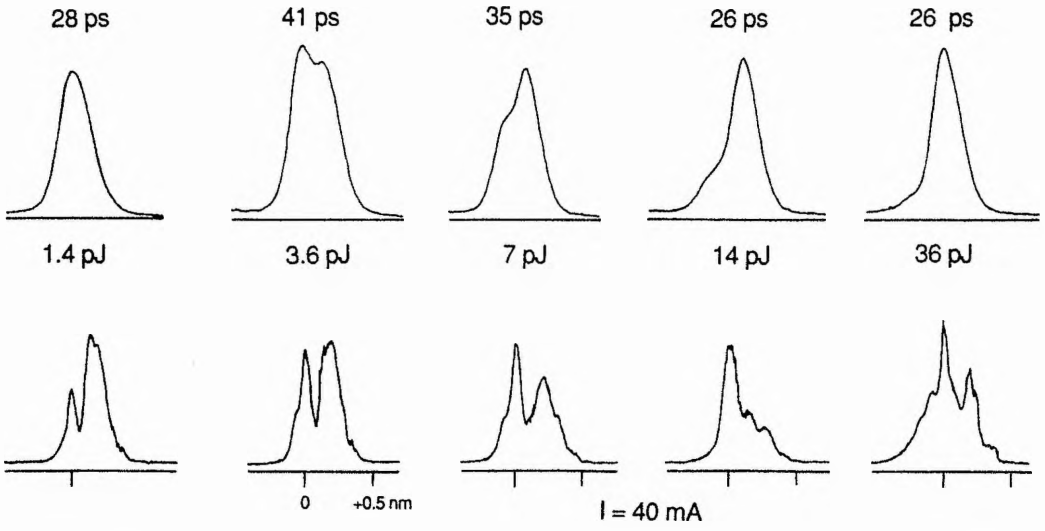

Figure 4.24 Measurements of the temporal (top) and spectral (bottom) profiles of the output pulses for 40 mA drive current.

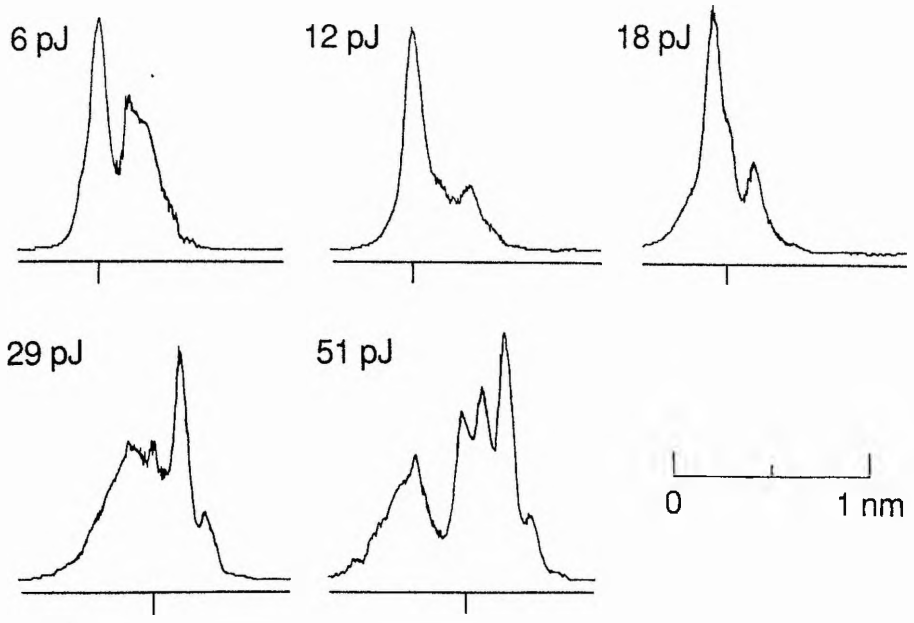

Figure 4.25 Clearer spectral data for 40 mA drive current.

In the loss regime (Figures 4.26 and 4.27), the temporal data was generally in good agreement with the model, clearly showing pulse shortening and a steepening of the leading edge. The spectra are broadened towards shorter wavelengths, with the low-lying wing clearly shown, but at the highest energy, there was again distinct deviation from the predictions of the model. This can be seen more easily in the second set of spectra reproduced in Figure 4.27.

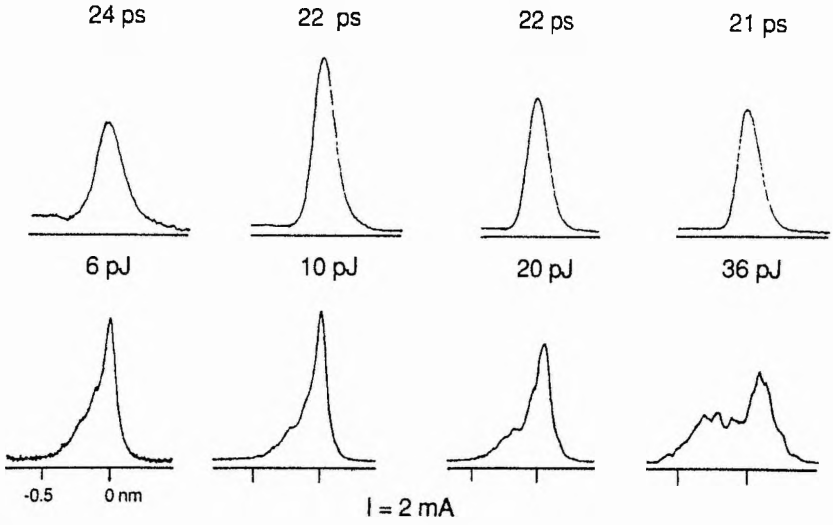

Figure 4.26 Measurements of the temporal (top) and spectral (bottom) profiles of the output pulses for 2 mA drive current.

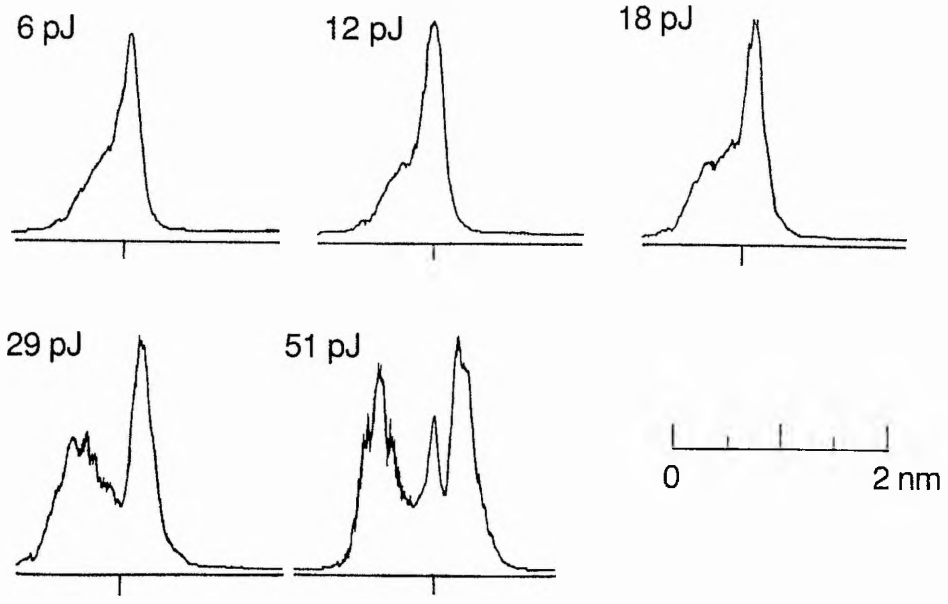

Figure 4.27 Clearer spectral data for 2 mA drive current.

While the temporal data are in good agreement with the predictions of the interband saturation model, the spectral data deviates at the higher pulse energies, indicating that an additional chirping mechanism is present. Because the additional broadening occurs to both sides of the launch wavelength this indicates that the nonlinearity has a relatively fast recovery time.

Further spectral measurements were taken with the current supply set to zero but still switched on. Under these conditions, the voltage applied to the device (as indicated by the meter on the power supply) was close to zero. Associated data (Figure 4.28) showed that the pulse has to be much more energetic to saturate the device and to experience significant spectral distortion. The three lobes of the previous figure can still be identified, although there is considerably greater asymmetry. This three-lobed feature which was observed at the highest energies was not predicted by the simple theory presented above, and therefore was probably not related to the interband movement of carriers. As discussed above, this additional effect may be faster than the pulse duration since spectral broadening was observed to occur to both sides.

To verify this, the synchronously mode-locked pulse was lengthened by detuning the cavity length of the laser by a few microns, thus decreasing the peak power while maintaining the pulse energy. Even when the pulse was approximately 100 ps long, the autocorrelation remained 3:1 and did not indicate the generation of noise bursts. With the input pulse energy fixed at around 50 pJ, the spectra shown in Figure 4.29 clearly show that the three-lobed structure is related to peak power, confirming that the additional nonlinearity must have a relatively fast recovery time, certainly faster than the shortest (25-30 ps) pulse durations.

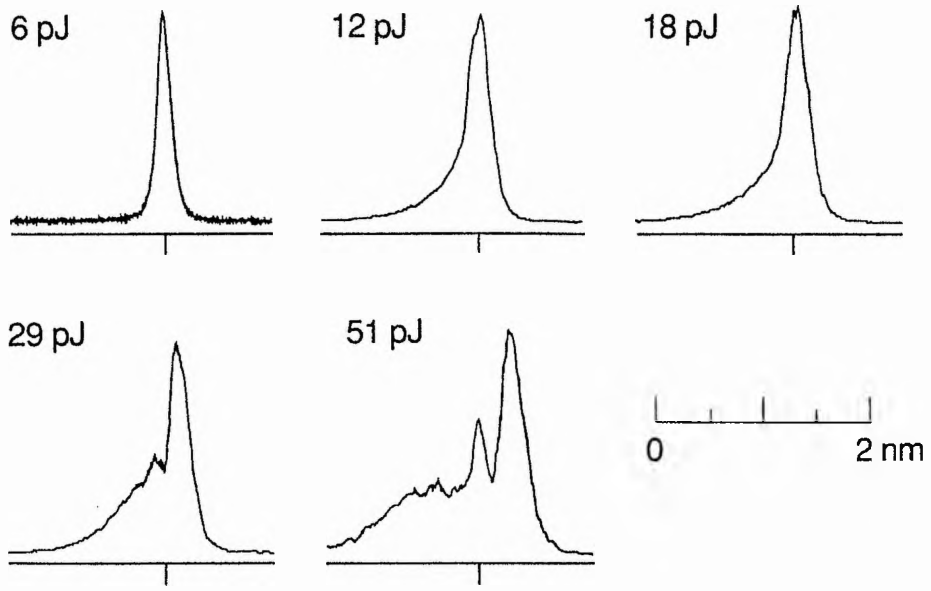

Figure 4.28 Spectral data taken for 0 mA. Pulse duration is fixed, while the input energy is changed.

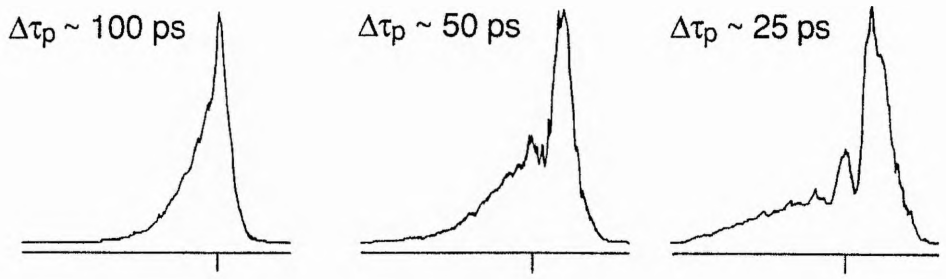

Figure 4.29 Spectral data taken for 0 mA. Input pulse energy is fixed, while the input duration is changed.

4.5.3 Spectral broadening at transparency

The additional spectral broadening mechanism observed at high pulse energies was isolated by driving the amplifier at the transparency current. At this carrier density, self-phase modulation from gain saturation or absorption saturation is eliminated. The results for the 27 ps duration pulses are reproduced in Figure 4.30. The broadening is almost symmetrical, indicating that the nonlinearity has a recovery time much faster than the pulse duration, with no additional contribution from slow effects. Furthermore, the maximum phase shifts appear to be proportional to the pulse energy. These phase shifts were large enough to allow an estimate of an effective n_2 for the effect, a technique often demonstrated with optical fibres.[55,56]

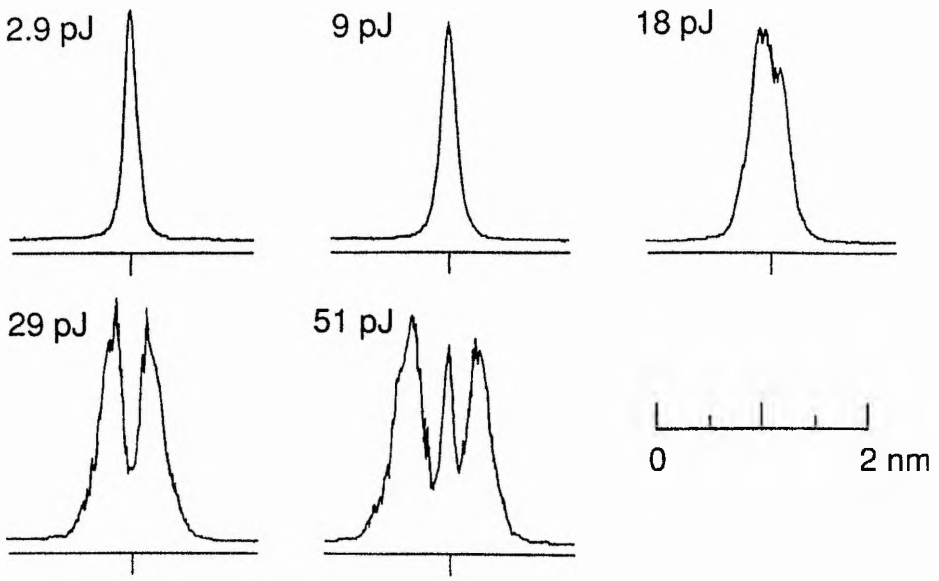

Figure 4.30 Spectral broadening of 27 ps pulses at transparency.

An intensity-dependent refractive index results in a phase shift ϕ_{nl} given by

$$\phi_{nl}(t) = \frac{2\pi L}{\lambda} n_2 I(t) \tag{4.35}$$

where L is the length of the guide, λ is the free-space wavelength, and I is the intensity. The peak intensity of the pulse is given by $I_{max} = P_0/A_{eff}$ where A_{eff} is the effective area of the guided mode, given by (height x width) / Γ. The pulse shape was assumed to be Gaussian, hence the peak power $P_0 = E/1.065\ \Delta\tau_p$ where E is the pulse energy and $\Delta\tau_p$ is the pulse duration (full width at half maximum). Rearrangement of (4.35) now gives

$$n_2 = \frac{\lambda A_{eff} \Delta\tau_p}{5.9L} \frac{\phi_{max}}{E} \tag{4.36}.$$

The spectra in Figure 4.30 with energies of 29 pJ and 51 pJ have maximum phase shifts of magnitude $3\pi/2$ and $5\pi/2$ radians respectively. Hence the magnitude of the n_2 associated with this ultrafast nonlinearity can be estimated to be $(2.0 \pm 0.6) \times 10^{-11}$ cm^{2}W^{-1}, where the error is dominated by the uncertainty in the input coupling efficiency.

Further transmission measurements at transparency (depicted in Figure 4.31) showed that the 30 ps pulses incurred little loss, only around 0.8 dB at the pulse energy which corresponded to the $5\pi/2$ radians phase shift. The effect of this small loss is essentially

negligible given the magnitude of the other possible errors in the calculation. It was acknowledged in section 4.3 that the transparency current may not correspond to the absolute transparency owing to losses due to scattering. The effect of this loss on the above calculation can be readily considered. Firstly, it is usual in such calculations to compensate for the presence of a linear loss by replacing the length of the guide by a reduced or effective length, which can be easily calculated given the loss (see chapter 1). Secondly, the presence of this loss would mean that the input coupling efficiency was incorrectly calculated. The incorporation of the loss into the estimate for coupling efficiency would result in an increase in the estimated input pulse energy. It can be shown that this second correction cancels out with the first correction. In other words, by using the output pulse energy, the value of n_2 calculated remains valid no matter what the linear loss is.

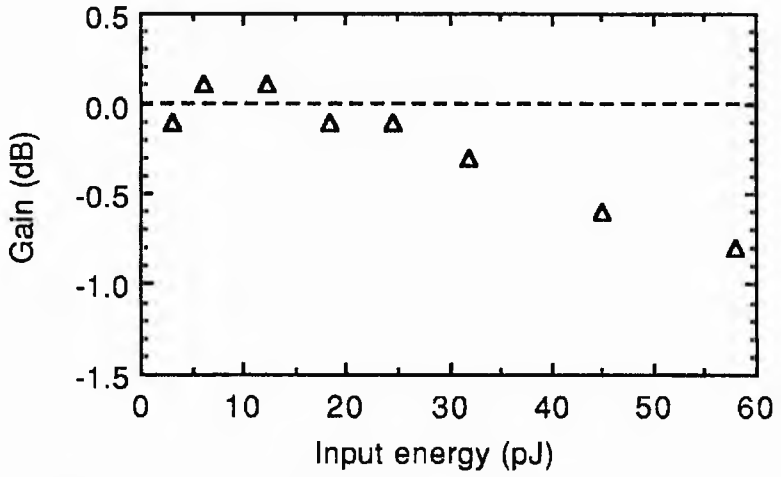

Figure 4.31 Transmission of the 30 ps pulses at the transparency current.

To determine the sign of the n_2, the experimental setup was modified as illustrated in Figure 4.32. The pulses were now prechirped by passage through an optical fibre before being coupled into the device. Self-phase modulation in the fibre will induce a frequency upchirp on the pulse, since the n_2 in the fibre is positive. The chirp from the ultrafast nonlinearity in the amplifier will either oppose, or add to this chirp, depending on whether the sign of the n_2 for the amplifier is negative or positive.

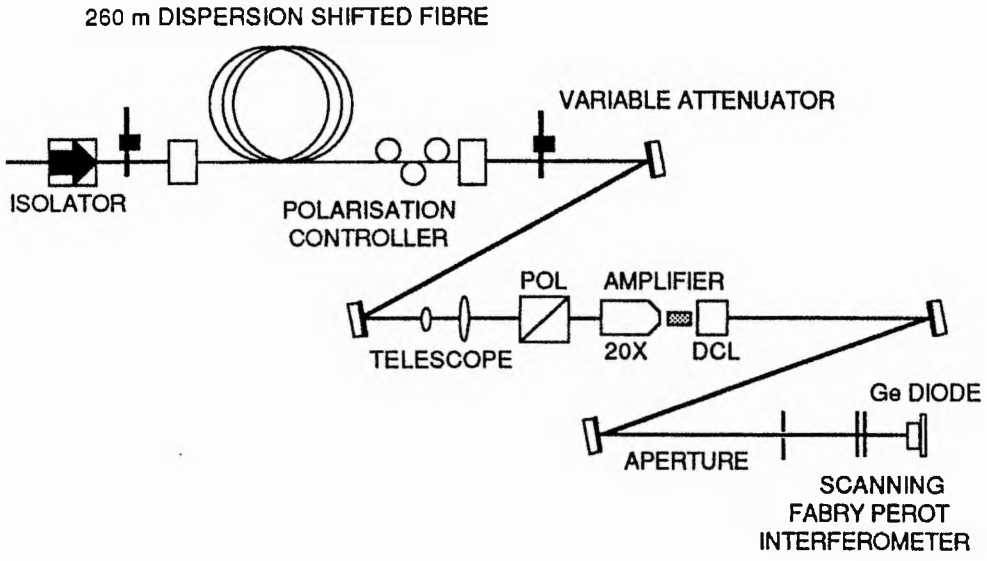

Figure 4.32 Experimental arrangement for determining the sign of the ultrafast nonlinearity.

A 260 m length of Corning dispersion-shifted fibre was used to prechirp the pulses. The group-velocity dispersion (GVD) parameter $D \approx -4$ ps/(nm.km) at 1500 nm (see chapter 3). For pulse durations of 25 ps, the dispersion length L_D can be calculated to be ~ 50 km which is considerably longer than the fibre. Therefore, there is negligible broadening of the pulses due to GVD, even when frequency chirped by self-phase modulation. This was verified by comparing autocorrelations of the input and output pulses at powers where the peak phase shift exceeded $7\pi/2$ radians. The fibre was not polarisation maintaining, so a Glan-Taylor polariser was placed between the fibre and the amplifier to ensure that light was coupled into the TE mode, consistent with the previous measurements. The output tail of the fibre was wound around a three-loop polarisation controller which was adjusted to maximise the light transmitted by the bulk polariser.

Spectra of the pulses were recorded after the passing both the fibre and the amplifier under two different operating conditions (Figure 4.33). In the first measurement the pulse energy coupled into the fibre was set to approximately 300 pJ, while the pulse energy in the amplifier was attenuated using a variable neutral density wheel to less than 2 pJ. The resulting SPM, shown in Figure 4.33 (a), was attributed to the fibre, giving a nonlinearity parameter $\gamma \approx 2.8$ $W^{-1}km^{-1}$. With the energy in the fibre remaining at around 300 pJ, the pulse energy in the amplifier was then raised to an estimated 25 pJ. This resulted in a

contraction of the spectrum, clearly indicating that the sign of the n_2 for the ultrafast nonlinearity in the amplifier is negative (see Figure 4.33 (b)).

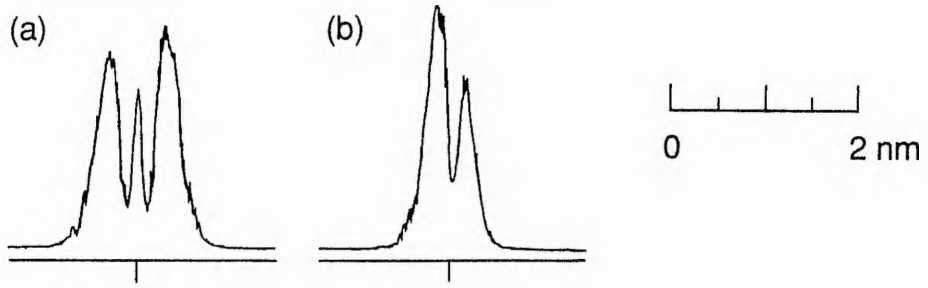

Figure 4.33 Spectra of the pulses transmitted by the fibre and the amplifier (see text).

In an attempt to estimate the recovery time of the nonlinearity, the KCl:Tl laser was coupled-cavity mode locked to generate picosecond and femtosecond pulses. If the nonlinearity was caused by a nonresonant effect then the spectral broadening would be expected to be symmetrical, even with pulses of a few hundred femtoseconds duration. Figures 4.34 and 4.35 show the spectra of the transmitted pulses where the input duration was 1 ps and 200 fs respectively. For the 1 ps pulses, the broadening occurs almost entirely to shorter wavelengths, while for the 200 fs pulses the broadening is indistinct and relatively weak given the very high peak powers coupled into the device (> 100 W). It was thought that the nonlinearity was not instantaneous, but had a recovery time of about a picosecond or so. The only physical mechanism which has a time constant of this order is carrier heating. It is clear that considerable distortion of the pulse profile will occur for these ultrashort pulses, even at transparency, due to group-velocity dispersion (GVD)[57] and nonlinear absorption, and hence the spectral distortion cannot be analysed as simply as for the 30 ps pulses. An attempt was made to measure the temporal distortion of the output pulses using the autocorrelator, but there was insufficient signal. A further set of spectral measurements for the 200 fs pulses is illustrated in Figure 4.36, where the drive current is set to 40 mA. When these data are compared to Figure 4.34, it can be seen that the asymmetric broadening at 1.2 pJ input pulse energy is similar to the SPM associated with gain saturation, although can is only speculative without a comparison with a more rigorous model which takes into account additional effects such as intraband processes and GVD.

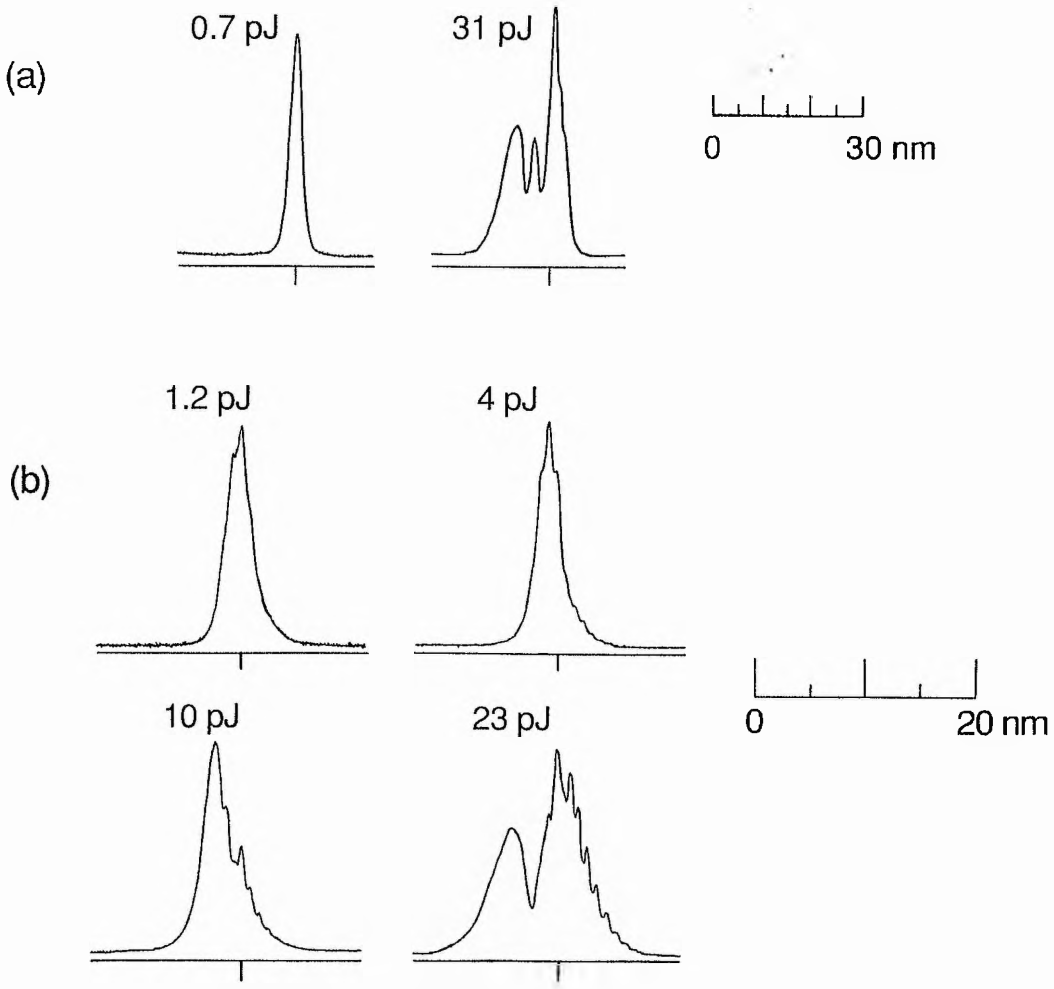

Figure 4.34 Spectra: drive current = 6mA, input pulse duration = 1 ps. (a) Initial measurements and (b) measurements taken later showing intermediate energy levels and with a higher resolution.

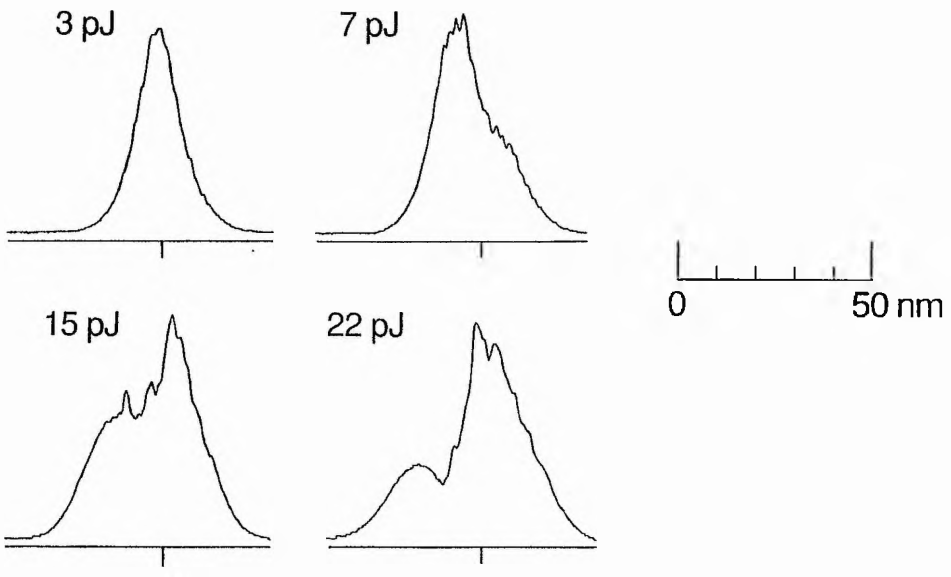

Figure 4.35 Spectra: drive current = 6 mA, input pulse duration = 200 fs.

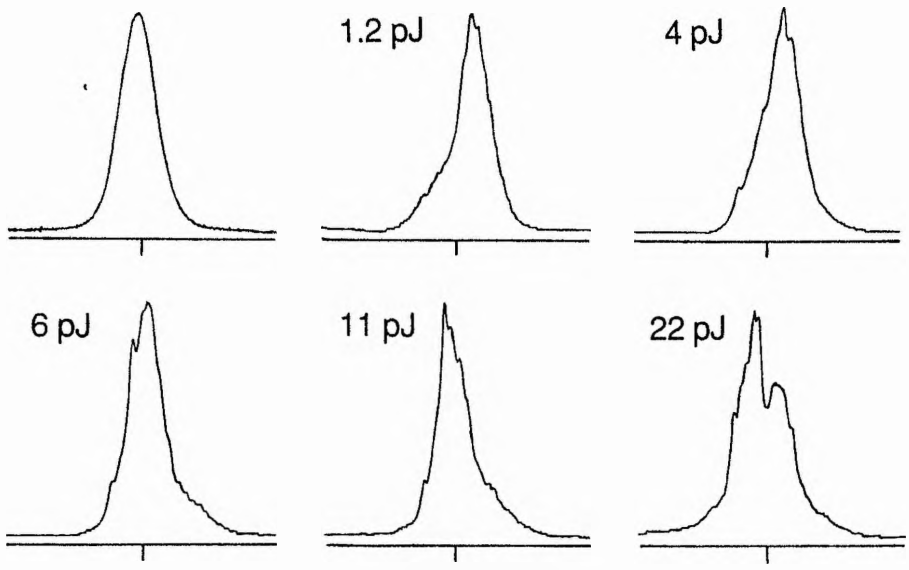

Figure 4.36 Spectra: drive current = 40 mA, input pulse duration = 200 fs.

Since the publication of these observations, other researchers[58,59] have published their own findings. The time-resolved measurements of refractive index changes, reported by Hultgren and Ippen,[59] are particularly relevant. Although their measurements were with a GaAs laser chip, its behaviour would be expected to be broadly similar to the InGaAsP amplifier discussed here. Their technique of time-division interferometry,[60] is essentially a modified pump-probe layout which can detect changes in phase. Two probe pulses and a pump pulse are sent through the guide. One of the probe pulses is sent through first to act as a reference for the other probe pulse which experiences refractive index changes induced by the pump pulse. The two probe pulses are then added to detect any phase shifts. With these measurements, two distinct, opposing contributions to the ultrafast refractive index changes have been resolved. The dominant nonlinearity has a nonlinear index coefficient $n_2 \approx -5 \times 10^{-12}$ cm^2W^{-1} and has an instantaneous recovery time, while the opposing, weaker effect has a slower recovery time comparable to that of carrier heating. (This positive n_2 agrees with Kramers-Krönig transform of the transmission changes caused by carrier heating.[34])

Although the sign of the dominant effect is a factor of 4 smaller that observed by the SPM measurements presented in this thesis, it should be remembered that if it is caused by a Stark-like effect, it will scale with the inverse of the fourth power of the bandgap energy, ie. approximately 12 times stronger in InGaAsP than in GaAs.[61] Unfortunately, the asymmetry

of the spectral broadening of the 1 ps pulses cannot be explained by simply considering the time-resolved measurements. This may be because there are a number of other effects which are important at the large pulse energies used in the SPM experiments. These include significant increases in the real carrier density due to the nonlinear absorption, which will cause a long lived negative index changes (since the pulse duration is of the same order as the intraband relaxation time) and pulse distortion due to nonlinear absorption. If two-photon absorption is dominant, then the pulse distortion will be symmetric, with the greatest attenuation at the peak thereby flattening and broadening the profile. On the other hand, if carrier heating is dominant, then asymmetric distortion will occur, since the carrier temperature will reach a peak towards the rear of the pulse. Therefore the trailing edge will suffer the greatest attenuation.

Ultrafast refractive nonlinearities have been predicted for semiconductor lasers in the context of nondegenerate four-wave mixing,[62] where the underlying physical mechanism is cited as spectral hole burning. Yamada predicts a nonlinear susceptibility for this process, equivalent to an $|n_2| \approx 1.1 \times 10^{-11}$ cm^2W^{-1} under typical conditions.[63] The 100 fs recovery time associated with SHB means that four-wave mixing should be possible for frequency detunings approaching 10 THz. Detunings of 17 Ghz,[64] 1 THz,[65] and 500 GHz,[66] have been reported, although this last observation was attributed to carrier heating. Although the index changes associated with SHB have a similar magnitude to the effect observed here, the contribution from SHB at transparency would be expected to be zero.

4.6 Cross-phase modulation related to gain saturation

For pulse durations much longer than the spectral hole burning recovery time (approximately 100 fs or less), the gain of the semiconductor amplifier is effectively homogeneously broadened, and therefore the gain at one wavelength will be affected by the presence of a signal at a second wavelength.[19,67,68] The reduction in gain induced by an energetic pulse could conceivably be used to shape a pulse at a different wavelength, provided that the two pulses have some temporal overlap. Furthermore, coupling between the pulses will occur through the refractive index changes that accompany gain saturation, resulting in frequency

chirping. This interaction corresponds to the phenomenon of cross-phase modulation (XPM) that has been extensively studied in optical fibres.[69]

To observe XPM, energetic pump pulses together with weaker probe pulses were injected into the amplifier in the same direction. The probe pulses were sufficiently weak that there was no significant saturation of the amplifier gain and negligible spectral broadening from SPM. On the other hand, the pump pulses saturated the gain and sustained considerable SPM. The refractive index changes induced by the pump pulses were experienced by the probe pulses and frequency chirp and spectral broadening were thereby induced solely through XPM.

The experimental set up is shown schematically in Figure 4.37. Independent, wavelength-tunable, trains of pulses were generated by dual synchronously mode-locked KCl:Tl and NaCl:OH^- colour-centre lasers, both excited by the Nd:YAG laser. An adjustable optical delay in the KCl:Tl laser beam enabled the relative timing between the two pulse trains to be altered. The two pulse trains were combined at a beamsplitter, and subsequently polarised to match the amplifier TE mode. As before, the beams were coupled into and out of the device using bulk optics, and an aperture was used to eliminate the light not coupled into the waveguide. The two pulse trains exiting the device were separated from each other by a monochromator which acted as a bandpass filter (bandwidth $\approx$ 5 nm). As previously described, the spectra of the pulses were resolved with the scanning Fabry-Perot interferometer.

The KCl:Tl laser was operated at a wavelength of 1526 nm and generated probe pulses of approximately 40 ps duration, while the NaCl:OH^- laser, tuned to 1506 nm, was used to provide the pump pulses. To simplify the analysis of the results, the NaCl:OH^- pulse duration, normally 5-10 ps, was increased to ~ 40 ps by bandwidth limitation and slight cavity length detuning. The amplifier drive current was set to 40 mA, giving a small-signal gain at the probe-pulse wavelength of around +16 dB.

The pump pulse energy coupled into the amplifier was estimated to be approximately 10 pJ. This was large enough to strongly saturate the gain, and consequently only the leading portion of the pulse was amplified and spectrally broadened to longer wavelengths by SPM.

The trailing portion of the pump pulse was transmitted unamplified and unchirped. A typical spectrum of the pump pulses transmitted by the amplifier is reproduced in Figure 4.38 together with an undistorted spectrum recorded in the small-signal regime.

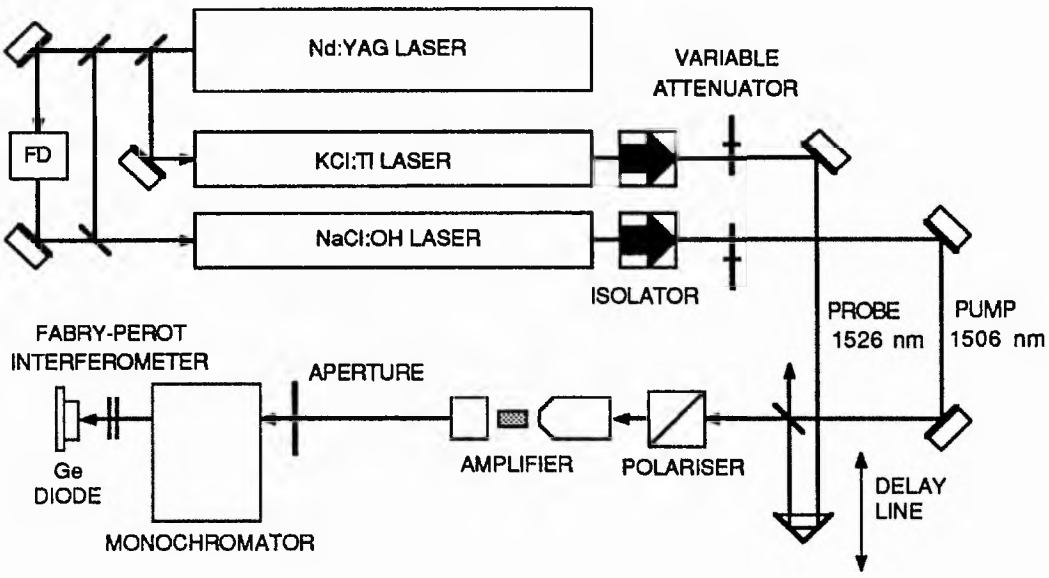

Figure 4.37 Schematic of the XPM experiment. FD:frequency doubler.

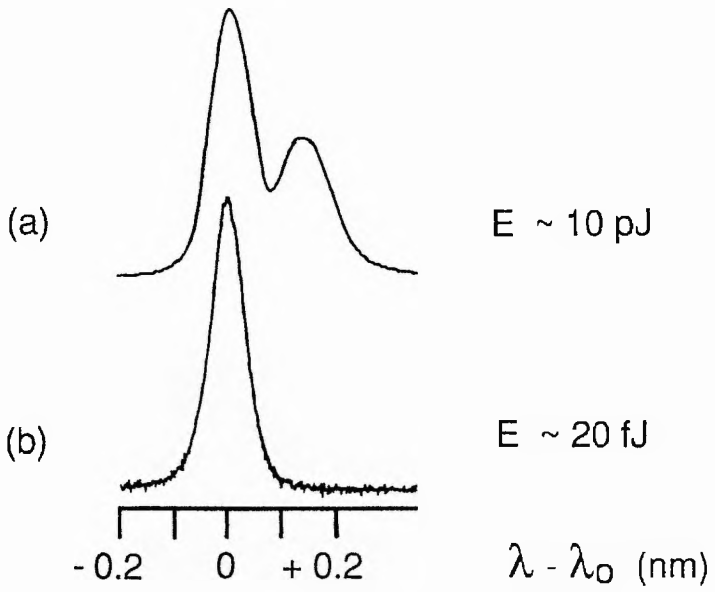

Figure 4.38 Spectra of the pump pulses for (a) linear and (b) nonlinear propagation.

The spectra of the probe pulses (input energy ~ 80 fJ) transmitted by the amplifier are shown in Figure 4.39. Spectra (a) - (e), distorted by XPM, are labelled by the time delay

relative to the pump pulse, i.e. in (a) the probe pulse precedes the pump pulse. The point of zero delay was chosen somewhat arbitrarily as the position where the maximum spectral distortion was recorded and does not necessarily imply complete overlap of pump and probe pulses. As discussed above, the probe pulse will only be noticeably chirped where it overlaps with the pump pulse, and so for the conditions of (a) and (e) the frequency chirp on the probe pulse will be confined to the trailing and leading edges respectively.

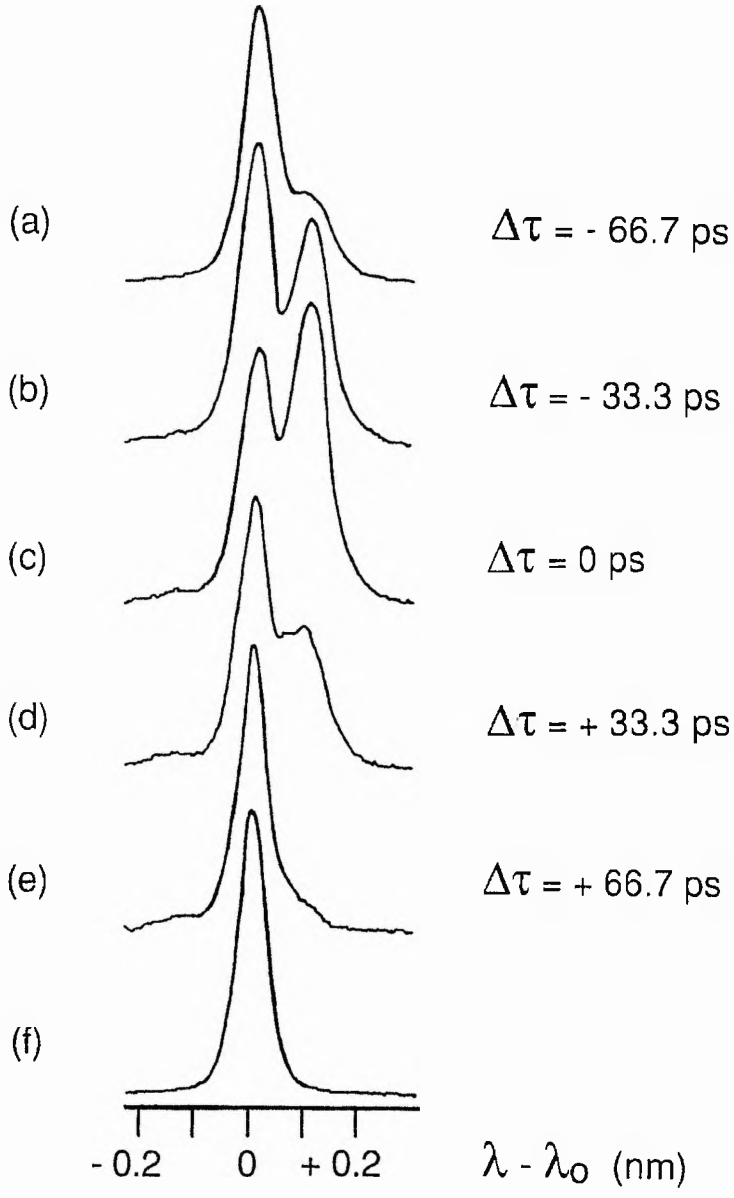

Figure 4.39 Spectra of the probe pulses. (a)-(e) Distortion due to XPM for various delay times relative to the pump pulse and (f) with the pump pulse absent.

The spectra are broadened asymmetrically to longer wavelengths when compared to the spectrum taken when the pump pulse train was blocked, see Figure 4.39 (f). This asymmetry is not the result of any group-velocity mismatch and subsequent walk-off, which affects XPM in fibres.[69] For the case described here, the pulses are much longer than the length of the nonlinear medium and walk-off is negligible. Instead, the spectral asymmetry is attributed to the long recovery time of the refractive index change compared to the pulse durations, as shown in the preceding investigations of SPM.

The pump pulse energy used here was rather excessive, and it should be possible to observe similar effects using much lower pump pulse energies, say 1 pJ. Furthermore, for an amplifier with a higher small signal gain than that used here, the spectral distortion would be more dramatic and would appear at even lower pump pulse energies. The effect might have some application in all-optical switching, but it should be remembered that the recovery time will be the same as for the SPM related to gain saturation, ie. ≈ 500 ps. Its effects may be important in WDM systems that employ intensity modulation, where XPM could be a potential source of cross-talk.

After the completion of this work, it was discovered that cross-phase modulation in a semiconductor amplifier had been recently reported at a conference.[70] In a subsequent publication[71], they confirmed that the α parameter associated with cross-phase modulation is identical to the α parameter for self-phase modulation. This might have been expected since the refraction is based on real carrier density changes.*

4.7 Summary

Both linear and nonlinear optical properties of an InGaAsP amplifier have been characterised using the KCl:Tl laser. The transmission has been measured using conventional and time-resolved techniques, and nonlinear absorption has been identified. The temporal and spectral distortion of pulses by the device have been studied, and by comparing the experimental results with the predictions of a model for saturation-related effects, an ultrafast refractive nonlinearity has been identified. This nonlinearity has been deduced to have an effective n_2 of -2×10^{-11} cm^2W^{-1}, with a recovery time much faster than 25 ps. The magnitude, speed and

* XPM in optical fibres is twice as effective as SPM, see reference 69.

large phase shifts associated with this nonlinearity make it potentially attractive for all-optical switching applications. The suitability of this effect can be verified by evaluating the figure of merit defined by DeLong et al.[42,72] as $T = 2\beta\lambda/n_2$, where $T < 1$ is required for complete switching using a nonlinear directional coupler.* Using the effective β coefficient found of approximately 30 cm/GW, $T \approx 0.45$. For pulse durations much shorter than 20 ps, the situation is less clear, and further work is required in this direction. Finally, cross-phase modulation related to gain saturation has been demonstrated. In the following chapter, the performance of the coupled-cavity KCl:Tl laser when the amplifier is used as the control-cavity nonlinearity will be described.

* The use of a travelling-wave, twin-stripe semiconductor amplifier as a nonlinear directional coupler has recently been considered by Trillo et al.[73] They predict that when using the slow SPM associated with gain saturation, switching is limited to 50%. No mention is made of the possible use of ultrafast nonlinearities.

4.8 References

1. J. C. Simon, J. Lightwave Technol. **LT-5**, 1286 (1987).
2. M. J. O'Mahony, J. Lightwave Technol. **6**, 531 (1988).
3. T. Saitoh and T. Mukai, J. Lightwave Technol. **6**, 1656 (1988).
4. G. P. Agrawal and N. A. Olsson, IEEE J. Quantum Electron. **25**, 2297 (1989).
5. N. A. Olsson and G. P. Agrawal, Appl. Phys. Lett. **55**, 13 (1989).
6. A. Yariv, *Quantum Electronics* (3rd edition) (John Wiley, New York, 1989), chapter 11.
7. S. M. Sze, *Physics of Semiconductor Devices* (John Wiley, New York, 1981), chapter 12.
8. Y. Suematsu, K. Iga, and K. Kishino, "Double-Heterostructure Lasers" (chapter 14), in *GaInAsP Alloy Semiconductors*, T. P. Pearsall, ed. (John Wiley, Chichester, 1982).
9. G. P. Agrawal and N. K. Dutta, *Long Wavelength Semiconductor Lasers* (Van Nostrand Reinhold, New York, 1986).
10. N. K. Dutta, " Optical Sources for Lightwave System Applications" (chapter 9), in *Optical-Fiber Transmission*, E. E. Basch, ed. (Howard Sams, Indianapolis, 1987).

10. D. Botez, IEEE J. Quantum Electron. **QE-17**, 178 (1981).
11. G. Eisenstein, R. S. Tucker, J. M. Wiesenfeld, P. B. Hansen, G. Raybon, B. C. Johnson, T. J. Bridges, F. G. Storz, and C.A. Burrus, Appl. Phys. Lett. **54**, 454 (1989).
12. K. Vahala, L. C. Chiu, S. Margalit, and A. Yariv, Appl. Phys. Lett. **42**, 631 (1983).
13. C. H. Henry, IEEE J. Quantum Electron. **QE-18**, 259 (1982).
14. M. Osinski and J. Buus, IEEE J. Quantum Electron. **QE-23**, 9 (1987).
15. M. J. Adams, H. J. Westlake, and M. J. O'Mahony, "Optical Bistability in Semiconductor Laser Amplifiers" (chapter 15), in *Optical Nonlinearities and Instabilities in Semiconductors*, H. Haug, ed. (Academic Press, San Diego, 1988).
16. J. F. Erhart, A. Villeneuve, G. Assanto, G. I. Stegeman, B. Mersali, A. Accard, G. Kelly, and B. Fernier, Appl. Phys. Lett. **58**, 816 (1991).
17. H. Nakajima and R. Frey, Appl. Phys. Lett. **47**, 769 (1985).
18. G. P. Agrawal, Opt. Lett. **12**, 260 (1987).
19. K. Inoue, T. Mukai, and T. Saitoh, Appl. Phys. Lett. **51**, 1051 (1987).
20. M. J. Adams and M. Osinski, Electron. Lett. **19**, 627 (1983).
21. J. Manning, R. Olshansky, D. M. Fye, and W. Powazinik, Electron. Lett. **21**, 496 (1985).
22. J. E. Bowers, T. L. Koch, B. R. Hemingway, D. P. Wilt, T. J. Bridges, and E. G. Burkhardt, Electron. Lett. **21**, 392 (1985).
23. R. S. Tucker, J. Lightwave Technol. **LT-3**, 1180 (1985).
24. R. Frankenburger and R. Schimpe, Appl. Phys. Lett. **57**, 2520 (1990).
25. J. Eom, C. B. Su, W. Rideout, R. B. Lauer, and J. S. LaCourse, Appl. Phys. Lett. **58**, 234 (1991).
26. K. L. Hall, E. P. Ippen, J. Mark, and G. Eisenstein, in *Technical Digest of Conference on Lasers and Electro-Optics* (Optical Society of America, Washington, D.C., 1989), paper THI1.
27. D. Renner, A. J. Collar, P. D. Greene, and G. D. Henshall, Electron. Lett. **21**, 1006 (1985). Details of the amplifier described here were provided by G. D. Henshall of STC Technology Ltd., (now BNR (Europe) Ltd.), (Amplifier provided by R. Wyatt of B. T. Labs., Ipswich.).

28. Vu Van Lyk, P. G. Eliseev, and M. A. Man'ko, in *Injection Lasers in Optical Communications and Information Processing Systems*, Yu. M. Popov, ed. (Nova Science, Commack, NY, 1989), pp. 75-82
29. J. C. Simon, B. Landousies, Y. Bossis, P. Doussiere, B. Fernier, and C. Padioleau, Electron. Lett. **23**, 334 (1987).
30. P. B. Hansen, J. M. Wiesenfeld, G. Eisenstein, R. S. Tucker, and G. Raybon, IEEE J. Quantum Electron. **25**, 2611 (1989).
31. T. Saitoh, H. Itoh, Y. Noguchi, S. Sudo, and T. Mukai, IEEE Photon. Technol. Lett. **1**, 297 (1989).
32. T. Saitoh and T. Mukai, IEEE J. Quantum Electron. **26**, 2086 (1990).
33. Y. Lai, K. L. Hall, E. P. Ippen, G. Eisenstein, IEEE Photon. Technol. Lett. **2**, 711 (1990).
34. M. S. Stix, M. P. Kesler, and E. P. Ippen, Appl. Phys. Lett. **48**, 1722 (1986).
35. M. P. Kesler and E. P. Ippen, Appl. Phys. Lett. **51**, 1765 (1987).
36. M. P. Kesler and E. P. Ippen, Electron. Lett. **24**, 1102 (1988).
37. S. A. Lyon, J. Luminescence **35**, 121 (1986).
38. W.-Z. Lin, R. W. Schoenlein, J. G. Fujimoto, and E. P. Ippen, IEEE J. Quantum Electron. **24**, 267 (1988).
39. K. L. Hall, J. Mark, E. P. Ippen, and G. Eisenstein, Appl. Phys. Lett. **56**, 1740 (1990).
40. W. H. Knox, D. S. Chemla, G. Livescu, J. E. Cunningham, and J. E. Henry, Phys. Rev. Lett. **61**, 1290 (1988).
41. K. L. Hall, Y. Lai, E. P. Ippen, G. Eisenstein, and U. Koren, Appl. Phys. Lett. **57**, 2888 (1990).
42. K. W. DeLong, K. B. Rochford, and G. I. Stegeman, Appl. Phys. Lett. **55**, 1823 (1989).
43. J. S. Aitchison, M.K. Oliver, E. Kapon, E. Colas, and P. W. E. Smith, Appl. Phys. Lett. **56**, 1305, (1990).
44. B. S. Wherrett, J. Opt. Soc. Am. B **1**, 67 (1984).
45. E. W. Van Stryland, H. Vanherzeele, M. A. Woodall, M. J. Soileau, A. L. Smirl, S. Guha, and T. F. Boggess, Opt. Eng. **24**, 613 (1985).
46. E. W. Van Stryland, M. A. Woodall, H. Vanherzeele, and M. J. Soileau, Opt. Lett. **10**, 490 (1985).
47. A. Villeneuve, M. Sundheimer, N. Finlayson, G. I. Stegeman, S. Morasca, C. Rigo, R. Calvani, and C. DeBernardi, Appl. Phys. Lett. **56**, 1865 (1990).
48. H. K. Tsang, R. V. Penty, I. H. White, R. S. Grant, W. Sibbett, J. B. D. Soole, H.P. LeBlanc, N. C. Andreadakis, R. Bhat, and M. A. Koza, J. Appl. Phys. **70**, 3992 (1991).
49. R. J. Manning, (B. T. Labs., Ipswich), private communication.
50. W. L. Smith, "Two-Photon Absorption in Condensed Media" (section 1.2), in *Handbook of Laser Science and Technology Vol. 3*, M. G. Weber, ed. (CRC, Cleveland, OH, 1986).
51. M. Willatzen, J. Mørk, H. Olesen, J. Mark, and A. Uskov, in *Technical Digest of Quantum Electronics and Laser Science*, (Optical Society of America, Washington, D.C., 1991), paper QThD4.
52. M. Willatzen, A. Uskov, J. Mørk, H. Olesen, B. Tromborg, and A.-P. Jauho, IEEE Photon. Technol. Lett. **3**, 606 (1991).
53. R. Frankenburger and R. Schimpe, in *Technical Digest of Quantum Electronics and Laser Science*, (Optical Society of America, Washington, D.C., 1991), paper QThD5.

54. N. Finlayson, E. M. Wright, and G. I. Stegeman, IEEE J. Quantum Electron. **26**, 770 (1990).
55. R. H. Stolen and C. Lin, Phys. Rev. A **17**, 1448 (1978).
56. M. A. Newhouse, D. L. Weidman, and D. W. Hall, Opt. Lett. **15**, 1185 (1990).
57. K. Naganuma and H. Yasaka, IEEE J. Quantum Electron. **27**, 1280 (1991).
58. P. J. Delfyett, Y. Silberberg, and G. A. Alphonse, Appl. Phys. Lett. **59**, 10 (1991).
59. C. T. Hultgren and E. P. Ippen, Appl. Phys. Lett. **59**, 635 (1991).
60. M. J. LaGasse, K. K. Anderson, H. A. Haus, and J. G. Fujimoto, Appl. Phys. Lett. **54**, 2068 (1989).
61. M. Sheik-Bahae, D. C. Hutchings, D. J. Hagan, and E. W. Van Stryland, IEEE J. Quantum Electron. **27**, 1296 (1991).
62. G. P. Agrawal, Appl. Phys. Lett. **51**, 302 (1987).
63. M. Yamada, J. Appl. Phys. **66**, 81 (1989).
64. R. Nietzke, P. Panknin, W. Elsässer, and E. O. Göbel, IEEE J. Quantum Electron. **25**, 1399 (1989).
65. S. Murata, A. Tomita, J. Shimizu, M. Kitamura, and A. Suzuki, Appl. Phys. Lett. **58**, 1458 (1991).
66. L. F. Tiemeijer, Appl. Phys. Lett. **59**, 499 (1991).
67. R. M. Jopson, K. L. Hall, G. Eisenstein, G. Raybon, and M. S. Whalen, Electron. Lett. **23**, 510 (1987).
68. T. Mukai, K. Inoue, and T. Saitoh, Appl. Phys. Lett. **51**, 381 (1987).
69. G. P. Agrawal, *Nonlinear Fiber Optics* (Academic Press, San Diego, 1989).
70. S. P. Dijaili, J. M. Wiesenfeld, G. Raybon, C. A. Burrus, J. S. Smith, A. Dienes, and J. R. Whinnery, in *Optical Amplifiers and their Applications* (Optical Society of America, Washington, D.C., 1990), paper TuE2.
71. S. P. Dijaili, J. M. Wiesenfeld, G. Raybon, C. A. Burrus, A. Dienes, J. S. Smith, and J. R. Whinnery, "Cross-Phase Modulation in a Semiconductor Laser Amplifier Determined by a Dispersive Technique", to be published in IEEE J. Quantum Electron., Jan. 1992. Preprint provided by A. Dienes.
72. K. W. DeLong and G. I. Stegeman, Appl. Phys. Lett. **57**, 2063 (1990).
73. S.Trillo, S. Wabnitz, J. M. Soto-Crespo, and E. M. Wright, IEEE J. Quantum Electron. **27**, 410 (1991).

5 The KCl:Tl laser : part II

5.1 Introduction

The application of an InGaAsP semiconductor diode optical amplifier as the control-cavity nonlinearity in a coupled-cavity KCl:Tl laser was first reported by Kean et al. in 1988.[1] Although the laser produced pulses as short as 1.4 ps (later reduced to 250 fs, see reference 2), it suffered from regular drop-outs in its output (ie. momentary dips observable in the level of second harmonic signal generated in the autocorrelator). The cause of this instability was not understood, but it was noted that the frequency of the drop-outs was related to the lengths of the cavities.

The experiments using the amplifier had been inspired by the modelling of Blow and Wood who had shown that a pulse broadening element, represented by a saturable amplifier, worked as well as a pulse shortening element (represented by a saturable absorber) in the control cavity.[3] Their model treated these effects in their simplest form, by assuming instantaneous recoveries and ignoring any associated self-phase modulation. Therefore, the saturable amplifier caused temporal broadening and spectral narrowing. The successful operation using such an element was interpreted as an enhancement in the communication of phase information amongst the longitudinal modes, rather than simply the reinjection of energy into the extremities of the pulse spectrum. The pulse shortening element worked when the intracavity and control cavity pulses were added in phase, whilst the pulse broadening element worked when the pulses were added in antiphase. The significance of that result was overlooked, but it was wholly consistent with the subsequent theories which concentrated on pulse shaping due to the interferential addition of the pulses in the master cavity.[4,5]

In the previous chapter, a characterisation was presented of the linear and nonlinear properties of the semiconductor amplifier that was originally used in the experiment of Kean et al.[1,2] This characterisation formed a useful background before attempting further coupled-cavity mode-locking experiments using the amplifier, which will now be described.

5.2 Coupled-cavity mode locking using an InGaAsP optical amplifier

5.2.1 Initial experiments

In initial experiments the original scheme was replicated. The synchronously mode-locked KCl:Tl laser was constructed in the conventional Fabry-Perot configuration, with the (original) optical amplifier located approximately 30-60 cm from the end mirror of the control cavity, shown schematically in Figure 5.1. The beam was coupled into and out of the device using the 20x microscope objective and 0.5 NA collimating lens as described in chapter 4. The control cavity end mirror was mounted on a piezo-electric translator (PZT), driven by the stabilisation electronics described in chapter 3. A quartz birefringent plate of either 2 mm or 1 mm thickness was inserted into the master cavity for bandwidth limitation and wavelength tuning. Output was derived by a placing a beamsplitter (S1) of 50% reflectivity in the control cavity, and a variable neutral density wheel was occasionally inserted within the control cavity to control the power incident on the amplifier. The average power incident on the facet was always limited to less than 40 mW, and was generally nearer 5-15 mW.

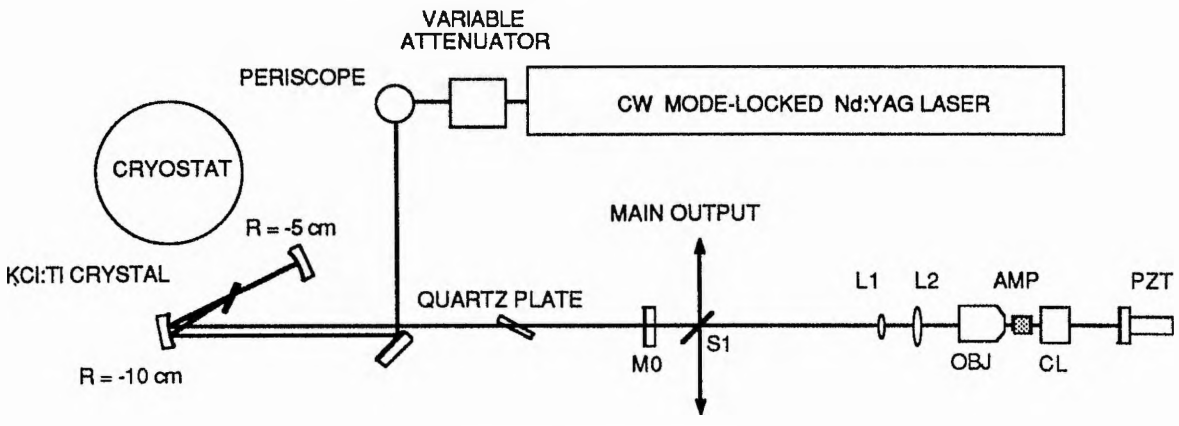

Figure 5.1 Conventional coupled-cavity arrangement used in preliminary experiments. L1 & L2: telescope, OBJ: 20x microscope objective, CL: diode collimating lens, AMP: InGaAsP amplifier, M0: common mirror (reflectivities from 93% to 78% were tried).

Pulse durations of a few picoseconds were readily obtained, and subsequently reduced to a around 400-600 fs by rotating the birefringent plate to reduce the selectivity (optic axis was either perpendicular or parallel to the beam), or by its removal altogether (see Figure 5.2). However, the pulses were accompanied by drop-outs as previously mentioned. The frequency and nature of the drop-outs were extremely sensitive to alignment of the beam through the device, and it was found that short pulses were only obtained when the beam in the control cavity was slightly misaligned. With perfect alignment, feedback from the device facets completely destroyed the synchronous mode-locking. When the alignment was readjusted to obtain short pulses, it was found that the beam returning from the amplifier towards the KCl:Tl crystal only partially overlapped the main beam in the master cavity, and therefore the control cavity had only a weak influence on the pulses in the master cavity. In addition, at drive currents in excess of approximately 35 mA, the amplifier tended to oscillate, with the control cavity forming an external resonator. These features made it difficult to characterise the laser, since the results were highly dependent on the alignment.

On one occasion, continuous drop-out free mode locking was obtained for a period lasting over an hour, with pulses as short as 560 fs being recorded (see Figure 5.3). Unfortunately this performance could not be repeated, and was therefore attributed to a fortuitous alignment. This observation had important implications, for it proved that the drop-outs were not an inevitable side-effect of the mode locking mechanism particular to this type of nonlinearity.

Feedback from the amplifier facets was suspected to be the source of the problem. Although the internal reflectivity of the amplifier had been deduced to be only 0.2% (see chapter 4), the external reflectivity as seen by a beam entering the guide was expected to be different due to a mismatch between the beam shape and the transverse mode in the guide. Measurements of the external facet reflectivity were made by placing a 50% reflectivity beamsplitter in front of the device and comparing the reflected and incident powers. The incident light was chopped in order that the spontaneous emission could be distinguished. The average incident power was set to around 1 mW, and either 30 ps mode-locked pulses or CW light was coupled into the guide. With pulses, a reflectivity of approximately 2% was

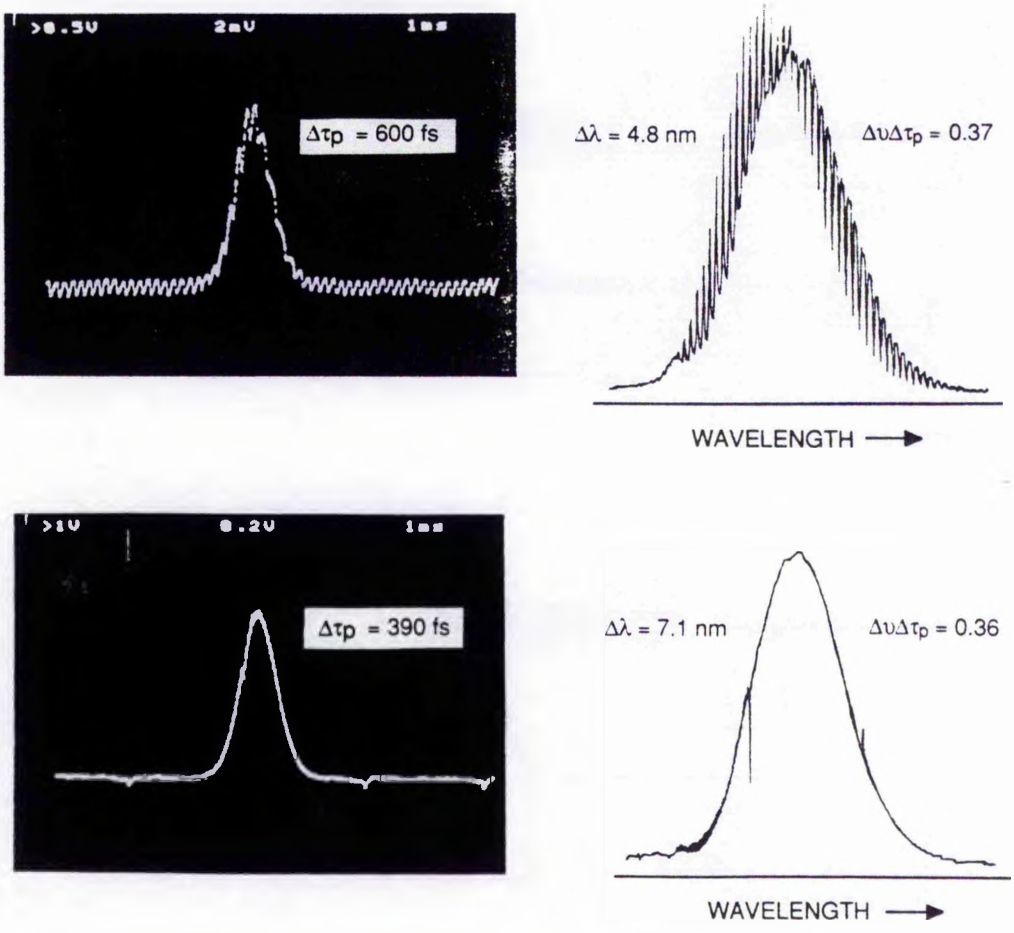

Figure 5.2 Autocorrelations and spectra for typical operation with the conventional cavity arrangement.

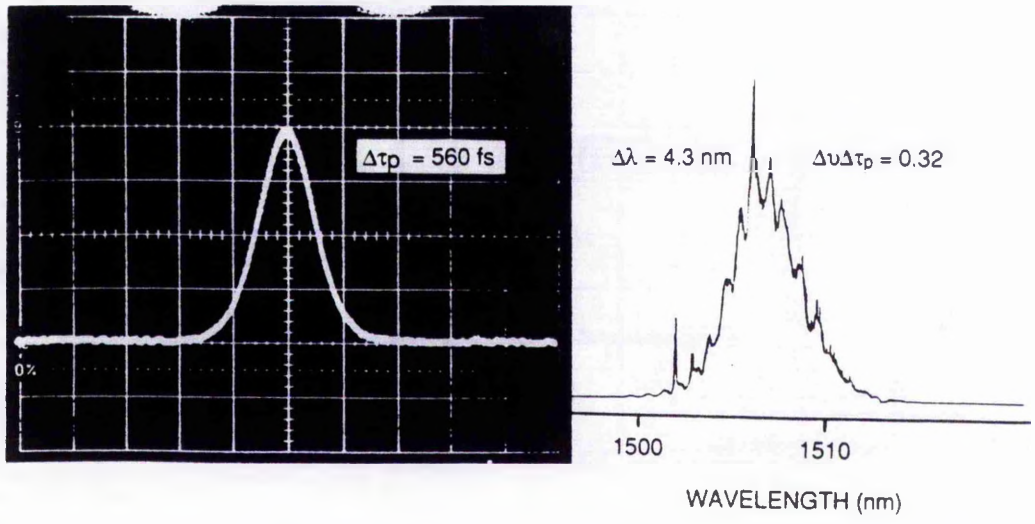

Figure 5.3 Autocorrelation and spectrum for drop-out free operation in the conventional arrangement.

deduced, more or less independent of drive current, but reflectivities as high as 10% were measured when CW light was incident. For CW light, the reflectivity was strongly dependent on drive current, increasing from ~ 2% with no drive current to 10% at 30 mA and then decreasing to 8% at 50 mA.

These results can be explained as follows. For the CW light, the 0.2% internal reflectivity of the exit facet will play a significant role at the higher drive currents, because for the average powers coupled into the guide, approximately -0.8 dBm, the single-pass internal gain approached 16 dB (see Figure 4.11 (a)). At these high gains, the double-pass amplification will be important, and the movement of the gain ripple with changes in drive current may explain the apparent peak in the reflectivity observed for 30 mA current. In the case of the 30 ps pulses, the single-pass gain would only be around 7 or 8 dB, and so the contribution from the exit facet would be less significant, which explains the insensitivity to drive current. Hence, the basic external reflectivity is around 2%. This value should be compared with the reflections from the fibre ends when they are immersed in index matching oil, as described in chapter 3. For refractive indices of 1.47 (germania-doped silica) and 1.41 (Halocarbon Oil 700), the Fresnel reflectivity from either of the ends is only 0.04%. Modal mismatch effects can be ignored due to the similarity of the core and cladding indices. In both cases, retroreflection from the microscope objectives back into the master cavity will be minimal since, in general, the beam will not be perpendicular to the various glass/air interfaces.

Essentially, the high reflectivity of the device prevented an optimal alignment such that the amplitude modulation caused by the feedback pulse interfering with the master cavity pulse was not sufficient to totally dominate the weak gain modulation induced by the Nd:YAG pump pulses. Because coupled-cavity mode locking is a form of passive mode locking,[6] the repetition frequency is normally not determined by the pulses from the Nd:YAG laser, but by the length of the master cavity, with any mismatch with the control cavity length causing a slight "pulling" effect (see chapter 3, section 3.7.2). Inevitably, there is usually a small mismatch in the repetition frequencies of the pump and pumped lasers. This effect was first observed by Mitschke and Mollenauer who monitored the pulse train from

their soliton laser with a fast photodiode and oscilloscope, using the Nd:YAG mode locker drive signal as a trigger source.[6] They observed the 1.5 μm pulses drifting across the screen with a beat signal of upto ± several kHz. Using this simple technique, it was confirmed that the laser described here did not run entirely passively, such that the pulses drifted only 1-2 ns relative to the Nd:YAG pulses before resetting.

This behaviour can be explained by considering the small reduction in gain (due to the finite gain storage time of KCl:Tl) for pulses which are not in phase with the Nd:YAG pulses. The coupled-cavity pulse develops from the synchronously mode-locked pulse and then can drift in time relative to the pump pulse as the passive mode locking takes over. However, due to the relatively weak level of feedback, the round-trip gain for a pulse in phase with the pump pulses may become greater than that for the coupled-cavity pulse after it reaches some time delay from the pump pulse. A second pulse may then form and grow rapidly at the expense of the existing pulse, leading to the eventual destruction of that pulse. This process will repeat in regular intervals in a cycle. In fact, it was sometimes possible to observe the growth of one pulse train as the other diminished using a fast photodiode and oscilloscope. It is quite likely that a reflection from the control cavity may also seed and initiate the second pulse, and this could explain why the phase delay for the drop-out frequently had certain preferred values. The above explanation predicts that operation with a repetition frequency higher than the pump pulses is unlikely, since there will be a significant reduction in gain immediately the laser operates passively. This asymmetry in the cavity length detuning was frequently observed, although it was often possible to run with a negatively detuned cavity length, which might suggest that a reflection initiates the drop-out.

5.2.2 Self-starting mode locking

To prevent optical feedback from the amplifier facets, while permitting the pulses transmitted by the semiconductor amplifier to return to the main laser cavity (or master cavity), the arrangement illustrated in Figure 5.4 was implemented. A high level of isolation between the master cavity and the amplifier facets was ensured by placing the amplifier between two Faraday isolators, resulting in unidirectional transmission through the amplifier. By using this ring configuration (similar in appearance to a Sagnac interferometer although it is

emphasised that the ring transmitted in one direction only) feedback was permitted. The isolator on the input side (Optics For Research, yittrium-iron-garnet (YIG), 2 mm diam. aperture) was followed by a half-wave plate ($\lambda/2$) to maximise the light coupled into the TE mode of the amplifier. As before, the beam was coupled into the guide with a 20x microscope objective, antireflection coated for 1.5 μm. The output was collimated by the usual Melles Griot lens and telescoped down by a factor of 3 to allow transmission through the second isolator (Optics For Research, bismuth-iron-garnet film (BIG), 4 mm diam. aperture), and also to optimise the spatial overlap with the intracavity beam in the master cavity. Two mirrors were placed in a Z configuration between the amplifier and the second isolator in order that the alignment of the return beam could be easily optimised. A second half-wave plate was not available to compensate the rotation due to this isolator and so the return beam was polarised at approximately 45 degrees relative to the master cavity polarisation.

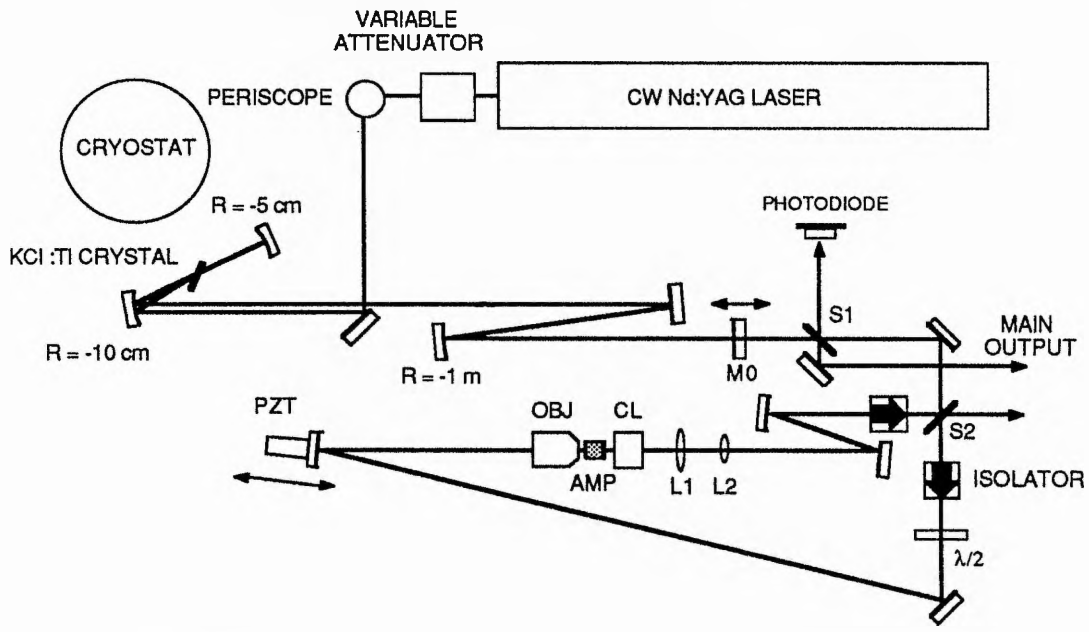

Figure 5.4 Second arrangement, where the amplifier is inserted between two optical isolators.

The master cavity length remained at 182 cm (repetition frequency ≈ 82 MHz), and an output power measured after mirror M0, of ~ 60 mW for a mirror M0 transmission of 7%, and ~ 80 mW for M0 transmissions of either 12% or 22%. Beamsplitter S1 having a reflectivity of 30%, served as the output coupler of the coupled-cavity laser, and also directed

part of the feedback beam returning to the master cavity, onto the large area Ge photodiode to provide a monitor signal for the stabilisation electronics. Beamsplitter S2, reflectivity 50%, directed the feedback signal to the master cavity. The PZT mounted mirror was incorporated in the ring section of the control cavity.

In principle, it was still possible for the amplifier to oscillate in this new arrangement but this was prevented by greater losses, and also by the fact that, for one round trip of the control cavity, the beam made only a single pass of the device rather than a double pass, as in the previous arrangement. In initial investigations using the new configuration, drop-out free, subpicosecond mode locking was easily established. The alignment for optimum operation also coincided with that for best coupling efficiency into the device, verifying that the facet reflectivity had hindered the previous studies. The laser output was again monitored using the fast photodiode, triggered as before from the Nd:YAG mode-locker drive electronics. This time, the laser was observed to operate passively, and the repetition frequency was unaffected by the pump pulses, however, the output power was modulated by 1-2% amplitude modulation due to the beating effect between the two lasers (see Figure 5.5 (a)), an effect that had been occasionally observed when using an optical fibre in the control-cavity. Drop-outs could be induced by misaligning the control-cavity, and reducing the feedback power. To study the beating of the two pulse trains, the electrical pulse train produced by the Ge photodiode (which monitored the colour-centre laser) was mixed with the sine wave generated by the BPW 28 photodiode / tunnel-diode oscillator system (which monitored the Nd:YAG laser) using a double-balanced mixer (Mini-Circuits SRA-1). When the laser operated in an entirely passive manner, the kHz beat signal was approximately sinusoidal as illustrated in Figure 5.5 (b), indicating that the two pulse trains were continuously "walking" through each other. When the drop-outs were induced, the signal had a sawtooth profile, with the drop-outs (or phase resets) shown as vertical lines (see Figure 5.5 (c)).

Using this arrangement, self-starting mode locking could be obtained. It was found that mode locking could be reliably started by temporarily reversing the polarity control (to the LHS) of the stabilisation electronics to make the PZT-mounted mirror position ramp repeatedly. With good alignment, mode locking was observed at interferometric intervals

during the *reset* phase of the ramp cycle. If the cavity length was set such that the second harmonic remained at the end of the reset phase, the polarity could be switched (to the RHS) to maintain the mode locking. Mode locking could also be initiated with the polarity control positioned to the RHS, but with the speed and gain controls increased to improve the speed response. In other words, both direction and speed were important for initiating mode locking. It was determined that a rapid *expansion* of the cavity length was required, with a speed estimated as approximately 8 mm/s (1 interference fringe in 200 μs).

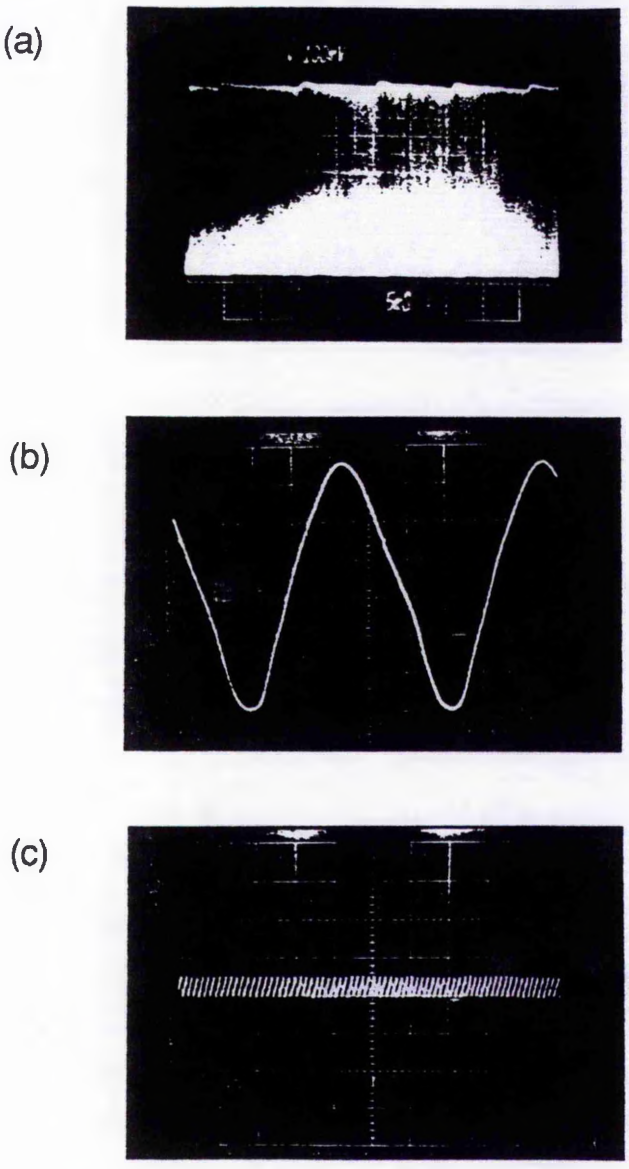

Figure 5.5 (a) Sawtooth modulation of the pulse train. (b, c) Mixing of the pump laser and coupled-cavity laser signals: (b) beat signal obtained with good alignment, (c) regular resets with poor alignment.

A number of lasers have been reported to mode lock with continuously moving mirrors, although velocities of the order of 4 cm/s have been used,[7-9] with the coupled-cavity lasers being particularly relevant.[8,9] In contrast to the effect documented here, in those experiments, mode locking was observed for both directions of travel, over ranges of a 1 mm or so with no interferometric drop-outs. A rapid mirror movement has been found to initiate self mode locking[10] and Kerr-lens mode locking[11] in Ti:sapphire lasers. Haus and Ippen have suggested that rapid changes in the cavity length can overcome the deleterious effects of etalons and spurious reflections in the cavity.[12] An alternative explanation for the system described here is given in the discussion section.

Mode locking was observed with amplifier drive currents exceeding 20 mA but the shortest pulses were observed at current levels above 35 mA. It was found that by lowering the transmission of mirror M0 from 22% to 7%, the pulse durations could be reduced from 440 fs to 280 fs (sech^2 intensity profiles assumed.) The intensity autocorrelation and corresponding spectrum for such 280 fs pulses are shown in Figure 5.6, with the corresponding interferometric autocorrelation depicted in Figure 5.7. In generating these shortest pulses, the bandwidth-duration product increased from around 0.34 to 0.40, indicating either a small change in pulse shape or the presence of some excess frequency chirp.

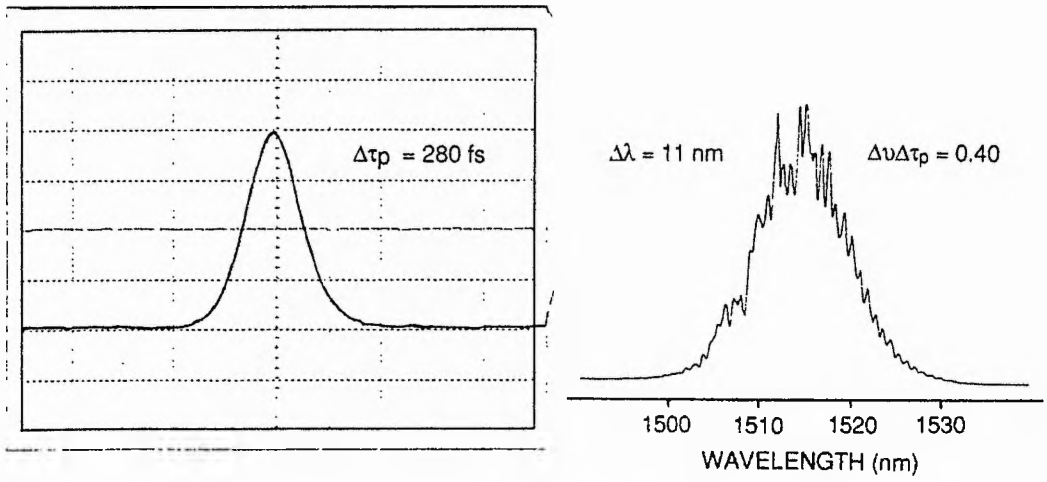

Figure 5.6 Intensity autocorrelation and corresponding spectrum. (The fine structure on the spectrum is due to etalon effects within the KCl:Tl crystal and/or the cryostat windows.)

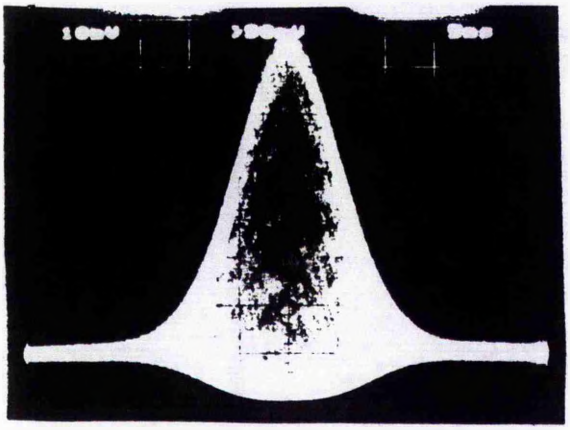

Figure 5.7 Interferometric autocorrelation corresponding to the data in Figure 5.6.

Figure 5.8 compares the spectra of the pulses from the master cavity with those transmitted by the amplifier under similar conditions to the results just described. Clearly, the pulses returning to the master cavity are spectrally broadened by the amplifier to longer wavelengths, consistent with self-phase modulation due to gain saturation. However, for this duration, the ultrafast effects described in chapter 4 will be significant, and the source of the frequency chirp cannot be identified with any certainty. The two spike features superimposed on the return spectrum are evidence of a pedestal. Their prominence in the return spectrum can be explained by considering the greater amplification given for a low intensity pedestal compared to a short pulse. These spike features were almost always observed when using the amplifier, but their contribution to the output could be reduced to less than 1% by reducing the reference level of the PZT stabilisation electronics.

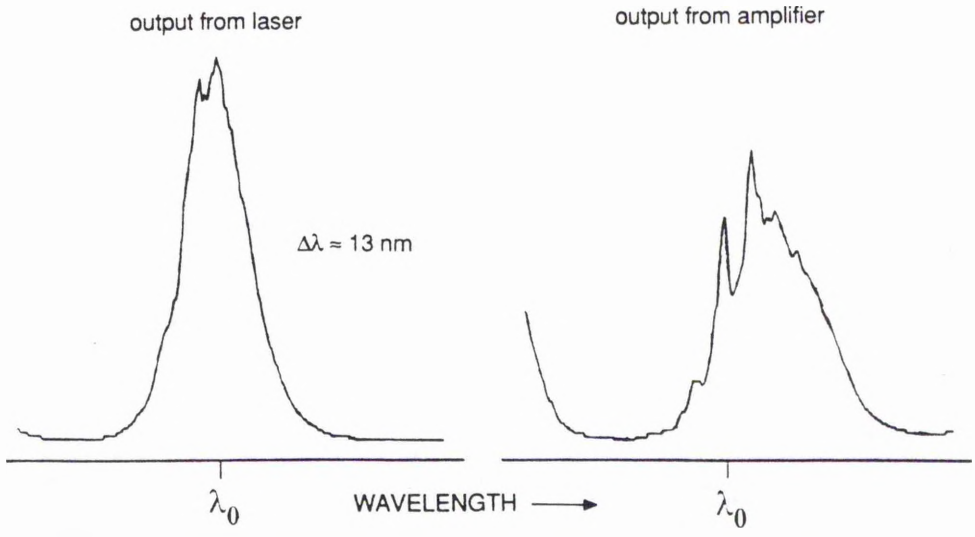

Figure 5.8 Comparison of spectra for pulses exiting the master and control cavities.

Self-starting operation was also observed for bias currents of approximately 2 mA. Mode locking was not achieved when M0 had a transmission of 7%, whereas pulse durations of 480 fs and 560 fs were obtained when M0 had transmissions of 12% and 22% respectively (see Figure 5.9). The relation between the pulse duration and drive current is illustrated in Figure 5.10 for a mirror M0 transmission of 12%. In general, the quality of the mode locking was inferior to that obtained with the higher bias currents, and approximately 3% amplitude noise was apparent on the pulse train.

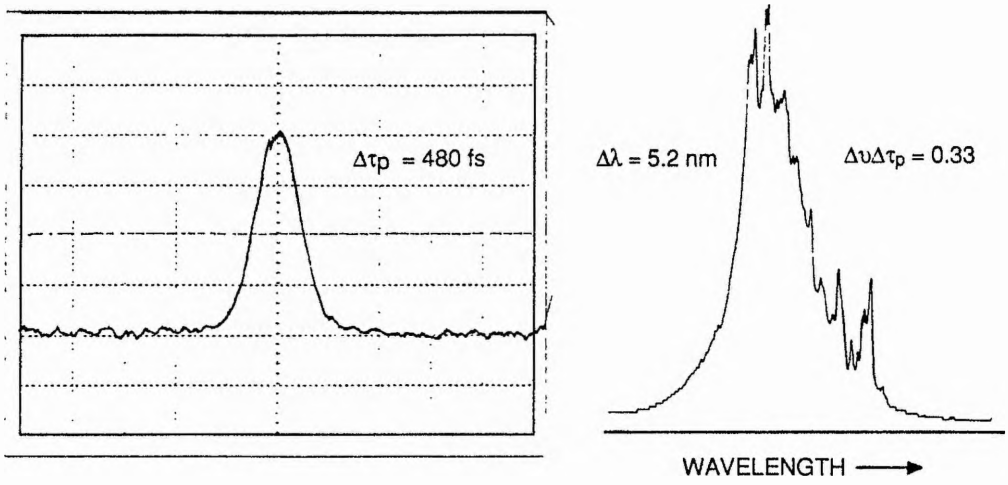

Figure 5.9 Autocorrelation and spectrum for pulses obtained for a drive current of 2 mA.

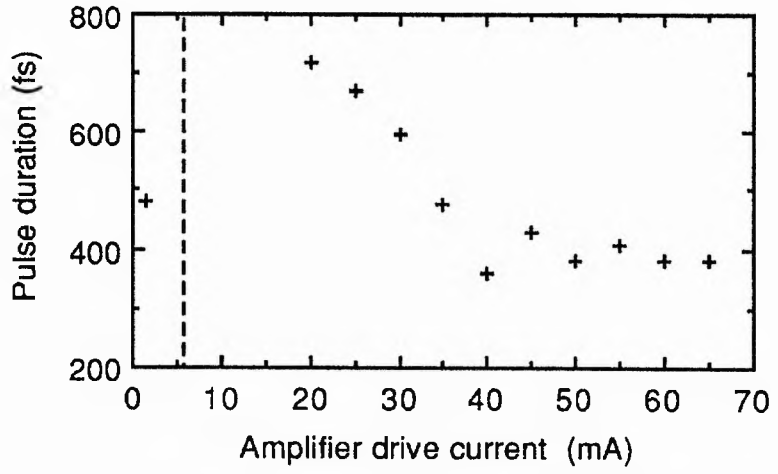

Figure 5.10 Pulse duration as a function of amplifier drive current. Note that mode locking was obtained at currents in excess of the oscillation threshold (55 mA). The vertical dashed line denotes the transparency current.

5.2.3 Discussion

The fact that mode locking was not observed at drive currents close to transparency implies that the dominant mechanism in the amplifier (at least during the initial evolution) is the resonant nonlinearity associated with carrier density changes arising from gain saturation and absorption saturation. The estimated pulse energy coupled into the amplifier was in the 3-10 pJ range, sufficient to cause strong saturation, see chapter 4.

As discussed in chapter 4, the resonant nonlinearity associated with the saturation of gain and loss in the amplifier combines amplitude modulation with significant phase modulation. These refractive index changes are much larger than those associated with an atomic medium, and can result in phase changes of the order of π radians. Therefore, any discussions on the pulse shaping caused by the interference of the pulses after recombining in the master cavity must include the possible effect of the amplitude *and* phase modulation caused by the resonant nonlinearity. Thus, the effect of various nonlinearities on a coupled-cavity mode-locked laser will be considered, and suitable operating conditions will be suggested.

Firstly, pure amplitude modulation by an instantaneous nonlinearity will be discussed. Gain saturation or absorption saturation will cause temporal broadening or temporal narrowing of a pulse respectively, and hence the phase bias between the interfering pulses should be set for destructive ($\phi = \phi_b \approx \pi$) or constructive ($\phi = \phi_b \approx 0$) interference respectively. When the nonlinearity has a long recovery time, the amplitude modulation will be asymmetric. With gain saturation, the broadening will occur mainly to the leading edge and with absorption saturation, the erosion will be confined to the leading edge. The pulses should be added together as before, destructively for a saturable amplifier and constructively for a saturable absorber, however additional pulse shaping will be required to balance the asymmetric shaping. This can be provided by (dynamic) gain saturation in the master cavity, and the situation is then closely related to slow absorber passively mode-locked lasers. The principal advantage of the coupled-cavity arrangement is that the interference effect allows pulse shortening to be obtained even when using nonlinearities which cause temporal broadening.

In the case of a pulse shortening element, when the pulses require to be added constructively, in certain circumstances it is possible to obtain mode locking without active control of the cavity lengths. This has been observed by Keller et al. where a multiple-quantum well saturable absorber was used in the control cavity.[13-15] The laser operated with a mismatch in the lengths of its master and control cavities, and adjusted its operating wavelength automatically in an attempt to obtain constructive interference (in order that it satisfied the maximum emission principle, see reference 16). This behaviour can be understood by considering the following. If both the master and control cavities are identical in length to within an optical cycle, the phase bias ϕ_b between the interfering pulses is constant with wavelength. However, if there is a large mismatch in the lengths of the two cavities, say a few hundred microns, the phase bias will vary sinusoidally with operating wavelength, and the laser can then seek the wavelength for constructive interference, $\phi_b = 0$. This may also explain the operation of actively mode-locked coupled-cavity lasers where no mention was made of active length stabilisation.[17]

Secondly, consider the effect of pure self-phase modulation. The use of instantaneous Kerr-like refractive nonlinearities in coupled-cavity lasers is well understood, due to the continued dominance of optical fibres in this field. The maximum nonlinear phase shift ϕ_{nl} occurs at the peak of the pulse and in simple terms, pulse shortening is obtained when the phase bias is set such that the peaks of the pulses add constructively

$$\phi = \phi_b + \phi_{nl} \approx 0 \qquad (5.1).$$

For a positive n_2, the phase bias should lie in the range $-\pi < \phi_b < 0$, with a bias around $-\pi/2$ being particularly favourable for initiation because the conversion from phase modulation to amplitude modulation is at its most efficient (see Figure 3.30). These conditions imply that the largest nonlinear phase shift for which the system behaves as a straightforward saturable absorber is around π radians. In practice, phase shifts of around $3\pi/2$ can be observed on the pulse returning from the control cavity, as mentioned in chapter 3. This might be due to a small amount of chirp already present on the master cavity pulse.

If the refractive nonlinearity has a slow recovery time, then the situation is less clear. The phase shift, or more correctly the phase difference, is now proportional to the integrated energy passing through the nonlinearity. Again, one requires the peak of the pulse to be returned in phase with the master cavity pulse, ie. $\phi = 0$. For a positive index change, the phase bias should again be negative. For example, if the maximum phase difference between the front and back of the feedback pulse was π radians, the optimum phase bias ϕ_b would be $-\pi/2$. A maximum phase difference of just less than 2π would work with a phase bias close to $-\pi$. The problem arises during the recovery phase, well after the pulse has passed through the nonlinear element. During the recovery, the phase will pass through $\phi = 0$ again, allowing any noise to grow at this particular delay after the pulse. Therefore, when using a slow refractive nonlinearity, some dynamic gain saturation will be required in order to suppress this noise. It is also obvious that the gain must then have a slower recovery time than the nonlinearity.

If we accept that that dynamic gain saturation is required, then another possibility can be considered. If the pulse shaping from gain saturation is relatively strong, and the feedback power is weak, it may be possible for gain saturation to erode the trailing edge even when the trailing edges are added constructively. In this situation, there will be no maximum allowable phase bias, only the restriction that the phase difference between the leading edge and the peak be of the order of π radians.

Thirdly, the combined effects of amplitude modulation and phase modulation can be considered. The amplitude modulation of the control-cavity pulse merely affects the magnitude of the amplitude modulation exerted on the master cavity pulse, but not its sign, which is controlled by the phase modulation. The broadening or shortening of the control-cavity pulse will influence its ability to control the master pulse, but the overall shortening process is fundamentally linked to the phase effects, because they determine whether the interference is constructive or destructive. Therefore, it is argued that the pulse shortening process in the master cavity is dominated by the phase modulation. With the slow nonlinearities present in the optical amplifier, it is presumed that the amplitude modulation effects in the amplifier are relatively unimportant, and that the phase modulation shapes the

leading edge of the pulse, with assistance from dynamic gain saturation in the KCl:Tl crystal controlling the trailing edge. Ippen at al. reached a similar conclusion about the need for gain saturation when using slow nonlinearities in the control cavity.[18] This requirement might explain why the pulse duration was reduced by lowering the transmission of mirror M0, thereby increasing the pulse energy in the master cavity.

The strengths of the various refractive nonlinearities present in the amplifier should be compared. The index changes associated with the saturation of gain and loss can be characterised by an effective n_2 when the pulse duration is much greater than the recovery time. This would be true during the initial stages, if the laser was oscillating on a few closely spaced axial modes, which would result in mode beating features of, say, 1 or 2 ns in duration. For $\Delta\tau_p >> \tau_{rec}$, $dh/dt \approx 0$ and equation (4.22) may be written as

$$\frac{g_0 L - h(t)}{\tau_{rec}} = \frac{P_{in}(t)}{E_{sat}} (\exp[h(t)] - 1) \qquad (5.2).$$

With modest levels of saturation, $\exp[h(t)] \approx \exp[h_0] >> 1$, and equation (5.2) may then be rewritten as

$$\Delta h \approx - \frac{P_{in}(t)\, \tau_{rec}}{E_{sat}} \exp[h_0] \qquad (5.3)$$

where $g_0 L - h(t)$ has been replaced by $-\Delta h$. The change in the modal refractive index Δn caused by a change in carrier density ΔN is given by (see equation 4.26)

$$\Delta n = - \frac{\alpha\lambda a}{4\pi} \Gamma(\Delta N) = - \frac{\alpha\lambda \Delta g}{4\pi} \qquad (5.4).$$

With modest saturation Δg is constant along the guide length L and so $\Delta g \approx \Delta h/L$, therefore, it can be shown that

$$\Delta n \approx + \frac{\alpha\lambda}{4\pi} \frac{P_{in}(t)\, \tau_{rec}}{L\, E_{sat}} \exp[h_0] \qquad (5.5).$$

This can now be rearranged to give

$$\Delta n = + \frac{\alpha\lambda a\tau_{rec}}{4\pi h\upsilon L} \exp[h_0]\ I_{in} = n_2 I_{in} \qquad (5.6)$$

where $h\upsilon$ represents the photon energy and $\exp[h_0]$ is the linear small-signal gain factor, eg. 100 for a 20 dB device. This is essentially the same result as derived by Agrawal and Olsson,[19] but is given here in terms of the input rather than the output intensity. Using typical parameters for the amplifier used here, ie. $\exp[h_0] \approx 40$ at the wavelength where mode locking is observed, $\tau_{rec} \approx 0.5$ ns, $a \approx 2 \times 10^{-16}$ cm^2, and $\alpha \approx 5$, giving an effective n_2 of approximately $+5 \times 10^{-8}$ cm^{2}W^{-1}. This tends to overestimate the n_2 since the small-signal gain has been used, but it does provide a useful insight. The corresponding γ value can be estimated to be approximately 3×10^{10} km^{-1}W^{-1}, *ten* orders of magnitude larger than an optical fibre. Even when the large difference in lengths and the poorer coupling efficiencies of the amplifier are taken into account, the amplifier is still more than five orders of magnitude more nonlinear than a typical length of fibre. The refractive nonlinearity associated with the absorption saturation is a factor of 400 weaker (also calculated in terms of input power, hence the term $\exp[h_0] \approx 0.1$). In comparison, the ultrafast refractive nonlinearity is a factor of 2500 times weaker than the one associated with gain saturation.

During the initial phase of the evolution, the slow nonlinearities clearly dominate over the ultrafast effect, which explains why mode locking was not observed at drive currents close to transparency. As the pulse becomes shorter, the ultrafast effect will be become increasingly important, and time resolved measurements of the index changes indicate that these effects dominate in the femtosecond regime.[20] Since the ultrafast effect is around two orders of magnitude greater than the nonlinearity of a typical length of fibre, it is perhaps surprising that it does not initiate the process, but it should be remembered that the level of feedback is also considerably less (at least a factor of ten) compared to the case of a fibre.

To illustrate the effect of the self-phase modulation associated with gain saturation in the amplifier during the pulse evolution, the program listed in Appendix 3 was used to model the distortion for five different pulse durations ranging from 2 ns to 100 ps. The input pulse was assumed to have an energy of 5.2 pJ, equal to the saturation energy and close to the

range of pulse energies estimated to be coupled into the device (4-8 pJ). Table 5.1 summarises the parameters determined by the model for a drive current of 40 mA. Figure 5.11 shows the dependence of the amplifier gain on pulse duration with a fixed input pulse energy. (For pulses less than 10 ps, nonlinear absorbing effects and intraband relaxation will cause additional decreases in gain not shown.)

Parameter	Symbol	Value
Carrier density at I_t	N_t	1.36×10^{18} cm^{-3}
Carrier density at 40 mA	N_2	3.27×10^{18} cm^{-3}
Differential gain	a	1.67×10^{-16} cm^2
Saturation energy	E_{sat}	5.2 pJ
Input energy	E_{in}	5.2 pJ
Recovery time	τ_{rec}	490 ps

Table 5.1 Parameters determined for a drive current of 40 mA. Small-signal gain was assumed to be +19 dB, and the transparency current, 6 mA.

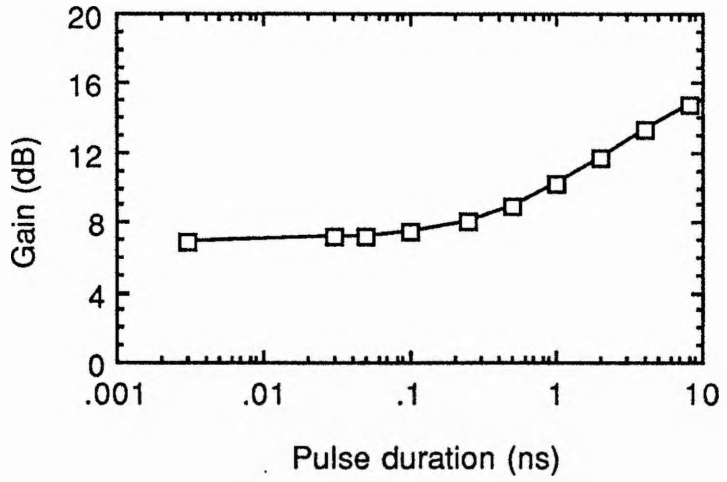

Figure 5.11 Theoretical gain as a function of the pulse duration. Input pulse energy = 5.2 pJ = E_{sat}.

In the initial stages of the evolution, when the pulse might be 2 ns long, the nonlinearity is effectively fast and almost symmetrical pulse broadening due to gain saturation is evident (see Figure 5.12). At this stage the initial phase shift (relative to the small-signal phase shift at the leading edge of ~ -11 radians) is already $+3\pi/2$ radians. As the pulse

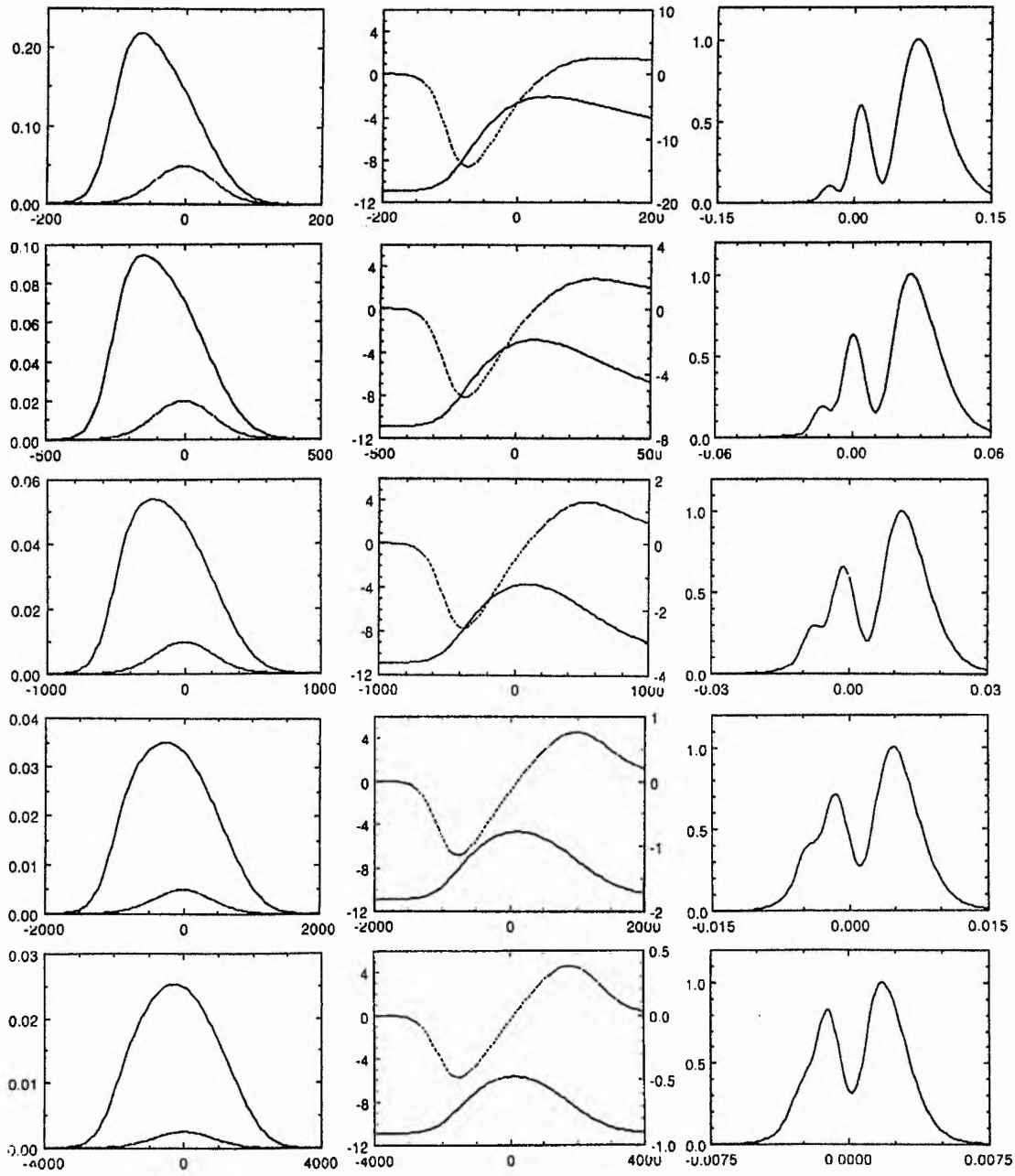

Figure 5.12 Pulse distortion related to gain saturation for pulse durations of (top to bottom): 100 ps, 250 ps, 500 ps, 1 ns and 2 ns (input pulse energy fixed at 5.2 pJ). The left hand column shows the output pulse (*Y* axis in W, *X* axis in ps) , while the right hand column shows the spectrum (*X* axis in nm). The centre column shows $\Delta\phi$ (left hand *Y* axis in radians) and $\Delta\upsilon$ (right hand *Y* axis in GHz), with the *X* axis in ps.

duration is decreased, the nonlinearity becomes slow compared to the pulse duration, and the total phase shift limits at around $+5\pi/2$ radians. Such a large phase shift would be expected to cause unstable operation, but it should be remembered that the single-lobed broadening

observed experimentally (Figure 5.8) at the steady state is consistent with a much lower phase shift.

It was noted that the polarity control of the stabilisation electronics was the same for drive currents above or below transparency, and yet the refractive nonlinearities associated with gain and absorption saturation have opposite signs. This might indicate that the ultrafast nonlinearity dominates at the steady state. The concept of a switch between the slow and fast nonlinearities during the pulse evolution introduces a dilemma. The nonlinearity associated with gain saturation and the ultrafast nonlinearity have opposite signs, and therefore require opposite signs of phase bias for pulse shortening. The rapid movement of the PZT during the initiation phase might be altering the phase bias as the pulse evolves, but this ramping was not required in later experiments with the NaCl:OH^- laser (chapter 6).

The most obvious difference between using Kerr media and the optical amplifier is the change in transmission with pulse duration. The feedback power incident on the common mirror was estimated by measuring the power incident on the stabilisation photodiode. In the case of saturable amplification, the power incident was 1.6 mW before start-up, falling to only 280 μW once short pulse mode locking was obtained. With output powers of 60-80 mW at the common mirror M0, the intracavity power can be estimated to be 850-360 mW depending on the output coupler. The feedback power transmitted into the master cavity can be estimated to be in the range 350 μW to 20 μW, therefore, the ratio of the amplitudes of the feedback beam to the intracavity beam can be as low as 200:1 (cf. 10:1 or 20:1 for the fibre). For saturable absorption, the level of feedback is even weaker, with powers incident on M0 of only 130 μW, rising to 170 μW when mode locking was obtained. It is not surprising that mode locking using saturable absorption was not observed when mirror M0 was reduced to 7% transmission.

These intensity-related reductions in transmission will tend to limit the pulse shortening. For the femtosecond pulses, group-velocity dispersion (GVD) may have significant influence on the temporal shaping and chirping of the pulses in the control cavity. The active materials in the isolators were expected to make a sizeable contribution. Using a Sellmeier expansion[21] for YIG, $d^2n/d\lambda^2$ of +0.051 μm^2 was calculated for 1500 nm, giving

β_2 = +305 fs^2/mm. To induce a 45^0 polarisation rotation, a YIG crystal of around 2 mm thickness is required.[22] For pulses of Gaussian profile, a percentage broadening factor of around 10% is predicted for a pulse FWHM of 60 fs (using equation (1.29)), therefore distortion due to this isolator is expected to be negligible. The polariser material was unknown but was expected to contribute even less dispersion. No refractive index information could be found for the BIG material, and so both isolators were tested by measuring the broadening of pulses. Using 90 fs pulses generated by the Michelson coupled-cavity laser described in chapter 3, temporal broadening of about 2% and 8% was measured for the BIG and YIG isolators respectively, confirming that the isolators contributed negligible distortion for the shortest pulses obtained (280 fs).

The amplifier itself will contribute considerable dispersion due to the proximity of the band edge, the high refractive index, and waveguide dispersion. Recently published measurements of the group delay in a 1.35 μm amplifier indicate a GVD of $D \approx -10^4$ ps/(nm.km).[23] Assuming a similar value applies to 1.5 μm devices, the parameter β_2 can be estimated to be +1.2 x 10^4 fs^2/mm, which gives 10% broadening for a pulse FWHM of 160 fs. The low transmission of the device for femtosecond pulses made a direct measurement of any distortion impracticable.

It should be noted that *if* the ultrafast refractive nonlinearity is assumed to be instantaneous, then there is a possibility of solitonic effects due to the combination of normal GVD and negative n_2. For the 280 fs pulse with an energy of around 6 pJ, a peak power of 20.1 W can be calculated. This gives a nonlinear length L_{NL} of 0.024 mm and a dispersion length L_D of 2.1 mm, ie. $N \approx 9$ propagation. For this soliton number, the optimum compression distance is 160 μm,[24] with a compression factor of 37, ie. a duration of only 8 fs (two optical cycles)! The nonlinear absorption probably prevents any significant narrowing, although this effect is sufficiently interesting to warrant further investigation.

A further distortion mechanism has recently been suggested by Agrawal.[25] He modified his earlier theory of pulse distortion in semiconductor amplifiers to include the effect of the finite gain bandwidth (or gain dispersion), and predicted considerable temporal broadening and distortion of 1 ps pulses, even with energies only 0.1 x E_{sat}. It should be

noted that Agrawal's publication does not take account either the carrier heating effect nor the ultrafast refractive nonlinearity described in this thesis, and therefore it is not clear whether that model is valid.

5.3 Summary

By using an InGaAsP optical amplifier in the control cavity, self-starting coupled-cavity mode locking of the KCl:Tl laser has been obtained. The primary reason for the self-starting is the very high strength of the nonlinearities present in the device when compared to an optical fibre. In addition, the use of isolators to eliminate parasitic optical feedback is also likely to have assisted the self-starting operation.

The major disadvantages when using a semiconductor amplifier are the large coupling losses and the nonlinear absorption, although if the coupling efficiencies were improved, the power in the device would probably be too large for stable operation.

Coupled-cavity mode locking of a semiconductor laser using another, identical laser as the nonlinearity has recently been reported.[26] At first, this seems reasonable, since there is no large power mismatch. However, it was previously argued that when using slow nonlinearities, the nonlinear element requires to have a faster recovery than the gain in order that stable single pulse operation is obtained. It was shown in chapter 4 that the gain recovery time of the semiconductor amplifier is inversely related to the drive current. The low drive currents associated with saturable absorption imply relatively long recovery times, certainly longer than the recovery of the dominant, higher current device, thus violating the condition suggested above. No further analysis of the results can be made until more details are published.

5.4 References

1. P. N. Kean, R. S. Grant, D. W. Crust, X. Zhu, D. Burns, and W. Sibbett, in *Technical Digest of Conference on Lasers and Electro-Optics* (Optical Society of America, Washington, D.C., 1988), paper PD7.
2. P. N. Kean, X. Zhu, D. W. Crust, R. S. Grant, N. Langford, and W. Sibbett, Opt. Lett. **14**, 39 (1989).
3. K. J. Blow and D. Wood, J. Opt. Soc. Am. B **5**, 629 (1988).
4. J. Mark, L. Y. Liu, K. L. Hall, H. A. Haus, and E. P. Ippen, Opt. Lett. **14**, 48 (1989).
5. M. Morin and M. Piché, Opt. Lett. **14**, 1119 (1989).
6. F. M. Mitschke and L. F. Mollenauer, IEEE J. Quantum Electron. **QE-22**, 2242 (1986).
7. P. W. Smith, Appl. Phys. Lett. **10**, 51 (1967).
8. P. M. W. French, S. M. J. Kelly, and J. R. Taylor, Opt. Lett. **15**, 378 (1990).
9. P. G. J. Wigley, P. M. W. French, and J. R. Taylor, Electron. Lett. **26**, 1239 (1990).
10. D. E. Spence, P. N. Kean, and W. Sibbett, Opt. Lett. **16**, 42 (1991).
11. L. Spinelli, B. Couillaud, N. Goldblatt, and D. K. Negus, in *Technical Digest of Conference on Lasers and Electro-Optics* (Optical Society of America, Washington, D.C., 1991), paper CPDP7.
12. H. A. Haus and E. P. Ippen, Opt. Lett. **16**, 1331 (1991).
13. U. Keller, W. H. Knox, and H. Roskos, Opt. Lett. **15**, 1377 (1990).
14. U. Keller, T. K. Woodward, D. L. Sivco, and A. Y. Cho, Opt. Lett. **16**, 390 (1991).
15. H. A. Haus, U. Keller, and W. H. Knox, J. Opt. Soc. Am. B **8**, 1252 (1991).
16. G. H. C. New, Rep. Prog. Phys. **46**, 877 (1983).
17. M. DiDomenico and V. Czarniewski, Appl. Phys. Lett. **6**, 150 (1965).
18. E. P. Ippen, L. Y. Liu, and H. A. Haus, Opt. Lett. **15**, 183 (1990).
19. G. P. Agrawal and N. A. Olsson, IEEE J. Quantum Electron. **25**, 2297 (1989).
20. C. T. Hultgren and E. P. Ippen, Appl. Phys. Lett. **59**, 635 (1991).
21. He Yu-Quan and Guan Tie-Liang, Acta Phys. Sin (China) **31**, 138 (1982).
22. R. C. Booth and E. A. D. White, J. Phys. D: Appl. Phys. **17**, 579 (1984).
23. K. Naganuma and H. Yasaka, IEEE J. Quantum Electron. **27**, 1280 (1991).
24. G. P. Agrawal, *Nonlinear Fiber Optics* (Academic Press, San Diego, 1989).
25. G. P. Agrawal, IEEE J. Quantum Electron. **27**, 1843 (1991).
26. E. M. Dianov and O. G. Okhotnikov, IEEE Photon. Technol. Lett. **3**, 499 (1991).

6 The NaCl:OH^- laser

6.1 Introduction

Mollenauer and his coworkers developed a colour-centre laser using F_2^+ centres in NaCl for soliton propagation experiments in the 1.5 μm spectral region.[1] This laser was superseded with the development of the KCl:Tl^0(1) laser in 1982 (see chapter 3), although those crystals also suffered from a fading of their output power, but over a much longer timescale, around 6-12 months. More recently, long-lived, nonfading laser operation has been observed using F_2^+-like centres in additively coloured NaCl crystals.[2-4] This new centre, designated $(F_2^+)_H$, has absorption and emission bands similar in shape to the ordinary F_2^+ centre, but shifted by a few tens of nanometres. Although the crystals require continuous auxiliary illumination to counteract reorientational bleaching, they are capable of output powers in excess of 2 W and a tuning range approaching 300 nm.[5]

The application of various types of mode locking to a NaCl:OH^- colour-centre laser will be described in this final experimental chapter. Many of the techniques were only briefly evaluated, and there remains considerable scope for further development of this laser.

6.2 The $(F_2^+)_H$ centre in NaCl:OH^-

In their attempt to produce a stable colour-centre laser emitting at 1.5 μm, Pinto and coworkers additively coloured NaCl crystals doped with potassium K^+ ions. In their first paper[2] describing the operation of a laser based on the new centre, the stabilising ion was therefore identified as K^+. Subsequently it was found that unintentionally incorporated OH^- impurity ions were the stabilising ingredient.[3] The performance of the laser was then optimised by adjustment of the NaOH concentration at the melt stage prior to growth of the NaCl boules. The addition of Na_2O_2 to NaCl at the melt stage has produced similar centres.[4]

Like the NaCl:F_2^+ and KCl:$Tl^0(1)$ centres, the NaCl:$OH^-(F_2^+)_H$ centre may be efficiently excited by Nd:YAG lasers operating on the 1064 nm transition. An auxiliary stabilising beam excites the centre, either directly or by a two-stage process where the 1064 nm pump light assists, to the $2_p\pi_u$ state, from where a radiationless decay takes place to the $2_p\sigma_u$ state (the upper laser level in the excited state configuration) accompanied by reorientation. A full discussion of the processes involved and a description of the optical properties of the centre is given elsewhere.[6] The centre consists of an F_2^+ centre lying along a <110> axis, accompanied by an O^{2-} ion in a neighbouring Cl^- ion site as shown in Figure 6.1. The advantages of the F_2^+ centre, such as high efficiency and broad tunability are retained, but with the elimination of the tiresome fading.

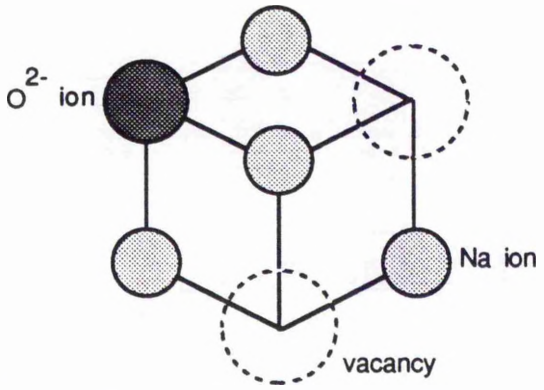

Figure 6.1 Configuration of the $(F_2^+)_H$ centre proposed by Georgiou et al.[6]

Parameter	Value	Reference
Refractive index of NaCl	1.53	**7**
Absorption peak	1090 nm	**6**
Emission peak	1550, 1590 nm	**6,4**
Emission FWHM	33, 30 THz	**6,4**
τ_{rad}	150 ns	**6**
η (quantum efficiency)	1	**6**
σ_{em}	8×10^{-17} cm^2	

Table 6.1 Optical characteristics of the $(F_2^+)_H$ centre in NaCl at 77K.

The optical properties of the centre, including an estimate of the stimulated emission cross-section, are summarised in Table 6.1. The cross-section was estimated using equation (1.1), which assumes a random orientation of centres, and hence may be an underestimate when a significant proportion of the centres are aligned by the stabilisation beam into the optimum orientation.

The crystals used in these experiments had approximately 5×10^{-4} NaOH added to the NaCl melt.[8] The preparation of the laser crystals will be described briefly (see reference 9 for a more detailed description). The boule was cleaved into $(10 \times 10 \times 2.5)$ mm^3 crystals, and polished on fabric mats using fine aluminium powder followed by diamond finishing compound. The crystals were additively coloured using the 'bomb' technique.[2] Two stainless steel vacuum flanges were machined such that when bolted and sealed together, a void was left between them to hold the crystal together with a few grams of Na metal. The bomb was then placed in a 700^{0}C oven for around one hour, allowing the Na to migrate through the NaCl crystal, thereby creating F centres. On removal from the oven, the bomb was cooled quickly to prevent the formation of colloids. Usually, to obtain the correct olive green colour, it was necessary to reheat the crystal, but this time sealed in a piece of thin copper foil to allow a more rapid quenching.

Prior to use the crystal was given a final polish in darkness to remove any blemishes caused by the colouration process, and then loaded into the cryostat. The F centres aggregated to form F_2^+ centres when exposed to F band light (455 nm) from a filtered mercury arc lamp for 60 minutes. After cooling the crystal to 77 K, a second shorter exposure to F band light resulted in the formation of the $(F_2^+)_H$ centres. This was confirmed by monitoring a shift in the peak of the F_2^+ absorption band from 1020 nm to 1090 nm.

6.3 Synchronous mode locking

The NaCl:OH⁻ laser was excited by the Spectra-Physics model 3800 Nd:YAG laser. The stabilisation beam was conveniently derived by frequency doubling a portion of the 1064 nm beam in a KTP doubling unit (Spectra-Physics 3220).[10] Average powers in excess of 30 mW were required at 532 nm, and it was necessary to mode lock the Nd:YAG laser to obtain reasonable conversion efficiencies (the average power of the frequency-doubled beam being

proportional to the [peak x average] power of the fundamental). Thus, the power output characteristics of the NaCl laser were investigated with mode locked excitation. The upper state lifetime was long enough to allow oscillation at any cavity length, although not surprisingly, it was found that the output power peaked when the length of the cavity was closely matched to that of the pump laser.

The cavity was based on the 3-mirror astigmatically compensated configuration, and extended by the 1 m radius of curvature mirror to a length of 183 cm, as described in chapter 1. To allow independent adjustment of the directions and the polarisations of the stabilisation and pump beams, 30% of the 1064 nm beam was split off at the beamsplitter BS and directed to the frequency doubler, and then recombined and made collinear with the pump beam at a dichroic mirror (DM), as shown in Figure 6.2. Previous work had shown that the optimum performance was obtained when the 532 nm beam was horizontally polarised and the 1064 nm beam circularly polarised. This was achieved using half-wave ($\lambda/2$) and quarter-wave ($\lambda/4$) plates respectively. This arrangement resulted in average pump powers of upto 4.9 W at 1064 nm, and 90 mW at 532 nm as measured at the folding mirror. (With 2 W of 1064 nm, the accompanying 532 nm power was reduced to 22 mW.) The folding mirror, designed for high reflectivity in bands centred on 1.55 μm and 1.06 μm, afforded a useful reflectivity of around 80% at 532 nm, principally from the 1.55 μm stack.

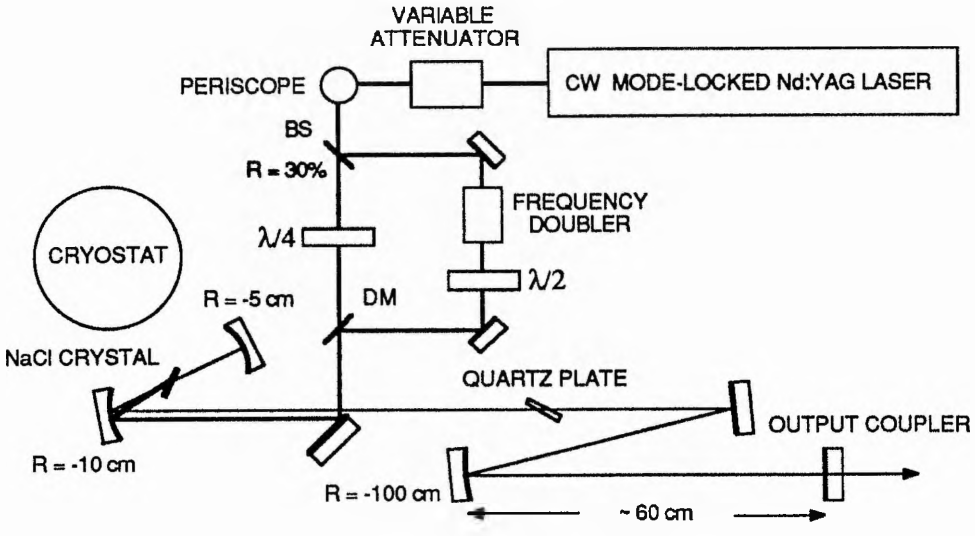

Figure 6.2 Schematic of the synchronously mode-locked NaCl:OH⁻ laser.

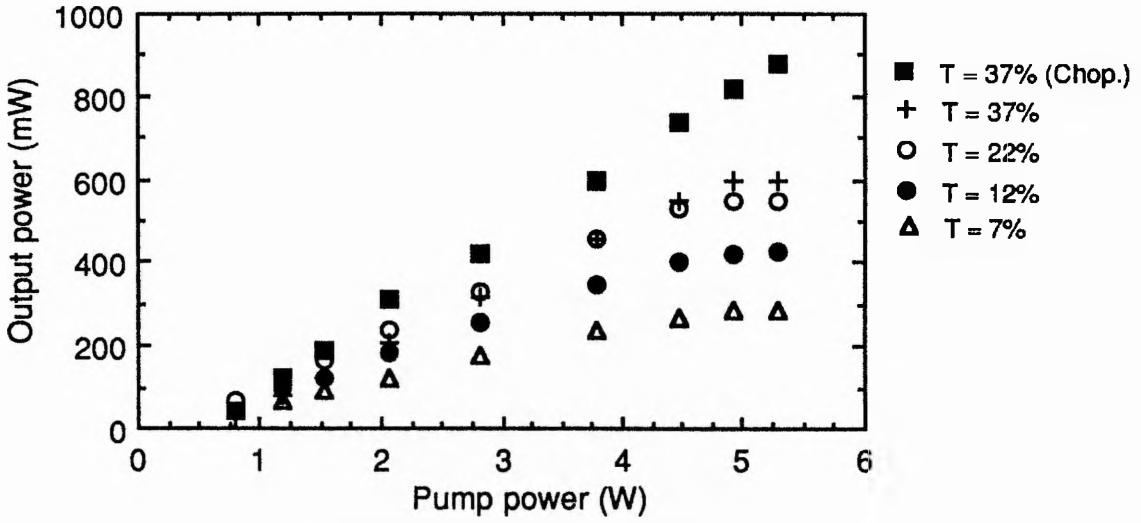

Figure 6.3 Power transfer characteristics for four different output couplers. Pump power refers to the incident power (at 1064 nm) and not absorbed power.

The power transfer characteristic of the mode-locked laser was measured for four different output couplers ranging from 7% to 37% transmission (see Figure 6.3), and with the laser tuned to 1580 nm for maximum power. The incident pump power for threshold was relatively high at around 500 mW, due to the reduced 532 nm power accompanying the 1064 nm beam and also because the crystal had an optical density of only 0.6. At pump powers exceeding 4 W the output tended to saturate, but this effect could be reduced by using the chopper on a 10% duty cycle, resulting in average powers approaching 1 W with a slope efficiency of 18%. The saturation effect is almost certainly of thermal origin, and may be related to the cryostat. At these high pump powers, one of the aluminium steering mirrors tended to burn after a few hours and subsequently, the pump power was restricted to 3 W.

The wavelength tuning curve shown in Figure 6.4 was obtained with a pump power of 2.8 W at 1064 nm (with 40 mW at 532 nm). It can be seen that the NaCl laser provides a superior performance to the KCl:Tl laser, especially at the useful wavelengths around 1550 nm. The laser was tuned from 1450 nm to 1640 nm using a 0.5-mm-thick quartz plate. Attempts to tune beyond 1640 nm resulted in the quartz plate switching to another order, with the operating wavelength shifting to around 1460 nm. The use of a prism (as described in chapter 3) would have allowed a fuller investigation of the long wavelength limit to the

tuning. Some of the mirror coatings were optimised for the KCl:Tl laser, and would probably have prevented tuning beyond around 1680 nm.

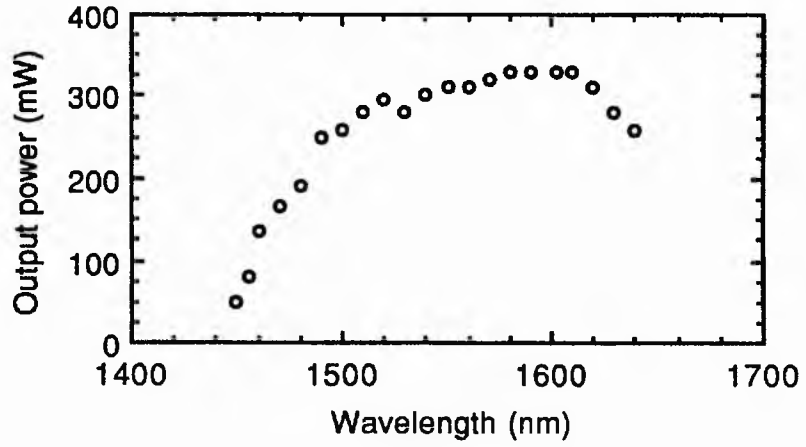

Figure 6.4 Tuning curve for 2.8 W pump power (T ≈ 22%).

The length detuning characteristics of synchronously mode-locked colour-centre lasers, including LiF:F_2^+, NaCl:$(F_2^+)_H$ and KCl:$(F_2^+)_{AH}$, have been reported previously.[11-13] The pulses from the synchronously pumped NaCl laser were studied over an 80 μm range of cavity length detuning using the SHG autocorrelator and the scanning Fabry-Perot interferometer as diagnostics (see Figure 6.5). For these measurements, the output coupler had a transmission of 22%, and a 2-mm-thick quartz plate was used to limit the bandwidth. Table 6.2 summarises the relevant data from Figure 6.5.

The spectra clearly show that the laser is stable only at one length, denoted by $\Delta l = 0$. At this position a localised dip occurs in the second harmonic signal. At cavity lengths longer than the optimum, the laser generated noise bursts, indicated by the 3:2:1 shaped autocorrelation traces. The FWHM of the autocorrelation at the 67% level (ie. the duration of the coherence spike) was in good agreement with the inverse of the spectrum FWHM as might be expected. The data are consistent with poor phase locking. At negative detuning, the pulse duration appears to become shorter, but the spectrum becomes broad and noisy as for positive detuning. The clean nature of the autocorrelation profile, together with the spectral data, could be interpreted as wavelength jitter by a well mode-locked pulse. At $\Delta l \sim -30$ μm, the rising wings suggest that the pulse is accompanied by a broad pedestal or subpulse. The narrow spectrum implies that the bulk of the energy is in a feature around 80 ps long.

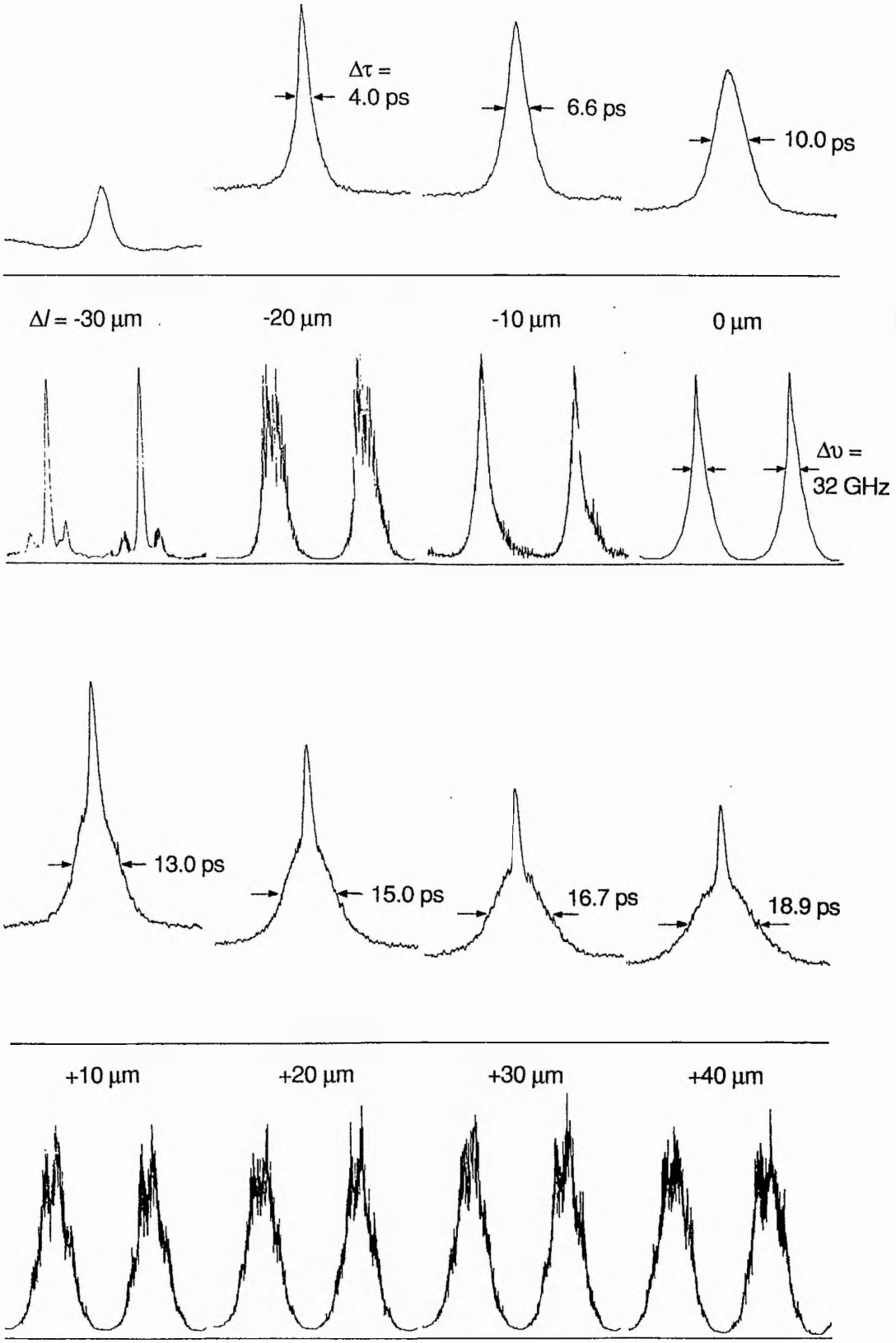

Figure 6.5 Detuning characteristics of the synchronously mode-locked laser.

Δl (μm)	$\Delta\tau$ (ps)	$\Delta\tau_p$ (ps)	$\Delta\upsilon$ (GHz)	$\Delta\tau_p\Delta\upsilon$
-30	4.9	(3.5)	12	(0.042)
-20	4.0	2.8	223	0.62
-10	6.6	4.7	49	0.23
0	10.0	7.1 (4.1)$	32	0.23 (0.13)$
+10	13.0 (4.5)*	9.2	234	2.2
+20	15.0 (3.8)*	10.6	258	2.7
+30	16.7 (3.8)*	11.8	270	3.2
+40	18.9 (3.8)*	13.4	281	3.8

Table 6.2 Length detuning characteristics of the synchronously mode locked laser (mirror transmission = 22%). The first column shows the cavity length relative to optimum. The other columns show the autocorrelation FWHM, the pulse FWHM deconvolved assuming a Gaussian profile, the spectral bandwidth and the duration-bandwidth product. * = the FWHM of the coherence spike in the case of noise bursts. $ = deconvolved values assuming a double-sided exponential pulse shape.

At the optimum cavity length, the duration-bandwidth product and the shape of the spectrum suggest that the pulse neither had a Gaussian nor a sech^2 shape. A better fit could have been obtained by assuming either asymmetric, Lorentzian, or double-sided exponential pulse shapes. Indeed, this last shape gave the best agreement between the measured (0.13) and theoretical (0.142) duration-bandwidth products. The mode locking was also studied with other output couplers (see Table 6.3).

Transmission	$\Delta\tau_p$ (ps)	$\Delta\upsilon$ (GHz)	$\Delta\tau_p\Delta\upsilon$
37%	5.5	36	0.20
22%	6.5	30	0.20
12%	7.9	24	0.19
7%	7.1	24	0.17

Table 6.3 Pulse duration against mirror transmission (Gaussian profile assumed).

The shortest pulses were produced with the higher transmission mirrors, in agreement with the previous study by Kurobori et al.[12] When using a 4-mm-thick quartz plate, the pulses broadened by a few picoseconds, but the duration-bandwidth product increased to around 0.3 and the spectrum exhibited a rounded peak, suggesting a return to a more conventional pulse shape.

6.4 Raman soliton generation

Pulses of a few picoseconds duration may be compressed in anomalous GVD fibre using high-order soliton effects.[14] When the launched pulses are relatively energetic, modulation instability[15] dominates initially and causes the pulse to break up into fragments that form solitons.[16,17] These solitons then collide to form a single pulse of a few hundred femtoseconds duration. Spectrally, the long wavelength modulation instability sideband grows at the expense of the short wavelength sideband due to the Raman effect. This long wavelength sideband grows to form a continuum extending over two hundred nm due to self-frequency shifting of the short pulses caused by intrapulse Raman scattering.

Unfortunately, the autocorrelations of the short pulses generated by this process indicate that a significant proportion of the power remains in a pedestal. Although the spectrum is broad enough to support pulse durations around a few tens of femtoseconds, the pulses obtained are almost a factor of ten longer. Numerical modelling has shown that the evolution of the pulse is highly susceptible to noise and initial conditions.[17-19] The central frequency of the transmitted pulse varies from shot to shot, giving rise to considerable timing jitter (ie. poor phase noise) and variation in the pulse durations.

The Raman soliton generation technique was briefly studied to assess pulse quality, and ascertain its potential as short pulse source. The experiment duplicates the arrangement used by Islam et al. except that the λ_0 of the fibre used in this experiment is much closer to the wavelength of the launched pulses. Pulses from the synchronously mode-locked NaCl:OH⁻ laser, operating around 1560-1580 nm, were passed through an optical isolator and then coupled into a 265 m length of the dispersion-shifted Corning fibre described in chapters 3 and 4 ($\lambda_0 \approx 1550$ nm). At the laser operating wavelength, this fibre has anomalous GVD ($D \approx +1$ ps/(nm.km)). The maximum average power coupled into the fibre was 180

mW (peak power ≈ 300 W). Under these conditions, it can be shown that the nonlinear length L_{NL} ≈ 1-2 metres and the dispersion length $L_D \geq 10$ km. Therefore, $N \approx 70\text{-}100$ (soliton order), whilst the fibre length is only 1-2% of the soliton period Z_0. In this regime SPM dominates the GVD and induces the modulation instability.[15]

The pulses transmitted by the fibre were monitored using the autocorrelator and the scanning Fabry-Perot interferometer. A short (FWHM << 1 ps) feature upon a raised background was observed on the autocorrelator for average powers greater than 10 mW. As the power was increased, the cavity length of the synchronously mode-locked laser became less critical, and the short feature could be obtained even when launching broad noise bursts into the fibre, although at this detuning (many tens of microns) a further increase in the background level was apparent.

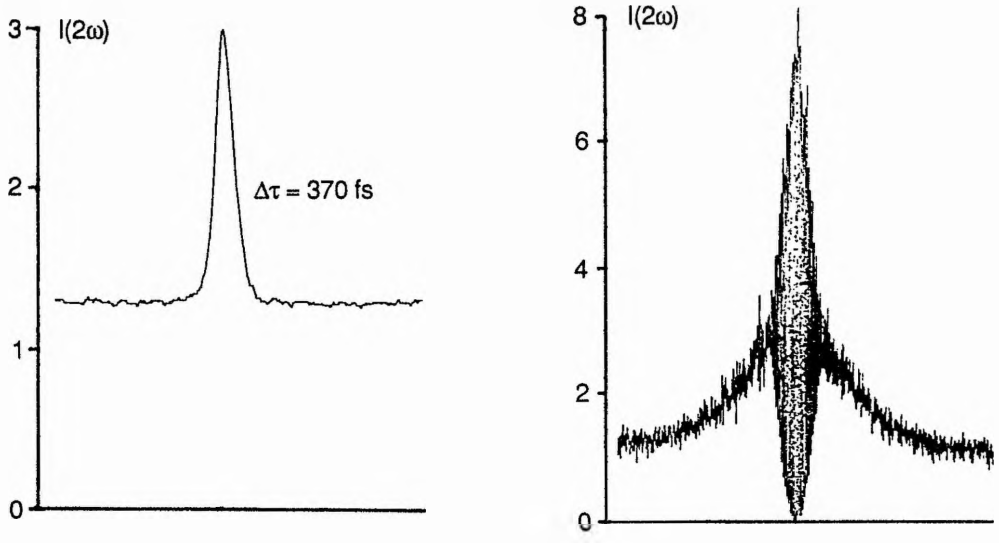

Figure 6.6 Intensity and interferometric autocorrelations for the Raman soliton pulses.

Figure 6.6 shows the intensity and interferometric autocorrelation profiles for the pulse transmitted by the fibre when the background level was minimised by adjustment of the power level and cavity length. The peak-to-background level of the intensity autocorrelation is in the ratio 3:1.3 instead of the usual 3:1. The spectrum was extended to long wavelengths, too broad to be measured by the scanning Fabry-Perot interferometer, but certainly greater than 50 nm, broadly in agreement with the observations of Islam et al.[17] Obviously, this bandwidth is much greater than that required to support the feature (370 fs length at the 2

level). Indeed, the interferometric autocorrelation confirms that the coherence length is much shorter than the pulse, and is consistent with a spectral width of the order of 10 THz (85 nm at 1.6 μm). Although the interference fringes only occupy the central region of the interferometric autocorrelation, the intensity autocorrelation confirms that the pulse is not a noise burst.

As pointed out be Islam et al.,[17] the application of this pulse source is confined to linear measurements due to the shot-to-shot fluctuations in the peak power of the pulse. For example, the relatively powerful continuum could be filtered by a monochromator and used for measurements of group-velocity dispersion.

6.5 Coupled-cavity mode locking using an optical fibre

The generation of subpicosecond pulses using a NaCl:OH⁻ laser has been achieved using two methods. Passive mode locking using a multiple-quantum well (MQW) saturable absorber has been reported by Islam et al. where pulses of less than 300 fs were obtained with average powers of around 100 mW.[20,21] Subsequent work indicated that the MQW structure was not required, since similar durations could be obtained using bulk InGaAsP.[22] Although particularly simple, this technique requires several different samples to cover the bandwidth of NaCl:OH⁻. Using MQW samples grown by the University of Sheffield, passive mode locking of both KCl:Tl and NaCl:OH⁻ lasers has been attempted at St. Andrews, but the results have been disappointing with the shortest pulses being many tens of picoseconds long.

An alternative technique for generating femtosecond pulses with the NaCl:OH⁻ laser is coupled-cavity mode locking. The coupled-cavity technique has a number of advantages over using semiconductor saturable absorbers, eg. (potentially) greater output power, shorter pulses and a broader tuning range since a nonresonant nonlinearity can be used. Yakymyshyn et al. obtained pulses as short as 75 fs obtained using dispersion-shifted fibre, understood to be similar to the Corning fibre discussed in chapter 3.[23,24] The basic synchronously mode-locked laser was harmonically mode locked, presumably by using a cavity half the length of the Nd:YAG laser (rather than by harmonically mode locking the Nd:YAG laser).

In a preliminary experiments the cavity was built in the conventional three-mirror cavity in the Fabry-Perot arrangement. Either a 20 cm length of the STC Technology erbium-doped fibre, or a 60 cm length of Corning dispersion-shifted fibre was used in the control-cavity. Immediately, it was noted that the laser was difficult to stabilise. This might have been due to the much larger output power of the NaCl:OH⁻ laser compared to the KCl:Tl laser, although even when the master cavity length was halved and the laser was harmonically mode locked to half the pulse energy, this unstable operation persisted. A Michelson configuration was also tried but did not appear to offer any benefit. When the stabilisation electronics were able to maintain lock, a regular modulation in the SHG autocorrelation signal was observed. This was in the shape of a sawtooth with a modulation depth of upto 10%, and its frequency could be varied upto ± a few kHz by adjustment of the cavity lengths relative to the Nd:YAG pulse repetition frequency. This regular modulation was not reported by Yakymyshyn et al. although they did concede that the laser was difficult to stabilise.[23] The intensity and interferometric autocorrelation depicted in Figure 6.7 were recorded when the cavity lengths were matched to the Nd:YAG laser, eliminating the modulation for a few seconds at a time. While a full characterisation of the laser was therefore not possible, when using the Corning fibre, it was noted that the power requirements and the pulse duration appeared to reach a minimum around the fibre λ_0.

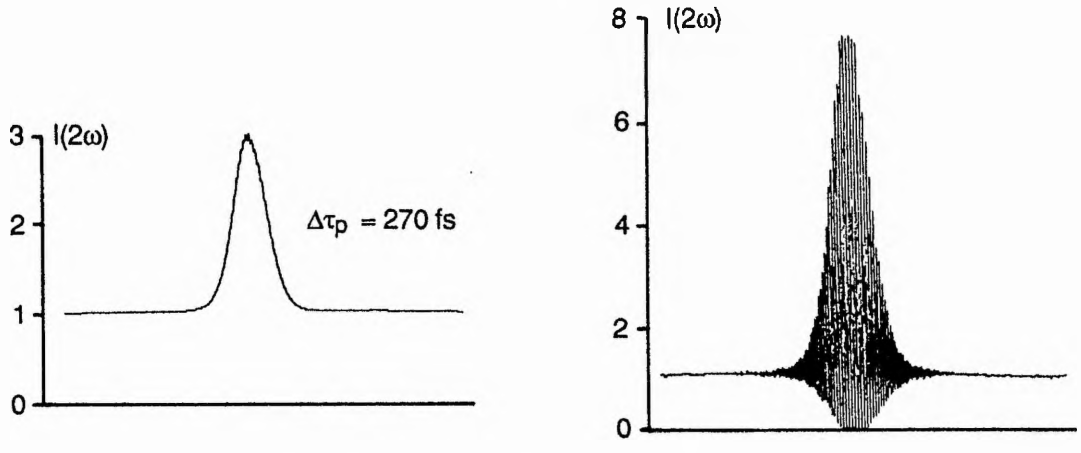

Figure 6.7 Intensity and interferometric autocorrelation profiles for the coupled cavity mode-locked laser where a 20 cm length of the STC Technology erbium-doped fibre has been used in the control cavity.

The cause of the instability is related to the much shorter gain storage time of NaCl:OH⁻ laser as compared to that of KCl:Tl which is over a factor of 10 longer. When the coupled-cavity mode locking takes over from the synchronous pumping, the gain seen by the NaCl:OH⁻ laser pulses appears modulated since they are no longer synchronised to the pump pulses (this effect was also discussed in chapter 2). One possible solution would be to scale up the pump pulse repetition frequency, such that the gain is recharged more often, hence reducing the depth of the modulation in the gain caused by the spontaneous decay. Alternatively, one could synchronise the pulses with the pump pulses by using electronic stabilisation of the master cavity length. (This will be discussed in the concluding chapter.) The simplest solution is to obtain self-starting with continuous pumping. This has been observed by Sucha (described in the previous chapter), using a similar length and type of fibre to that described here.[25] In the following section, self-starting operation is described where the InGaAsP amplifier characterised in chapter 4 was inserted in the control-cavity.

6.6 Coupled-cavity mode locking using an optical amplifier

To demonstrate coupled-cavity mode locking of the NaCl:OH⁻ laser using the InGaAsP amplifier, the arrangement incorporating isolators within the control-cavity as described in chapter 5 was used. Since the power output of the NaCl:OH⁻ laser was much greater than the KCl:Tl laser, both the master and control cavities were half the length of the Nd:YAG laser. This restriction resulted in the compact arrangement illustrated in Figure 6.8.

Initial experiments were undertaken with mode locked excitation in order that the lengths of the master and control cavities could be matched. Although this matching point was easily located, no coupled-cavity mode locking was obtained and only a weak perturbation of the synchronously mode-locked pulses was observed. The Nd:YAG mode locker was then switched off and the front mirror readjusted to compensate for the misalignment caused by a small decrease in the modulator temperature. With CW operation the conversion efficiency from 1064 nm to 532 nm was considerably reduced and there was insufficient power in the 532 nm beam to permit unchopped pumping of the laser. The periscope and the first beamsplitter of the frequency doubling arrangement were moved such that the 70% (rather than 30%) of the CW 1064 nm beam was now directed (≈ 7 W) to the

frequency doubler, as shown in Figure 6.8. This resulted in maximum powers incident on the NaCl:OH⁻ crystal of around 1.8 W at 1064 nm combined with 30-35 mW at 532 nm. Unchopped pumping was possible albeit with a maximum output power at the common mirror of only 65-70 mW with 12% or 22% transmission output couplers, see Figure 6.9. (When the pump beams were chopped with a 10% duty cycle, the output power rose to around 150 mW.) By comparison, output powers of around 200 mW were recorded using mode-locked (unchopped) pumping for similar average powers in the 1064 nm and the 532 nm beams, see Figure 6.3. This seems to indicate that the stabilisation beam is more effective when pulsed, implying that the reorientation process used here involves multiphoton excitation rather than the normal two-stage process. This aspect requires further study to find the optimum pump beam polarisations under CW and CW mode-locked excitation.

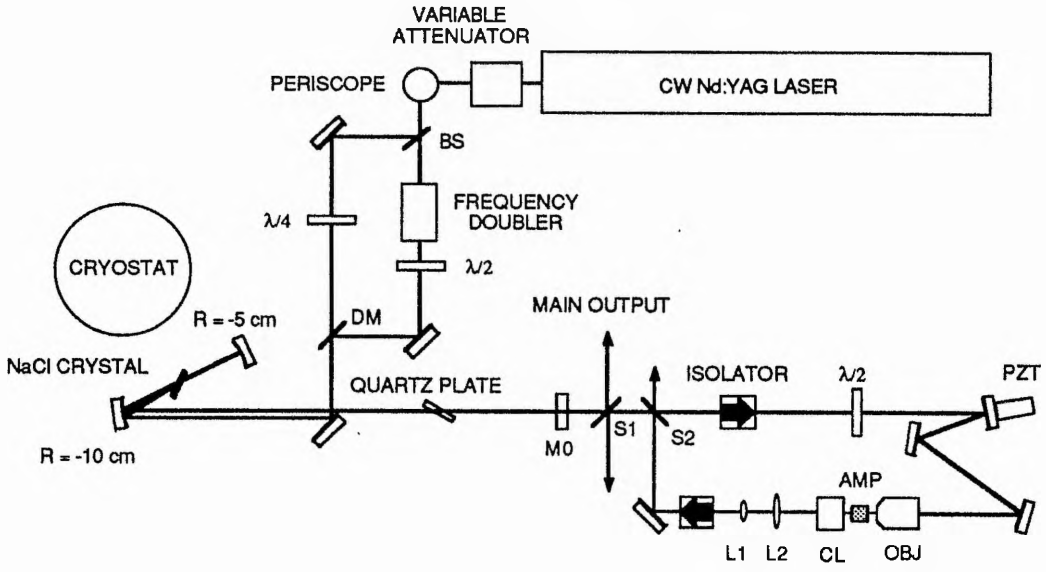

Figure 6.8 Schematic of the coupled-cavity NaCl:OH⁻ laser.

Under CW pumping with the master and control cavity lengths matched, self-starting mode locking was obtained after incorporating a 0.5-mm-thick quartz birefringent plate in the master cavity to tune the laser away from the peak of the NaCl:OH⁻ laser emission (1590 nm, see Figures 6.6 & 6.9) to around 1530 nm, closer to the peak of the amplifier gain (1480 nm). Figure 6.10 depicts the intensity autocorrelation and spectrum obtained using the scanning Fabry-Perot interferometer where the pulse duration is 0.85 ps assuming a sech^2 profile.

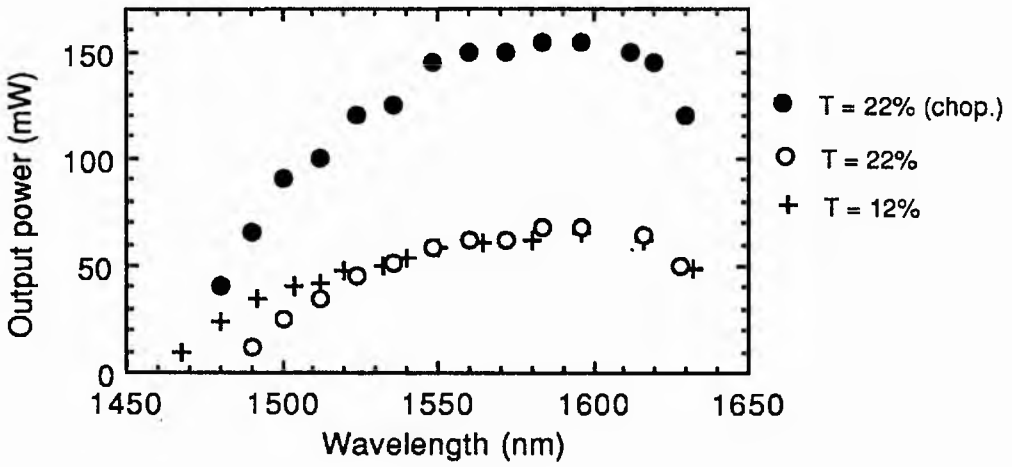

Figure 6.9 Tuning curve for the 91 cm long, CW pumped laser (2 W pump power).

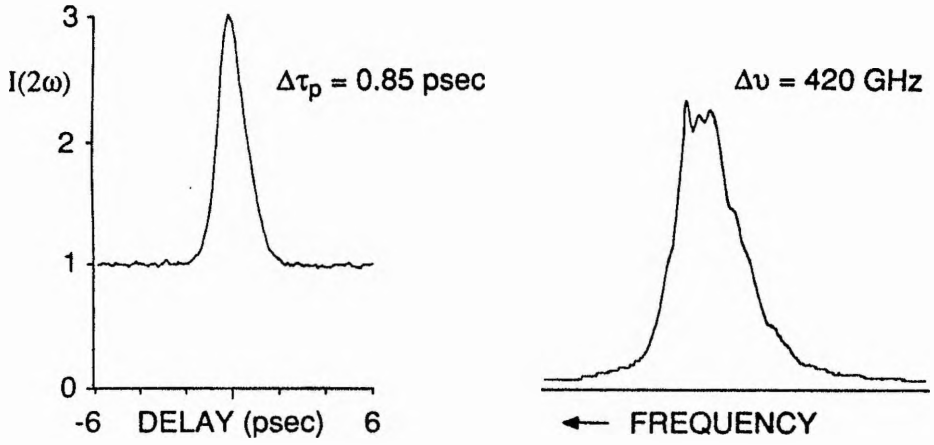

Figure 6.10 Intensity autocorrelation and spectrum for the self-starting, coupled-cavity NaCl:OH⁻ laser.

In contrast to the KCl:Tl laser, self-starting occurred spontaneously and did not require assistance by ramping the PZT. However, many other parameters such as the common mirror transmission and the amplifier drive current settings were more critical, and operation in the saturable absorption regime was not observed. Mode locking was only achieved when the common mirror had a transmission of either 12% or 22% and then only when the drive current was greater than 50 mA. Nevertheless, this preliminary demonstration does provide a useful background to further experiments using more suitable amplifiers.

6.7 Summary

The stabilised NaCl:OH⁻ laser offers many advantages over the KCl:Tl laser including broader tunability, greater output power and, in addition, there was no perceivable fading of the output power during the course of this work. While the basic synchronously mode-

locked laser is superior to an equivalent KCl:Tl laser, with pulse durations in the 5-10 ps range, the stability of the coupled-cavity mode-locked laser leaves much to be desired. The stability was improved by substituting the optical fibre for the InGaAsP optical amplifier in the control cavity to obtain self-starting operation. Unfortunately, under CW pumping, the coupled-cavity laser could only produce a meagre 15 mW of useful output power.

There remains considerable room for development of the NaCl:OH^- laser to bring its femtosecond performance upto the standard of the KCl:Tl laser, and may even involve the use of alternative techniques to coupled-cavity mode locking (and discussed in the concluding chapter). In time, the NaCl laser will surely become a formidable pulse source in the 1.55 μm region, due to its high average output power, tunability and longevity.

6.8 References

1. L. F. Mollenauer, R. H. Stolen, and J. P. Gordon, Phys. Rev. Lett. **45**, 1095 (1980).
2. J. F. Pinto, L. W. Stratton, and C. R. Pollock, Opt. Lett. **10**, 384 (1985).
3. J. F. Pinto, E. Georgiou, and C. R. Pollock, Opt. Lett. **11**, 519 (1986).
4. D. Wandt, W. Gellermann, F. Lüty, and H. Welling, J. Appl. Phys. **61**, 864 (1986).
5. R. Beigang, K. Klameth, B. Becker, Z. Yoon, and H. Welling, Opt. Commun. **65**, 383 (1988).
6. E. Georgiou, J. F. Pinto, and C. R. Pollock, Phys. Rev. B **35**, 7636 (1987).
7. W. L. Wolfe, "Properties of Optical Materials" (chapter 7), *Handbook of Optics*, W. G. Driscoll, ed. (McGraw-Hill, New York, 1978).
8. Matthew C. DeLong, Crystal Growth Laboratory, University of Utah, Salt Lake City, UT 84112.
9. C. I. Johnston, PhD Thesis (University of St. Andrews, 1991).
10. K. R. German and C. R. Pollock, Opt. Lett. **12**, 474 (1987).
11. N. J. Langford, PhD Thesis (University of London, 1989).
12. T. Kurobori, A. Nebel, R. Beigang, and H. Welling, Opt. Commun. **73**, 365 (1989).
13. K. Möllmann, F. Mitschke, and W. Gellermann, Opt. Commun. **83**, 177 (1991).
14. L. F. Mollenauer, R. H. Stolen, J. P. Gordon, and W. J. Tomlinson, Opt. Lett. **8**, 289 (1983).
15. G. P. Agrawal, *Nonlinear Fiber Optics* (Academic Press, San Diego, 1989), pp. 104-111.
16. A. S. Gouveia-Neto, M. E. Faldon, and J. R. Taylor, Opt. Commun. **69**, 325 (1989).
17. M. N. Islam, G. Sucha, I. Bar-Joseph, M. Wegener, J. P. Gordon, and D. S. Chemla, J. Opt. Soc. Am. B **6**, 1149 (1989).
18. K. J. Blow and D. Wood, IEEE J. Quantum Electron. **25**, 2665 (1989).
19. E. A. Golovchenko, P. V. Mamyshev, A. N. Pilipetskii, and E. M. Dianov, J. Opt. Soc. Am. B **8**, 1626 (1991).
20. M. N. Islam, E. R. Sunderman, I. Bar-Joseph, N. Sauer, and T. Y. Chang, Appl. Phys. Lett. **54**, 1203 (1989).
21. M. N. Islam, E. R. Sunderman, C. E. Soccolich, I. Bar-Joseph, N. Sauer, T. Y. Chang, and B. I. Miller, IEEE J. Quantum Electron. **25**, 2454 (1989).
22. C. E. Soccolich, M. N. Islam, M. G. Young, and B. I. Miller, Appl. Phys. Lett. **56**, 2177 (1990).
23. C. P. Yakymyshyn, J. F. Pinto, and C. R. Pollock, Opt. Lett. **14**, 621 (1989).
24. C. R. Pollock, J. F. Pinto, and E. Georgiou, Appl. Phys. B **48**, 287 (1989).
25. G. Sucha, Opt. Lett. **16**, 922 (1991).

7 General conclusions

7.1 Summary and conclusions

Various mode-locking techniques for colour-centre lasers have been evaluated, with an emphasis being directed towards passive techniques. In chapter 1, the passive mode locking of a LiF:F_2^+ laser was described, where either a saturable absorber dye was used, or by using coupled-cavity mode locking. The application of the former technique resulted in pulse durations of less than 180 fs, but the resonant nature of the saturable absorber restricted the operating wavelength to the range 845-870 nm (with adjustment of dye concentration), and in addition, the unavoidable losses caused by the absorber made the laser relatively inefficient. The coupled-cavity technique permits the utilisation of effects such as self-phase modulation which normally cannot be used to shape the temporal profile of a pulse. The technique converts the phase modulation into amplitude modulation by (essentially) two beam interference. One obvious advantage over conventional passive mode locking is that nonresonant, and hence lossless, nonlinearities can be used to mode lock a laser. Coupled-cavity mode locking was investigated for three different gain media, namely LiF:F_2^+, KCl:Tl and NaCl:OH^- crystals.

The use of optical fibres as the control-cavity nonlinearity was evaluated for all three coupled-cavity lasers. The technique was not found to be particularly effective with the LiF:F_2^+ laser due to the relatively large, normal group-velocity dispersion at the operating wavelength. This gave rise to chirped pulses of 1-2 ps duration being recorded. It was proposed that dispersion compensation in the control cavity would have reduced the chirp and the pulse duration. More recently, the dispersion compensation of a coupled-cavity Ti:sapphire laser has been reported,[1] where it was found that the dispersive elements were more effective if inserted in the master cavity, hence compensating for the normal GVD and

SPM caused by the Ti:sapphire rod, and the chirp transferred into the main cavity from the control-cavity fibre. Strongly chirped pulses have also been observed for a coupled-cavity Nd:glass laser.[2] This was remedied by using a Michelson interferometer arrangement, where dispersion compensation was placed in the linear branch, in effect the master cavity.

The LiF:F_2^+ laser stands as the gain medium with the shortest upper state lifetime (29 ns) in which coupled-cavity mode locking has been implemented. It is now realised that the use of an ultrafast, nonresonant nonlinearity to mode lock such a dye-like gain medium is inappropriate. For this laser or dye lasers, a control cavity would be more usefully employed to achieve passive mode locking using either a slow refractive nonlinearity or a slow saturable absorber with excessive nonsaturable loss. In addition, for stable coupled-cavity mode locking with these lasers, CW pumping and hence "self-starting" would be essential due to the inability of the gain media to store energy over the cavity round-trip period. Recently, it has been reported that low levels of feedback from an empty control cavity has a dramatic effect on the stability of a synchronously mode-locked dye laser.[4] In this scheme, the control cavity is slightly shorter than the master cavity, and hence the laser works by a seeding mechanism, and not on the interferential pulse shaping used in the coupled-cavity colour-centre lasers.

More satisfactory results were achieved with the KCl:Tl and the NaCl:OH^- lasers. With the KCl:Tl laser, coupled-cavity mode locking was obtained using either the conventional Fabry-Perot configuration or the Michelson interferometer scheme, where the latter was found to be more stable in the presence of pump power fluctuations. Both schemes generated sub-100 fs pulses when using a small-core, erbium-doped fibre which was shown to have low group-velocity dispersion. Synchronous pumping was generally required to induce peak intensities sufficient to initiate the coupled-cavity mode locking. Although it had no influence on the pulse durations produced once the (passive) coupled-cavity mode locking was established, it was observed to cause saw-tooth amplitude modulation related to the beating of the pump pulse train with the colour-centre laser pulse train. This effect was particularly significant with the NaCl:OH^- laser due to its shorter gain storage time compared to KCl:Tl, and operation with CW excitation would have obvious benefits in coupled-cavity NaCl:OH^- lasers. Self-starting was obtained with the coupled-cavity KCl:Tl laser by using a

symmetrical master cavity to enhance the strength of the mode beating, but the threshold pump power required to initiate mode locking exceeded that for stable, pedestal free pulses. Recently published theory[5] has highlighted the importance of reflections and etalons (both internal and external to the master cavity) on the threshold for starting. Future modifications to the laser should therefore include the substitution of the plane cryostat windows by wedged equivalents, and the use of fibre ends polished to a non-normal angle.[6] Wedged quartz tuning plates would be somewhat problematical, but fortunately, since they are easily accessible, their orientation can be adjusted to minimise Fabry-Perot etalon effects.

The KCl:Tl laser was used in CW, synchronously mode locked and coupled-cavity mode locked forms to characterise the linear and nonlinear properties of a 1.5 μm InGaAsP optical amplifier. The nonlinearities included slow and fast effects, related to interband and intraband relaxation respectively, with each of these subdivided into transmissive and refractive effects. An ultrafast refractive nonlinearity was observed for which an effective n_2 of -2 x 10^{-11} cm^2W^{-1} was deduced. Recently published time-resolved measurements[7] of nonlinear refraction in a GaAs laser have shown evidence for two opposing effects, a picosecond effect related to carrier heating (positive) and an instantaneous Stark-like effect (negative).

The speed, magnitude, and large phase shifts caused by this nonlinearity make it promising for all-optical switching applications and it should be compared to the ultrafast nonresonant nonlinearity currently being studied at the two-photon bandgap.[8-10] Whilst that effect has greater ultimate operating speed (ie. > 10 THz), it is over two orders of magnitude weaker. In any case, only speeds of upto 100 GHz are being contemplated at present, a speed that would be suitable for the much stronger, but slower, nonlinearity present in the active device.

In chapters 5 and 6, the use of the semiconductor optical amplifier as a control-cavity nonlinearity for the KCl:Tl and NaCl:OH^- lasers was described, with pulses as short as 280 fs obtained for the KCl:Tl laser. Stable, self-starting operation was achieved once parasitic reflections from the device facets were eliminated and the control cavity alignment improved. Although both amplitude and phase modulation nonlinearities were present, it was argued that the self-phase modulation was the more important in the mode locking process. Mode

locking was not obtained at the drive currents close to transparency and so the strong, slow nonlinearities associated with the interband transition (ie. gain and loss saturation) are responsible for the initiation of the mode locking, although it is likely that the ultrafast refractive nonlinearity makes a large contribution at the steady state. Poor coupling efficiencies and nonlinear absorption reduced the level of feedback to a level of between one and two orders of magnitude smaller than for an optical fibre, and this may have limited the ultimate pulse duration, although pulse broadening from the nonlinear absorption and from group-velocity dispersion may also have had an influence.

7.2 Future work

Although the NaCl:OH^- laser is already in widespread use, there remains considerable potential for the improvement of its coupled-cavity mode locking and for the identification and development of new techniques. The sawtooth amplitude modulation that affects the coupled-cavity mode locking would be eliminated if self-starting can be achieved, but it was generally found necessary to pump the NaCl:OH^- laser with a mode-locked Nd:YAG laser in order to generate sufficient 532 nm light to stabilise the $(F_2^+)_H$ centres. One possible solution presently being investigated is to retain the mode-locked pump laser, and lock the repetition frequency of the coupled-cavity laser to the Nd:YAG laser by controlling the length of the master cavity with a (second) piezo-electric translator. The basic principles have already been proved with a coupled-cavity KCl:Tl laser which was locked to a crystal oscillator to improve phase noise.[11] If sufficient 532 nm can be generated with CW pumping, then further studies using semiconductor amplifiers as the control-cavity nonlinearity are envisaged. In particular, by using an angled-facet device[12] to minimise parasitic optical feedback, it may be possible to operate with a conventional control cavity without isolators.

Several new techniques for which stabilisation electronics are not required have recently been demonstrated with other gain media, and it is hoped that some of these will prove effective with the NaCl:OH^- laser. These include coupled-cavity mode locking using a Sagnac interferometer arrangement,[13] and the insertion into the cavity of a self-focussing element combined with an aperture, as successfully used with Ti:sapphire lasers.[14] With the Sagnac interferometer, the losses associated with coupling into and out of a waveguide

would have a catastrophic effect on output power, and so bulk nonlinearities would be preferred. The main technical difficulty with this technique is the introduction of a linear phase bias between the two directions in the interferometer, such that the short pulse is sent back to the gain medium and the broad one ejected from the laser. The self-focussing effect (or Kerr-lens mode locking) is probably the simpler technique, but it is a relatively weak effect and self-starting may prove difficult. Initial experiments would probably be made with a synchronously pumped laser in order that the cavity geometry could be optimised.

In the longer term, 1.5 μm colour-centre lasers might be replaced by erbium-doped fibre lasers. Using an all-fibre, figure of eight configuration (closely related to the Sagnac interferometer/loop mirror scheme, see reference 13), femtosecond pulses have already been reported,[15,16] although the repetition frequencies of the pulse trains were unstable, and for a 320 fs pulse, the energy was reported to be only 16 pJ.[16] It is likely that colour-centre lasers will remain the preferred source for some time, certainly for the production of high-power, tunable, femtosecond pulses.

7.3 References

1. D. E. Spence and W. Sibbett, J. Opt. Soc. Am. B **8**, 2053 (1991).
2. Ch. Spielmann, F. Krausz, T. Brabec, E. Wintner, and A. J. Schmidt, IEEE J. Quantum Electron. **27**, 1207 (1991).
3. Ch. Spielmann, F. Krausz, T. Brabec, E. Wintner, and A. J. Schmidt, Appl. Phys. Lett. **58**, 2470 (1991).
4. P. Beaud, J. Q. Bi, W. Hodel, and H. P. Weber, Opt. Commun. **80**, 31 (1991).
5. H. A. Haus and E. P. Ippen, Opt. Lett. **16**, 1331 (1991).
6. G. Sucha, Opt. Lett. **16**, 922 (1991).
7. C. T. Hultgren and E. P. Ippen, Appl. Phys. Lett. **59**, 635 (1991).
8. S. T. Ho, C. E. Soccolich, M. N. Islam, W. S. Hobson, A. F. J. Levi, and R. E. Slusher, Appl. Phys. Lett. **59**, 2558 (1991).
9. H. K. Tsang, R. S. Grant, R. V. Penty, I. H. White, J. B. D. Soole, E. Colas, H. P. LeBlanc, N. C. Andreadakis, M. S. Kim, and W. Sibbett, Electron. Lett. **27**, 1994 (1991).
10. J. S. Aitchison, A. H. Kean, C. N. Ironside, A. Villeneuve, and G. I. Stegeman, Electron. Lett. **27**, 1710 (1991).
11. D. R. Walker, D. W. Crust, W. E. Sleat, and W. Sibbett, "Reduction of Phase Noise in Passively Mode-Locked Lasers", to be published in IEEE J. Quantum Electron., Jan. 1992.
12. P. E. Barnsley, J. J. Isaac, D. J. Elton, Electron. Lett. **26**, 825 (1990).
13. T. F. Carruthers and I. N. Duling III, Opt. Lett. **15**, 804 (1990).
14. L. Spinelli, B. Couillaud, N. Goldblatt, and D. K. Negus, in *Technical Digest of Conference on Lasers and Electro-Optics* (Optical Society of America, Washington, D.C., 1991), paper CPDP7.
15. I. N. Duling III, Electron. Lett. **27**, 544 (1991)
16. D. J. Richardson, R. I. Laming, D. N. Payne, M. W. Philips, and V. J. Matsas, Electron. Lett. **25**, 730 (1991).

Acknowledgements

I wish to thank my supervisor Professor Wilson Sibbett for his support and eternal optimism. I am also grateful to the other members of the W squad, in particular:

Nigel Langford for showing me the ropes on the LiF laser and the "IC" cryostat,

Pete Kean for discussions regarding the coupled-cavity lasers,

David Burns for discussions regarding the semiconductor optical amplifier,

Colin Johnston for preparing the NaCl:OH^- crystal,

Gordon "Fish" Kennedy for assistance with the XPM experiment (chapter 4),

and Bill Sleat and Dave Walker for imparting some of their vast electronics knowledge, and for assistance with the streak cameras.

I thank the technical staff in the department for their help, and single out:

Bob Mitchell for his cryogenic expertise and prowess with the mass spec.,

Reg Gavine for his instruction on the student lathes and milling machine,

Andy Barman for supplying approximately 13,587 litres of liquid nitrogen,

and Jimmy Lindsay and other members of the Mechanical Workshop for machining numerous bases and mounts.

Finally, I am grateful to the Science and Engineering Research Council for providing overall financial support for the project.

Appendix 1 Calculation of the dye jet thickness (see chapter 2)

The thickness of the saturable absorber dye jet was determined by studying interference fringes caused by reflections off the two surfaces, as shown in Figure A1.1.

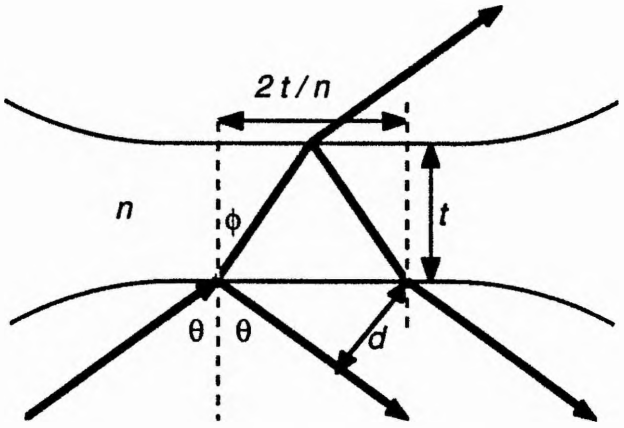

Figure A1.1 Schematic of the jet showing the origin of the interfering beams.

Although the dye jet, thickness t, was oriented close to Brewster's angle, there was sufficient light reflected from its surfaces such that interference fringes were observed at some distance D. The fringes are formed by the interference of a beam which is reflected from the entry surface of the jet, with a beam which reflected from the exit surface. These two beams have almost equal intensities and therefore, the resultant fringes have a high contrast. Using the assumption that the light is incident at Brewster's angle, the following relations can be used:

$$\tan\theta = n \quad , \quad \tan\phi = 1/n \quad , \quad \theta = (90^0 - \phi) \text{ ie. } \sin\phi = \cos\theta. \tag{A1.1}$$

where n is the refractive index of the jet. The two beams are, in effect, produced by two point sources separated by the distance d. Now

$$d = s\sin\phi = s\cos\theta \tag{A1.2}$$

where s is given by

$$s = \frac{2t}{\tan\theta} = \frac{2t}{n} \tag{A1.3}.$$

Substituting (A1.3) into (A1.2),

$$d = \frac{2\,t}{n}\cos\theta \qquad \text{(A1.4).}$$

This can be simplified further, since

$$\cos\theta = \sin\phi = \frac{t/n}{\sqrt{t^2/n^2 + t^2}} = \frac{1}{\sqrt{1 + n^2}} \qquad \text{(A1.5).}$$

The fringe separation x is given by the usual approximation

$$x \approx \frac{\lambda D}{d} \qquad \text{(A1.6).}$$

Rearranging (A1.6) in terms of d and substituting into (A1.5), gives after rearrangement, an expression for the dye jet thickness in terms of the fringe separation x.

$$t \approx \frac{\lambda D n \sqrt{1 + n^2}}{2 x} \qquad \text{(A1.7).}$$

The refractive index of the jet (a 10:1 solvent mixture of ethylene glycol and propylene carbonate), was taken as 1.43 (see reference 1). Thus, for example, with λ = 900 nm, D = 1 m, and x = 13 mm, the jet thickness is found to be approximately 87 μm.

Reference

1. M. E. Lusty and M. H. Dunn, Appl. Phys. B **44**, 193 (1987).

Appendix 2 Optical treatment of LiF:F_2^+ crystals (see chapter 2)

The performance of the LiF:F_2^+ laser was disappointing when compared to the data published by Mollenauer for his laser, where for example, an output power of some 600 mW was obtained for 2.15 W pump power (T = 8% output coupler).[1,2] Part of this can be attributed to the noncollinear pumping arrangement with incomplete overlap of the pump and intracavity beams, however Langford[3] has analysed the threshold pump power for various output couplers and deduced a round trip loss of some 14%. During the work described in this thesis, it was found that a 1 mm thick crystal gave a superior performance to the usual 2 mm crystals, and hence absorption within the LiF crystal was suspected to be the source of the losses. The extra 1 mm can only contribute loss since substantial overlap of the pump and pumped beams only exists in the first millimetre. The LiF boules were not deliberately doped with divalent metal cations, and so it was likely that some of the excess electrons were held in F_2^- centres, which absorb in a broad region centred at 960 nm, within the F_2^+ emission band.[4]

Absorption measurements of a crystal (while maintained at 77 K) were made to determine if the parasitic F_2^- centres were present. Light from a tungsten projection lamp was filtered by a scanning monochromator and then focussed through the cryostat windows and crystal. Kodak Wratten filters were used to block the second-order beams passed by the grating. The throughput was measured using either a photomultiplier, or at the longer wavelengths, a large area germanium photodiode. The presence of F_2^- centres was confirmed by the identification of the F_2^- zero-phonon line at 1040 nm. To determine the absolute absorption, the measurement was repeated with the crystal moved out of the beam path, providing a calibration. After analysing the data, the absorption in inverse centimetres was calculated at 10 nm intervals (see Figure A2.1). The peak absorption at 960 nm was only 0.4 cm^{-1}, small when compared to the features at 650 nm (F_2^+ centres) and 440 nm (F_2 centres) where values of 15-20 cm^{-1} were obtained, however 0.4 cm^{-1} corresponds to an optical density of about 0.04, or around 10% attenuation.

The destruction of the parasitic F_2^- centres by thermal means was not desirable, since the laser active F_2^+ centre population would also have been reduced. An alternative, more selective means of destruction is by exposure to narrow band light. The bleaching of F_2^- (or

M') centres in NaCl (absorption peak 1470 nm) crystals (at 4 K) has been reported where 820 nm light was used.[5] This indicated that a wavelength of around 510-540 nm might have a similar effect with LiF.

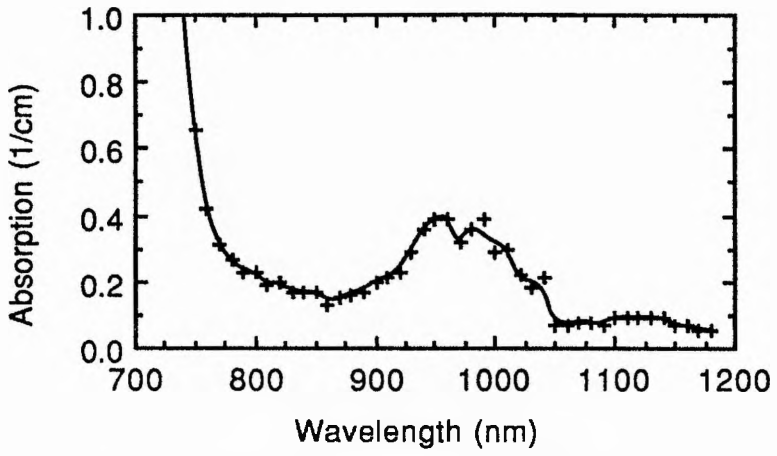

Figure A2.1 Absorption measurements in the range 700-1180 nm.

The performance of the crystal prior to, and after, treatment was monitored by measuring the power transfer characteristic (shown in Figure A2.2) when configured in the 183 cm long, three mirror cavity with the T = 10% output coupler, and excited by the CW krypton laser operating on the 647 nm and 676 nm lines. The LiF:F_2^+ crystal had a fairly typical performance, with a threshold of 500-550 mW for CW pumping (around 450 mW under synchronous mode locking), and a slope efficiency of approximately 15%. After two weeks of use, the threshold pump power had increased by around 50 mW, with a reduction in the slope efficiency to 11%. The crystal was then exposed to 500 mW of horizontally polarised, 514 nm argon ion beam, focussed down to a diameter of approximately 1 mm, for a period of around 30 minutes. There was a significant increase in performance, with an increase in slope efficiency to 21% and a reduction in the threshold to 400 mW.

It should be stated that the mechanism for this improvement may not be a reduction in the F_2^- centre population. It has been reported that the exposure of coloured LiF crystals (at room temperature) to 532 nm light causes the reaction $F_2 \rightarrow F_2^+ + e^-$,[6] therefore this might be expected to give an increase in F_2^- centres by F_2 centres capturing the excess electrons. The reduction of F_2^- centre populations has been obtained where 920 nm or 1064 nm light was used to excite the fundamental absorption band, and 532 nm photoionised from the

relaxed excited state.[7-9] Unfortunately, it was not possible to repeat the absorption measurements after the treatment and confirm if a reduction in F_2^- centres had occurred, nevertheless the treatment did give a substantial increase in efficiency.

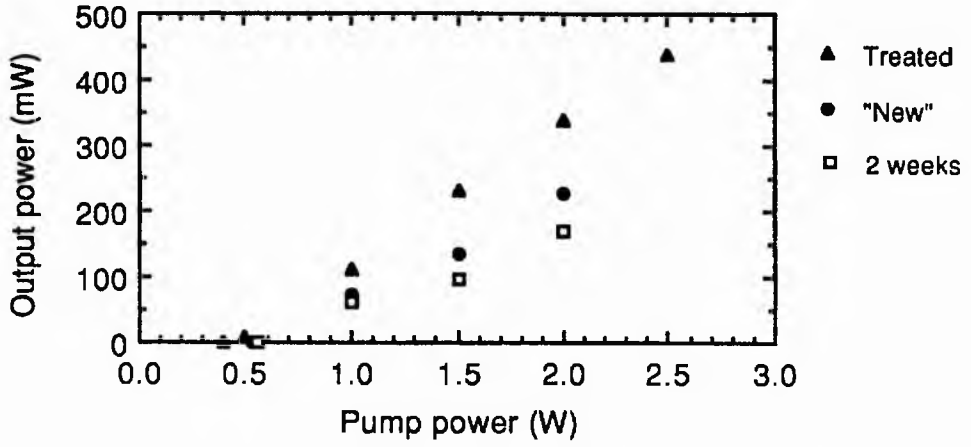

Figure A2.2 Performance of the crystal at various stages. The laser was operated with chopped pump light (10% duty cycle).

References

1. L. F. Mollenauer, D. M. Bloom, and A. M. DelGaudio, Opt. Lett. **3**, 48 (1978).
2. L. F. Mollenauer, "Color Center Lasers" (chapter 6), in *Quantum Electronics* part B, C. L. Tang, ed. (Academic Press, New York, 1979).
3. N. J. Langford, PhD Thesis (University of London, 1988).
4. W. Gellermann, A. Müller, D. Wandt, S. Wilk, and F. Lüty, J. Appl. Phys. **61**, 1297 (1987).
5. I. Schneider and C. E. Bailey, Solid State Commun. **7**, 657 (1969).
6. T. T. Basiev, Yu. K. Voron'ko, S. B. Mirov, V. V. Osiko, and A. M. Prokhorov, JETP Lett. **30**, 626 (1979).
7. K. Smith, PhD Thesis (University of London, 1985).
8. T. T. Basiev, F. A. Vakhidov, Yu. K. Voron'ko, and S. B. Mirov, Sov. J. Quantum Electron. **16**, 277 (1986).
9. T. T. Basiev, S. B. Mirov, and V. V. Osiko, IEEE J. Quantum Electron. **24**, 1052 (1988).

Appendix 3 "Amplifier" program (see chapters 4 & 5)

```
program Amplifier (input, output);
(*  R S Grant 1990  *)
  uses
    SANE;
  const
    pi = 3.141592654;
    Planck = 6.626176e-34;
    LightSpeed = 299792458;
    Charge = 1.6021892e-19;
    Wavelength = 1.5e-6;
    alpha = 5;
    A = 1e+8;
    B = 1e-16;
    C = 4e-41;
  type
    gainLarray = array[-501..501] of double;
    timearray = array[-50..50, 1..6] of double;
    freqarray = array[-50..50, 1..2] of double;
  var
    Amplitude, TauPulse, TauNought, DeltaTau, Tau, dTau : double;
    Length, Volume, Gamma, DiffGainCoeff : double;
    BiasCarriers, TransparencyCarriers, Gain, Energy, Esat : double;
    BiasCurrent, TransparencyCurrent, Trec, SmallSigGain, H : double;
    Dn, Dfi, Dmu, Dw, Wrange, Woffset, Wstart, Wfinish, Maxspec : double;
    gainL : gainLarray;
    temporal : timearray;
    spectral : freqarray;
    Screen : rect;
    f : text;
    textname : string;
  function AmpIn (Ein, t0, Tau : double) : double;
(*  Defines the amplitude of a Gaussian pulse.  *)
  begin
    AmpIn := (sqrt(Ein / (t0 * sqrt(pi))) * exp((-1 * sqr(Tau)) / (2 * sqr(t0))));
  end;
  procedure DiffGain;
(*  The differential gain coefficient is estimated by calculating the carrier density *)
(*  at the drive current and the transparency current, and using the value for  *)
(*  small-signal gain which has been input. The gain recovery time is estimated.  *)
    var
      Current, N : double;
    procedure FindCarriers;
(*   Uses the Newton Raphson method to find carrier density.   *)
      var
        NewN, F, Fdash : double;
    begin
      NewN := 2e24;
      repeat
        N := NewN;
        F := (A * N) + (B * sqr(N)) + (C * Xpwrl(N, 3)) - (Current / (Charge * Volume));
        Fdash := A + (2 * B * N) + (3 * C * sqr(N));
        NewN := N - (F / Fdash);
      until (abs(NewN - N) < 1e18);
      N := NewN;
    end;  (*   FindCarriers  *)
  begin
    Current := BiasCurrent;
    FindCarriers;
```

```
    BiasCarriers := N;
    write('Carrier density at bias current = ');
    writeln((BiasCarriers * 1e-24) : 5 : 5, '  x 10^18 cm^-3');
    Current := TransparencyCurrent;
    FindCarriers;
    TransparencyCarriers := N;
    write('Carrier density at transparency = ');
    writeln((TransparencyCarriers * 1e-24) : 5 : 5, '  x 10^18 cm^-3');
    DiffGainCoeff := abs(abs(Gain) / (Gamma * (BiasCarriers - TransparencyCarriers)));
    write('Differential gain coefficient a = ');
    writeln((DiffGainCoeff * 1e20) : 5 : 5, ' x 10^16 cm^2');
    Esat := (Planck * LightSpeed * Volume) / (Wavelength * Length * DiffGainCoeff * Gamma);
    write('Saturation Energy Esat = ');
    writeln((Esat * 1e12) : 4 : 4, ' pJ');
    N := BiasCarriers;
    Trec := 1 / (A + (2 * B * N) + (3 * C * sqr(N)));
    write('Recovery time Trec = ');
    writeln((Trec * 1e12) : 2 : 2, ' ps');
  end;
  procedure AmplifyAndChirp;
(*    First section calculates the gain as a function of time by    *)
(*    numerical integration using the Runge Kutta method.          *)
(*    Second section uses these values of gain to calculate the    *)
(*   shape, phase, and carrier frequency of the output pulse.      *)
    var
      Pin, Pout, Stimulated, RKA, RKB, RKC, RKD, H : double;
      dHdt : double;
      T : integer;
  begin
    SmallSigGain := DiffGainCoeff * Gamma * (BiasCarriers - TransparencyCarriers);
    gainL[-501] := SmallSigGain * Length;
    for T := -500 to 501 do
      begin
        Tau := (T - 1) * dTau;
        H := gainL[T - 1];
        Pin := sqr(AmpIn(Energy, TauNought, Tau));
        Stimulated := (Pin * (exp(H) - 1)) / Esat;
        RKA := (((SmallSigGain * Length - H) / Trec) - Stimulated) * dTau;
        Tau := (T - 0.5) * dTau;
        H := gainL[T - 1] + (RKA / 2);
        Pin := sqr(AmpIn(Energy, TauNought, Tau));
        Stimulated := (Pin * (exp(H) - 1)) / Esat;
        RKB := (((SmallSigGain * Length - H) / Trec) - Stimulated) * dTau;
        H := gainL[T - 1] + (RKB / 2);
        Stimulated := (Pin * (exp(H) - 1)) / Esat;
        RKC := (((SmallSigGain * Length - H) / Trec) - Stimulated) * dTau;
        Tau := T * dTau;
        H := (gainL[T - 1] + RKC);
        Pin := sqr(AmpIn(Energy, TauNought, Tau));
        Stimulated := (Pin * (exp(H) - 1)) / Esat;
        RKD := (((SmallSigGain * Length - H) / Trec) - Stimulated) * dTau;
        gainL[T] := gainL[T - 1] + (RKA + (2 * RKB) + (2 * RKC) + RKD) / 6;
      end;
    for T := -50 to 50 do
      begin
        Tau := T * dTau * 10;
        H := gainL[T * 10];
        Pin := sqr(AmpIn(Energy, TauNought, Tau));
```

```
        Pout := Pin * exp(H);
        Dfi := -1 * ((alpha * H) / 2);
        dHdt := (gainL[(T * 10) + 1] - gainL[(T * 10) - 1]) / (2 * dTau);
        Dw := (alpha * dHdt) / 2;
        Dmu := Dw / (2 * pi);
        write((Tau * 1e12) : 2 : 2, ' ps  ', Pout : 4 : 4, ' watts ', '  ');
        writeln(Dfi : 3 : 3, ' radians ', (Dmu * 1e-9) : 4 : 4, ' GHz ');
        temporal[T, 1] := Tau;
        temporal[T, 2] := Pin;
        temporal[T, 3] := Pout;
        temporal[T, 4] := H * 4.3429;
        temporal[T, 5] := Dfi;
        temporal[T, 6] := Dw;
      end;
  end;(*  IndexChange  *)
  procedure EnergyOut;
(*    Integrates the output pulse to determine the output energy and net gain.    *)
    var
      T : integer;
      Eout, ActualGain : real;
  begin
    T := -50;
    Eout := temporal[T, 3] * dTau * 10;
    repeat
      T := T + 1;
      Eout := Eout + temporal[T, 3] * dTau * 10;
      T := T + 1;
      Eout := Eout + temporal[T, 3] * dTau * 10;
    until T = 48;
    T := T + 1;
    Eout := Eout + temporal[T, 3] * dTau * 10;
    T := T + 1;
    Eout := Eout + temporal[T, 3] * dTau * 10;
    ActualGain := Eout / Energy;
    writeln('Gain = ', ActualGain : 3 : 3);
  end;
  procedure FourierTransform;
(*   Calculates the frequency spectrum of the pulse.    *)
(*   The amplitude/phase is integrated at 101 frequencies using  *)
(*    Simpsons rule.   *)
    var
      DeltaFi, Phase : double;
      dW, Winc : double;
      Amplitude : double;
      RealPart, ImagPart : double;
      W, T : integer;
    procedure AmplitudeAndPhase;
    begin
      Amplitude := sqrt(temporal[T, 3]);
      DeltaFi := temporal[T, 5];
      Phase := (T * 10 * dTau * dW) + DeltaFi;
    end;
  begin
    Winc := Wrange / 100;
    MaxSpec := 0;
    for W := -50 to 50 do
      begin
        T := -50;
```

```
        dW := (Winc * W) + Woffset;
        spectral[W, 1] := (-1 * dW * sqr(Wavelength) * 1e9) / (2 * pi * LightSpeed);
        AmplitudeAndPhase;
        RealPart := amplitude * cos(Phase);
        ImagPart := amplitude * sin(Phase);
        repeat
          T := T + 1;
          AmplitudeAndPhase;
          RealPart := RealPart + 4 * (Amplitude * cos(Phase));
          ImagPart := ImagPart + 4 * (Amplitude * sin(Phase));
          T := T + 1;
          AmplitudeAndPhase;
          RealPart := RealPart + 2 * (Amplitude * cos(Phase));
          ImagPart := ImagPart + 2 * (Amplitude * sin(Phase));
        until T = 48;
        T := T + 1;
        AmplitudeAndPhase;
        RealPart := RealPart + 4 * (Amplitude * cos(Phase));
        ImagPart := ImagPart + 4 * (Amplitude * sin(Phase));
        T := T + 1;
        AmplitudeAndPhase;
        RealPart := RealPart + Amplitude * cos(Phase);
        ImagPart := ImagPart + Amplitude * sin(Phase);
        spectral[W, 2] := sqr(RealPart) + sqr(ImagPart);
        if spectral[W, 2] > MaxSpec then
          MaxSpec := spectral[W, 2];
        writeln(spectral[W, 1] : 5 : 5, ' ', spectral[W, 2] : 5 : 5);
      end;
  end;
  procedure Normalise;
(*    Spectral intensities are normalised.    *)
    var
      W : integer;
  begin
    for W := -50 to 50 do
      spectral[W, 2] := spectral[W, 2] / MaxSpec;
  end;
  procedure DataWrite;
(*    Data is output to a file which can be read by Cricket Graph and plotted. *)
    var
      N : integer;
  begin
    for N := -50 to 50 do
      begin
        write(f, (temporal[N, 1] * 1e12) : 5 : 5, chr(9), temporal[N, 2] : 5 : 5, chr(9));
        write(f, temporal[N, 3] : 5 : 5, chr(9), temporal[N, 4] : 5 : 5, chr(9));
        write(f, temporal[N, 5] : 5 : 5, chr(9), (temporal[N, 6] / (2 * pi * 1e9)) : 5 : 5, chr(9));
        writeln(f, spectral[N, 1] : 5 : 5, chr(9), spectral[N, 2] : 5 : 5);
      end;
  end;
begin (*      main program body     *)
  HideAll;
  Screen.top := 40;
  Screen.left := 0;
  Screen.bottom := 345;
  Screen.right := 510;
  SetTextRect(Screen);
  ShowText;
```

```
  write('Enter amplifier length in microns ');
  readln(Length);
  Length := Length * 1e-6;
  write('Active region volume in cubic microns ? ');
  readln(Volume);
  Volume := Volume * 1e-18;
  write('Confinement factor gamma ? ');
  readln(Gamma);
  write('Transparency current in mA ? ');
  readln(TransparencyCurrent);
  TransparencyCurrent := TransparencyCurrent * 1e-3;
  write('Operating current in mA ? ');
  readln(BiasCurrent);
  BiasCurrent := BiasCurrent * 1e-3;
  write('Small signal gain in dB at the operating current ? ');
  readln(Gain);
  Gain := XpwrY(10, (Gain / 10));
  Gain := ln(Gain) / Length;
  DiffGain;
  write('Input pulse energy in pJ ? ');
  readln(Energy);
  Energy := Energy * 1e-12;
  write('And finally, the FWHM of your Gaussian pulse in ps ?');
  readln(TauPulse);
  TauPulse := TauPulse * 1e-12;
  textname := newfilename('Name for new text file ?');
  If textname <> '' then
    begin
      rewrite(f,  textname);
      TauNought := TauPulse / 1.665;
      dTau := TauNought / 150;
      AmplifyAndChirp;
      EnergyOut;
      write('Enter start of FT in GHz ');
      readln(Wstart);
      write('Enter finish of FT in GHz ');
      readln(Wfinish);
      Wrange := Wfinish - Wstart;
      Woffset := (Wfinish + Wstart) / 2;
      Wrange := Wrange * 1e9 * 2 * pi;
      Woffset := Woffset * 1e9 * 2 * pi;
      FourierTransform;
      Normalise;
      DataWrite;
      close(f);
    end
end.
```

Appendix 4 Related publications

Group-velocity-dispersion compensation of a passively mode-locked ring LiF:F_2^+ color-center laser,
N. Langford, R. S. Grant, C. I. Johnston, K. Smith, and W. Sibbett,
Opt. Lett. **14**, 45 (1989).

Enhanced mode locking of color-center lasers,
P. N. Kean, X. Zhu, D. W. Crust, R. S. Grant, N. Langford, and W. Sibbett,
Opt. Lett. **14**, 39 (1989).

Cavity configurations for coupled-cavity mode locking,
R. S. Grant and W. Sibbett,
Opt. Commun. **86**, 177 (1991).

Observations of ultrafast nonlinear refraction in an InGaAsP optical amplifier,
R. S. Grant and W. Sibbett,
Appl. Phys. Lett. **58**, 1119 (1991).

Cross-phase modulation in semiconductor optical amplifier,
R. S. Grant, G. T. Kennedy, and W. Sibbett,
Electron. Lett. **27**, 801 (1991).

Passive coupled-cavity mode-locked color-center lasers,
R. S. Grant, P. N. Kean, D. Burns, and W. Sibbett,
Opt. Lett. **16**, 384 (1991).

Reprinted from Optics Letters, Vol. *14*, page 45, January 1, 1989.

Group-velocity-dispersion compensation of a passively mode-locked ring LiF:F_2^+ color-center laser

N. Langford, R. S. Grant, C. I. Johnston, K. Smith,* and W. Sibbett

J. F. Allen Physics Research Laboratories, University of St. Andrews, St. Andrews, Fife KY16 9SS, Scotland, UK

Received August 1, 1988; accepted September 29, 1988

By using an intracavity prism sequence to control group-velocity dispersion, pulses as short as 180 fsec have been generated near 850 nm from a passively mode-locked, traveling-wave LiF:F_2^+ color-center laser.

The development of cw mode-locked dye lasers in which the pulse evolution kinetics are optimized by balancing the intracavity self-phase modulation and group-velocity dispersion (GVD) with an adjustable amount of intracavity GVD has permitted the routine generation of optical pulses with sub-100-fsec pulse durations over the visible and near-infrared spectral regions[1–4] and the attainment of pulses as short as 19 fsec at a wavelength of 630 nm.[5] Recently the passive mode locking of a cw color-center laser based on the F_2^+-type center in a LiF alkali halide host lattice was demonstrated, and pulses with durations of 390 fsec were obtained from a colliding-pulse mode-locked ring resonator configuration.[6] The time–bandwidth product of these pulses was well in excess of the theoretical value associated with the assumed sech^2 pulse profiles, and this discrepancy was attributed to the presence of uncompensated intracavity GVD. In this Letter the compensation of the GVD is described for this traveling-wave laser in which pulses having durations as short as 180 fsec have been generated.

The color-center laser based on the F_2^+ center in LiF has been demonstrated as a highly tunable and efficient laser covering the 800–1000-nm spectral region.[7] The design of the laser[8] used in this research differs from that used in other color-center lasers in that only the laser crystal is located in the vacuum chamber and optical access to it is afforded by two Brewster-angled Infrasil windows. To minimize the reorientational and thermal bleaching effects associated with the F_2^+ center, an optical chopper operating with a duty reduction cycle of 10:1 and frequency of ~28 Hz was employed; under these conditions stable operation from the same spot in the crystal was observed for more than 200 h.

The studies of the dispersion compensation of the passively mode-locked color-center laser were performed with the traveling-wave resonator illustrated in Fig. 1. The cavity was formed by the active folded section consisting of the mirrors M_1 amd M_2 (radii of curvature 10 cm, 100% reflecting over the 800–1000-nm wavelength range), the passive folded section M_3 and M_4 (radii of curvature 5 cm, 100% reflecting over the 800–1000-nm wavelength range), the output coupler M_5 (3% transmitting over the 800–1000-nm range), and the plane mirror M_6 (100% reflecting over the 800–1000-nm range). Owing to the physical restrictions imposed by the vacuum chamber, it was difficult to arrange an independent focusing mirror to couple the Kr^+ pump beam into the laser crystal, so M_1 of the active folded section also served as the focusing mirror. In order to couple the pump beam efficiently into the crystal, the dielectric coating on this mirror was a double stack for which the phase distortions[9] were minimized by ensuring that the pump-light-reflecting stack was deposited below the infrared-reflecting stack. This coating was also used on mirrors M_2–M_4. The 2-mm-thick Brewster-angled LiF crystal was located at the common focus of mirrors M_1 and M_2, and a 200-μm-thick Brewster-angled saturable-absorber dye jet was positioned at the common focus of mirrors M_3 and M_4. The saturable absorber used in this work was the laser-active dye 5,5′-dichloro-11-diphenylamino-3,3′-diethyl-10,12-ethylenethiatricarbo-cyanine perchlorate (IR140), which exhibits a peak absorption of $\sim 6 \times 10^{-16}$ cm^2 at a wavelength of 810 nm in a propylene carbonate solution[10] and an equally strong photoisomer peaking at the slightly longer wavelength of 865 nm.[11]

In the case of passively mode-locked dye lasers it is understood that contributions to the intracavity self-phase modulation arise from the optical Kerr effect in the solvents used to form the dye jet stream[12] and also from off-resonant transitions in both the gain and absorber media.[13] Contributions to the GVD arise from reflections off the dielectric coatings of the cavity optics and also from propagation of the optical pulse through various transparent elements in the cavity.[14]

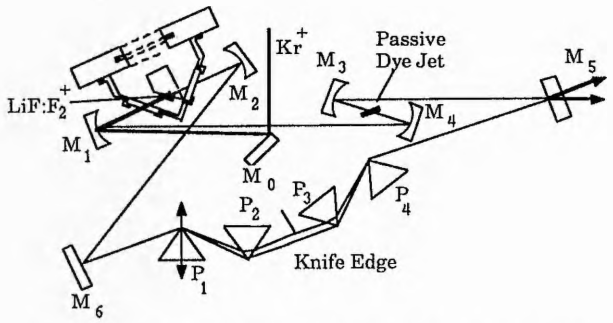

Fig. 1. Color-center ring resonator configuration.

0146-9592/89/010045-03$2.00/0

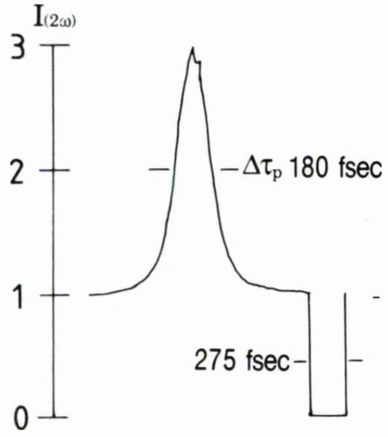

Fig. 2. Autocorrelation trace associated with the shortest pulse generated from the dispersion-compensated LiF:F_2^+ laser.

For the color-center laser these factors will also be present, but since mode-locked operation occurs on the short-wavelength side of the gain peak and the short-wavelength side of the peak absorption of the photoisomer, it is believed that a downchirp arises from the off-resonant transitions in the gain medium, while off-resonant saturation of the photoisomer also results in the introduction of an upchirp. Saturation of the ground state of the absorber leads to a downchirp. Passage of the color-center laser pulses through the passive dye-solvent jet stream results in the introduction of a GVD. Unlike with dye lasers, however, there is also a large contribution to the intracavity GVD from the Brewster-angled Infrasil windows and the LiF host crystal. The magnitude, D, of the GVD introduced by the Brewster-angled windows and LiF crystal may be estimated by considering the following equation:

$$D = \frac{-l_e \lambda^3}{2\pi c^2}\left(\frac{d^2 n}{d\lambda^2}\right), \tag{1}$$

with l_e the effective thickness of the material, λ the operating wavelength, c the speed of light, and $(d^2n/d\lambda^2)$ the material dispersion. Contributions of 150 and 45 fsec^2 were estimated for the Brewster-angled windows and the LiF crystal, respectively.[15] To compensate for these factors, a Brewster-angled prism sequence similar to that developed by Valdmanis *et al.*,[1] consisting of the prisms P_1–P_4, was inserted into the cavity between mirrors M_5 and M_6. The separation of the two prism pairs, P_1 and P_2 and P_3 and P_4, was calculated to be ~50 cm,[16] to compensate for the GVD introduced by the Infrasil windows, the LiF crystal, and the prism material. As the laser beam is collimated but spectrally dispersed between prisms P_2 and P_3, it is possible, by translating a knife edge across the dispersed spectrum, to frequency-tune the laser. The saturable absorber acts as a filter, inhibiting laser action on the short-wavelength side of the LiF:F_2^+ gain spectrum, while the knife edge frustrates laser action at the long wavelengths. Operating with a prism sepa-

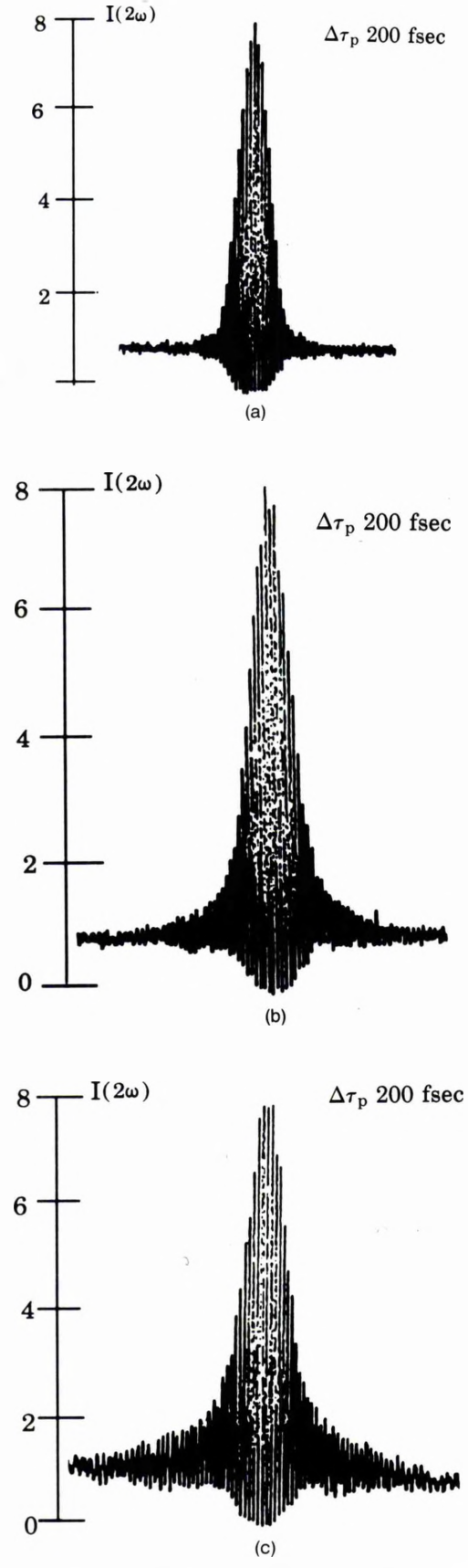

Fig. 3. Interferometric autocorrelation traces of the output pulse train from the passively mode-locked color-center laser for (a) optimum, (b), (c) optimum plus 5-mm and 7-mm path lengths of glass, respectively.

ration of ~50 cm resulted in a cavity round-trip period of ~25 nsec for the experimental resonator.

The wavelength of the color-center laser was fixed to 845 nm, and the concentration of the saturable absorber was optimized to yield the shortest pulses. At a concentration of 1×10^{-4} mole/liter, pulses were obtained with durations between 200 and 250 fsec (assuming sech^2 pulse profiles), while the shortest pulses observed had durations of 180 fsec, as illustrated in Fig. 2. Simultaneous measurements of the laser bandwidth yielded a value of 4.2 nm, implying a time–bandwidth product of 0.317, which compares favorably with the theoretical value of 0.315 for bandwidth-limited sech^2 pulses. The peak average output power[17] associated with these pulses was 16 mW per arm, which corresponds to a pulse peak power of ~2.2 kW. Increasing the concentration of the saturable absorber resulted in a shift of the central wavelength of the laser to a longer wavelength while the pulse duration remained constant. By varying both the saturable-absorber concentration and the position of the knife edge it was possible to tune the lasing wavelength from 845 to 860 nm.

Although the pulses generated from the laser indicate near-bandwidth-limited characteristics, a more precise method by which the pulses may be studied involves interferometric autocorrelation techniques,[18] allowing the coherence features to be determined. Interferometric autocorrelations were therefore made of the dispersion-compensated color-center laser pulse trains, and a selection is reproduced in Fig. 3. (It should be noted that the recorded fringes are not actual interference fringes but are an average of several fringes owing to an insufficient number of data storage points on our digital storage oscilloscope.) This figure depicts the effects of varying the amount of intracavity GVD on the pulse train. With the amount of intracavity glass optimized [Fig. 3(a)] it can be seen that the resultant pulses are well mode locked and stable. As the amount of intracavity glass was increased [Figs. 3(b) and 3(c)], thus increasing the amount of positive GVD in the cavity, the duration of the pulses increased from 200 to 250 fsec and the degree of phase coherence was reduced as indicated by the rising wings in the autocorrelation traces. Decreasing the amount of intracavity glass and thus the positive GVD from the optimum position resulted in the output trains' becoming unstable.

Thus, in conclusion, the dispersion compensation of a passively mode-locked LiF:F_2^+ color-center laser has been demonstrated for the first time, to our knowledge, and pulses as short as 180 fsec have been obtained from a traveling-wave resonator over a wavelength range of 845–860 nm. These pulses should find applications in time-domain spectroscopic studies of resonant and nonresonant interactions in GaAs/GaAlAs multiple-quantum-well- and waveguide-type structures.

Research studentship support for R.S. Grant from the Science and Engineering Research Council (SERC), and for C. I. Johnston from the Department of Education of Northern Ireland, is acknowledged. Personal support for N. Langford from the Procurement Executive of the Ministry of Defence and general SERC research funding are also gratefully acknowledged, as is the specialist technical assistance from R. H. Mitchell concerning the vacuum and cryogenic equipment used in this research.

* Present address, AT&T Bell Laboratories, Crawfords Corner Road, Holmdel, New Jersey 07733.

References

1. J. A. Valdmanis, R. L. Fork, and J. P. Gordon, Opt. Lett. **10,** 131 (1985).
2. P. M. W. French and J. R. Taylor, Opt. Commun. **61,** 224 (1987).
3. J. Dobler, H. H. Shulz, and W. Zinth, Opt. Commun. **57,** 407 (1986).
4. M. D. Dawson, T. F. Boggess, and A. L. Smirl, Opt. Lett. **12,** 254 (1987).
5. A. Finch, G. Chen, W. Sleat, and W. Sibbett, J. Mod. Opt. **35,** 345 (1988).
6. N. Langford, K. Smith, and W. Sibbett, Opt. Lett. **12,** 903 (1987).
7. L. F. Mollenauer, in *Methods of Experimental Physics*, C. L. Tang, ed. (Academic, New York, 1979), Vol. 15, Part B, Chap. 6.
8. N. Langford, K. Smith, and W. Sibbett, Opt. Commun. **64,** 274 (1987).
9. P. Laporta and V. Magni, Appl. Opt. **24,** 2014 (1985).
10. K. Smith, W. Sibbett, and J. R. Taylor, Opt. Commun. **49,** 359 (1984).
11. J. P. Fouassier, D. J. Lougnot, and J. Faure, Opt. Commun. **18,** 263 (1976).
12. O. E. Martinez, R. L. Fork, and J. P. Gordon, J. Opt. Soc. Am. B **2,** 753 (1985).
13. J. C. Diels, W. Dietel, J. J. Fontaine, W. Rudolph, and B. Wilhelmi, J. Opt. Soc. Am. B **2,** 682 (1985).
14. S. De Silvestri, P. Laporta, and O. Svelto, IEEE J. Quantum Electron. **QE-20,** 533 (1984).
15. The values for $(d^2n/d\lambda^2)$ for the Brewster-angled windows were evaluated by using the Sellmeier coefficients given in D. Marcuse, Appl. Opt. **19,** 1916 (1980); $(d^2n/d\lambda^2)$ for the LiF crystal was calculated by using Sellmeier coefficients given in D. E. Gray, ed., *American Institute of Physics Handbook*, 3rd ed. (McGraw-Hill, New York, 1972), p. 6–34.
16. R. L. Fork, O. E. Martinez, and J. P. Gordon, Opt. Lett. **9,** 150 (1984).
17. The peak average power was evaluated by multiplying the average output power from the laser by the duty reduction factor of the optical chopper.
18. J.-C. M. Diels, J. J. Fontaine, I. C. McMichael, and F. Simoni, Appl. Opt. **24,** 1270 (1985).

Reprinted from Optics Letters, Vol. 14, page 39, January 1, 1989.

Enhanced mode locking of color-center lasers

P. N. Kean, X. Zhu, D. W. Crust, R. S. Grant, N. Langford, and W. Sibbett

Department of Physics and Astronomy, University of St. Andrews, St. Andrews, Fife KY16 9SS, Scotland

Received July 18, 1988; accepted October 14, 1988

A significant enhancement in the mode locking of a KCl:Tl color-center laser has been observed when a length of optical fiber having positive group-velocity dispersion was incorporated within an external control cavity. Pulse durations of ~260 fsec were obtained by this method, representing a compression factor ~60× that with the color-center laser alone. Similar results have also been observed with an InGaAsP semiconductor diode amplifier as the nonlinear element within the control cavity.

The synchronously mode-locked KCl:Tl color-center laser can typically produce pulses of ~8–20-psec duration at a wavelength of approximately 1.5 μm. In the research by Mollenauer and Stolen,[1] the mode-locked characteristics of such a laser were dramatically improved by incorporating a length of optical fiber into an optical feedback loop, or control cavity. A small fraction of the output from the color-center laser was fed into the fiber, where the combined effects of self-phase modulation and negative group-velocity dispersion (GVD) caused the pulses to be temporally compressed. These compressed pulses are then reinjected into the master cavity, stimulating the production of narrower pulses from the laser itself. This process continues until the pulses have essentially the same shape on entering and returning from the fiber, i.e., they become optical solitons. Although it was observed that for a single length of fiber a variety of pulse durations could be obtained,[2] the pulses returning from the control cavity and injected back into the laser were always observed to be as short or shorter than those exiting the composite cavity laser. In this Letter we describe experiments whereby an optical fiber having positive GVD was inserted into a control cavity (similar results have also recently been observed by other authors[3]). Pulses propagating along such a fiber are dispersively broadened, and the fiber is unable to support (bright) solitons. Nevertheless, we have found that even these temporally broadened pulses reinjected back into the master cavity can significantly improve the mode locking of the color-center laser in a dramatic way.

A schematic diagram of the coupled-cavity laser is shown in Fig. 1. The color-center laser alone, bounded by mirrors M_1 and M_0, typically produced pulses of ~15-psec duration and was tunable from 1.45 to 1.55 μm. The control cavity containing the fiber was formed by the output coupler M_0 of the color-center laser, beam splitter S_1, and a small dielectric mirror M_3 mounted on a piezoelectric translator (PZT). An elliptical-core fiber[4] (produced by the Andrew Corporation) was used to provide polarization-preserving and single-mode propagation at 1.5 μm. The relatively large germania content of the fiber (giving a Δn ~0.046) necessitates a small core (2.8 μm × 1.6 μm) in order to obtain propagation in a single mode, and this in turn produces a large waveguide dispersion, giving the fiber a net positive GVD. The average power coupled into the fiber was adjusted by a variable neutral-density (ND) filter.

With the control cavity unblocked and its length made equal to (or a multiple of) the master cavity, a significant shortening of the laser output pulses was seen to occur. An electronic stabilization scheme similar to that described in Ref. 2 was employed in order to provide for the correct relative optical phase matching between the pulses fed back from the fiber and those circulating in the master cavity. Once this stabilization loop was in operation, the output pulses from the composite cavity laser were very stable, with ~1% noise fluctuations. For a fiber length of 2.2 m the composite cavity laser produced pulses of ~1.1-psec duration, and the shortest pulses of 260 fsec (see inset of Fig. 3) were obtained with a fiber length of 24 cm. For the 2.2-m fiber, the laser produced stable pulses of constant duration for a power range of 10–25 mW within the fiber (measured just before M_3), and for shorter fiber lengths, the stability range shifted to

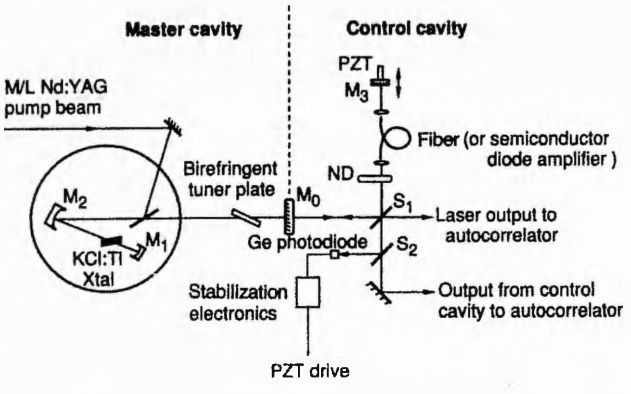

Fig. 1. Experimental arrangement of the coupled-cavity color-center laser. M/L, mode locked. Mirror reflectivities: M_1, M_2, M_3, ~100%; M_0, ~80%. Beam-splitter reflectivities: S_1, ~50%; S_2, ~30%.

0146-9592/89/010039-03$2.00/0

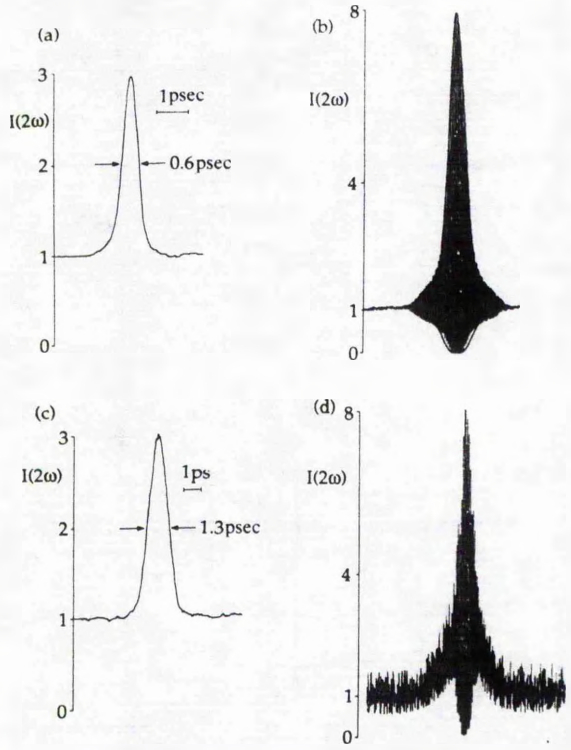

Fig. 2. Intensity and interferometric autocorrelation traces for pulses exiting the laser [(a) and (b)] and for pulses returning from the control fiber [(c) and (d)] with a fiber length of 55 cm. The fringes seen on the interferometric autocorrelations are not actual interference fringes but are due to sampling limitations on the digital oscilloscope.

slightly higher powers, approximately 30 mW for 24 cm. As can be seen from Fig. 1, we were also to monitor the pulses returning from the control cavity, and it was found that the duration of these pulses exceeded the duration of those exiting the laser for all the fiber lengths used. For the 2.2-m and 24-cm lengths, the fed-back pulse durations were 3.0 and 0.6 psec, respectively. Typical second-harmonic intensity and interferometric autocorrelation traces of the pulses are shown in Fig. 2 for a control fiber length of 55 cm. The laser output pulses had durations of 0.6 psec, whereas those fed back into the master cavity had durations of ~1.3 psec. The interferometric autocorrelation traces show a substantial difference between the two pulse trains. For the laser output [Fig. 2(b)] the pulses are well phase locked (as shown by the 8:1 contrast ratio); for comparison, a sech^2 fit to the envelope is also shown. There is a slight departure in the wings of the pulse, which may imply some excess frequency chirp, but it should be remembered that since the pulses are not solitons, there is no particular reason why the pulses should have sech^2 intensity profiles. The pulses returning from the control cavity [Fig. 2(d)] show a substantial linear frequency chirp due to the positive GVD of the fiber (indicated by the rising wings of the autocorrelation[5]), with only the central portion of the pulse being coherent. A similar structure was seen in all cases for these pulses. A plot of the pulse durations obtained from the coupled-cavity laser as a function of fiber length is shown as Fig. 3. In contrast to the soliton laser, where the output-pulse duration is proportional to the square root of the fiber length, no such simple relationship is observed here. It may also be inferred from this graph that an optimum fiber length exists for the production of the shortest output pulses. Owing to physical constraints of our experimental arrangement, further data around this minimum were not taken, but this would be required in order to establish the true existence of an optimum fiber length.

In our experimental configuration (Fig. 1), although the fiber itself provided positive GVD, any glass within the master cavity (e.g., Brewster-angled plates, an output coupler) may provide negative GVD and thereby lead to temporal compression of the frequency-chirped pulses. To verify that this was not the case and that negative GVD is not necessary for enhanced mode locking, a similar experiment was performed using a synchronously mode-locked LiF:F_2^+ color-center laser.[6] This laser produced pulses of typically 4-psec duration at a wavelength near 900 nm, where the material dispersion for glass is positive. A coupled-cavity arrangement was set up with a 2-m length of fiber, which was polarization preserving and monomode in the lasing wavelength region (Andrew Corporation fiber) similar to that previously described. With feedback from the control cavity, preliminary results have shown an observable pulse reshaping and narrowing, with the laser output pulses shortened to ~1 psec (Fig. 4).

The results described here seem to be in general agreement with the theoretical modeling characteristics reported recently by Blow and Wood.[7] They showed that pulses broadened by passage through a nonlinear element in the control cavity could still enhance the mode locking of a homogeneously broadened laser. The mechanism may be described as being due to the enhanced phase coupling involving additional longitudinal modes of the laser cavity (induced by the processes occurring within the nonlin-

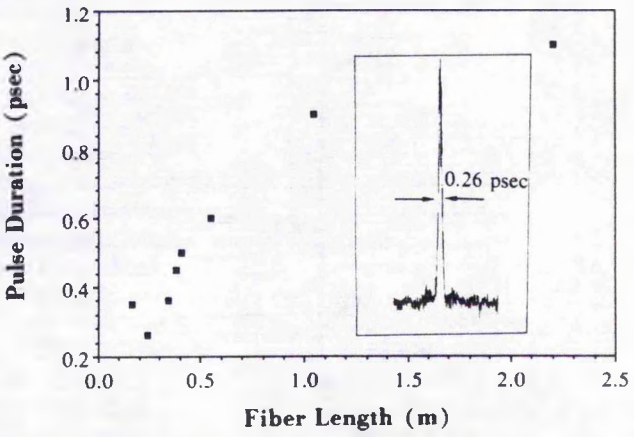

Fig. 3. Variation of the pulse duration from the coupled-cavity laser as a function of fiber length. The inset shows an autocorrelation trace of the 0.26-psec pulse with L = 24 cm.

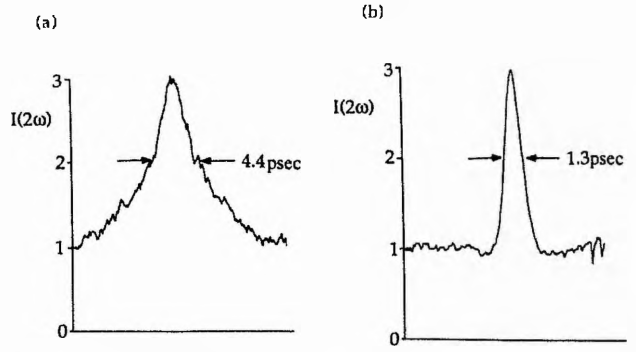

Fig. 4. Autocorrelation traces of the pulses obtained (a) from the LiF:F_2^+ laser alone and (b) with feedback from the control cavity for a fiber length of 2 m.

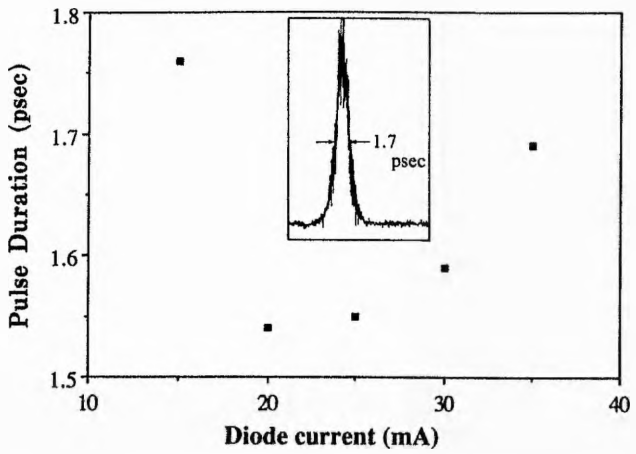

Fig. 5. Pulse duration versus drive current to the InGaAsP diode amplifier in the control cavity of the KCl:Tl color-center laser. The inset shows typical intensity autocorrelation of the output pulses for a 35-mA diode injection current.

ear element), thereby increasing the mode-locked bandwidth. Our experimental data are qualitatively consistent with this, but we did observe that the pulses reinjected into the master cavity had a broader bandwidth (owing to self-phase modulation) than the pulses exiting the laser. The role of saturable amplification in the control cavity has also been studied theoretically,[7] and we have evaluated this experimentally by using an InGaAsP semiconductor diode amplifier as the nonlinear element within a control cavity. The diode was operated at injection currents in the 10–35-mA range, and higher currents were not used in order to prevent lasing between one facet of the diode and mirror M_3 (Fig. 1). Our initial results showed pulse shortening to ~1.4 psec for a current of 20 mA. A plot of the pulse durations from the coupled-cavity laser as a function of diode current is shown in Fig. 5, where the inset is a typical autocorrelation trace of the output pulses for a current of 35 mA. Most recently, by optimization of the laser we have obtained pulses as short as 250 fsec, which is comparable with that of the fiber-based control cavity. In the diode-amplifier case, however, the laser has been observed to suffer regular dropouts, i.e., switching to the much broader color-center-laser pulses. The stabilization loop, although compensating for relatively slow cavity-length changes, was not able to eliminate these higher-frequency (~1-kHz) dropouts. It was also noted that the period of these could be varied by altering the length of the master cavity, and further study of these features is ongoing. The average power fed back into the master cavity was estimated to be less than 1 mW, yet, interestingly, this is still sufficient to produce the dramatic narrowing of the laser pulses reported here.

In summary, we have found that the existence of negative GVD in the control cavity of a color-center laser is not necessary to provide an enhanced mode locking of the laser. A semiconductor diode amplifier has also been demonstrated to produce a similar effect, in agreement with previous theoretical considerations.[7] Finally, it would seem from the results described here that actual soliton formation in the control cavity is a specific case of a more general phenomenon, whereby pulses reinjected into the master cavity from a control cavity containing a nonlinear element can completely dominate the mode-locking characteristics (i.e., coupled-cavity mode locking) of color-center lasers and will perhaps be applicable to other broad-bandwidth laser systems.

We wish to thank K. C. Byron (STC Technology Ltd.) and I. White (Cambridge University) for the loan of the samples of the Andrew Corporation fiber and K. J. Blow and B. P. Nelson (British Telecom Research Laboratories) for communicating their results to us before publication. The overall funding of this research by the UK Science and Engineering Research Council is gratefully acknowledged. Part of this funding was provided through the Joint Opto-Electronics Research Scheme initiative.

References

1. L. F. Mollenauer and R. H. Stolen, Opt. Lett. **9,** 13 (1984).
2. F. M. Mitschke and L. F. Mollenauer, IEEE J. Quantum Electron. **QE-22,** 2242 (1986).
3. K. J. Blow and B. P. Nelson, Opt. Lett. **13,** 1026 (1988).
4. K. C. Byron, Electron. Lett. **23,** 1324 (1987).
5. J. C. Diels, J. J. Fontaine, I. C. McMichael, and F. Simoni, Appl. Opt. **24,** 1270 (1985).
6. N. Langford, K. Smith, and W. Sibbett, Opt. Commun. **64,** 247 (1987).
7. K. J. Blow and D. Wood, J. Opt. Soc. Am. B **5,** 629 (1988).

Optics Communications 86 (1991) 177–182
North-Holland

OPTICS
COMMUNICATIONS

Cavity configurations for coupled-cavity mode locking

R.S. Grant and W. Sibbett
J.F. Allen Physics Research Laboratories, University of St. Andrews, St. Andrews, Scotland KY16 9SS, UK

Received 29 April 1991; revised manuscript received 12 July 1991

The mode locking of a coupled-cavity KCl:Tl color-centre laser in a Michelson cavity has been compared experimentally with that of the more conventional Fabry-Perot configuration. Either solitonic fibre or low-dispersion, erbium-doped fibre was used in the control cavity. Although both arrangements produced similar pulse durations, the Michelson configuration offered the practical advantage of greater stability. Self-starting mode locking has been observed when the KCl:Tl crystal was located close to the centre of the master cavity, but the ultrashort pulses were accompanied by a cw background or pedestals.

1. Introduction

The soliton laser [1,2] produced ultrashort pulses by using optical feedback from a control cavity appended directly onto the main laser cavity. The control cavity incorporated an optical fibre which provided pulse compression through the combined effects of anomalous dispersion and self-phase modulation (SPM). Numerical modelling and experimental results showed that similar pulse durations were generated when a pulse broadening element was used in the control cavity [3–5]. This was explained by considering the enhanced communication of phase information among the laser axial modes by the nonlinearity. In the temporal regime, the concept of additive-pulse mode locking identified the pulse shortening mechanism [6,7]. A pulse would be shaped when added to a phase modulated version of itself, with shortening obtained at particular phase mismatches between the two pulses.

Independently, a CO_2 laser was passively mode locked by including a fast Kerr-type nonlinearity (provided by a germanium crystal) in one branch of a Michelson interferometer which replaced an end mirror of the laser cavity [8,9]. The interferometer was used as a nonlinear mirror, becoming more reflective with higher intensities, and thus favouring the production of short pulses from the laser. Later work established that mode locking with this interferential technique [10] was essentially similar to that described above, where the nonlinearity is located within a separate control cavity.

We now refer to this general technique of using optical feedback to produce ultrashort pulses as coupled-cavity mode locking. This paper builds upon earlier work [11] with a comparison of the mode-locking characteristics of a coupled-cavity KCl:Tl colour-centre laser having either a Michelson cavity configuration or the more common Fabry-Perot arrangement. Samples of anomalous-dispersion fibre or erbium-doped fibre with zero group-velocity dispersion (GVD) at ~ 1.52 μm, having been used as the nonlinear elements. We have also found that by locating the gain medium centrally in the master cavity the initial mode beating is enhanced, thereby reducing the threshold for self-starting operation.

2. Comparison of Michelson and Fabry-Perot cavities

The KCl:Tl colour-centre laser was excited in a noncollinear geometry by a cw mode-locked Nd:YAG laser. In the Fabry-Perot arrangement, shown schematically in fig. 1a, the beamsplitter (BS) reflectivity was 37%, and mirror M_0 had a transmission of either 12% or 22%. The Michelson cavity, fig. 1b, had a beamsplitter (BS) of relatively high reflectivity, either 93% or 88%, making the power levels in the gain medium and in the fibre similar to

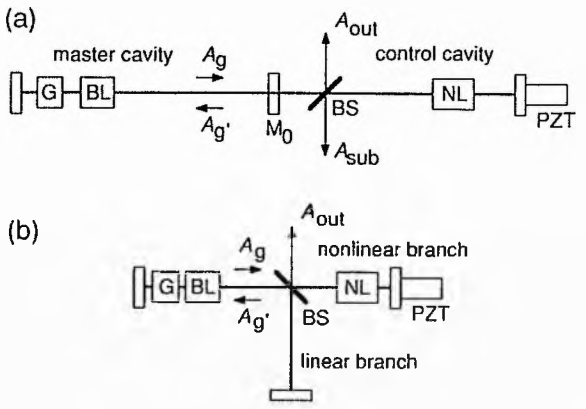

Fig. 1. Schematic of Fabry-Perot (a) and Michelson (b) coupled-cavity laser configurations. G, gain; BL, bandwidth limitation; NL, nonlinearity (provided here by an optical fibre); A_{out}, main output; A_{sub}, subsidiary output.

those in the Fabry-Perot arrangement, and allowing direct comparison of the two configurations. The usable output power from each arrangement was similar at approximately 30 mW. Stabilisation of the cavity/branch lengths was achieved by using a mirror mounted on a piezo-electric translator (PZT) controlled by an electronic feedback system [2]. Light was coupled into and out of the fibre with antireflection coated lenses, where index-matching oil was used between the front element and the fibre end to reduce parasitic optical feedback.

Initial studies were made using anomalously dispersive fibre. This fibre was similar to that used in the original soliton laser, i.e. polarisation preserving, with a GVD of $D \sim +15$ ps/(nm km) at the operating wavelength around 1.5 μm, and a modal area quoted as 65 μm^2 [1] or 86 μm^2 [2]. The fibre length was chosen after considering the power requirements for the $N=2$ soliton propagation. A relatively long length of 1.57 m was required due to the large core area and the rather large GVD of the fibre. The condition $Z_0 = 2L$ implies a pulse duration of ~330 fs (full width at half maximum), assuming a squared hyperbolic secant intensity profile [1]. Furthermore, for $n_2 = 3.2 \times 10^{-16}$ cm^2 W^{-1}, and a repetition frequency of 82 MHz, the average power required for $N=2$ soliton propagation in the control fibre is approximately 30–40 mW, depending on the assumed modal area.

With both arrangements, stable mode locking was obtained by limiting the oscillating bandwidth with a single quartz birefringent plate of 0.8 mm thickness. For the Fabry-Perot cavity, with a mirror M_0 transmission of 12%, pulse durations as short as 330 fs were obtained, decreasing to 280 fs when the transmission of this mirror was increased to 22%. These durations were obtained for estimated average power levels in the fibre of approximately 25–30 mW, in accord with the calculations above. The pulses from the control cavity were significantly shorter, around 180 fs in both cases. Even in an optimum operation the pulse in the fibre never reaches the $N=2$ soliton condition. Despite this, expressions outlined by Mollenauer and Stolen [1] enable the pulse duration (of the main output) and the power requirements to be predicted remarkably well. The laser cannot operate precisely on the $N=2$ soliton condition, because in that situation the feedback pulse would not be frequency chirped, and furthermore, its temporal and spectral shape would be similar to the master cavity pulse. Pulse shortening in the laser, which is necessary at the steady state to overcome the broadening caused by spectral filtering and GVD in the master cavity, therefore would not be obtained under such conditions.

Using a Michelson cavity the laser produced a similar performance, where pulse durations as short as 310 fs were generated using a 93% reflectivity beamsplitter, and 290 fs when this beamsplitter had a lower reflectivity of 88%. The output was significantly more stable than that of the Fabry-Perot configuration, and in particular, the PZT stabilisation system was able to maintain mode locking when the average power fluctuations in the master cavity reached ~20% peak-to-peak (caused by untypically large amplitude fluctuations of the pump laser combined with beam movement). This should be compared to the Fabry-Perot configuration, where fluctuations of around 10% could not be tolerated by the stabilisation electronics, such that sporadic drop-outs of the mode locking occurred. For both configurations, increasing the average power in the fibre beyond ~35 mW resulted in unstable operation. Typically, one or more sharp spikes would appear superimposed within the broad spectrum of the short pulse, implying the presence of a pedestal or cw component. Double pulsing was observed at somewhat higher power levels, followed by triple and higher-order pulsing.

The comparison of the two cavity arrangements was extended to shorter pulses by using an alternative, nonsolitonic fibre. Pulse durations of less than 100 fs have been obtained at modest powers by using small-core, erbium-doped fibre in the control cavity [12]. A 19 cm length of this particular fibre, which has a germania-doped-silica core of ~ 4.6 μm diameter, a Δn of 0.020, and an erbium ion doping level of 6×10^{18} cm^{-3}, was incorporated into the control cavity.

Mode locking was obtained in both arrangements for average power levels in excess of 15 mW in the fibre, with the shortest pulses recorded for an estimated intrafibre power range of 20–30 mW, with unstable operation at higher powers. Neither arrangement required a birefringent filter for stable operation. In the Fabry-Perot arrangement, pulse durations as short as 75 fs were recorded (see fig. 2) with a mirror M_0 of 88% reflectivity, with similar durations obtained for the 78% reflectivity mirror. As shown by the data in fig. 3, the pulses returning from the control cavity were strongly frequency chirped and considerably longer, the autocorrelation having a full width half maximum of 370 fs.

Pulse durations as short as 90 fs were obtained using the Michelson configuration with a beamsplitter reflectivity of 93% (see fig. 4). Although these pulses were somewhat longer than those observed when using the Fabry-Perot cavity, the laser performance was noticeably more stable. In decreasing the beamsplitter reflectivity to 88%, the pulse durations increased to ~ 110 fs, and the associated relatively large bandwidth-duration products of 0.65, together with the interferometric autocorrelation data confirmed the existence of substantial frequency chirp.

The excellent performance of the laser with the erbium-doped fibre in the control cavity leads us to believe that it has low dispersion in the 1.5 μm region. Although coupled-cavity mode locking works for either sign of fibre GVD, the magnitude of the GVD can influence the steady-state pulse duration, particularly with near-infrared colour-centre lasers which

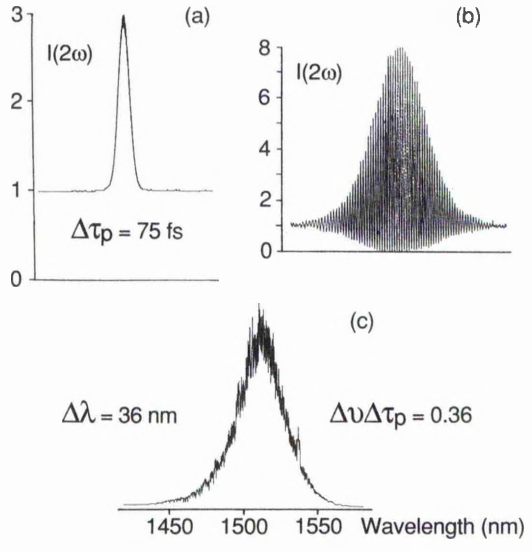

Fig. 2. Intensity (a) and interferometric (b) autocorrelations and spectrum (c) for the main output of the Fabry-Perot arrangement.

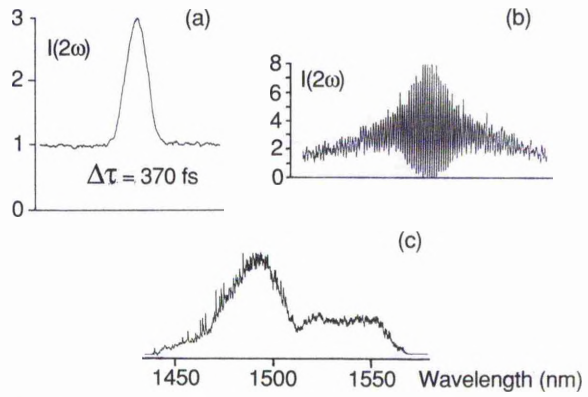

Fig. 3. Intensity (a) and interferometric (b) autocorrelations and spectrum (c) for the subsidiary output of the Fabry-Perot arrangement.

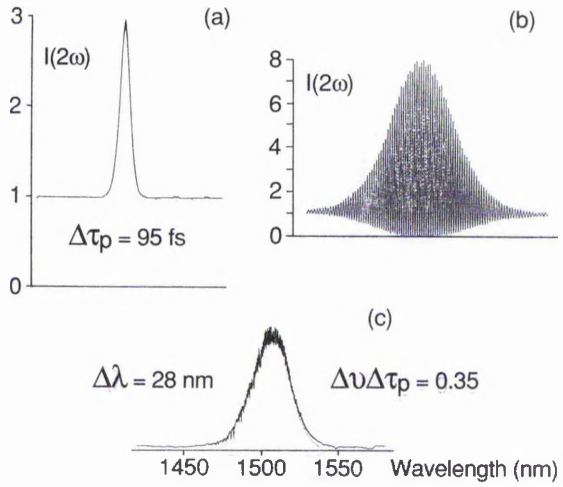

Fig. 4. Intensity (a) and interferometric (b) autocorrelations and spectrum (c) for the output of the Michelson cavity.

have broad gain bandwidths and where the master cavity GVD is small. In the initial stages of mode locking, when the pulse is tens of hundreds of picoseconds in duration, there will be insignificant temporal distortion of the pulse in the fibre due to dispersion. However, as the pulse becomes shorter, dispersion will have an increasingly important effect. With normally dispersive fibre, the pulse will broaden temporally and tend to flatten. The chirp over the central portion of the pulse, the part which interferes with the master cavity pulse, will decrease and reduce the pulse shortening velocity. For anomalously dispersive fibre, the temporally compressed pulses cannot interfere effectively with the leading and trailing edges of the master cavity pulse. As discussed earlier, the chirp of the feedback pulse will, in any case, be reduced as the $N=2$ soliton condition is approached. Therefore to produce the shortest pulses, low dispersion is required as in any other mode-locked laser.

To measure the GVD of the erbium-doped fibre, we monitored the changes in length of the control cavity necessary to maintain mode locking while the laser was tuned across a range of wavelengths. The length versus wavelength tuning characteristic shown in fig. 5 was obtained with a fibre length of 4.13 m, where an average power of around 60 mW were required in order to bleach the erbium absorption. The technique has not resolved dispersive features associated with the erbium transition (e.g. see ref. [13], fig. 3), presumably because of bleaching. The results were fitted using a quadratic expression (i.e. assuming constant third-order dispersion), and D was deduced to be ~ -1.3 ps/(nm km) at 1500 nm, with zero GVD at approximately 1520 nm, thus confirming our expectation of low dispersion at the operating wavelength.

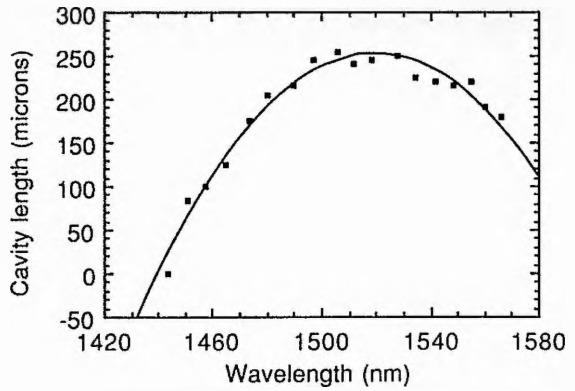

Fig. 5. Variation of control cavity length with wavelength for 4.13 m of the erbium-doped fibre.

The compactness of the Michelson cavity, compared to the Fabry-Perot arrangement, makes it less vulnerable to vibrations and this is partly responsible for its better stability. We can suggest here the reason for its tolerance to pump power fluctuations. The automatic length stabilisation employed with these lasers relies upon the interferometric modulation in the average power of the monitored beam as the length of one cavity (or branch) changes relative to the other [2]. If the pump power fluctuates, the power levels within the coupled-cavity laser also fluctuate, inducing the stabilisation electronics to make an unnecessary adjustment in the length (or phase) mismatch to bring the power at the photodiode back to a preset reference level. Excessive power fluctuations can cause the mismatch to exceed the range associated with stable mode locking, resulting in an abrupt cessation of the short pulse operation. If the depth of modulation in power of the output beam can be increased, then the stabilisation electronics will become less sensitive to these perturbations. We contend that the Michelson configuration can give rise to an intrinsically greater modulation in its output beam power than the equivalent Fabry-Perot counterpart.

For the Fabry-Perot arrangement, the waves within the master cavity are related by the equation

$$A'_g = A_g\{r + (1-r^2)(1-b^2)\theta \times [\exp(i\phi) - (1-b^2)\theta r \exp(i2\phi) + \ldots]\}, \quad (1)$$

where A_g denotes the amplitude of the wave incident on the common mirror having an (amplitude) reflectivity r, and A'_g is the wave travelling in the opposite direction, as shown in fig. 1. Here, b is the reflectivity of the beam splitter, θ is the double-pass transmission of the nonlinear medium, and ϕ denotes the phase-mismatch angle of the feedback signal. The amplitude of the main output beam A_{out} is related to the wave in the master cavity by

$$A_{out} = A_g b(1-r^2)^{1/2}[1 - (1-b^2)\theta r \exp(i\phi) + (1-b^2)^2\theta^2 r^2 \exp(i2\phi) - \ldots]. \quad (2)$$

Terms of the order of $\exp(i2\phi)$ and higher account for optical ringing within the control cavity. The equivalent expressions for the Michelson cavity are

$$A'_g = A_g[r^2 + \theta(1-r^2)\exp(i\phi)], \quad (3)$$

$$A_{out} = A_g r(1-r^2)^{1/2}[1-\theta\exp(i\phi)], \quad (4)$$

where A_g is the wave travelling from the gain towards the Michelson interferometer, A'_g is the return wave, and r is the interferometer beamsplitter reflectivity. In this case, the expressions are much simpler because there is no ringing. For both arrangements, θ was ~ 0.7. By comparing eqs. (1) and (3), it can be seen that the Fabry-Perot scheme with a mirror M_0 of 12% transmission has a similar ratio of feedback level to the master cavity level (about 1:18 in terms of amplitudes) as the Michelson with a beamsplitter transmission of 7%. There is, however, a difference in the modulation of the output beams, given by eqs. (2) and (4). We believe it to be significant that with the Fabry-Perot configuration the two largest terms have a ratio of 1:0.41, whereas with the Michelson counterpart the amplitudes of the two interfering beams are more similar, with a ratio of 1:0.70, giving increased modulation and reducing the influence of fluctuations in pump-power on the stabilisation system. (When the ringing terms for the Fabry-Perot configuration are included, the shape of the modulation is modified slightly, but the overall depth of modulation is not significantly different.)

3. Self-starting operation

Self-starting mode locking has already been achieved in colour-centre lasers by using a semiconductor optical amplifier in the control cavity [14], but the nonlinear absorption in these devices makes it unlikely that sub-100 fs pulses will be produced, and thus self-starting using an optical fibre is of considerable interest. Self-starting was not seen in any of the configurations discussed above, and even the incorporation of a 10 m length of fibre, to increase the effective nonlinearity, was insufficient to induce mode locking. An alternative approach was pursued by locating the gain medium at the centre of the master cavity to enhance the initial mode beating.

The Fabry-Perot arrangement was used with the master cavity length remaining at 1.82 m and the mirror M_0 transmission at 22%. With cw excitation, there was a significant enhancement in the second harmonic autocorrelation signal when the gain medium was within a few mm of the cavity centre. Examination of the output on a fast photodiode showed the dominant modulation was at twice the fundamental cavity frequency. Once feedback from the control cavity was established, the mode-beating frequency changed to the fundamental cavity frequency (82 MHz). Mode locking was obtained with a 2.65 m length of dispersion-shifted fibre (Corning, $\lambda_0 \sim 1550$ nm), and a single 4 mm thick quartz plate for bandwidth limitation. The reliability of the self-starting was increased by reducing the beamsplitter reflectivity to 22%. Pulses of ~ 0.7 ps duration were recorded (see fig. 6) with 50–60 mW power in the fibre, but the associated spectra contained narrow features implying the presence of a pedestal or a cw background. Regular switching between these features (which typically made up $\sim 20\%$ of the output power) was related to the noise on the autocorrelation trace. The general behaviour was indicative of excessive peak powers in the fibre, where the peak phase shifts exceeded an estimated 2π radians. Normally, either the power level or the fibre length could be reduced to achieve stable operation, but this would have prevented self-starting of the mode locking. This instability would probably be alleviated by restricting the steady-state pulse duration by adding further bandwidth limitation, but unfortunately no suitable cavity elements were available for this purpose. Our results differ significantly from those published recently for a self-starting coupled-cavity NaCl:OH^- laser, where a symmetrical cavity has not been employed [15]. We believe that the latter data may have been achieved by the effective suppression of para-

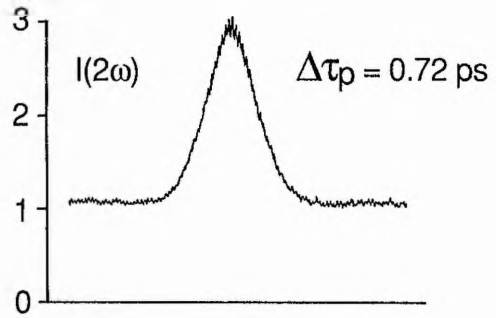

Fig. 6. Intensity autocorrelation for self-starting operation.

sitic feedback from the fibre ends, and we intend to investigate this interpretation.

4. Conclusions

Similar pulse durations in the sub-100 fs range were obtained from a mode-locked KCl:Tl laser in both Fabry-Perot and Michelson coupled-cavity configurations, but the latter scheme had the advantage of better stability and a higher tolerance to fluctuations in pump power. In addition, we have described a self-starting operation of a coupled-cavity KCl:Tl laser where a symmetrical master cavity was exploited to enhance the strength of the mode beating.

Acknowledgements

We are grateful to L.F. Mollenauer of AT&T Bell Laboratories for supplying the sample of solitonic fibre, and to K.C. Byron and R.A. Baker, both of BNR (Europe), for providing the erbium-doped fibre and the dispersion-shifted fibre. This work was supported by the UK Science and Engineering Research Council.

References

[1] L.F. Mollenauer and R.H. Stolen, Optics Lett. 9 (1984) 13.
[2] F.M. Mitschke and L.F. Mollenauer, IEEE J. Quantum Electron. QE-22 (1986) 2242.
[3] K.J. Blow and D. Wood, J. Opt. Soc. Am. B 5 (1988) 629.
[4] K.J. Blow and B.P. Nelson, Optics Lett. 13 (1988) 1026.
[5] P.N. Kean, X. Zhu, D.W. Crust, R.S. Grant, N. Langford and W. Sibbett, Optics Lett. 14 (1989) 39.
[6] J. Mark, L.Y. Liu, K.L. Hall, H.A. Haus and E.P. Ippen, Optics Lett. 14 (1989) 48.
[7] E.P. Ippen, H.A. Haus and L.Y. Liu, J. Opt. Soc. Am. B 6 (1979) 1736.
[8] F. Oullette and M. Piche, Optics Comm. 60 (1986) 99.
[9] F. Oullette and M. Piche, Can. J. Phys. 66 (1988) 903.
[10] M. Morin and M. Piche, Optics Lett. 14 (1989) 1119.
[11] R.S. Grant, P.N. Kean and W. Sibbett, paper 147, 9th National Quantum Electronics Conference, Oxford, UK, 1989.
[12] X. Zhu, P.N. Kean and W. Sibbett, Optics Lett. 14 (1989) 1192.
[13] E. Desurvire, IEEE J. Ligthwave Technol. 8 (1990) 1517.
[14] R.S. Grant, P.N. Kean, D. Burns and W. Sibbett, Optics Lett. 16 (1991) 384.
[15] G. Sucha, Optics Lett. 16 (1991) 922.

Observations of ultrafast nonlinear refraction in an InGaAsP optical amplifier

R. S. Grant and W. Sibbett
J. F. Allen Physics Research Laboratories, University of St. Andrews, St. Andrews, Scotland KY 16 9SS, United Kingdom

(Received 15 October 1990; accepted for publication 15 January 1991)

Spectral broadening due to self-phase modulation has been observed for ultrashort pulses propagating through an InGaAsP optical amplifier. This is not associated with gain saturation or absorption saturation, since it can be observed at the transparency current. At transparency, the broadening and structure of the spectra are symmetrical for pulses of approximately 27 ps duration, implying that the underlying nonlinearity has a relatively fast recovery time. The associated nonlinear index coefficient n_2 is estimated to be approximately -2×10^{-11} cm^2 W^{-1}.

Spectral broadening of optical pulses experiencing gain saturation in semiconductor optical amplifiers has been attributed to self-phase modulation (SPM) resulting from the strong dependence of the active region refractive index on the charge carrier density.[1,2] The reduction in carrier density, associated with the dynamic saturation of the gain, increases the refractive index. Since the recovery time of the carrier density is generally limited to hundreds of picoseconds,[3] the refractive index does not recover significantly during the passage of an optical pulse of a few tens of picoseconds duration. This gives rise to asymmetric spectral broadening towards longer wavelengths. By contrast, absorption saturation is accompanied by broadening towards shorter wavelengths, since carrier generation corresponds to a decrease in refractive index.[4]

We present evidence of SPM in a semiconductor optical amplifier which cannot be related to gain saturation or absorption saturation, because of its observation at the transparency current. In particular, at transparency, the spectral broadening is approximately symmetrical for pulses as short as 20 ps duration, implying an ultrafast recovery time.

The pulse source for these experiments was a synchronously mode-locked KCl:Tl^0(1) color-center laser, which was configured to give stable, transform-limited pulses of around 27 ps duration. The pulses were monitored with an autocorrelator and in addition, for part of this work, a streak camera was used. A Faraday optical isolator between the color-center laser and the amplifier prevented any optical feedback from degrading the mode locking. After passing the isolator, the polarization of the beam was reoriented by a $\lambda/2$ plate to match the TE mode of the amplifier. A 3× beam expander, followed by a 20× microscope objective, was used to couple the beam into the amplifier with an efficiency of up to 15%, but more typically ~12%. The output of the amplifier was focused through a 1-mm-diam aperture positioned ~3 m away. This aperture acted as a filter to select the guided mode only. The spectra of the pulses transmitted by the amplifier were monitored with a scanning Fabry–Perot interferometer.

The 350-μm-long InGaAsP optical amplifier was a double-channel planar-buried heterostructure (DCPBH), with antireflection coatings on both facets (with the modal reflectivity estimated to be ~0.2%). The active region had a cross-sectional area of 1.5×0.17 μm^2, with a confinement factor of 0.39 deduced by using the approximation of Botez.[5] All measurements were performed at 1500 nm where the small-signal resonant chip gain of the device was 20 dB for a drive current of 40 mA, and the transparency current was ~6 mA. This was determined by coupling a cw signal into the active region, and adjusting the drive current to minimize the photoinduced voltage (or optoelectronic signal). Spectrally, the transparent region used in these experiments lies at wavelengths shorter than the peak of the gain.

For pulse energies up to several pJ, spectral broadening of the pulses due to SPM arising from gain saturation, and to a lesser extent absorption saturation, could be identified for currents above and below transparency, respectively. However, for energies exceeding 10 pJ, additional broadening was apparent that did not conform to that predicted by simple theory.[2] Furthermore, spectral broadening occurred at the transparency current which indicates that the effect is not related to absorption saturation or gain saturation. The symmetrical, oscillatory structure of the broadening at transparency was recognizable as self-phase modulation due to a nonlinear refractive index change with a recovery time much faster than the incident pulse duration.[6]

In Fig. 1 a sequence of spectra is shown for 27 ps pulses which had propagated through the amplifier (labeled by the estimated pulse energies coupled into the device). For these pulse durations, temporal broadening due to group-velocity dispersion (GVD) within the amplifier was expected to be negligible. The pulse energy and maximum phase shift, which can be deduced by examining the structure of the spectra, allow an estimate to be made of the magnitude of the nonlinear index coefficient n_2 associated with this particular broadening mechanism.[7] An intensity-dependent refractive index induces a phase shift Φ_{nl} which is related to the instantaneous intensity $I(t)$, the guide length L, and to the free space wavelength λ by

$$\Phi_{nl}(t)=(2\pi L/\lambda)n_2 I(t). \quad (1)$$

Thus the pulse experiences a maximum phase shift

 0003-6951/91/111119-03$02.00

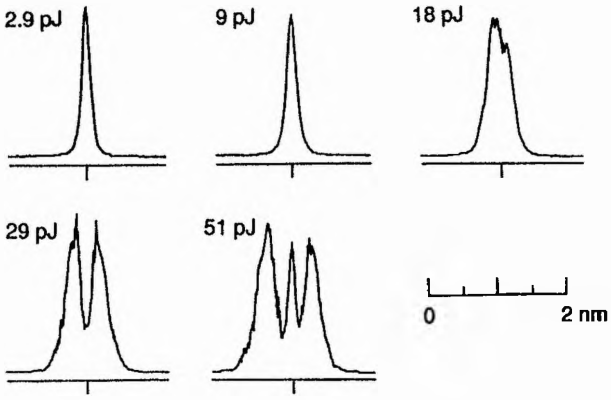

FIG. 1. Spectra of 27 ps duration pulses transmitted by the amplifier.

$\Phi_{nl} = \Phi_{max}$ at its most intense point. The pulse peak intensity is given by $I_{max} = P_0/A_{eff}$, where A_{eff} is the effective area of the guided mode given by (height×width)/Γ where Γ is the modal confinement factor. For an assumed Gaussian pulse shape, the peak power P_0 is related to the pulse energy E by the expression $P_0 = E/1.065T_p$ where T_p is the full width at half maximum (FWHM) of the pulse. Substituting Φ_{max} and expressions for I_{max} into (1), subsequent rearrangement gives

$$n_2 = (\lambda A_{eff} T_p/5.9L)(\Phi_{max}/E). \quad (2)$$

Using the values of $E = 29$ pJ at $\Phi_{max} = 3\pi/2$, or $E = 51$ pJ at $\Phi_{max} = 5\pi/2$, the magnitude of n_2 has been deduced to be $(2.0 \pm 0.6) \times 10^{-11}$ cm^2 W^{-1}.

To determine the sign of the n_2, the experimental arrangement as used above was modified slightly. The synchronously mode-locked pulses were propagated in a 260 m length of monomode optical fiber [having a normal GVD of $D \sim -4$ ps/(nm km)] before being coupled into the optical amplifier, which was again set to transparency. The fiber GVD was sufficiently low that negligible temporal broadening occurred in the fiber, even in the presence of significant SPM. A fiber polarization controller was used to maximize the polarization of the beam in the TE orientation and variable attenuators were placed before the fiber and before the amplifier. With the pulse energy in the fiber set to ~260 pJ and with the attenuator before the amplifier set at minimum transmission (pulse energy in the amplifier was estimated to be less than 2 pJ), spectral broadening due to SPM in the optical fiber was observed, with a maximum phase shift of $\sim 5\pi/2$ [Fig. 2(a)]. With the pulse energy in the fiber maintained at ~260 pJ, the attenuator

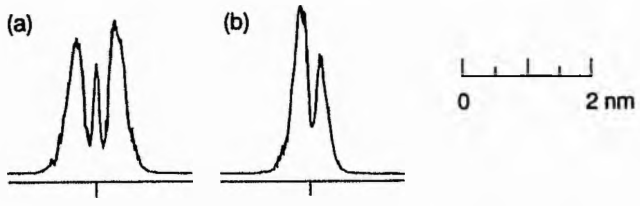

FIG. 2. Spectral narrowing by the amplifier of 27 ps duration pulses prechirped by passage through an optical fiber.

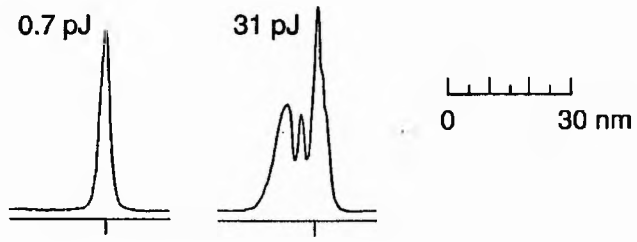

FIG. 3. Spectra of 1 ps duration pulses transmitted by the amplifier.

before the amplifier was adjusted to increase the pulse energy in the amplifier to ~25 pJ, so that the amplifier now behaved nonlinearly. The addition of chirping from the amplifier resulted in spectral narrowing and the maximum phase shift was reduced to approximately $3\pi/2$ [Fig. 2(b)]. This spectral narrowing and dechirping can be explained if the sign of the n_2 of the amplifier is negative, given that the sign of the n_2 of the fiber is positive.

As discussed previously, when the incident pulse durations are comparable to the recovery time of the nonlinear refraction, the spectral broadening will become asymmetric. Pulses of 1 ps duration, generated by coupled-cavity mode locking,[8] were used to test this effect. Again, the amplifier drive current was set to the small-signal transparency level of 6 mA. The results, shown in Fig. 3, indicate that the spectrum is asymmetrically broadened to higher frequencies, which suggests that the recovery time is of the order of 1 ps or greater, and confirms that the sign of the n_2 is negative, i.e., a self-defocusing nonlinearity.

In the calculation of n_2 it was assumed that the guide was lossless. As a check, the transmission characteristic of the amplifier at the transparency current were measured using mode-locked pulses from the KCl:Tl^0(1) laser, with input pulse energies in excess of 2 pJ (see Fig. 4). In addition to the 27 ps pulses generated by synchronous mode locking, pulses of 1 ps and 200 fs durations were obtained by using coupled-cavity mode locking. The maximum loss measured for the transmission of 27 ps duration pulses was approximately 0.8 dB for a pulse energy of around 60 pJ.

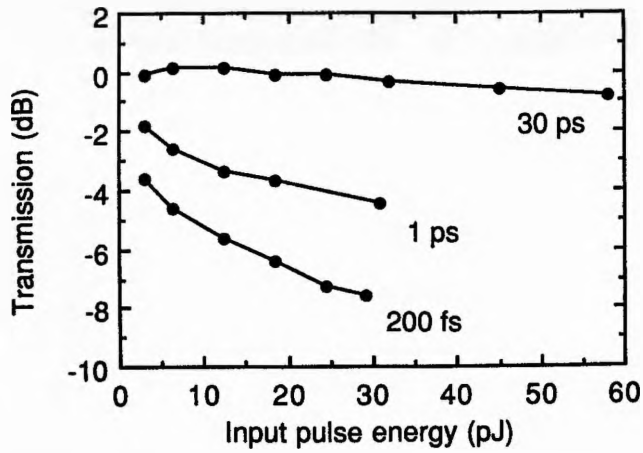

FIG. 4. Transmission characteristics of the amplifier for pulses of approximately 30 ps, 1 ps, and 200 fs duration.

The effect of this small loss on the above calculation of n_2 is essentially negligible in comparison to other errors, e.g., the pulse energy coupled into the guide. Clearly, the attenuation experienced by both the 1 ps and 200 fs duration pulses is considerable. The attenuation of the 30 ps, 1 ps, and 200 fs duration pulses is consistent with absorption mechanisms such as dynamic carrier heating (DCH)[9] or two photon absorption (TPA). At transparency, hot carriers can be caused by free-carrier absorption and TPA.

The asymmetric spectral broadening of the 1 ps pulses in Fig. 3 implies a finite recovery time. We discount an intrinsic field-induced nonlinearity which would be expected to have an instantaneous recovery. Instead, the nonlinearity may be related to the intensity-dependent absorption due to DCH, which has a recovery time of $\sim$0.7 ps in InGaAsP devices[10] or alternatively to the associated transient increase in carrier density that such an absorption would cause. Because the incident light is close to resonance with the band gap, any increase in carrier density will have a recovery time limited by the intraband relaxation processes of thermalization and carrier cooling, since recombination itself will occur largely through stimulated emission. Additionally, carrier pairs can be generated directly by TPA. Using the scaling law of Van Stryland *et al.*[11] and assuming similar parameters to GaAs, the TPA coefficient β for the active region can be estimated to be approximately 60–80 cm/GW. Thus, in addition to dynamic carrier heating, two-photon absorption is a significant loss mechanism in long wavelength amplifiers.

In summary, we have presented experimental evidence of an ultrafast refractive nonlinearity in InGaAsP optical amplifiers. The value of the nonlinear index coefficient n_2 has been deduced to be approximately -2×10^{-11} $cm^2\,W^{-1}$ from measurements of the spectral broadening of mode-locked pulses. It is our contention that the recovery time of the nonlinearity is related to intraband relaxation for which a recovery time of the order of 1 ps can be inferred.

We thank I. H. White of the University of Cambridge for useful discussions. We are also grateful to R. A. Baker and G. D. Henshall of STC Technology Ltd. for the length of optical fiber and for providing details of the amplifier. This work was supported by the U.K. Science and Engineering Research Council.

[1] N. A. Olsson and G. P. Agrawal, Appl. Phys. Lett. **55**, 13 (1989).
[2] G. P. Agrawal and N. A. Olsson, IEEE J. Quantum Electron. **25**, 2297 (1989).
[3] G. Eisenstein, R. S. Tucker, J. M. Wiesenfeld, P. B. Hansen, G. Raybon, B. C. Johnson, T. J. Bridges, F. G. Storz, and C. A. Burrus, Appl. Phys. Lett. **54**, 454 (1989).
[4] N. Finlayson, E. M. Wright, and G. I. Stegeman, IEEE J. Quantum Electron. **26**, 770 (1990).
[5] D. Botez, IEEE J. Quantum Electron. **QE-17**, 178 (1981).
[6] G. P. Agrawal, *Nonlinear Fiber Optics* (Academic, Boston, 1989), Chap. 4.
[7] R. H. Stolen and C. Lin, Phys. Rev. A **17**, 1448 (1978).
[8] P. N. Kean, X. Zhu, D. W. Crust, R. S. Grant, N. Langford, and W. Sibbett, Opt. Lett. **14**, 39 (1989).
[9] M. S. Stix, M. P. Kesler, and E. P. Ippen, Appl. Phys. Lett. **48**, 1722 (1986).
[10] K. L. Hall, J. Mark, E. P. Ippen, and G. Eisenstein, Appl. Phys. Lett. **56**, 1740 (1990).
[11] E. W. Van Stryland, M. A. Woodall, H. Vanherzeele, and M. J. Soileau, Opt. Lett. **10**, 490 (1985).

CROSS-PHASE MODULATION IN SEMICONDUCTOR OPTICAL AMPLIFIER

Indexing terms: Amplifiers, Crosstalk, Nonlinear optics, Semiconductor lasers

Cross-phase modulation in a semiconductor optical amplifier has been demonstrated by using copropagating pump and probe pulse trains of different wavelengths. The relative time delay between the pump and probe pulses was varied and the effect on the spectral distortion is described.

Semiconductor optical amplifiers provide an efficient and straightforward method of signal amplification in optical fibre telecommunications systems. Travelling-wave amplifiers have been fabricated with gain bandwidths of the order of 50 nm, suitable for wavelength-division-multiplexed (WDM) links, or for amplifying pulses of a few picoseconds duration. In addition, effects related to the strong dependence of the active region carrier density and the refractive index have been studied. These include nearly degenerate four-wave mixing (NDFWM)[1] and self-phase modulation (SPM).[2]

For pulse durations much greater than the spectral hole burning recovery time (approximately 0·1 ps), the gain of a semiconductor amplifier is effectively homogeneously broadened, and therefore the gain at one wavelength will be affected by the presence of a signal at a second wavelength.[3–5] The reduction in gain induced by an energetic pulse could conceivably be used to shape a pulse at a different wavelength, provided that the two pulses have some temporal overlap. Furthermore, coupling between the pulses will occur through the refractive index changes that accompany gain saturation, resulting in frequency chirping. This interaction corresponds to the phenomenon of cross-phase modulation (XPM) that has been extensively studied in optical fibres[6] and also observed in a semiconductor optical amplifier near 1·3 μm.[7] We report the observation of spectral broadening and distortion due to XPM in a semiconductor optical amplifier.

To observe XPM we injected energetic pump pulses together with probe pulses into the amplifier (in the same direction). The probe pulses were sufficiently weak that there was no significant saturation of the amplifier gain and neglible spectral broadening from SPM. On the other hand, the pump pulses saturated the gain and sustained considerable SPM. The refractive index changes induced by the pump pulses were experienced by the probe pulses and frequency chirp and spectral broadening were thereby induced solely through XPM.

Independently-tunable pulse trains were generated by synchronously mode-locked KCl : Tl^0(1) and NaCl : OH^- colour-centre lasers (see Fig. 1). Pulse synchronism between the two colour-centre lasers was assured by using a single CW mode-locked Nd : YAG laser to excite both lasers, and an adjustable optical delay in the KCl : Tl^0(1) laser beam enabled the relative timing between the two pulse trains to be altered. Optical isolators were required to prevent the amplifier using the output couplers of the colour centre lasers to reach the threshold for laser oscillation, and also to avoid the degradation of mode locking by parasitic optical feedback. The two pulse trains were combined at a beamsplitter, and subsequently polarised to match the amplifier *TE* mode. Bulk optics were used to couple the pulses into and out of the 1·5 μm InGaAsP buried heterostructure amplifier. The pump and probe pulses transmitted by the amplifier were spatially filtered to remove the light not coupled into the waveguide, and then separated from each other by a monochromator which acted as a bandpass filter (bandwidth $\simeq$5 nm). The spectra of the pulses were monitored with a scanning Fabry–Perot interferometer.

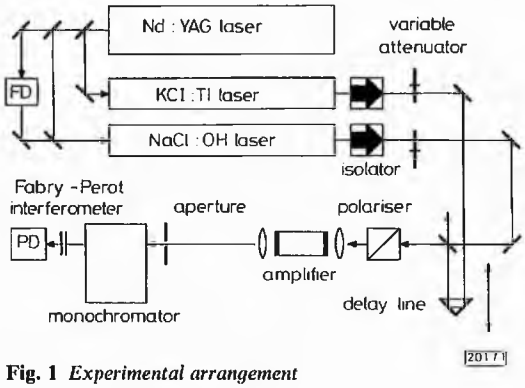

Fig. 1 *Experimental arrangement*
FD = frequency doubler
PD = photodiode

The mode-locked KCl : Tl^0(1) laser, which was operated at a wavelength of 1526 nm, generated probe pulses of approximately 40 ps duration (measured using second harmonic generation autocorrelation with a Gaussian pulseshape assumed), while the mode-locked NaCl : OH^- laser, tuned to 1506 nm, was used to provide the pump pulses. To simplify the analysis of the results, the NaCl : OH^- pulse duration, normally 5 ps, was increased to $\sim$40 ps by bandwidth limitation and slight cavity length detuning. The small-signal resonant gain of the amplifier at the probe pulse wavelength was approximately 16 dB at a drive current of 40 mA, with a gain ripple of $\sim$1·3 dB, hence travelling-wave characteristics were assumed. The saturation energy E_{sat} was estimated to be approximately 6 pJ at the probe wavelength.

The pump pulse energy was set to approximately 10 pJ at the input facet. This was large enough to strongly saturate the gain, and consequently only the leading portion of the pulse was amplified and spectrally broadened to longer wavelengths by SPM. The trailing portion of the pump pulse was transmitted unamplified and unchirped. A typical spectrum of the pump pulses transmitted by the amplifier is reproduced in Fig. 2 together with an undistorted spectrum recorded in the small-signal regime.

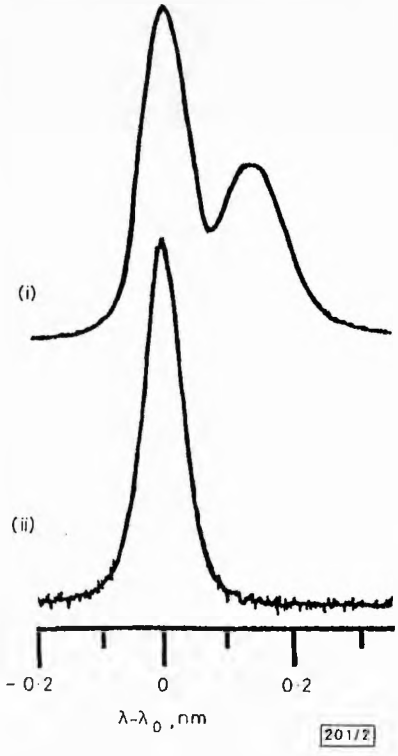

Fig. 2 *Normalised pump pulse spectra*
Pulses labelled by energy at input facet
(i) $E \simeq 10$ pJ
(ii) $E \simeq 20$ fJ

The spectra of the probe pulses (input energy $\sim$80 fJ) transmitted by the amplifier are shown in Fig. 3. The spectra in Figs. 3(i) to 3(v), distorted by XPM, are labelled by the time delay relative to the pump pulse, i.e. in Fig. 3(i) the probe pulse precedes the pump pulse. The point of zero delay was chosen somewhat arbitrarily as the position where the maximum spectral distortion was recorded and does not necessarily imply complete overlap of pump and probe pulses. As

discussed above, the probe pulse will only be noticeably chirped where it overlaps with the pump pulse, and thus for the conditions of Figs. 3(i) and 3(v) the frequency chirp on the probe pulse will be confined to the trailing and leading edges, respectively.

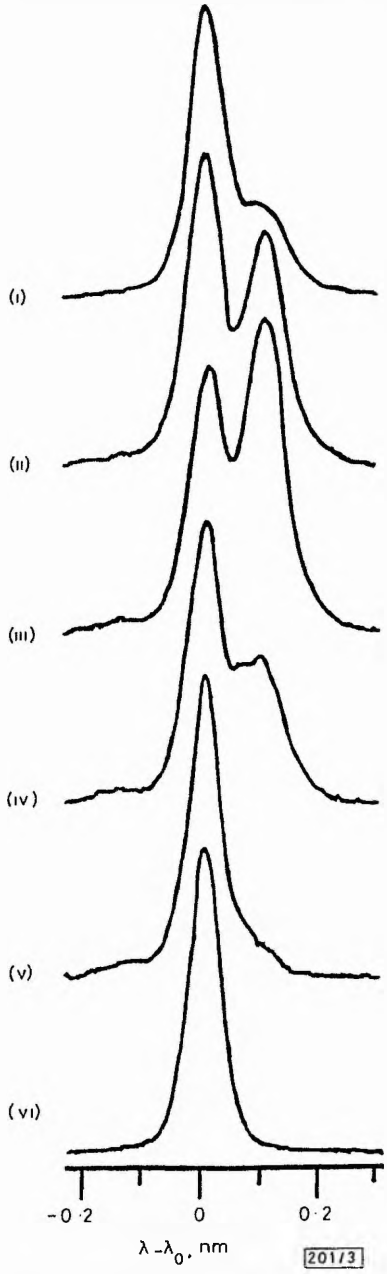

Fig. 3 *Normalised probe pulse spectra*
$\Delta\tau$ = delay relative to pump pulse
(i) $\Delta\tau = -66{\cdot}7$ ps
(ii) $\Delta\tau = -33{\cdot}3$ ps
(iii) $\Delta\tau = 0$ ps
(iv) $\Delta\tau = 33{\cdot}3$ ps
(v) $\Delta\tau = 66{\cdot}7$ ps
(vi) Pump pulse blocked

The spectra are broadened asymmetrically to longer wavelengths when compared to the spectrum taken when the pump pulse train was blocked (Fig. 3(vi)). This asymmetry is not the result of any group-velocity mismatch and subsequent walkoff, which affects XPM in fibres.[6] For the case described here, the pulses are much longer than the length of the nonlinear medium and walkoff is negligible. Instead, the spectral asymmetry is attributed to the long recovery time of the refractive index change compared to the pulse durations, as discussed in the context of SPM in amplifiers.[2]

In summary we have presented what we believe to be the first observations of XPM at $1{\cdot}5\,\mu$m in a semiconductor optical amplifier and the temporal detuning characteristics have been briefly described. We estimate that a much lower pump pulse energy of ~ 1 pJ should be sufficient to observe XPM and furthermore, for an amplifier with a higher small signal gain than that used here, the spectral distortion would be more dramatic and would appear at even lower pump pulse energies. Finally, XPM may be a source of crosstalk in pulsed or intensity-modulated WDM systems.

Acknowledgments: The authors thank C. I. Johnston for the preparation and coloration of the NaCl : OH^- crystal. G. T. Kennedy gratefully acknowledges the support of a CASE studentship with STC Technology Ltd. This work was supported by the Science and Engineering Research Council.

R. S. GRANT
G. T. KENNEDY
W. SIBBETT

J. F. Allen Physics Research Laboratories
University of St. Andrews
St. Andrews, Scotland KY16 9SS, United Kingdom

15th February 1991

References

1 INOUE, K., MUKAI, T., and SAITOH, T.: 'Nearly degenerate four-wave mixing in a traveling-wave semiconductor laser amplifier', *Appl. Phys. Lett.*, 1987, **51**, pp. 1051–1053
2 AGRAWAL, G. P., and OLSSON, N. A.: 'Self-phase modulation and spectral broadening of optical pulses in semiconductor laser amplifiers', *IEEE J. Quantum Electron.*, 1989, **QE-25**, pp. 2297–2306
3 JOPSON, R. M., HALL, K. L., EISENSTEIN, G., RAYBON, G., and WHALEN, M. S.: 'Observation of two-colour gain saturation in an optical amplifier', *Electron. Lett.*, 1987, **23**, pp. 510–512
4 MUKAI, T., INOUE, K., and SAITOH, T.: 'Homogeneous gain saturation in $1{\cdot}5\,\mu$m InGaAsP traveling-wave semiconductor laser amplifiers', *Appl. Phys. Lett.*, 1987, **51**, pp. 381–383
5 KESLER, M. P., and IPPEN, E. P.: 'Subpicosecond spectral gain dynamics in AlGaAs laser diodes', *Electron. Lett.*, 1988, **24**, pp. 1102–1104
6 AGRAWAL, G. P.: 'Nonlinear fiber optics' (Academic Press, Boston, 1989), Chap. 7
7 DIJAILI, S. P., WIESENFELD, J. M., RAYBON, G., BURRUS, C. A., SMITH, J. S., DIENES, A., and WHINNERY, J. R.: 'Observation of cross phase modulation in a semiconductor laser amplifier near $1{\cdot}3\,\mu$m'. Proc. 1st Topical Meeting on Optical amplifiers and their applications, 6th–8th August 1990, Monterey, California

Passive coupled-cavity mode-locked color-center lasers

R. S. Grant, P. N. Kean, D. Burns, and W. Sibbett

J.F. Allen Physics Research Laboratories, University of St. Andrews, St. Andrews, Scotland, KY16 9SS, UK

Received September 5, 1990; accepted January 7, 1991

Stable, self-starting operation of a coupled-cavity mode-locked KCl:$Tl^0(1)$ color-center laser has been achieved by incorporating a semiconductor diode optical amplifier into the control cavity. By adjustment of the amplifier drive current, nonlinearity in the regimes of either saturable gain or saturable absorption has been exploited to generate subpicosecond pulses. Under conditions of saturable gain, pulse durations as short as 280 fs were obtained. Self-starting has also been demonstrated for a coupled-cavity mode-locked NaCl:OH^- color-center laser by using the same technique.

Nonlinear external control cavities have now been used to generate optical pulses of picosecond and subpicosecond durations from a number of different lasers.[1–10] This technique is termed coupled-cavity mode locking,[3] additive-pulse mode locking,[5] or interferential mode locking.[11] To initiate coupled-cavity mode locking in color-center lasers, additional modulation such as synchronous pumping is imposed to bring the peak intensities within the nonlinear medium above some threshold value for mode locking.[1–6] Gain modulation is largely superfluous once the control cavity takes effect, since it is observed that the pulse-repetition frequency is determined by the laser cavity length, not by the active modulation.[2] In contrast, active modulation is not required with CO_2,[7] Ti:Al_2O_3,[8] or Nd:YAG (Refs. 9 and 10) lasers, and mode locking self-starts under a wide range of operating conditions.

In this Letter we describe the operation of a self-starting, coupled-cavity mode-locked KCl:$Tl^0(1)$ color-center laser. We use the resonant nonlinearity of a semiconductor diode optical amplifier in the control cavity to achieve passive mode locking. The 280-fs-duration pulses generated are significantly shorter than the 22-ps pulses observed for conventional passive mode locking of this type of laser.[12] In addition, the technique has been successfully applied to a NaCl:OH^- color-center laser. We acknowledge that self-starting of a coupled-cavity NaCl:OH^- laser with an optical fiber in the control cavity was recently observed,[13] but a clear explanation for this has not yet been advanced. The use of a resonant nonlinearity for mode locking was recently reported for a coupled-cavity Ti:Al_2O_3 laser,[14] in which electronic stabilization of the cavity lengths was not required for mode locking to be maintained.

In our original demonstration of enhanced mode locking using a semiconductor amplifier,[3] optical feedback from the amplifier facets prevented an optimal alignment of the control cavity. Consequently the coupled-cavity mode-locking process was not sufficiently strong to dominate the gain modulation introduced by the mode-locked Nd:YAG pump laser. Resynchronization of the color-center laser pulses with the pump laser pulses then occurred at regular intervals, which corresponded to the dropouts observed.

To prevent optical feedback from the amplifier facets, while permitting the pulses transmitted by the semiconductor amplifier to return to the main laser cavity (or master cavity), the arrangement shown in Fig. 1 was used. The average output power from the master cavity (repetition frequency ~82 MHz), measured after mirror M_0 was ~60 mW for a mirror M_0 transmission of 7% and ~80 mW for M_0 transmissions of either 12% or 22%. Beam splitter S_1, having a reflectivity of 30%, served as the output coupler of the coupled-cavity laser and also directed part of the feedback beam returning to the master cavity onto a large-area Ge photodiode (PD) to provide a monitor signal for the stabilization electronics. To ensure a high level of isolation between the master cavity and the amplifier facets, the amplifier was positioned between two Faraday isolators, this resulted in unidirectional transmission through the amplifier. The isolator on the input side was followed by a half-wave plate ($\lambda/2$) to maximize the light coupled into the TE mode of the amplifier. With a 20× microscope objective (OBJ), typical coupling efficiencies into the amplifier (AMP) were ~10%, and a collimating lens (CL) having a numerical aperture of 0.5 collected approximately 60% of the amplifier output. A telescope (lenses L_1 and L_2) was included to compress the beam diameter by approximately a factor of 3 to permit transmission by the second isolator, which was oriented to accept the TE

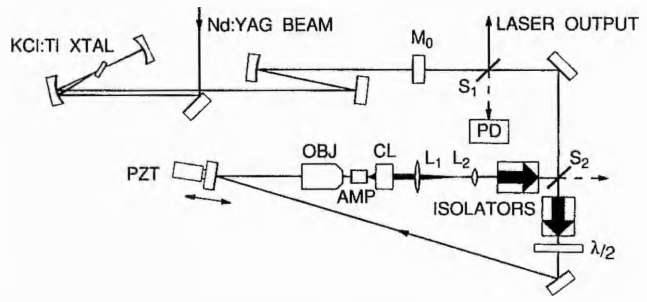

Fig. 1. Schematic of the coupled-cavity mode-locked KCl:$Tl^0(1)$ laser. XTAL, crystal.

0146-9592/91/060384-03$5.00/0

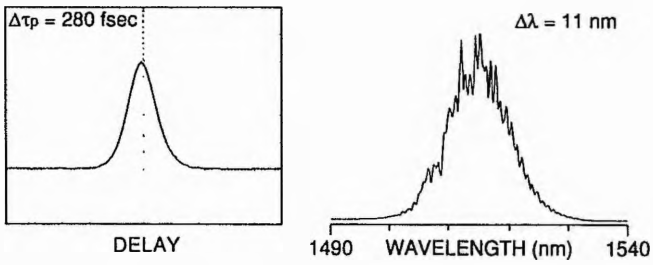

Fig. 2. Intensity autocorrelation (left, horizontal scale 370 fs/division) for the KCl:Tl^0(1) laser and corresponding spectrum (right). [The fine structure on the spectrum is due to étalon effects within the KCl:Tl^0(1) crystal and/or the cryostat windows.]

mode of the amplifier. A second half-wave plate was not available for this isolator, and so the return beam was polarized at approximately 45 deg relative to the master cavity. Beam splitter S_2, with reflectivity 50%, directed the feedback signal to the master cavity. As is usual for this type of configuration, the length of the control cavity was interferometrically matched to that of the master cavity by using a mirror mounted upon a PZT translator (driven by appropriate stabilization electronics[2]) to compensate for vibrations and thermal drift.

The InGaAsP double-channel planar buried heterostructure optical amplifier was antireflection coated on both facets. Measurements of the gain ripple indicated a mean TE modal reflectivity of ~0.2% at 1500 nm. It must be stressed that this is an internal reflectivity. Any beam coupled into the amplifier experiences an effective device reflectivity, which here was typically 2–10% depending on the drive current. With the antireflection coatings, the threshold for laser action was ~55 mA. At 1500 nm the TE small-signal resonant chip gain was measured to be 20 dB at 40 mA, with a peak gain of 21 dB near 1480 nm. The transparency current at 1500 nm was 6 mA, and at this wavelength the device had a small-signal absorption of 10 dB at a 2-mA drive current level. We estimated the carrier density recovery time to be ~400 ps at a 40-mA bias and the saturation energy E_{sat} to be 3–4 pJ.[15]

With the configuration as depicted in Fig. 1, no dropouts were observed when the Nd:YAG pump laser was mode locked, provided that the control cavity was well aligned. More significantly, the feedback was sufficiently strong to induce the mode locking to self-start when the pump laser was switched to cw emission. It was found that mode locking could be started reliably by temporarily reversing the polarity control of the stabilization electronics to make the PZT-mounted mirror position ramp repeatedly. With good alignment, mode locking was observed at interferometric intervals during the reset phase of the ramp cycle. The stabilization electronics were then switched to the original polarity to maintain stable mode locking.

Mode locking was observed with amplifier drive currents exceeding 20 mA, but the shortest pulses were observed at current levels above 35 mA. It was found that, by reducing the transmission of mirror M_0 from 22% to 7%, the pulse durations could be reduced from 440 to 280 fs. (Sech^2 intensity profiles are assumed throughout.) The intensity autocorrelation and the corresponding spectrum for such 280-fs pulses are shown in Fig. 2. In the generation of these shortest pulses, the bandwidth–duration product increased from 0.34 to 0.40, indicating either a small change in pulse shape or the presence of some excess frequency chirp.

Self-starting operation has also been observed for bias currents of approximately 2 mA. Mode locking was not achieved when M_0 had a transmission of 7%, whereas pulse durations of 480 and 560 fs were obtained when M_0 had transmissions of 12% and 22%, respectively. The relation between the pulse duration and the drive current is illustrated in Fig. 3 for a mirror M_0 transmission of 12%. In general the quality of the mode locking was inferior to that obtained with the higher bias currents, and ~3% amplitude noise was apparent on the pulse train.

We have also demonstrated self-starting operation for a NaCl:OH^- color-center laser in a configuration similar to that of the KCl:Tl^0(1) laser described above. The same semiconductor amplifier was employed, but both the master and the control cavity lengths were shortened by a factor of 2. In these preliminary studies, short-pulse operation was not observed when the NaCl:OH^- laser was synchronously pumped, but self-starting coupled-cavity mode locking was obtained when the laser was excited by cw emission from the Nd:YAG pump laser. This operation did not require any assistance by ramping the position of the PZT-mounted mirror. The relatively large difference in wavelength between the peak of the NaCl:OH^- gain (1590 nm) and the peak of the amplifier gain (1480 nm) necessitated the use of a 0.5-mm-thick quartz birefringent tuning plate to achieve mode locking. With a bias current of 50 mA, and with a mirror M_0 transmission of 22%, the pulse duration was 0.85 ps and the bandwidth–duration product was estimated to be 0.36 (see Fig. 4).

For both the KCl:Tl^0(1) and the NaCl:OH^- color-center lasers mode locking was not established at drive

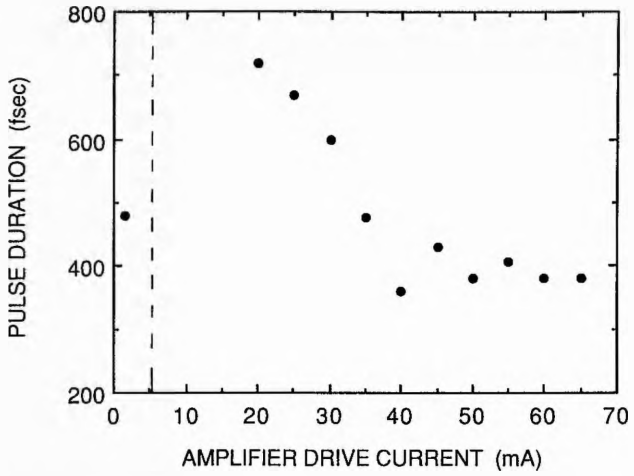

Fig. 3. Pulse duration as a function of amplifier drive current. The vertical dashed line denotes the transparency current.

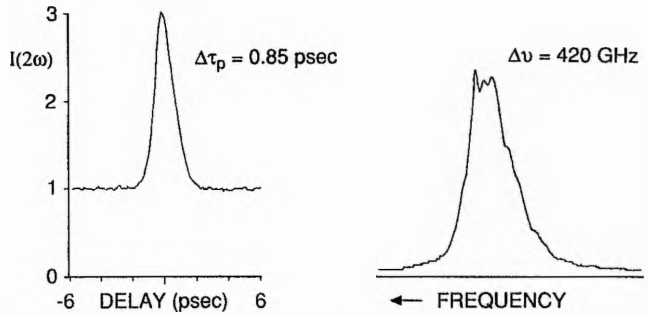

Fig. 4. Intensity autocorrelation (left) and corresponding spectrum (right) for the coupled-cavity mode-locked NaCl:OH^- laser operating at a wavelength of 1530 nm.

currents close to transparency. This implies that the dominant mechanism in the amplifier during the evolution of mode locking is the resonant nonlinearity associated with carrier density changes arising from gain saturation and absorption saturation. The estimated pulse-energy coupled into the amplifier, which was in the 3–10-pJ range, is indeed sufficient to cause strong saturation. Since the recovery time for these nonlinearities generally exceeds several hundred picoseconds, the experiment described here is not directly comparable with the modeling of Blow and Wood,[16] who assumed an instantaneous recovery for their amplifier or absorber element. It has been indicated that, if the nonlinearity in the control cavity has a slow recovery, then dynamic gain saturation in the master cavity will be important for pulse formation.[17] This could explain why the pulses became shorter when the transmission of mirror M_0 was reduced, because the average power within the master cavity was thereby increased.

The steady-state pulse durations are similar to the time scales of intraband relaxation processes, and we believe that a reduction in amplifier transmission associated with dynamic carrier heating may limit any further shortening of the pulses.

In summary, by using an InGaAsP optical amplifier in the control cavity we have demonstrated self-starting operation for coupled-cavity mode-locked KCl:Tl^0(1) and NaCl:OH^- color-center lasers. The energy-dependent (or flux-driven) nature of the slow nonlinearity assists self-starting by relaxing any requirements for strong mode beating or short noise bursts.

We thank G. D. Henshall of STC Technology Ltd, Harlow, Essex, for providing the amplifier details and C. I. Johnston for the coloration and preparation of the NaCl:OH^- crystal. We gratefully acknowledge overall financial support from the Science and Engineering Research Council UK.

References

1. L. F. Mollenauer and R. H. Stolen, Opt. Lett. **9,** 13 (1984).
2. F. M. Mitschke and L. F. Mollenauer, IEEE J. Quantum Electron. **QE-22,** 2242 (1986).
3. P. N. Kean, X. Zhu, D. W. Crust, R. S. Grant, N. Langford, and W. Sibbett, Opt. Lett. **14,** 39 (1989).
4. K. J. Blow and B. P. Nelson, Opt. Lett. **13,** 1026 (1988).
5. J. Mark, L. Y. Liu, K. L. Hall, H. A. Haus, and E. P. Ippen, Opt. Lett. **14,** 48 (1989).
6. C. P. Yakymyshyn, J. F. Pinto, and C. R. Pollock, Opt. Lett. **14,** 621 (1989).
7. F. Oullette and M. Piche, Opt. Commun. **60,** 99 (1988).
8. J. Goodberlet, J. Wang, J. G. Fujimoto, and P. A. Schulz, Opt. Lett. **14,** 1125 (1989).
9. J. R. M. Barr and D. W. Hughes, Appl. Phys. B **49,** 323 (1989).
10. J. Goodberlet, J. Jacobson, J. G. Fujimoto, P. A. Schulz, and T. Y. Fan, Opt. Lett. **15,** 504 (1990).
11. M. Morin and M. Piche, Opt. Lett. **14,** 1119 (1989).
12. M. N. Islam, E. R. Sunderman, C. E. Soccolich, I. Bar-Joseph, N. Sauer, T. Y. Chang, and B. I. Miller, IEEE J. Quantum Electron. **25,** 2454 (1989).
13. G. Sucha, M. Wegener, S. Weiss, and D. S. Chemla, in *Ultrafast Phenomena VII*, C. B. Harris, E. P. Ippen, G. A. Mourou, and A. H. Zewail, eds., Vol. 53 of Springer Series in Chemical Physics (Springer-Verlag, Berlin, 1990), p. 32.
14. U. Keller, W. H. Knox, and H. Roskos, in *Ultrafast Phenomena VII*, C. B. Harris, E. P. Ippen, G. A. Mourou, and A. H. Zewail, eds., Vol. 53 of Springer Series in Chemical Physics (Springer-Verlag, Berlin, 1990), p. 69.
15. P. B. Hansen, J. M. Wiesenfeld, G. Eisenstein, R. S. Tucker, and G. Raybon, IEEE J. Quantum Electron. **25,** 2611 (1989).
16. K. J. Blow and D. Wood, J. Opt. Soc. Am. B **5,** 629 (1988).
17. E. P. Ippen, L. Y. Liu, and H. A. Haus, Opt. Lett. **15,** 183 (1990).